

DISS. ETH NO. 26901

# HYGROMECHANICS AND SHAPE MEMORY OF WOOD CELL WALL INVESTIGATED WITH MULTISCALE MODELING

A thesis submitted to attain the degree of  
DOCTOR OF SCIENCES of ETH ZURICH  
(Dr. Sc. ETH Zurich)

presented by

CHI ZHANG

M. Eng. in Materials Engineering, University of Chinese Academy of Sciences

born on May 4<sup>th</sup>, 1989

citizen of China

accepted on the recommendation of

Prof. Dr. Jan Carmeliet, examiner  
Prof. Dr. Sinan Keten, co-examiner  
Prof. Dr. Andre Studart, co-examiner

2020



To Lishu and Shuyang,

Can the grass ever repay the spring sun's kindly rays?

## Abstract

Wood is an important material for mankind, not only because of its profound impact on the industry and everyday life, but also for its enormous potential for providing sustainable solutions to futuristic, advanced materials. One crucial characteristic of wood is the strong hygroscopicity. When subjected to moisture, a series of mechanical and physical phenomena are induced, such as swelling, weakening and shape memory effect, the fundamental mechanisms of which are still not clear. The difficulty originates from the limited resolution of current imaging methods and the intrinsic perplexing hierarchical nanoscale ultrastructure of wood. The ideal way to tackle these issues is to resort to numerical modeling that enables fast prototyping of material configurations with the knowledge of atomistic interactions. Therefore this study proposes a framework combining molecular dynamics and finite element method, where the microscopic mechanisms of various hygromechanical phenomena are elucidated at atomistic scale, and the crucial mechanical properties as functions of moisture extracted from molecular simulations are incorporated into finite element model that reducing the modeling complexity while retaining essential mechanisms.

Softwood cell wall S2 layer is a representative system of wood mechanics, containing various hydrophilic biopolymers as well as their interfaces that are intensely affected by hydration. There is considerable interest in characterizing the mechanical performance of the components of the S2 layer. Arabinoglucuronoxylan is modeled using molecular simulation presenting a general picture of the thermodynamic and mechanical response of hydrophilic biopolymer upon moisture adsorption. The heat of adsorption, heat capacity, thermal expansion and elastic moduli, all as functions of moisture, are found to approach the value of pure water and moreover show a crossover occurring around  $m \sim 0.3$ . The saturation of the first layer of adsorption and the subsequent fast growth of the second layer of adsorption is asserted to be the main mechanisms underneath the crossover. Another biopolymer, i.e. uncondensed lignin, is used as a prototype to probe the mechanisms of moisture-induced swelling and weakening effect. The microscopic motion of polymer chain segments, or more precisely the local stiffness which is the ratio of temperature to caging size, nearly perfectly relates to macroscopic stiffness of the material. As an extension, the similarity and difference of the impacts of heat and moisture on biopolymer mechanics are also discussed. The time-temperature-moisture superposition is only valid phenomenologically, whereas mechanistically heat and moisture are different as revealed by dynamics and energetics analyses.

Succeed in the investigation of bulk material, another aspect as important is the interfaces. Cellulose fibers feature superior tensile strength reinforcing the compliant matrix of the S2 layer. However, the overall mechanical performance of the composite is predominantly determined by the mechanics of the interfaces either between fibers or between fiber and matrix. Cellulose crystal interfaces display interfacial stick-slip behavior, where regardless of the various loading conditions, interfacial stress, shear velocity and interaction energy correlate with the density of interfacial

hydrogen bonds. Moisture excessively concentrates at the interface and reduces the strength by several times, which can be seen as a mechanism for the molecular switch. The moisture dependent properties are then transferred to finite element models. A series of composite models of different material arrangements and boundary conditions are examined, and a possible mechanism of moisture-induced shape memory emerges. Contrary to the conventional glass transition or (re)crystallization hypotheses, a mechanism dominated by the stick-slip behavior of the interface is proposed: first, the breakage and reformation of hydrogen bonding at the fiber-matrix interface serve as the molecular switch responsible for shape fixation and recovery; second, the elastic energy stored in the fibril serves as the driving force of shape recovery.

Following the exhibition of the hygromechanics of the basic components of the S2 layer, i.e. individual materials, matrices and interfaces, a state-of-the-art atomistic model softwood cell wall S2 layer complying with the most advanced experimental indications is proposed. The swelling coefficient, elastic moduli, and Poisson's ratio show good agreement with experiments. Comprehensive rule of mixture analysis is carried out on the rich compilation of wood polymer hygromechanical data, elucidating the mechanical roles of interphase, different components of cell wall material, etc.

In summary, this thesis presents a computational framework investigating the mechanics of a nanoscale fiber-reinforced composite, softwood cell wall S2 layer. The moisture dependent mechanical properties and mechanisms of moisture-induced swelling, weakening and shape memory effects are elucidated, filling the gap of experimental study and extends the understanding of the moisture effect on the fascinating natural material, wood.

## Zusammenfassung

Holz ist ein wichtiges Material für die Menschheit, nicht nur wegen seiner tiefgreifenden Auswirkungen auf die Industrie und den Alltag, sondern auch aufgrund seines enormen Potentials, nachhaltige Lösungen für futuristische, fortschrittliche Materialien bereitzustellen. Ein entscheidendes Merkmal von Holz ist die starke Hygroskopizität. Wenn es Feuchtigkeit ausgesetzt wird, treten verschiedene mechanische und physikalische Phänomene auf wie Schwellungs-, Schwächungs- und Formgedächtniseffekte deren zu Grunde liegende Mechanismen noch ungeklärt sind. Schwierigkeiten in der Erklärung dieser Effekte ergeben sich aus der begrenzten Auflösung aktueller, bildgebender Verfahren und der intrinsisch verkomplizierenden, hierarchischen Nano-Ultrastruktur von Holz. Lösungsansätze basieren auf numerischen Modellen, die ein schnelles Prototyping von Materialkonfigurationen mit dem Wissen über atomistische Wechselwirkungen ermöglichen. In dieser Arbeit wird ein Verfahren vorgeschlagen, das Molekulardynamik und Finite-Elemente-Methoden kombiniert. Dabei werden die mikroskopischen Mechanismen verschiedener hygromechanischer Phänomene auf atomarer Ebene aufgeklärt und die entscheidenden mechanischen Eigenschaften als Funktionen der aus molekularen Simulationen extrahierten Feuchtigkeit in das Finite-Elemente-Modell einbezogen. Dies verringert die Komplexität der Modellierung unter Beibehaltung wesentlicher Mechanismen.

Die Weichholzzellwand S2-Schicht ist ein repräsentatives System der Holzmechanik, das verschiedene hydrophile Biopolymere sowie deren Grenzflächen beinhaltet, welche stark von der Hydratation beeinflusst werden. Dabei besteht ein erhebliches Interesse an der Charakterisierung der mechanischen Leistung der Komponenten der S2-Schicht. Arabinoglucuronoxylan wird mithilfe einer molekularen Simulation modelliert, die ein allgemeines Bild der thermodynamischen und mechanischen Reaktion des hydrophilen Biopolymers auf die Feuchtigkeitsadsorption liefert. Die Adsorptionswärme, die Wärmekapazität, die Wärmeausdehnung und die Elastizitätsmodule, alle als Funktionen der Feuchtigkeit, nähern sich dem Wert von reinem Wasser an und zeigen darüber hinaus einen charakteristischen Übergang, der um  $m \sim 0,3$  auftritt. Die Sättigung der ersten Adsorptionsschicht und das anschließende schnelle Wachstum der zweiten Adsorptionsschicht werden hierbei als Hauptmechanismen unterhalb der Frequenzweiche identifiziert. Ein weiteres Biopolymer, d. h. nicht kondensiertes Lignin, wird als Prototyp verwendet, um die Mechanismen der feuchtigkeitsinduzierten Quell- und Schwächungswirkung zu untersuchen. Die mikroskopische Bewegung von Polymerkettensegmenten oder genauer die lokale Steifheit, die das Verhältnis von Temperatur zu Käfiggröße ist, korreliert nahezu perfekt mit der makroskopischen Steifheit des Materials. Als Erweiterung werden auch die Ähnlichkeiten und Unterschiede der Auswirkungen von Wärme und Feuchtigkeit auf die Biopolymermechanik diskutiert. Die Zeit-Temperatur-Feuchtigkeits-Überlagerung ist nur phänomenologisch gültig, denn Wärme und Feuchtigkeit unterscheiden sich mechanistisch wie aus dynamischen und energetischen Analysen hervorgeht.

Ein weiterer wichtiger Aspekt bei der Untersuchung der Volumenmaterialien sind die Schnittstellen. Cellulosefasern weisen eine überlegene Zugfestigkeit auf, die die nachgiebige

Matrix der S2-Schicht verstärkt. Die mechanische Gesamtleistung des Verbundwerkstoffs wird jedoch hauptsächlich durch die Mechanik der Grenzfläche zwischen verschiedenen Fasern oder zwischen Faser und Matrix bestimmt. Cellulosekristallgrenzflächen zeigen ein Grenzflächen-Stick-Slip-Verhalten, bei dem unabhängig von den verschiedenen Belastungsbedingungen Grenzflächenspannung, Schergeschwindigkeit und Wechselwirkungsenergie mit der Dichte der Wasserstoffbrückenbindungen an der Grenzfläche korrelieren. Feuchtigkeit konzentriert sich übermäßig an der Grenzfläche und verringert die Festigkeit um ein Vielfaches, welches als Mechanismus für den molekularen Schalter angesehen werden kann. Die feuchtigkeitsabhängigen Eigenschaften werden dann auf Finite-Elemente-Modelle übertragen. Eine Reihe von Verbundmodellen unterschiedlicher Materialanordnungen und Randbedingungen wird untersucht, und ein möglicher Mechanismus des feuchtigkeitsinduzierten Formgedächtnisses ergibt sich. Im Gegensatz zu den herkömmlichen Hypothesen zum Glasübergang oder zur (Re-) Kristallisation wird ein Mechanismus vorgeschlagen, der vom Stick-Slip-Verhalten der Grenzfläche dominiert wird: Erstens dienen der Bruch und die Reformation der Wasserstoffbindung an der Faser-Matrix-Grenzfläche als molekularer Schalter, der für die Formfixierung und Wiederherstellung verantwortlich ist; zweitens dient die in der Fibrille gespeicherte elastische Energie als treibende Kraft für die Formwiederherstellung.

Nach dem Aufzeigen der Hygromechanik der Grundkomponenten der S2-Schicht, d. h. einzelner Materialien, Matrizen und Grenzflächen, wird eine aktuelle atomistische Modell-Weichholzzellwand-S2-Schicht vorgeschlagen, die den fortschrittlichsten experimentellen Angaben entspricht. Der Quellkoeffizient, die Elastizitätsmodule und das Poisson-Verhältnis stimmen gut mit Experimenten überein. Eine umfassende Mischungsregelanalyse wird für die umfassende Zusammenstellung hygromechanischer Daten von Holzpolymeren durchgeführt, wobei die mechanischen Rollen der Interphase, verschiedener Komponenten des Zellwandmaterials etc. aufgeklärt werden.

Zusammenfassend stellt diese Arbeit eine Methode zur computergestützten Untersuchung der Mechanik eines nanoskaligen, faserverstärkten Verbundwerkstoffs der Weichholz Zellwand S2-Schicht vor. Die feuchtigkeitsabhängigen, mechanischen Eigenschaften und die Mechanismen feuchtigkeitsbedingter Quell-, Schwächungs- und Formgedächtniseffekte werden aufgeklärt, wodurch die Lücke der experimentellen Untersuchung geschlossen und das Verständnis des Feuchtigkeitseffekts auf das faszinierende Naturmaterial Holz erweitert wird.

## Acknowledgment

Curiosity, the strong drive of my mind, has always been motivating me to learn and carry out research. Without the kind help of many people, it would be impossible for me to enjoy the pleasure of exploring the unknown ground of human knowledge fully. Here I would like to state my acknowledgments to those who enlightened and supported me and made this challenging research possible.

First of all, I would like to express my immense gratitude to my supervisors, Prof. Jan Carmeliet and Prof. Dominique Derome. Their expertise, integrity, passion, connections and strict demand for quality profoundly influence me and lay a solid foundation for this thesis. Prof. Dominique Derome guided me to the frontiers of the fascinating world of wood research, handed over her precious research project on the shape memory of wood and supports me with her best effort. The discussions with Prof. Jan Carmeliet are always inspiring and filled with insightful advice, which significantly broadens my horizon and deepens my understanding of research. Several years of co-working experiences gave us plenty of opportunities to exchange ideas far beyond science and research. They are role models from all aspects.

I sincerely thank my collaborators, Dr. Benoit Coasne, Prof. Robert Guyer, Prof. Sinan Keten, Prof. Lennart Salmen. It is a great privilege for me to work closely with these top-tier scientists. The fruitful discussion we had and the informed opinions they gave are the treasures of this thesis. I express my special gratitude to Dr. Karol Kulasinski, whose pioneering work inspires the early stage of this thesis.

I owe gratitude to my colleagues in the group who shared the joy and sorrow with me and supported me on numerous occasions. Thank Martina Koch-Jetzer for her administrative assistance. Thank the dear fellows, Dr. Mingyang Chen, Dr. Feifei Qin, Dr. Lento Manickathan, Dr. Omid Dorostkar, Dr. Sreeyuth Lal, Dr. Jaebong Lee and many others, for their diverse senses of humor and practical suggestions which greatly relieved my stress.

The generous funding from the Swiss national science foundation and the Swiss tax-payers is appreciated. The ideal working and living conditions in Switzerland facilitated me to concentrate on the research.

It is not possible to find the words to thank my family, Lishu Shao, Shuyang Zhang, Qingling Li, Lianbo Wang, Xuyi Wang and particularly the love of my life, Dr. Xiaopu Wang, who devoted hearts and souls to the well-being of mine.

Chi Zhang

May 2020



# Contents

|  |            |
|--|------------|
| <b>ABSTRACT</b> .....  | <b>I</b>   |
| <b>ZUSAMMENFASSUNG</b> .....   | <b>III</b> |
| <b>ACKNOWLEDGMENT</b> .....  | <b>V</b>   |
| <b>CONTENTS</b> .....  | <b>VI</b>  |
| <b>NOTATION</b> .....  | <b>IX</b>  |
| <b>LIST OF ACRONYMS</b> .....  | <b>X</b>   |
| <b>CHAPTER 1 INTRODUCTION</b> .....  | <b>1</b>   |
| 1.1 MOTIVATION AND BACKGROUND .....  | 1          |
| 1.2 SCOPE AND OBJECTIVES.....  | 2          |
| 1.3 OUTLINE OF THE THESIS.....   | 4          |
| <b>CHAPTER 2 STATE OF THE ART</b> .....  | <b>6</b>   |
| 2.1 WOOD CELL WALL S2 LAYER CHEMICAL COMPOSITION AND MATERIAL ARRANGEMENT .....  | 6          |
| 2.1.1 <i>Wood subcellular arrangement</i> .....  | 6          |
| 2.1.2 <i>Cellulose</i> .....   | 8          |
| 2.1.3 <i>Hemicelluloses</i> .....  | 10         |
| 2.1.4 <i>Lignins</i> .....   | 11         |
| 2.1.5 <i>S2 material organization</i> .....  | 12         |
| 2.1.6 <i>Summary of wood chemical composition and material arrangement</i> .....   | 15         |
| 2.2 MECHANICAL ASPECTS OF WOOD-MOISTURE RELATIONSHIP .....   | 15         |
| 2.2.1 <i>Moisture sorption</i> .....   | 16         |
| 2.2.2 <i>Moisture-induced deformation</i> .....  | 17         |
| 2.2.3 <i>Moisture-induced mechanical weakening</i> .....   | 18         |
| 2.2.4 <i>Moisture-induced shape memory effect</i> .....  | 22         |
| 2.2.5 <i>Summary of mechanical aspect of wood-moisture relationship</i> .....  | 23         |
| 2.3 COMPUTATIONAL STUDY OF S2 LAYER AT WOOD CELL WALL SCALE.....   | 23         |
| 2.3.1 <i>Continuum methods: micromechanics and poromechanics</i> .....   | 23         |
| 2.3.2 <i>Discrete method: atomistic and coarse-grain simulations</i> .....   | 27         |
| 2.4 CHALLENGES AND RESEARCH NEEDS.....   | 32         |
| 2.5 CONCLUSION .....   | 34         |
| <b>CHAPTER 3 MOISTURE-INDUCED CROSSOVER IN THE THERMODYNAMIC AND MECHANICAL RESPONSE OF A HYDROPHILIC BIOPOLYMER: SOFTWOOD XYLAN</b> ..... | <b>35</b>  |
| 3.1 INTRODUCTION .....   | 35         |
| 3.2 MATERIALS AND METHODS .....  | 36         |
| 3.2.1 <i>Chemical structure and atomistic modeling of arabinoglucuronoxylan</i> .....  | 36         |
| 3.2.2 <i>Simulation of water sorption</i> .....  | 37         |
| 3.2.3 <i>Material properties measurement</i> .....   | 38         |
| 3.2.4 <i>Validation of the atomistic model</i> .....   | 43         |
| 3.3 RESULTS AND DISCUSSIONS .....  | 45         |

|                  |   |            |
|------------------|---|------------|
| 3.3.1            | <i>Properties as a function of moisture content and occurrence of moisture-induced crossover</i>            | 45         |
| 3.3.2            | <i>Mechanisms of moisture-induced transition</i>  | 49         |
| 3.3.3            | <i>The general picture of moisture adsorption</i>   | 58         |
| 3.4              | CONCLUSION  | 59         |
| <b>CHAPTER 4</b> | <b>DISENTANGLING HEAT AND MOISTURE EFFECTS ON BIOPOLYMER MECHANICS: A CASE STUDY OF<br/>SOFTWOOD LIGNIN</b> | <b>61</b>  |
| 4.1              | INTRODUCTION  | 61         |
| 4.2              | MATERIALS AND METHODS   | 63         |
| 4.2.1            | <i>Preparation of the hydrated lignin system</i>  | 63         |
| 4.2.2            | <i>Evaluation of the free strain</i>  | 66         |
| 4.2.3            | <i>Evaluation of the bulk modulus</i>   | 66         |
| 4.2.4            | <i>Evaluation of the density of the polymer-polymer hydrogen bonds</i>                                      | 67         |
| 4.2.5            | <i>Evaluation of the local stiffness</i>  | 67         |
| 4.3              | RESULTS   | 69         |
| 4.3.1            | <i>Macroscopic results: heat and moisture-induced free strain and mechanical weakening</i>                  | 69         |
| 4.3.2            | <i>Microscopic results: weakening and straining explained by local stiffness</i>                            | 69         |
| 4.3.3            | <i>Link between microscopic and macroscopic results</i>   | 70         |
| 4.4              | DISCUSSION: BEYOND THE SIMILARITY OF HEAT AND MOISTURE  | 74         |
| 4.4.1            | <i>Free strain - the difference between the impacts of moisture and heat</i>                                | 74         |
| 4.4.2            | <i>Primary and secondary bond energy – different impacts of moisture and heat</i>                           | 76         |
| 4.5              | CONCLUSION  | 78         |
| <b>CHAPTER 5</b> | <b>CELLULOSE NANOCRYSTALS UNDERGOING FRICTIONAL STICK-SLIP</b>  | <b>79</b>  |
| 5.1              | INTRODUCTION  | 79         |
| 5.2              | MATERIAL AND METHOD   | 81         |
| 5.2.1            | <i>Cellulose nanocrystal structure and its molecular modeling</i>   | 81         |
| 5.2.2            | <i>Pulling tests and boundary conditions</i>  | 83         |
| 5.2.3            | <i>Measurements</i>   | 86         |
| 5.3              | RESULTS   | 87         |
| 5.3.1            | <i>Stick-slip behavior of dry and aligned interfaces undergoing shearing tests</i>                          | 87         |
| 5.3.2            | <i>Impact of moisture and misalignment</i>  | 93         |
| 5.3.3            | <i>Central role of hydrogen bond revealed by correlation analysis</i>                                       | 98         |
| 5.3.4            | <i>Adhesion energy of the interfaces</i>  | 101        |
| 5.4              | DISCUSSION  | 103        |
| 5.5              | CONCLUSION  | 106        |
| <b>CHAPTER 6</b> | <b>MECHANICS OF THE FIBER-MATRIX INTERFACE IN WOOD CELL WALL</b>  | <b>107</b> |
| 6.1              | INTRODUCTION  | 107        |
| 6.2              | MATERIALS AND METHODS   | 108        |
| 6.2.1            | <i>Preparation of the composite system</i>  | 108        |
| 6.2.2            | <i>Hydration</i>  | 111        |
| 6.2.3            | <i>Pulling test</i>   | 111        |
| 6.2.4            | <i>Measurements</i>   | 112        |
| 6.3              | RESULTS   | 113        |

|   |  |                                     |
|---|--|-------------------------------------|
| 6.3.1   | <i>Swelling of the composite and the constraining effect of fiber</i>        | 113                                 |
| 6.3.2   | <i>Composition and configuration of the interphase</i>                       | 114                                 |
| 6.3.3   | <i>Interface friction mechanics revealed by pulling tests</i>                | 117                                 |
| 6.4   | DISCUSSION   | 122                                 |
| 6.5   | CONCLUSION   | 123                                 |
| <b>CHAPTER 7 TOWARDS UNRAVELING THE MOISTURE-INDUCED SHAPE MEMORY EFFECT OF WOOD: THE ROLE OF INTERFACE MECHANICS</b> |  | <b>124</b>                          |
| 7.1   | INTRODUCTION   | 124                                 |
| 7.2   | METHOD   | 126                                 |
| 7.2.1   | <i>Geometry of the model</i>   | 126                                 |
| 7.2.2   | <i>Constitutive laws of the components and the interfaces</i>                | 129                                 |
| 7.2.3   | <i>Boundary conditions and loading protocol</i>                              | 131                                 |
| 7.3   | SHAPE MEMORY MECHANISM   | 132                                 |
| 7.3.1   | <i>Shape memory effect in the three models</i>                               | 132                                 |
| 7.3.2   | <i>The origin of shape memory effect: fixation and recovery mechanisms</i>   | 139                                 |
| 7.3.3   | <i>At the core of interface-controlled shape memory effect</i>               | 141                                 |
| 7.4   | DISCUSSION AND PERSPECTIVES  | 143                                 |
| 7.5   | CONCLUSIONS  | 143                                 |
| <b>CHAPTER 8 MECHANICS OF SOFTWOOD CELL WALL LAYER STUDIED WITH MOLECULAR SIMULATIONS</b>                             |  | <b>145</b>                          |
| 8.1   | INTRODUCTION   | 145                                 |
| 8.2   | MATERIALS AND METHODS  | 147                                 |
| 8.2.1   | <i>Preparation of dry polymer systems</i>                                    | 147                                 |
| 8.2.2   | <i>Hydration</i>   | 155                                 |
| 8.2.3   | <i>Characterization</i>  | 156                                 |
| 8.3   | RESULTS  | 160                                 |
| 8.3.1   | <i>Hygromechanics of S2-related materials and composites</i>                 | 160                                 |
| 8.3.2   | <i>Mixture rule analyses</i>   | 167                                 |
| 8.3.3   | <i>Structure of S2 model and the mechanics of its fiber-matrix interface</i> | 181                                 |
| 8.3.4   | <i>Enrichment of matrix and water at interface</i>                           | 181                                 |
| 8.3.5   | <i>Interface weakening and hydrogen bonding</i>                              | 183                                 |
| 8.4   | DISCUSSION AND PERSPECTIVES  | 186                                 |
| 8.5   | CONCLUSION   | 187                                 |
| <b>CHAPTER 9 CONCLUSIONS AND PERSPECTIVES</b>   |  | <b>189</b>                          |
| 9.1   | SUMMARY  | 189                                 |
| 9.2   | CONTRIBUTION TO THE RESEARCH FIELD   | 192                                 |
| 9.3   | OUTLOOK AND FUTURE WORK  | 193                                 |
| <b>BIBLIOGRAPHY</b>   |  | <b>197</b>                          |
| <b>CURRICULUM VITAE</b>   |  | <b>ERROR! BOOKMARK NOT DEFINED.</b> |

## Notation

|                       |  |  |
|-----------------------|--|--|
| #HB                   | number of hydrogen bond                    | -                                      |
| $\langle u^2 \rangle$ | cage size                                  | nm <sup>2</sup>                        |
| $a$                   | size of chain segment                      | nm                                     |
| $c$                   | wave speed in material                     | nm ns <sup>-1</sup>                    |
| $C_P$                 | heat capacity                              | kJ kg <sup>-1</sup> K <sup>-1</sup>    |
| $E$                   | Young's modulus                            | GPa                                    |
| $F$                   | Helmholtz free energy                      | J mol <sup>-1</sup>                    |
| $f_v$                 | volume fraction                            | -                                      |
| $G$                   | shear modulus                              | GPa                                    |
| $H$                   | enthalpy                                   | J mol <sup>-1</sup>                    |
| $k$                   | spring constant                            | J m <sup>-2</sup>                      |
| $K$                   | bulk modulus                               | GPa                                    |
| $k_B$                 | Boltzmann constant                         | J K <sup>-1</sup>                      |
| $m$                   | moisture content                           | -                                      |
| $P$                   | pressure                                   | Pa                                     |
| $Q$                   | integral heat of adsorption                | J mol <sup>-1</sup>                    |
| $R$                   | gas constant                               | J K <sup>-1</sup> mol <sup>-1</sup>    |
| RH                    | relative humidity                          | -                                      |
| $T$                   | temperature                                | K                                      |
| $U$                   | internal energy                            | J mol <sup>-1</sup>                    |
| $V$                   | volume                                     | nm <sup>3</sup>                        |
| $v$                   | speed                                      | m s <sup>-1</sup>                      |
| $w$                   | mass ratio                                 | -                                      |
| $\alpha$              | thermal expansion coefficient              | kJ kg <sup>-1</sup>                    |
| $\beta$               | swelling coefficient                       | -                                      |
| $\gamma$              | shear strain or deflection ratio           | -                                      |
| $\delta$              | solubility parameter                       | cal <sup>-1/2</sup> cm <sup>-3/2</sup> |
| $\hat{\delta}$        | fraction of inter-component hydrogen bonds | -                                      |
| $\varepsilon$         | normal strain                              | -                                      |
| $\eta$                | moisture content ratio between components  | -                                      |
| $\lambda$             | linear density                             | g nm <sup>-1</sup>                     |
| $\mu$                 | chemical potential                         | J mol <sup>-1</sup>                    |
| $\nu$                 | Poisson's ratio                            | -                                      |
| $\rho$                | density                                    | g cm <sup>-3</sup>                     |
| $\sigma$              | normal stress                              | GPa                                    |
| $\tau$                | shear stress                               | GPa                                    |
| $\varphi$             | porosity                                   | -                                      |
| $\omega$              | intrinsic vibration frequency              | ns <sup>-1</sup>                       |

## List of acronyms

|       |   |
|-------|---|
| AC    | amorphous cellulose                               |
| AFM   | atomic force microscopy                           |
| AGX   | arabinoglucuronoxylan                             |
| ATB   | automated topology builder                        |
| CC    | crystalline cellulose                             |
| CED   | cohesive energy density                           |
| cLGN  | condensed lignin                                  |
| DGD   | double Gaussian decomposition                     |
| DP    | degree of polymerization                          |
| DSC   | differential scanning calorimetry                 |
| FKT   | Frenkel-Kontorova-Tomlinson model                 |
| GAB   | Guggenheim-Anderson-de Boer model                 |
| GGM   | galactoglucomannan                                |
| HB    | hydrogen bond                                     |
| HOF   | Herman's orientation function                     |
| LCC   | lignin-carbohydrate-complex                       |
| MD    | molecular dynamics                                |
| MFA   | microfibril angles                                |
| MSD   | mean square displacement                          |
| NMR   | nuclear magnetic resonance                        |
| NPT   | isothermal-isobaric ensemble                      |
| OSP   | one-step perturbation                             |
| RH    | relative humidity                                 |
| RoM   | rule of mixture                                   |
| SPC   | single-point charge water model                   |
| SPC/E | single-point charge extended water model          |
| SSE   | sum of squared errors                             |
| TEC   | thermal expansion coefficient                     |
| TEM   | transmission electron microscopy                  |
| TTMSP | time-temperature-moisture superposition principle |
| TTSP  | time-temperature superposition principle          |
| uLGN  | uncondensed lignin                                |
| WAXS  | wide angle X-ray scattering                       |
| WLF   | Williams-Landel-Ferry equation                    |
| XRD   | X-ray diffraction                                 |

# Chapter 1 Introduction

## 1.1 Motivation and background

A versatile resource, wood has been employed over the ages as source of energy, material for furniture and tools, in construction of structures and buildings, source of pulp for making paper and so forth, covering vital aspects of the well-being of humans. Despite the availability of numerous innovative synthesized and fabricated materials, wood remains highly used nowadays, due to its many merits and advantages over counterparts. Firstly, wood is sustainable and eco-friendly, with a natural production mounting up to billions of tons per year, capturing and storing tons of the greenhouse gas CO<sub>2</sub>, as such contributing to limit climate change. Wood is used as biofuel, especially in developing countries for cooking and heating, but also in developed countries as a renewable energy source, as it is considered to be carbon neutral over its total carbon cycle. Secondly, wood has exceptional mechanical properties offering high stiffness with a high strength-mass ratio, a value comparable to or better than steel. Wood is nowadays used for manufacturing engineered wooden products by bonding together wood strands, veneers, lumber or other forms of wood fiber with adhesives to form larger, more efficient composite structural units. Wood is also used as a raw material for producing new materials, such as oriented strand board, hardboard and medium-density fiberboard used in manifold applications. Moreover, wood fibers are more and more used as reinforcement in new materials and composites. Thirdly, wood is made with various biopolymers organized in sophisticated ultrastructures displaying great potential for modification and functionalization, such as highly transparent wood (Zhu et al. 2016b) and stimuli-responsive wood (Keplinger et al. 2016). The merits of wood go on further, justifying wood as a strong candidate for innumerable applications and fields in the future.

In terms of material mechanics, wood is a porous fiber-reinforced composite material, actually, a masterpiece of evolution, which has a multiscale hierarchical structure, ranging from meter-scale all the way down to the nanometer scale. Taking softwood as an example, the cellular structure consists of mostly longitudinal tracheid cells and ~ 5 % ray horizontal cells. The large internal cavities of cells are referred to as lumens, enclosed by the cell walls which are multi-layer structures, consisting of primary (P) and three secondary layers (S1, S2 and S3). The S2 layer is the thickest and is the most important for the mechanical performance of wood. Cellulose fibers in S2 embedded in a hemicellulose and lignin matrix are at a small angle to the longitudinal axis of the cells and, due to their crystallinity, contribute highly to the strength and stiffness of wood.

Wood is strongly hygroscopic. The adsorption of ambient moisture yields physical and mechanical effects, such as anisotropic dimensional change due to swelling and shrinkage, non-linear mechanical weakening with increasing moisture content, and even shape memory. These hygromechanical behaviors are deemed to originate from the ultrastructure of cell wall material. The cellulose fiber and the adjacent hemicelluloses compose the microfibrils which have an aspect

ratio of  $\sim 50$ . The space between microfibrils is filled with other types of hemicelluloses and lignins. One of the most intriguing hygromechanical behavior of wood is the moisture-induced shape memory effect, where the deformed wood is fixed at an intermediate shape under the dry condition and recovers its original shape when wetted again. Although it is possible to modify almost permanently the shape of wood under different procedures, in certain cases, the recovery from the dried deformed state to the original undeformed state during water sorption is possible and undesirable. In other cases, full shape memory, i.e. full recovery from the deformed state, is wanted. An understanding of the fundamental mechanism of this moisture-induced shape memory effect, which is unfortunately still missing, may provide guidance on either recovery prevention or invention of natural actuators made of wood tissues. For regaining its original configuration, the system must shelter a mechanism that harbors the original shape. For wood, an interesting insight comes from biology recent atomic force microscopy studies that have revealed that cellulose microfibrils may merge into direct contact with each other, forming so-called “biomechanical hotspot”, forming or playing a role in a fiber network that could maintain a history of the shape. The validation and the explanation of the possible function of such material arrangement call for nanoscale investigations with high spatiotemporal resolutions, which is beyond the capability of contemporary instruments. To address these issues, a multiscale computational modeling study is warranted.

## **1.2 Scope and objectives**

Numerous studies exist on the topic of wood-moisture relations, most of which are macroscopic or phenomenological on the timber or cellular scale. Recent experimental investigations, using atomic force microscopy, X-ray tomography and others shed light on the micro- to nanometer-scale structures, their behavior and impact on cell wall material. There remains still a dearth of examination and elucidation of the microscopic mechanisms of the wood moisture-related behavior.

This thesis aims at revealing the microscopic mechanisms of a series of moisture-induced phenomena of softwood cell wall S2 layer, including swelling, mechanical weakening and moisture-induced shape memory effect. Softwood is specifically chosen, because it is the dominant wood stock in the Northern Hemisphere (Rennel and Dillén 2001), within a belt covering Northern Europe, Russia and North America. It is noted that the numerical framework of multiscale modeling of softwood cell wall materials and structures proposed in this thesis is nevertheless applicable to all wood species.

With the engineering goal of building a multiscale model, relying on both molecular dynamics (MD) and finite element (FEM) computational methods of the softwood cell wall S2 layer, the scope of this thesis is defined as follows. Several important components of the wood cell wall, specifically arabinoglucuronoxylan and a condensed type of lignin, have not been fully characterized experimentally due to the difficulty of extraction without altering their chemical structure. Through molecular modeling, the thermodynamics and mechanical properties of these

two materials will be presented to fill the gap in the literature. Meanwhile, these biopolymers will be employed as prototypical molecules to investigate the fundamental impact of hydration on the materials. Besides the bulk properties of components, relevant interfaces in S2 are also investigated, as well as their dependency on moisture. Various components are used to build up the atomistic model of the S2 layer under the most advanced structural assumptions from the literature. Atomistic simulations provide particularly interesting microscopic information, including hydrogen bonding and change of structure of polymers and their interfaces under hydration. With the harvested hygromechanical properties of involved materials, interfaces and composites, the molecular information is then used to implement a finite element model which permits much faster prototyping of models for the S2 layer with different material arrangements at larger length scales, and which facilitates the research on wood cell wall hygro-mechanics.

The main investigation efforts are placed into analyzing the topological, structural, dynamic and energetic ramifications of moisture adsorption, establishing the link from microscopic state to macroscopic mechanical performance and identifying the crucial factors in terms of hygromechanics. The softwood cell wall S2 layer composite is a polymeric material. Therefore, it is natural to relate the investigations with the established polymer research framework and contribute to this field. The tool, molecular simulation, is based on statistical thermodynamics with a rigorous physics basis and thus allows mechanistic discussion of the physics and mechanics of bulk materials, biopolymer interfaces and composites that may impact fields beyond wood research, such as polymers and composite materials.

In summary, the main scientific objectives of this thesis are to:

1. Advance the current understanding of hydration impact on biopolymer thermodynamics and mechanics and to demonstrate the structural evolution of biopolymer upon sorption and presenting the structure-property relation.
2. Provide a mechanistic elucidation and physical explanation of the moisture-induced swelling and mechanical weakening, to identify the pivotal factors at play of these hygro-mechanical phenomena.
3. Offer a complete dataset regarding hygro-mechanical properties of softwood biopolymers, filling the gaps of experimental studies and rendering critical material data to modeling studies of wood.
4. Characterize the influence of moisture on the prevailing interfaces of softwood cell wall layer, namely fiber-fiber and fiber-matrix interfaces, and to reveal the origin of interface stiffness and of its weakening upon moistening.
5. Present a methodological framework for the multiscale study of biopolymer composites combining MD and FEM, where the atomistic interactions are vital, however, the system size is exceedingly computationally expensive to be modeled fully atomistically so that proper upscaling is necessary.



6. Improve the molecular level knowledge of wood cell wall layers and to demonstrate the role of factors such as hydrogen bonds, interphase structure and different components in wood cell wall hygromechanics.
7. Unravel the mechanism of the moisture-induced shape memory effect of wood cell wall layers.

### **1.3 Outline of the thesis**

This thesis comprises nine chapters where, as is habitual, the initial and final chapters are the introduction, state of the art and conclusions. The main body is organized in the order of intricacy of the modeled systems, i.e. from individual polymers (Chapter 3 xylan and Chapter 4 lignin), interfaces (Chapter 5 cellulose-cellulose, Chapter 6 cellulose-matrix) to multi-component composites (Chapter 7 surrogate model and Chapter 8 S2 model).

Chapter 1 is the introduction of the thesis, where the background and motivation are depicted and the scope of the thesis is detailed with the aims defined.

Chapter 2 covers the state of the art of wood cell wall studies. The most recent literature on the wood cell wall chemical composition and material arrangements is summarized, and the undetermined issues are delineated. Experimental and computational studies of wood-moisture relationships are documented with a focus on sorption induced mechanical phenomena, including swelling, weakening and shape memory effects. The most advanced numerical modeling methodologies of cell wall S2 layer are reviewed and the possible paths of improvement are described.

Chapter 3 presents a general picture of the impact of moisture on a hydrophilic biopolymer, arabinoglucuronoxylan. Several mechanical and thermodynamic properties, such as elastic constants and heat capacity, are reported all as their dependency on moisture, where a moisture-induced crossover behavior is identified. The mechanism of the crossover is attributed to the water undergoing a layering in adsorption.

Chapter 4 concerns the microscopic mechanisms of moisture-induced swelling and weakening of a second biopolymer, i.e. uncondensed type of lignin. A model relating a microscopic quantity, referred to as local stiffness, to the macroscopic stiffness of the material is proposed, presenting a long-time missing piece of information of the structure-property relationship. The similarity and the differences between hydration and heating in terms of impact on mechanics are discussed.

Chapter 5 deals with the interfacial mechanics of cellulose crystals. The impacts of interfacial moisture, misalignment, loading direction and surface type are systematically examined. A series of findings are displayed, including stick-slip behavior, stiffness recovery after an irreversible slip, different behavior along with opposite shearing directions and weakening effect by hydration and/or misalignment, all of which can be explained by the density, orientation or distribution of the interfacial hydrogen bonds.

Chapter 6 tackles the mechanics of another type of interface, i.e. crystalline cellulose-amorphous matrix interface. The composition and structure of a region near the crystalline phase, referred to as the interphase, are documented, followed by the investigation of the combined roles of moisture and interphase stiffness on the interfacial shear strength. Moisture is found to excessively adsorb at the interface which significantly lowers the friction force, like what is found in the previous chapter for the cellulose-cellulose interface.

Chapter 7 proposes a possible mechanism for the moisture-induced shape memory effect of wood cell wall material, namely the molecular switch, with is a type of interface where the shear stress is altered greatly by moisture, controlling lock and release of potential energy. The interface mechanics extracted from molecular simulations in the previous two chapters are implemented into three finite element models representing different configurations of the cell wall.

Chapter 8 offers a state-of-the-art softwood cell wall S2 layer atomistic model, of which chemical composition and material arrangements comply with the most recent knowledge in this field. An unprecedented compilation of wood polymer hygromechanical data is presented, based on which a comprehensive mixture rule analysis is conducted trying to unravel the interactions between the matrix polymers and between matrix and crystalline cellulose and their impact on the composite behavior. Galactoglucomannan is found to play a critical role by forming strong connections with both cellulose fiber and interfibril matrices. The interaction effect is found nontrivial and the mixture rules taking the presence of an interphase into account show good agreement with atomistic modeling measurement.

Chapter 9 summarizes the thesis with conclusions and contributions. The outlooks and perspectives are depicted and possible future studies are envisaged.

## Chapter 2 State of the Art

This chapter covers the state of the art of knowledge and research on the moisture behavior of the S2 layer in wood cell wall. The chapter starts with reviewing the chemical composition and material arrangement of a softwood cell wall S2 layer, then discusses moisture-induced mechanical phenomena and finally addresses recent computational studies of wood hygromechanical behavior with continuum and discrete approaches, namely finite element method (FEM) and molecular dynamics (MD). Based on the state of the art, research gaps are identified.

### 2.1 Wood cell wall S2 layer chemical composition and material arrangement

This section summarizes the current status of the research on chemical composition and material organization of wood cell wall, with the focus on its mechanical aspects. Wood is a hierarchical porous material with different structural arrangements ranging from meter to nanometer scales, i.e. going from timber, growth ring configuration, towards cellular and sub-cellular arrangements as shown in Figure 2-1a. Growth rings are present in trees exposed to seasonal variations, e.g. Northern Hemisphere species display differences between spring (early) and summer (late) wood structures. The cellular structure is different for softwood (evergreen) and hardwood (deciduous) species, as hardwood displays also large conduits called vessels, in addition to tracheids and parenchyma cells.

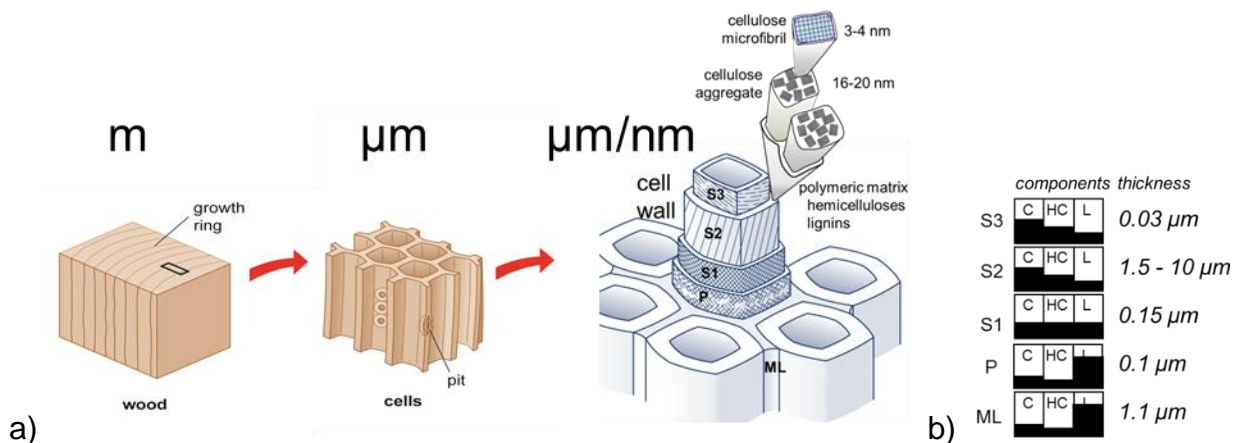


Figure 2-1 a) Hierarchical structure of wood, (Derome et al. 2012 with permission), ML middle lamella, P primary layer, S secondary layer. b) Chemical composition in proportion and thickness of different layers of wood cell walls, C cellulose, HC hemicelluloses, L lignins (Derome et al. 2012 with permission).

#### 2.1.1 Wood subcellular arrangement

Built as an exoskeleton to the living cell in the cambium, the wood cell wall is a layered composite structure synthesized and deposited by the cell. The density of the wood cell wall is generally  $\sim 1.5 \text{ g/cm}^3$ , independently from species (Stamm 1938).

Usually, wood cell walls possess three layers, i.e. middle lamella, primary and secondary cell wall layers. These three layers are different in chemical composition and material arrangement. As shown in Figure 2-1b, the three main categories of polymers, i.e. cellulose, hemicelluloses and lignins, are present in all layers of the cell, with in proportion more cellulose in the secondary wall layers and more lignins in the primary layer and the middle lamella. Figure 2-2a is an atomic force microscopy (AFM) image of a poplar cell wall.

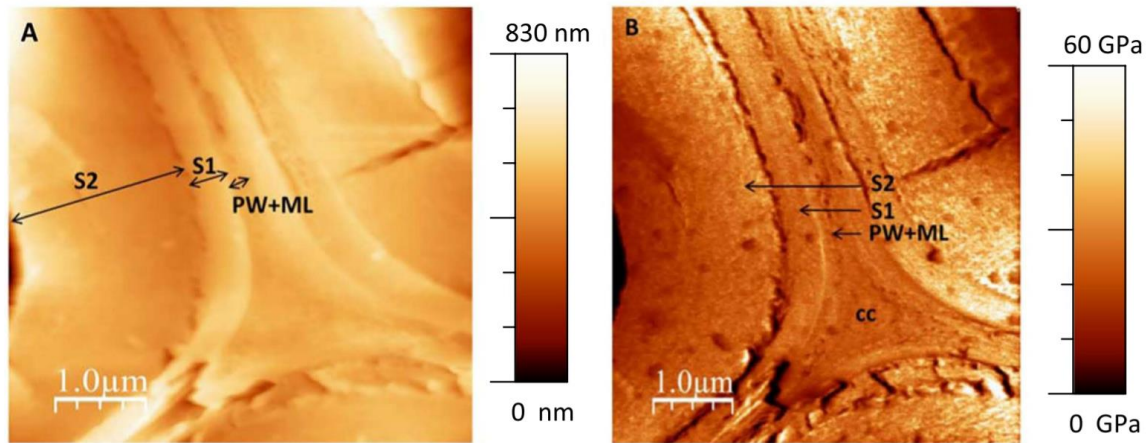


Figure 2-2 a) AFM image of the topography of a plant cell wall. b) Cartography of indentation modulus obtained by AFM (Muraille et al. 2017 with permission).

The formation of the cell wall has many steps (Cosgrove 2005; Samuels et al. 2006). During cell division, one cell is split into two due to the formation of a cell plate, which later turns into the middle lamella, a layer functioning as intercellular adhesion. During growth, the primary cell wall layer is a water-saturated composite, possessing 3~4 layers of randomly oriented cellulose microfibrils. It is thin and abundant in flexible hemicellulose and pectin, and lacks lignin, and therefore is relatively flexible. When the cell expansion approaches its limit, the secondary cell wall forms against the inside of the primary cell wall, thickening the wood cell wall. The secondary cell wall layer is, in contrast to the primary cell wall layer, rigid and thick (Figure 2-2) and is usually organized into three sub-layers, i.e. S1, S2 and S3, each with a different orientation of cellulose microfibrils. In the wood cell wall, the S2 layer is the thickest (as shown in Figure 2-2), and forms more than 80% by the wood total mass (Fengel and Stoll 1973). The S2 layer is thus the main contributor to the mechanical properties of wood. In this thesis, the focus is on the S2 layer of softwood cell wall.

The detailed wood cell wall structure and chemistry have been subject of ongoing research for decades. This knowledge is always pushed forward with new technological developments, especially in microscopy and scattering techniques. There is a great variation in wood cell wall structure. The chemistry and structure of wood cell wall not only vary among different wood species, but they also differ between cell types and between earlywood and latewood within one

specimen. These differences cause different physio-chemical behavior of wood material (Kim and Daniel 2016). For example, the juvenile and mature wood possess respectively large and small microfibril angles (MFA), the angle between the orientation of crystalline cellulose and the longitudinal direction of wood. Juvenile wood cell wall needs to be flexible, hence the occurrence of large MFA, to be able to bend to reduce the impact of wind load, whereas matured wood withstands wind and gravitational load by stiffening its cell walls which requires a small MFA value (Lindström et al. 1998; Bonham and Barnett 2001).

Softwood S2 layer generally consists of cellulose (C) (~45%, by mass), hemicelluloses (HC) (~27%), and lignins (LGN) (~28%) (Agarwal 2006). In softwood, the hemicellulose types are mainly galactoglucomannan (GGM) and arabinoglucuronoxylan (AGX) (Escalante et al. 2012; Stevanic et al. 2014). Lignins are composed of condensed (cLGN) and uncondensed state (uLGN) of lignin. The mass ratio of each substance is summarized in Table 2-1. The detailed chemical structure of these molecules is introduced in the following sections.

Table 2-1 Chemical composition of softwood S2 layer.

| component | mass ratio | sub-component | mass ratio of sub-component |
|-----------|------------|---------------|-----------------------------|
| C         | 45.0% ± 6% | CC            | 27.5% ± 2% <sup>1</sup>     |
|           |            | AC            | 17.6% ± 8% <sup>1</sup>     |
| HC        | 27.0% ± 2% | GGM           | 18.6% ± 9% <sup>2</sup>     |
|           |            | AGX           | ~8.4% <sup>2,3</sup>        |
| LGN       | 28.0% ± 3% | cLGN          | ~12.6% <sup>1,4</sup>       |
|           |            | uLGN          | ~15.4% <sup>1,4</sup>       |

<sup>1</sup>Petterson 1984; <sup>2</sup>Dinwoodie 2000; <sup>3</sup>Bergander and Salmén 2002; <sup>4</sup>Agarwal 2006.

### 2.1.2 Cellulose

Cellulose is the most abundant natural polymer on Earth with an annual natural production of 75 ~ 100 billion tons. Cellulose chain is a polymer of  $\beta$ -1-4 linked glucan organized in a 2-fold screw conformation, i.e. the glucosyl unit inverts by 180° with respect to its neighbor. Its degree of polymerization in wood is in the order of  $10^4$ . It is generally accepted that there exist both amorphous and crystalline celluloses in the cell wall, with the crystalline phase forming the bulk of this phase.

Crystalline cellulose is the main load-bearing component of the wood cell wall in longitudinal direction, giving wood its impressive mechanical performance. The crystalline cellulose chains have one inter-chain and two intra-chain hydrogen bonds per monomer, as shown in Figure 2-3a

(Gardner and Blackwell 1974). There exist multiple allomorphs for crystalline cellulose. The I $\alpha$  crystal is a one-chain triclinic structure and is the dominant allomorph for bacteria. The native cellulose allomorph in higher plants, e.g. wood, is cellulose I $\beta$ , a two-chain monoclinic structure (Figure 2-3a), as identified by analysis based on near-infrared spectroscopy (Horikawa 2017).

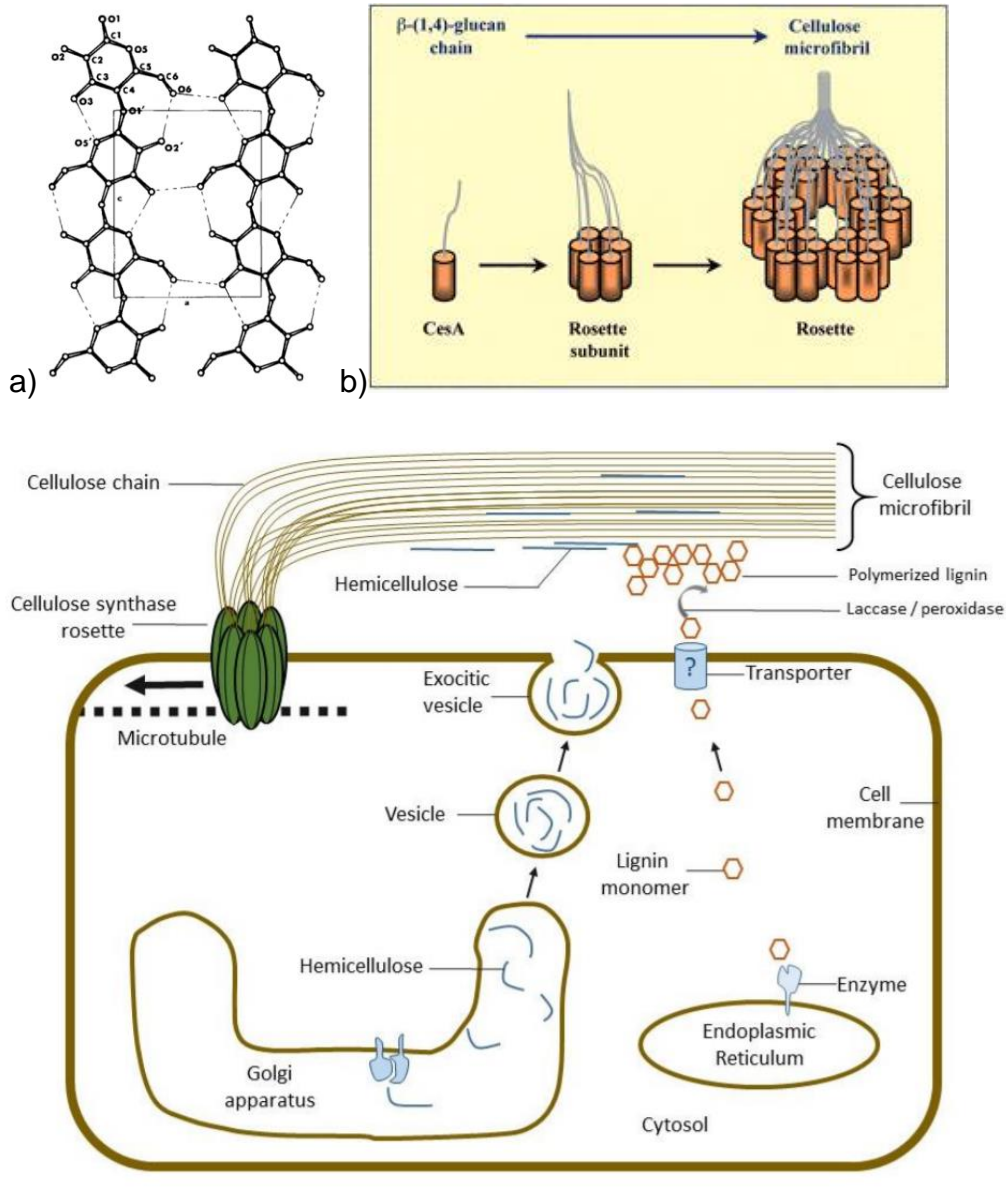


Figure 2-3 a) Hydrogen bonding at cellulose crystal (020) plane. Each glucose residue forms two intrachain hydrogen bonds, i.e. O3-H...O5' and O6...H-O2', and one interchain hydrogen bond, i.e. O6-H...O3 (Gardner and Blackwell 1974 with permission). b) Schematic of cellulose synthase complex, a rosette structure with six subunits composed of six cellulose synthase proteins (CesA) (Doblin et al. 2002 with permission). c) Synthesis of cellulose, hemicellulose and lignin. Cellulose is formed by the synthase protein CesA. Hemicellulose is produced in the Golgi apparatus and

transported by vesicles. The processes of lignin transportation and polymerization are less clear (Sorrieul et al. 2016 with permission).

Cellulose biosynthesis occurs at the cellulose synthase complex, a rosette structure with six subunits composed of six cellulose synthase proteins (Delmer 1999; Mutwil et al. 2008), as shown in Figure 2-3b and c. As a rosette structure possesses 36 synthase proteins (Delmer 1999; Mutwil et al. 2008), it is natural to assume that the elementary microfibril consists of 36 cellulose chains. Nevertheless, models of 18 (Jarvis 2013; Newman et al. 2013; Nixon et al. 2016), 24 (Fernandes et al. 2011) and 36 (Ding et al. 2014) chains had all been proposed according to various indirect proofs (Newman et al. 2013). At this stage, it is reasonable to assume that there exist multiple possible arrangements of crystalline cellulose, with various numbers of chains and diameters (Tejado et al. 2012; Thomas et al. 2013; Nixon et al. 2016).

The cellulose crystals are of finite dimensions. The width and length of cellulose nanocrystals depend on species. For softwood, it is reported that the width and length of cellulose nanocrystal are 3~5 nm and 100~200 nm respectively (Araki et al. 1999; Brinkmann et al. 2016). There are multiple models for the location of amorphous cellulose. It is currently widely acknowledged that the amorphous regions are distributed along the fibril as kinks, formed by strain distortion and twisting (Rowland and Roberts 1972; Fernandes et al. 2011; Ding et al. 2014), though the non-Gaussian distribution of kink angles of cellulose fibril may suggest that the kinks would not be a result of alternating amorphous and crystalline domains, but merely a result of mechanical processing (Usov et al. 2015). Recent Raman spectroscopy results of never dried wood cell wall speculatively indicate that native plant cell walls may not have crystalline cellulose, which in fact would be formed during drying or processing (Agarwal et al. 2016).

### **2.1.3 Hemicelluloses**

Hemicellulose, due to its bonding both to cellulose via hydrogen bonds and to lignin via hydrogen and covalent bonds, is the necessary material that holds the wood cell wall components together. Hemicelluloses are synthesized in the Golgi apparatus, and then transported by vesicles to the growing cell wall (see Figure 2-3c). Hemicellulose has a degree of polymerization of ~200. The chemical structure of hemicellulose is much more diverse than the one of cellulose, depending on the botanical sources and tissues. The more abundant hemicellulose monomers of softwood include mannose, xylose, glucose, galactose and arabinose. For softwood secondary cell wall the major hemicelluloses are galactoglucomannan (GGM) (Figure 2-4a) and arabinoglucuronoxylan (xylan) (Figure 2-4b) (Gibson 2012).

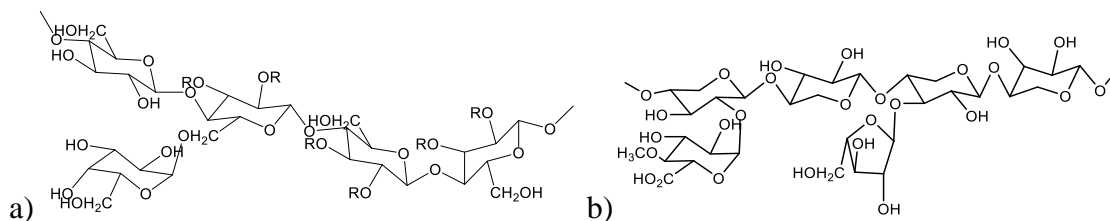


Figure 2-4 Chemical structure of **a)** galactoglucomannan and **b)** arabinoglucuronoxylan.

Galactoglucomannan is understood to be closely connected with crystalline cellulose (Åkerholm and Salmén 2001; Salmén and Burgert 2009) and consists in  $18.6\% \pm 9\%$  of the mass of softwood. GGM is generally a branched polymer, with the backbone of  $\beta$ -1-4 linked D-mannopyranose (Man) and D-glucopyranose (Glc) substituted by D-galactopyranose (Gal). The ratio of Man:Glc:Gal has been suggested to be 4:1:0.4 for Norway spruce (Xu et al. 2010). Spruce GGM can be produced on large scale for applications such as coatings and the paper industry (Xu et al. 2010) and its physiochemical properties have been thoroughly studied (Xu et al. 2008, 2010).

Xylan is the other main hemicellulose of softwood and is known to be closely associated with lignin, two constituents of the matrix between cellulose microfibrils in wood cell walls (Salmén and Burgert 2009). Representing 5~10 % of softwood by mass, it is one of the most abundant hemicelluloses (Pettersen 1984). Arabinoglucuronoxylan (AGX), the common xylan of softwood, consists of a backbone of  $\beta$ -1,4-linked  $\beta$ -D-xylopyranose units, which is partially substituted at O-2 by 4-O-methyl- $\alpha$ -D-glucopyranosyluronic acid and at O-3 by  $\alpha$ -L-arabinofuranose (Reid 1997). The degree of substitution depends on botanic sources and extraction methods (Den Haan and Van Zyl 2003). Softwood xylan possesses fewer acetyl groups than does hardwood xylan (Teleman et al. 2000). Generally, AGX from softwood is highly substituted, while AGX from hardwood has less arabinose (Luonteri et al. 1995). The detailed structure of AGX is still subject of on-going research but its branched structure is known. In enzymatically derived oligosaccharides from sugi, a softwood, AGX has regions consisting of eight contiguous unsubstituted D-xylopyranose units (Yamasaki et al. 2011). Matrix-assisted laser desorption/ionization mass spectrometry analysis of oligosaccharide mixtures of AGX from spruce, pine and larch, shows that, for most softwood AGX, 4-O-methyl-glucuronic acid residues are distributed every seventh or eighth xylopyranose residue (Jacobs et al. 2001). Conifer xylan is found to be decorated with methyl-glucuronic acid residues on every sixth xylosyl residue, while arabinose and methyl-glucuronic acid residues are located two xylosyl residues apart (Busse-Wicher et al. 2016a, b).

### 2.1.4 Lignins

In general, lignin is a randomly branched phenolic polymer, forming a complex 3D structure without a well-defined primary structure. Lignin is relatively hydrophobic when compared to amorphous cellulose and hemicelluloses. In land plants with limited access to water, lignin is seen to mechanically support, seal the pores of the cell wall and protect polysaccharides from microbial attacks.



Softwood lignin residing in S2 consists mainly of guaiacyl units whose chemical structure is shown in Figure 2-5. The C2, C5 and C6 positions of the monomer are free of substitution and the C3 position is substituted with a methoxyl group (Dorrestijn et al. 2000). The most common covalent linkage is  $\beta$ -O-4 (40~60%) (shown in Figure 2-5), followed by  $\beta$ -5', 5-5',  $\beta$ - $\gamma$ ,  $\beta$ - $\beta'$  and 4-O-5' linkages (Åkerholm and Salmén 2003; Higuchi 2014). There exist two main types of lignin, one is more linear, majorly formed by  $\beta$ -O-4 linkages, referred to as uncondensed lignin, and the other one is more cross-polymerized, referred to as condensed lignin. The condensed type of lignin is understood to be more closely related to GGM and cellulose fibril (Salmén and Burgert 2009).

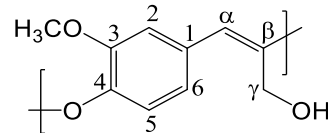


Figure 2-5 Chemical structure of guaiacyl unit, the major lignin monomer in softwood.

The monolignol is biosynthesized in the cytoplasm (Higuchi 2014; Mottiar et al. 2016). Contrary to most of the other biopolymers, lignin is synthesized in-situ by a radical polymerization reaction instead of a condensation reaction happening at the enzyme (Wang et al. 2013). This radical coupling path results in a randomly branched structure of lignin polymer. This occurs after the cell wall is formed and after the crystalline cellulose and hemicelluloses are in place.

### 2.1.5 S2 material organization

A network of cellulose fibrils exists in the S2 layer with a low MFA, determining its mechanical properties, i.e. stiffness, strength and toughness, of the cells, both alive or dead (Donaldson and Xu 2005; Burgert and Keplinger 2013). Cellulose microfibrils in S2 layer form aggregates, the arrangement of which is yet to be fully characterized. Currently, the concentric lamella model is the widely accepted model (Fahlén and Salmén 2002; Keplinger et al. 2014; Casdorff et al. 2018). The cross-section perpendicular to the longitudinal direction of Norway spruce tracheid cell wall imaged by AFM displays concentric lamellar structures are identified in Figure 2-6a and b by the white arrows (Fahlén and Salmén 2002). These lamellae seem to be made of somewhat aligned cellulose aggregates, which have a diameter of 20~25 nm. Keplinger et al. (2014) revealed a segmented circumferential nanostructure of plant cell wall in both a softwood (spruce) and a hardwood (beech) and proposed an image of the nanoscale texture of secondary cell wall (presented in Figure 2-6c). Besides the concentric model, radial (Sell and Zimmermann 1993, 1998) and random models (Donaldson and Frankland 2004; Zimmermann et al. 2006) are also proposed.

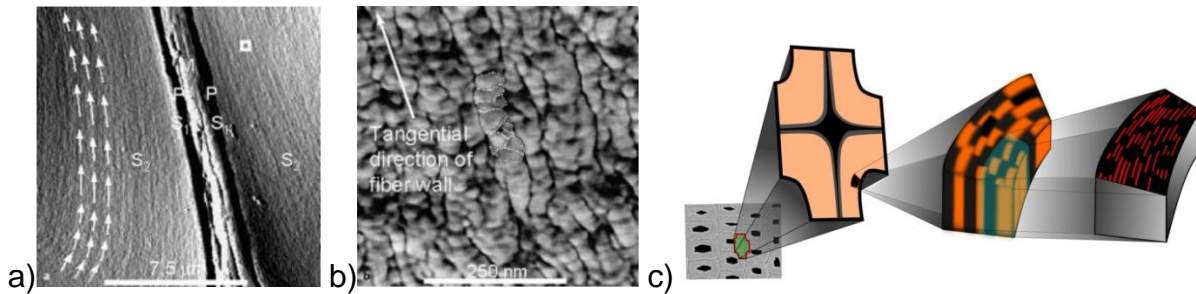


Figure 2-6 **a)** AFM images of different layers of Norway spruce tracheid wood cell wall are marked by M, P, S1, S2, S3. The white arrows indicate the concentric lamellae in the S2 layer (Fahlén and Salmén 2002 with permission); **b)** White arrow indicating the tangential direction of cell wall. Several cellulose aggregates are highlighted (Fahlén and Salmén 2002 with permission); **c)** Schematic of cell wall S2 layer with segmented lamellar structure, where cellulose fibrils and matrix are shown in red and black (Keplinger et al. 2014 with permission).

### 2.1.5.1 Microfibril

Cellulose crystals are closely surrounded with a matrix composed of hemicellulose and lignin, forming the smallest observable fiber referred to as microfibril (Salmén and Fahlén 2006; Gibson 2012). The microfibril extracted from wood has a length of 0.7~3 $\mu\text{m}$  (Prakobna et al. 2015) and an average diameter of 3~4nm (Keplinger et al. 2014). These microfibrils further combine into larger aggregates (Giddings 1980). The role of hemicelluloses and lignins on the formation of the fibril aggregates is not clear (Li et al. 2016a). The aggregates in the S2 layer of Norway spruce show average sizes with slight differences, i.e. 18~20 nm, as revealed by transmitted electron microscopy (TEM) (Bardage et al. 2007; Donaldson 2007). The spacing between fibrils or fibril aggregates is in the range of 3~14 nm. From a 2D tangential plane point of view, fibrils are undulating along the longitudinal direction, and the spaces between them are lenticular.

Fourier transform infra-red (IR) spectroscopy indicated the close connection of GGM to cellulose (Salmén and Fahlén 2006), which is supported by the recent results obtained via quartz crystal microbalance (Kumagai and Endo 2018). Chemical analysis indirectly indicates the association of GGM to the condensed type of lignin (Lawoko et al. 2005). There is no demonstration of the existence of covalent bonding between cellulose microfibril and its surrounding matrix (hemicellulose or lignin) (Salmén and Burgert 2009). Various experimental and modeling studies have suggested that hemicelluloses tend to form rather ordered structures aligned with cellulose fibril axis (Åkerholm and Salmén 2001; Stevanic and Salmén 2009). Similar to the observations of hemicellulose being aligned along the cell axis, studies are showing that lignin also forms similarly aligned ordered structures (Atalla and Agarwal 1985; Åkerholm and Salmén 2003), although lignin might have a relatively lower degree of orientation than hemicelluloses (Salmén et al. 2012). Cellulosic components are inferred to be the template for the organization of lignin based on photoconductivity experiments (Atalla 2009). The deformation of cellulose fibril in tensile loading

is elastic, according to Raman spectroscopy showing a stretching of C-C and C-O-C bonds, as the stretching almost fully recovers after rupture of the fibril (Gierlinger et al. 2006).

### 2.1.5.2 Matrix

TEM with immune labelling allows tracing the deposition of xylan, which is found to be closer to the non-condensed type of lignin (Ruel and Joseleau 2005), a finding also supported by chemical analysis (Lawoko et al. 2005). The interaction between hemicellulose and lignin in the matrix has an important economical role in the delignification and bleaching process, the core treatments in pulp and paper production. The presence of covalent bonds between hemicellulose and lignin is confirmed, forming the so-called lignin-carbohydrate-complex (LCC) (Eriksson et al. 1980; Meshitsuka et al. 1982; Lawoko et al. 2005), although it was also suggested that the lignin-hemicellulose covalent bond is not stable and may not involve all lignins (Westbye et al. 2008).

The matrix fills the inter-fibril space, gluing the fibrils. The interaction between the matrix and cellulose microfibril is still not clear, inducing various hypotheses. The widely accepted tethered network model (Figure 2-7a) is proposed based on experimental hints, e.g. xyloglucan links between microfibrils in the primary cell wall (Cosgrove and Jarvis 2012). In this model the two ends of xyloglucan chain attach to two microfibrils through intermolecular interactions, bridging between the two fibrils as a tether.

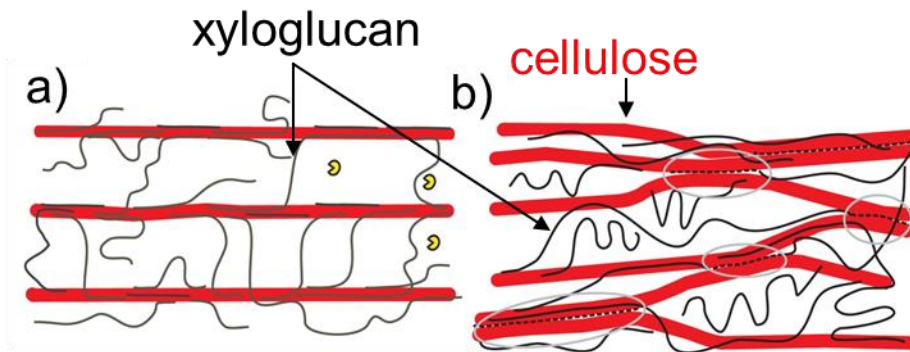


Figure 2-7 Two hypothetical models for the plant cell walls. a) tethered network model. b) biomechanical hotspot model (Cosgrove and Jarvis 2012 with permission).

However, results contradicting the tethered network model are accumulating (Park and Cosgrove 2012a). An alternative is the so-called mechanical hotspot model, where cellulose microfibrils make direct contacts (Xiao et al. 2016a) or contacts mediated by a monolayer of xyloglucan (Park and Cosgrove 2012b; Zhang et al. 2014, 2016) as depicted in Figure 2-7b and Figure 2-8.

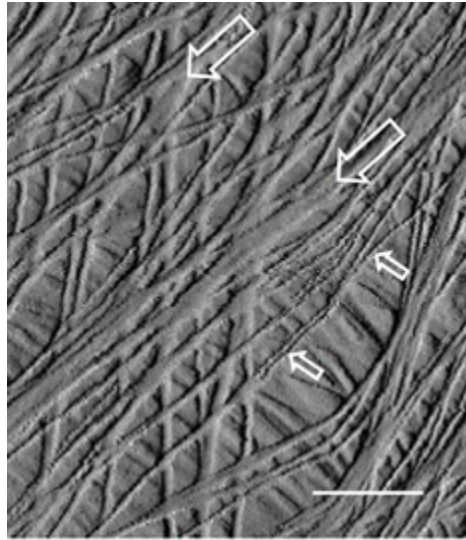


Figure 2-8 AFM image of an area of the abaxial epidermal wall of onion. The white arrows indicate the regions where cellulose fibrils come so close laterally to each other that mechanical hotspots may form (Zhang et al. 2014 with permission).

Synchrotron X-ray under tensile loading on wet wood foils or single cells allowed the observation of decrement of MFA happening together with sample stretching (Keckes et al. 2003; Burgert 2006), i.e. cellulose fibrils are continuously getting more and more aligned upon the cell axis. After a certain level of straining, failure happens and the MFA increases again, i.e. partly recovers to the original value, implying that the deformation of the matrix is partly elastic (Burgert 2006). This is different from the deformation of cellulose microfibril which is suggested to be fully elastic.

### **2.1.6 Summary of wood chemical composition and material arrangement**

In summary, thanks to the abundance of experimental analyses, a clear picture of the chemical composition of the softwood S2 layer has emerged, although some uncertainties remain to be clarified. Analytical chemistry provides the mass ratio and the chemical structure of each type of polymer, though the detailed bonding structure of AGX and condensed lignin is still under debate. However, the organization of different materials, i.e. fine structures of wood cell wall S2 layer at the nanometer scale, is only roughly known due to the limitation of the resolution of imaging technologies. Nevertheless, combining information and data from diverse sources and with soundly-based hypotheses, a tentative picture of the molecular arrangement of the S2 layer can be drawn and further probed. Multiscale computational modeling studies can also be utilized as will be presented in this work.

## **2.2 Mechanical aspects of wood-moisture relationship**

Wood is hygroscopic and the presence of moisture strongly influences the behavior and use of wood. Focusing on the wood cell wall S2 layer, as this layer largely determines the mechanical performance of wood, this section looks at the moisture-induced physical behavior of wood, i.e.

sorption, swelling, mechanical weakening and shape memory effect, reporting mainly experimental characterization.

### 2.2.1 Moisture sorption

Wood is highly hydrophilic, indicated by the differential heat of adsorption of  $1100 \text{ kJ kg}^{-1}$  for dry wood (Skaar 1988). At ambient conditions with changing relative humidity (RH), wood undergoes adsorption and desorption with increasing and decreasing RH, respectively, showing hysteresis between adsorption and desorption. The cell wall can adsorb water up to nearly half of its dry volume. Unless otherwise mentioned, moisture content is in this thesis reported as mass of water per mass of dry polymer.

Sorption is usually characterized by a sorption isotherm, a relationship between equilibrium moisture content and relative humidity (RH). There are generally six types of sorption isotherm as classified by IUPAC (Sing 1985), and wood physiosorption isotherm is akin to type II, the so-called sigmoidal curve (Figure 2-9).

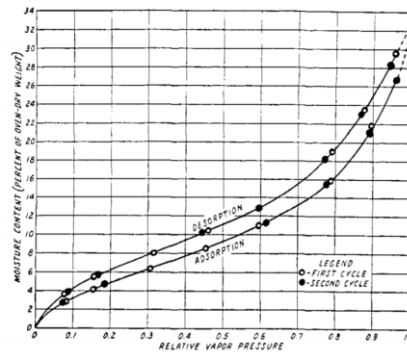


Figure 2-9 Sorption isotherms of white spruce (Stamm and Woodruff 1941 with permission).

For wood at low moisture level, the adsorbed water mainly interacts with polymer surfaces, especially the hydrophilic hydroxyl groups, replacing the polymer-polymer hydrogen bonds (HBs) by polymer-water hydrogen bonds. As adsorption goes on, reaching higher moisture levels, the sorption sites on polymer surface have been saturated with water molecules and therefore the newly adsorbed water interacts more with the formerly adsorbed water molecules. For wood, it is understood that the sorbed water leads to swelling which is due to relative displacement of the polymeric chains and thus exposure of new hydroxyl sites due to polymer-polymer HB breakage. Moisture adsorption and desorption in wood display a significant hysteresis. Recent work shows that a nanoporous material having type II isotherm like amorphous cellulose exhibits hysteresis which is associated with the history-dependent hydrogen bonding and the coupling between sorption and swelling (Chen et al. 2018). A large number of studies have measured sorption isotherms of wood e.g. (Seborg and Stamm 1931; Stamm and Woodruff 1941; Zillig 2009), as well as its individual components e.g. (Cousins 1978; Olsson and Salmen 2004; Beever and Valentine

2007). Figure 2-9 is an example of a sorption isotherm of white spruce at 20°C with ad- and desorption branches, showing the characteristic sigmoidal shape and hysteresis.

### **2.2.2 Moisture-induced deformation**

Moisture sorption is accompanied by deformation, i.e. shrinking and swelling, which provides drawbacks but also advantages in wood applications. As a positive example, ancient Egyptian quarry workers harness the swelling pressure of wood to break stones (El-Sehily 2016). However, the lack of dimensional stability of wood exposed to the exterior environment is a concern in many applications possibly leading to cracking and has been long characterized at macroscale.

Deformation of wood is anisotropic. For example, for Norway spruce, the tangential swelling strain varies between 1.3 (latewood) ~ 3 (earlywood) and is larger than its radial swelling strain. The longitudinal swelling strain is one order of magnitude lower than the ones in transverse directions (Derome et al. 2011). Currently, it is recognized that swelling originates from the sub-cellular scale, the composite cell wall. Additionally, macroscopic swelling of wood on the tangential direction is found to be proportional to that of the cell wall (Murata and Masuda 2006). The swelling of the wood cell wall is quite linear, except for the very low moisture content regime (Derome et al. 2018). Initial adsorption introduces minimum or even negative swelling, as the initial dry pores that are accessed by water molecules undergo almost zero (or even negative) swelling stress (Kulasinski et al. 2014a). As the initial pores are filled, the adsorbed water molecules, occupying space, exert a pressure on the wood cell constituents making the material swell. As the material is displaced, polymer-polymer HBs are broken making new sorption sites accessible for additional water molecules to be further adsorbed. The volume expansion equals the volume of water being adsorbed (Derome et al. 2011; Patera et al. 2013). At the sub-cellular scale, the anisotropic swelling of the wood cell wall S2 layer is experimentally observed (Rafsanjani et al. 2014), as shown in Figure 2-10. The axial and transverse swelling coefficients of micropillars are reported to be 0.3~0.6 and 0.5~1.2 respectively (Rafsanjani et al. 2014).

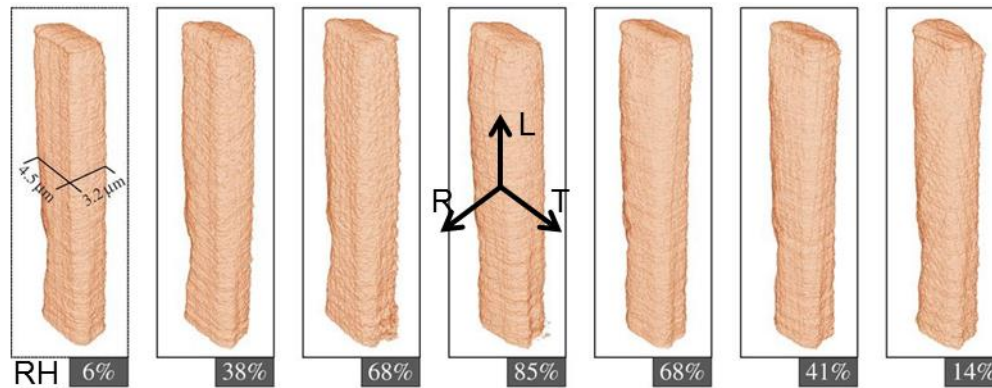


Figure 2-10 X-ray tomography of S2 micropillar under full sorption cycle (Rafsanjani et al. 2014 with permission). L, R and T denote longitudinal (axial), radial and tangential (transverse) directions of wood cell wall.

The deformation of the cell wall material is far from being completely understood. For example, the swelling coefficients of the individual cell wall components need to be measured. Currently available swelling data is limited by sample preparation or processing and may differ from the native material, as chemical extraction may modify the structure of molecules. Further, the swelling behavior of the S2 composite material could be described in more details. Previous preliminary work (Kulasinski et al. 2017; Chen et al. 2020) shows that composite mixture and interfaces may play a significant role. This thesis attempts to fill these gaps with molecular simulation.

### 2.2.3 Moisture-induced mechanical weakening

Moisture has a strong influence on the mechanical properties of biopolymers, such as dimensional stability, stiffness (Harper and Rao 1994) and glass transition (St. Lawrence et al. 2001). The adsorption of moisture usually weakens wood, though at very low moisture content an increase of stiffness with moisture adsorption has been observed. Elastic constants in the 0~30% moisture content range are relevant since, due to its hygroscopic behavior, wood in use under ambient varying RH conditions can actually visit this full range.

Due to the hierarchical ultrastructure of wood, the longitudinal mechanical stiffness of S2 is majorly defined by crystalline cellulose and its orientation, i.e. MFA. However, for tangential and radial directions, the contribution of the matrix polymers is not negligible. The impact of lignin content on the mechanical properties of wood cell wall is visible when MFA is high (Özparpucu et al. 2017). Despite the important role of hemicelluloses and lignins on the mechanical properties of S2, mechanical measurements of the individual polymers are still scarce. Moreover, the limited reports need to be referred to with caution, as the extraction processes may alter the chemical structure and material arrangement of such polymers, which may introduce deviation from material properties *in situ*.

The experimental mechanical characterization of the different layers of wood cell wall has just arisen. The quantitative imaging mode of AFM, recording a force-distance curve in every pixel (theoretical resolution limit 4 nm per pixel), has shown its potential in mechanically characterizing the S2 layer of spruce (Muraille et al. 2017; Casdorff et al. 2017). AFM has been employed to test the mechanical properties of the primary cell wall (Zhang et al. 2016). Peakforce quantitative nanomechanics technique is applied to characterize the mechanical properties of bamboo cell wall layers. Instead of a real cell wall, a bioinspired lignocellulosic film is fabricated and used to understand the mechanics of lignified plant cell wall at the nanoscale (Muraille et al. 2017). Up to now, these mechanical tests are all done under a single moisture condition which does not document the weakening effect of water, but AFM with controlled RH is recently available (Coste et al. 2020).

In addition to document the behavior of the composite structure, the mechanical properties of individual materials, i.e. GGM, AGX, cLGN and uLGN, of S2 are also needed, because applications, e.g. packaging, require the knowledge of their mechanical performance under moist condition. Currently known experimental and modeling measurements on this topic are summarized in Table 2-2, showing that a full moisture dependent behavior has still to be measured and reported.

Table 2-2 Mechanical properties of cell wall materials.

|                               | Method      | Name       | Value     | MC | Reference                    |
|-------------------------------|-------------|------------|-----------|----|------------------------------|
| crystalline<br>cellulose      | X-ray       | $E_L$      | 134       | 0% | (Sakurada et al. 1962)       |
|                               | theoretical | $E_L$      | 162       | 0% | (Tashiro and Kobayashi 1991) |
|                               | X-ray       | $E_L$      | 138       | 0% | (Nishino et al. 1995)        |
|                               | Raman       | $E_L$      | 143       | 0% | (Šturcová et al. 2005)       |
|                               | Raman       | $E_L$      | 105       | 0% | (Rusli and Eichhorn 2008)    |
|                               | MD          | $E_L$      | 107~113   | 0% | (Wu et al. 2014)             |
|                               | MD          | $E_L$      | 150       | 0% | (Kulasinski et al. 2014b)    |
|                               | MD          | $E_T$      | 11.3/72.6 | 0% | (Kulasinski et al. 2014b)    |
|                               | MD          | $E_T$      | 6.5~24.4  | 0% | (Wu et al. 2014)             |
|                               | theoretical | $E_T$      | 15.2/54.6 | 0% | (Tashiro and Kobayashi 1991) |
|                               | estimated   | $E_T$      | 27.2      | 0% | (Salmén 2004)                |
|                               | mechanical  | G          | 4.4       | 0% | (Mark 1967)                  |
|                               | mechanical  | $\nu$      | 0.1       | 0% | (Mark 1967)                  |
|                               | X-ray       | $\nu_{LT}$ | 0.38      | 0% | (Nakamura et al. 2004)       |
| microcrystalline<br>cellulose | Raman       | E          | 25±4      | 0% | (Eichhorn 2001)              |
|                               | MD          | $E_L$      | 33.5      | 0% | (Kulasinski et al. 2014b)    |



|                        |   |                |           |               |                           |
|------------------------|---|----------------|-----------|---------------|---------------------------|
| paracrystalline        | MD  | E <sub>T</sub> | 3         | 0%            | (Kulasinski et al. 2014b) |
| amorphous<br>cellulose | MD  | K              | 13.2±1.7  | 0%            | (Chen et al. 2004)        |
|                        | MD  | K              | 6.5       | 0%            | (Kulasinski et al. 2015a) |
|                        | MD  | K              | 2.1       | 30%           | (Kulasinski et al. 2015a) |
|                        | MD  | E              | 10.4±1.1  | 0%            | (Chen et al. 2004)        |
|                        | theoretical                               | E              | ~1        | 0%            | (Pienaar et al. 1989)     |
|                        | MD  | E              | 5.6±2.8   | 0%            | (Kulasinski et al. 2014b) |
|                        | MD  | G              | 6.0±0.7   | 0%            | (Chen et al. 2004)        |
|                        | MD  | v              | 0.12±0.03 | 0%            | (Chen et al. 2004)        |
| xylan                  | mechanical                                | E              | 5±0.4     | dry           | (Muraille et al. 2017)    |
|                        | mechanical                                | E              | 4.7       | 0%            | (Kulasinski et al. 2016)  |
|                        | mechanical                                | E              | 5.4       | 3%            | (Kulasinski et al. 2016)  |
|                        | mechanical                                | E              | 1.8       | 20%           | (Kulasinski et al. 2016)  |
|                        | mechanical                                | E              | 2.74      | moist         | (Escalante et al. 2012)   |
|                        | mechanical                                | E              | 2.9       | moist         | (Höjje et al. 2005)       |
| Galactoglucomannan     | mechanical                                | E              | 2.7       | 0%            | (Härdelin 2018)           |
|                        | mechanical                                | E              | 1.2±0.1   | 20% gly       | (Srndovic 2011)           |
|                        | mechanical                                | E              | 0.4±0.1   | 30% gly       | (Srndovic 2011)           |
|                        | mechanical                                | E              | 0.3±0.1   | 40% gly       | (Srndovic 2011)           |
| glucomannan            | mechanical                                | E              | 0.7±0.22  | 40% gly       | (Mikkonen et al. 2012)    |
|                        | MD  | K              | 6.6       | 0%            | (Kulasinski et al. 2015d) |
|                        | MD  | K              | 4         | 20%           | (Kulasinski et al. 2015d) |
|                        | mechanical                                | E              | 1.9±0.2   | dry           | (Muraille et al. 2017)    |
|                        | mechanical                                | E              | 4.3       | 0%            | (Kulasinski et al. 2016)  |
|                        | mechanical                                | E              | 5.1       | 4.5%          | (Kulasinski et al. 2016)  |
|                        | mechanical                                | E              | 2.5       | 20%           | (Kulasinski et al. 2016)  |
|                        | hemicellulose<br>(xylan &<br>glucomannan) | mechanical     | E         | 8             | 0~10%                     |
| mechanical             |   | E              | 0.1       | 50%           | (Cousins 1978)            |
| mechanical             |   | E              | 0.01      | 68%           | (Cousins 1978)            |
| estimated              |   | E <sub>L</sub> | 2         | 12%           | (Salmén 2004)             |
| estimated              |   | E <sub>L</sub> | 0.02      | moist         | (Salmén 2004)             |
| estimated              |   | E <sub>T</sub> | 0.8       | 12%           | (Salmén 2004)             |
| estimated              |   | E <sub>T</sub> | 0.008     | moist         | (Salmén 2004)             |
| estimated              |   | G              | 1         | 12%           | (Salmén 2004)             |
| estimated              |   | G              | 0.01      | moist         | (Salmén 2004)             |
| estimated              |   | v              | 0.2       | 12%           | (Salmén 2004)             |
| estimated              | v   | 0.2            | moist     | (Salmén 2004) |                           |

|  |            |                |         |       |                       |
|--|------------|----------------|---------|-------|-----------------------|
|  | estimated  | E <sub>L</sub> | 2       | 12%   | (Salmén 2004)         |
|  | estimated  | E <sub>L</sub> | 2       | moist | (Salmén 2004)         |
|  | estimated  | E <sub>T</sub> | 1       | 12%   | (Salmén 2004)         |
|  | estimated  | E <sub>T</sub> | 1       | moist | (Salmén 2004)         |
|  | mechanical | E              | 3.3±0.4 | 3%    | (Cousins et al. 1975) |
|  | mechanical | E              | 3.1     | 12%   | (Cousins 1976)        |
|  | mechanical | E              | 6.7     | 3.60% | (Cousins 1976)        |
| Lignin                                       | mechanical | E              | 5.7     | 0%    | (Cousins 1977)        |
| (exact chemical composition rarely reported) | mechanical | E              | 6.6     | 3%    | (Cousins 1977)        |
|  | mechanical | E              | 2.8     | 17%   | (Cousins 1977)        |
|  | estimated  | G              | 0.6     | 12%   | (Salmén 2004)         |
|  | estimated  | G              | 0.6     | moist | (Salmén 2004)         |
|  | mechanical | G              | 1.2     | 12%   | (Cousins 1976)        |
|  | mechanical | G              | 2.1     | 3.60% | (Cousins 1976)        |
|  | estimated  | v              | 0.3     | 12%   | (Salmén 2004)         |
|  | estimated  | v              | 0.3     | moist | (Salmén 2004)         |

The bulk and shear moduli are difficult to measure experimentally, as samples are usually prepared in the form of thin films. Tensile elastic modulus of crosslinked lignin slices, prepared by removing cellulose and hemicelluloses from Sugi tree wood sample retaining the in situ status of lignin, was measured to be 2.8 GPa (Takeichi et al. 2013). This value is found to be independent of the MFA of the original wood sample, suggesting that lignin is isotropic and may not form ordered structure aligning with cellulose fibril. On the contrary, the tensile elastic moduli of crosslinked polysaccharide slices prepared by removing lignin show MFA dependency (modulus decreases with increment of MFA), a tendency which is widely accepted. The elastic moduli of periodate and Klason lignins are measured under multiple moisture levels. The Young's modulus of periodate lignin drops from 7 GPa to 3 GPa when moisture content increases from 4% to 14%. At a similar moisture content range, the Young's modulus of Klason lignin drops from 4 GPa to 2.5 GPa (Cousins 1976).

Young's modulus of hemicellulose is measured to be 7 GPa (Cousins 1978) at dry and 2 GPa at moist conditions (Cousins 1976). Norway spruce AGX, composed of arabinose, 4-O-methylglucuronic acid and xylose in a ratio of 1:2:11 respectively, showed Young's modulus of 2.735 GPa at 23°C and 50% RH (Escalante et al. 2012). A film made of arabinoxylan extracted by alkali from barley husk at 23°C and 50% RH showed a Young's modulus around 2.9 GPa (Höije et al. 2005). Free films based on glucuronoxylan, isolated from aspen wood, shows Young's modulus of 1.6 GPa at 23°C and 50% RH and 20 wt.% plasticizer (Gröndahl et al. 2004). The reported Young's

moduli for xylan are unfortunately under only one moisture content condition, i.e. at equilibrium with 50%RH.

The mechanism of moisture-induced weakening of material has been generalized to a so-called “plasticization” (Tanner et al. 1991). From the intermolecular interaction point of view, the moisture-induced weakening can be seen as a breakage of the original polymer-polymer hydrogen bond network. From chain dynamic point of view, mechanical weakening can be seen as a relaxation of chain segmental movements facilitated by water molecules (Zhang et al. 2018).

#### 2.2.4 Moisture-induced shape memory effect

Shape memory effect is a characteristic of a family of smart materials where the deformation is maintained even after the removal of the environmental stimuli, and the original shape can be recovered spontaneously under certain conditions. One example of the shape memory effect is the springback of compressed wood when being re-moistened and reheated (Navi and Heger 2004). The recovery to the original shape of densified wood is not desirable, because the intermediate state (compression loaded wood) presents the required properties.

The shape memory effect of wood can be observed at different length scales. On the cellular level, Derome et al observed half-cell moisture-induced shape recovery, which is an indication that the memory effect originates from cell wall material, but also observed recovery for full cells (Derome et al. 2012). On the timber level, many researchers observed memory effect, which is attributed to the multi-scale hierarchical structure of wood tissue (Ugolev 2014). In terms of inducing conditions, there is temperature- (Ugolev 2014), moisture- (Ugolev 2014) and temperature-moisture-induced shape memory (Navi and Heger 2004; Jakes et al. 2014). In terms of loading conditions, there is stress memory and strain memory (Ugolev 2014). Figure 2-11 shows the shape memory effect observed on a ash thin sample (Ugolev 2014).

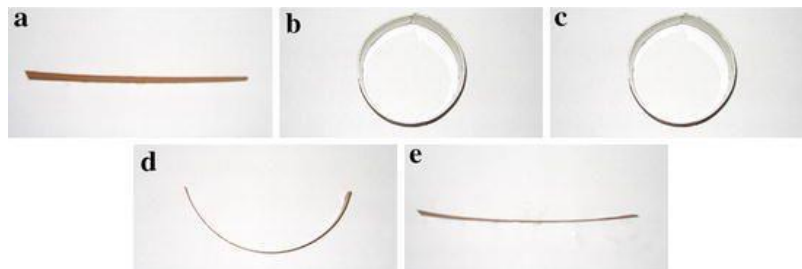


Figure 2-11 Shape memory of ash veneer (Ugolev 2014 with permission): a) original shape, b) bending, c) cooled under bending, d) unloaded, e) after heating the original shape is recovered.

Along with experimental reports of this phenomenon, researchers speculate on its different possible mechanisms. Navi and Heger claimed that elastic-strain energy stored in the helical semi-crystalline microfibrils is the main driving force of shape memory effect (Navi and Heger 2004). Ugolev indicated frozen strain, the result of temporary reconstruction of wood nanostructure in processes of drying or cooling, as the driving force of shape memory effect (Ugolev 2014). Plaza

et al related the effect to the moisture-dependent glass transition of polymeric components of wood (Plaza et al. 2013; Jakes et al. 2014). Derome et al advanced that interactions between sub-cellular cell wall components may lead to shape recovery of cell assembly (Derome et al. 2012). However, these mechanisms are mainly based on hypotheses, due to the difficulty of identifying or characterizing the mechanisms at play. There is a lack of convincing investigations about the origin of moisture-induced shape memory effect of wood. Recently, Cosgrove and colleagues reported that microfibrils tend to form direct contacts, called mechanical hot-spots, with each other in onion cell walls (Park and Cosgrove 2012b; Cosgrove 2014; Xiao et al. 2016a). This structural factor could also play a role in the memory effect of wood cell wall composite material, but all mechanisms listed above should still be considered in future studies.

### **2.2.5 Summary of mechanical aspect of wood-moisture relationship**

The study of moisture and wood relationship is an ancient topic holding continuous attention to this day. A better understanding of the impact of moisture on wood, this highly hygroscopic composite material with hierarchical composite structure, may guide many applications. Experimental studies have characterized wood cell wall mechanics, including moisture-induced swelling, weakening and shape memory effect. However, a lot more remains to be unraveled, such as the swelling of individual wood components, mechanical properties of wood components as functions of moisture and the microscopic mechanism underlying moisture-induced shape memory effect. As current experimental techniques cannot fulfill the demanding task of resolving these issues, computational studies can well provide readily available means to fill the gap.

## **2.3 Computational study of S2 layer at wood cell wall scale**

The computational studies of wood, given it is a hierarchical material, can be performed at different scales. Continuum methods, i.e. micromechanics or poromechanics possibly implemented in and solved by the finite element method, are more suited to simulate wood behavior at timber, growth ring and cellular scales. Discrete methods, such as all-atom molecular simulations and coarse-graining methods can adequately consider the sub-cellular scale. Amongst these scales, there is a bracket of scales, looking at the subcellular components, where both continuum and discrete methods are applicable. A major issue is the coupling of results between different scales, called up- or downscaling leading to multiscale approaches (Hofstetter et al. 2005). The current status of cell wall modeling studies, using continuum or discrete approaches, is summarized in this section.

### **2.3.1 Continuum methods: micromechanics and poromechanics**

The plant cell wall is considered with the analogy of a fiber-reinforced material, i.e. with cellulose microfibrils embedded in a matrix of hemicelluloses and lignins. This permits the application of micromechanics, which intrinsically implies the modeling of composite materials based on the information of individual components, such as the elastic constants and volume fractions of components and their arrangement. Alternatively, poromechanics could also be employed to model

the (poro)mechanical behavior wood cell wall S2 layer, fully coupling moisture and mechanical behavior.

Continuum models of cell wall layer can be purely analytical, where the overall elastic behavior is described through mathematical expressions containing physical and mechanical parameters (Bergander and Salmén 2002; Hofstetter et al. 2005; Mishnaevsky and Qing 2008). Otherwise, the finite element method can be applied, incorporating the constitutive behavior of a material/composite with the discretization of bulk material (Naik and Fronk 2013; Zhao et al. 2017; Rindler et al. 2017). It should be noted that the material properties used in almost all micromechanical studies of wood are more or less the same, because there is only a limited number of available experimental sources. The currently known mechanical properties of cell wall materials are summarized in Table 2-2. Some of the physical properties of the cell wall materials have unfortunately not been determined experimentally. This is at least one area where reliable molecular simulation results are expected to fill in gaps.

All the models require certain levels of homogenization, according to which the models can be categorized into three classes. Firstly, the cell wall layer is modeled as homogeneous continuum containing the least structural details, referred to as a fully homogenized model. Secondly, the matrix and cellulose microfibril can be distinguished, forming the so-called composite model. In the third approach, the matrix is further divided into the different cell wall polymeric components.

### ***2.3.1.1 Fully homogenized model***

In the fully homogenized model, the different cell wall components, considered as micro-heterogeneous continua, are homogenized into a macro-homogeneous continuum. The mechanical properties at macroscale are obtained via homogenization (Harrington et al. 1998; Derome et al. 2013). The homogenization is based on the existence of a representative volume element (RVE), the smallest volume representative of the medium with characteristic length. On one side, this length has to be much larger than the typical size of inhomogeneities within RVE. On the other side, the characteristic length of the RVE must be sufficiently smaller than the length over which macroscopic variations in material properties occur. The proper definition of a characteristic length allows the application of the principle of separation of scales between micro- and macroscale allowing for homogenization. For periodic structures, the unit cell is usually taken as the RVE.

Astley et al. modeled micromechanically the softwood cell, reflecting the effects of cell wall thickness, moisture content and MFA (Astley et al. 1997). Harrington et al. used a two-stage analytic homogenization, treating the cell wall as a macro-homogeneous continuum (Harrington et al. 1998). Faisal et al. (Faisal et al. 2013) modeled plant tissue with two orders of structural hierarchy, i.e. cell wall and tissue. The mechanical properties of individual components are taken from literature and the mechanical property of the composite is obtained from the rule of mixture (RoM) considering the orientation of cellulose fibril. They show that the MFA, especially of S2, governs the stiffness of the cell wall. Similarly, Qing and Mishnaevsky (Qing and Mishnaevsky

2009, 2010) and Hofstetter et al. (Hofstetter et al. 2005) also model the layers of wood cell wall using parameters taken from literature, such as layer thickness, MFA and volume fraction of various polymers, stiffness of wood constituents, which are later homogenized using the self-consistent and Mori-Tanaka schemes for respectively polymer matrix and cell wall material. Figure 2-12 illustrates the homogenization procedure of the wood cell wall as proposed by Hofstetter et al. (2005b). This homogenization scheme is advantageous especially for upscaling across several scales, i.e. in model spanning several orders of magnitude.

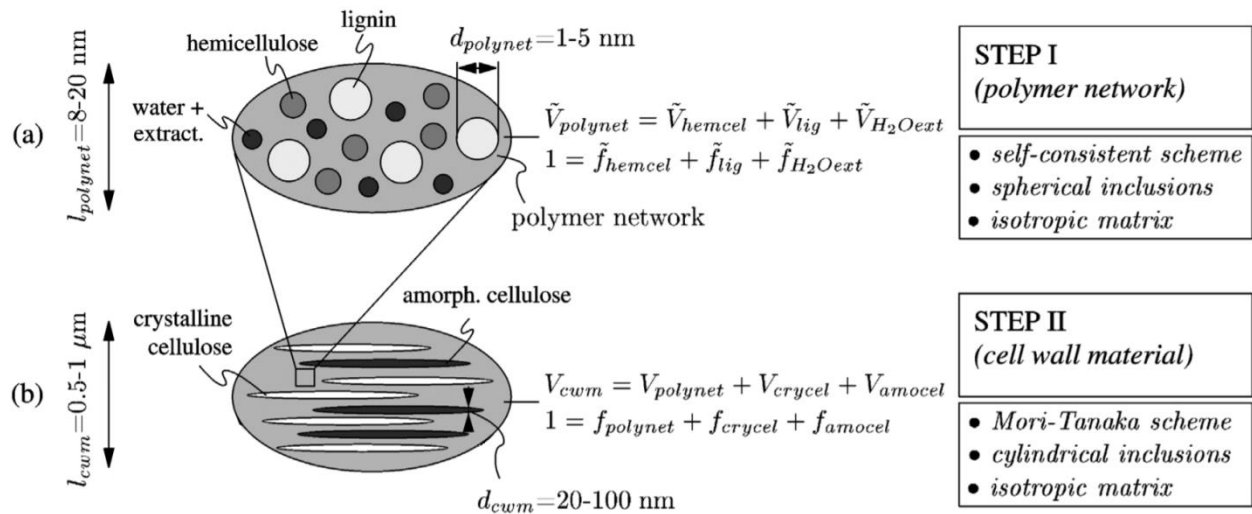


Figure 2-12 Homogenization procedure for wood cell wall (Hofstetter et al. 2005 with permission).

### 2.3.1.2 Composite model

Unlike the fully homogenized model, another popular approach is to treat the cell wall as a multilayer composite, where layers are idealized into unidirectional fibril reinforced composites with straight and parallel microfibrils (Barber 1968; Cave 1972; Yamamoto and Kojima 2002; Thuvander et al. 2002; Yamamoto 2004; Sun et al. 2014).

In Yamamoto and Kojima (2002), the cellulose fibrils and matrix are considered separate materials. The deformation of the matrix is assumed to be equal to the deformation of the cellulose fibril (equal strain assumption), expressed by the strain tensor in the local longitudinal-tangential-radial coordinates. The longitudinal Young's modulus and the Poisson's ratio can be expressed by several parameters, including thickness and elastic constants. Their model not only includes structural factors but also environmental conditions, e.g. moisture content, because some of the mechanical parameters are dependent on moisture content. The moisture dependency of the longitudinal Young's modulus of the wood predicted by the model (solid lines in Figure 2-13) agrees with the experimental results (dots in Figure 2-13).

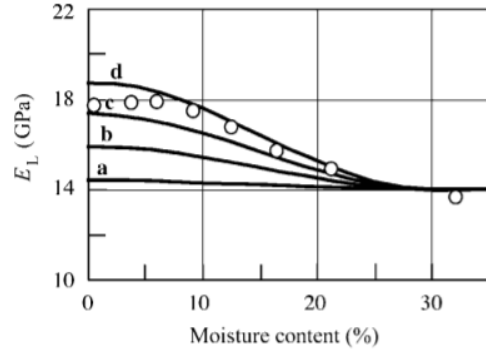


Figure 2-13 Longitudinal Young's modulus as a function of moisture content. Dots are the experimental results for spruce (Kollmann and Krech 1960). Solid lines are the prediction of the laminate fiber-reinforced composite model (Yamamoto and Kojima 2002 with permission).

Another approach of composite model of the cell wall considers the different wall layers as concentric multiple orthotropic lamellae, each lamella consisting of various materials. For example, Bergander and Salmen (Bergander and Salmén 2002) model the cell wall matrix as a mixture of serially- and parallelly-aligned hemicellulose and lignin. The matrix and the fiber are coupled by Halpin-Tsai equations (Affdl and Kardos 1976). Neagu and Gamstedt extended the stress function approach (Davies and Bruce 1997) to include moisture-induced swelling (Neagu and Gamstedt 2007). The swelling behavior is described using a linear hygro-expansion coefficient and the moisture content is not coupled with stress. This lack of coupling is unphysical, as the development of local stress during swelling will affect the attained moisture content which, in return, affect the swelling (Chen et al. 2018).

### 2.3.1.3 Poromechanics

To fully couple sorption and mechanical behavior, poromechanics should be employed (Biot 1941; Coussy 2003). Carmeliet et al. developed a nonlinear poroelastic constitutive model for an unsaturated porous material, e.g. wood, based on a higher-order formulation of free energy, where the material properties can be determined from mechanical and swelling tests (Carmeliet et al. 2013). The framework is able to describe the mechano-sorptive effect (Kulasinski et al. 2015a) and anisotropic swelling at the cellular scale (Rafsanjani et al. 2015).

Traditional poroelastic models use porosity and pore pressure as the basic variables. These variables are not applicable to wood cell wall material, which is a nanoporous material. The pores are not well defined at that scale and the pressure is simply a description for macroscopic scale which is not applicable at the nanoscale. Kulasinski et al. (2015a) replaced porosity and pressure with the molar concentration of water and chemical potential, formulating poroelastic constitutive equations for the nanoporous material. They determined the parameters for such formalism from MD simulation of adsorption, swelling at zero external stress and moisture-induced weakening of bulk modulus. This model can predict the drained bulk modulus being stress-dependent, i.e. when under tension loading the material is softer than at stress-free state (Kulasinski et al. 2015a).

Rafsanjani et al. developed a double porosity poromechanical model to investigate the swelling of wood cells. The model is capable of reproducing several phenomena in line with experiments. It was found that the anisotropic swelling of cells partly originates from the cell wall material anisotropic elastic property (Rafsanjani et al. 2015). Recently, a poromechanical model was developed to reproduce the coupling between sorption and deformation of soft nanoporous material observed in both experiments and molecular simulations. Three categories of parameters were involved in such a model, i.e. mechanical stiffness, sorption and structural parameters. Varying these parameters can greatly change the sorption and mechanical behavior of the material (Chen et al. 2019).

### **2.3.2 Discrete method: atomistic and coarse-grain simulations**

Discrete methods, including atomistic and coarse-grain simulations, provide a unique view on the molecular-level interactions in the material. After decades of development, these discrete methods have become prevalent tools for mechanical behavior investigation. Comparing with continuum methods and current experimental methods, atomistic and coarse grain methods offer a finer resolution, capturing information, such as explicit atoms dynamics and hydrogen bonding, which is critical to the understanding of wood-moisture relationship. Comparing with the quantum chemistry methods, such as Hartree-Fock and density function theory (DFT), molecular simulations possess a better balance between physical accuracy and computation costs given the sizes of the relevant systems. Most frequently, such quantum chemistry studies are applied to systems of tens of atoms (Lee et al. 2015), a size too small for mechanically relevant investigations. Instead, quantum chemistry methods majorly focus on the chemical reactions, e.g. pyrolysis (Choi et al. 2016; Mar and Kulik 2017; Zhang et al. 2017). At the other spectrum of atomistic methods, course grain methods bundle several atoms into one discrete unit, enabling modeling at micrometer to millimeter scales. However, this approach has yet to resolve the proper consideration of hydrogen bonding, a crucial actor in hygroscopic materials. In this thesis, MD is used as the main tool of investigation. Therefore, the most relevant MD investigations performed on wood-inspired systems are presented below.

#### **2.3.2.1 Cellulose**

Cellulose, in crystalline, paracrystalline and amorphous states, is extensively studied, due to its important role in wood mechanics as well as its industrial relevance. The I $\beta$  cellulose crystal is the dominant cellulose allomorph in softwood. Nevertheless, there exist eight stable cellulose crystal structures as revealed by systematic molecular dynamic simulations (Kroon-Batenburg et al. 1996). The decrystallization of cellulose crystalline fibril has been investigated. The deterministic factor of decrystallization is the number of intra-layer neighbors and their affiliated hydrogen bonds (Payne et al. 2011). MD simulations yielded elastic properties of cellulose microfibrils corresponding to experimental results (Tanaka and Iwata 2006; Nishiyama 2009; Wu et al. 2013a; Mazeau 2015). Hydrated cellulose crystal was investigated. A 20% hydration was found to maximize the stiffness of cellulose crystal by water bridging cellulose monomers with hydrogen bonding (Petridis et al. 2014). A coarse-grain model of crystalline cellulose was developed, able to



maintain a stable structure in water that resembles I $\beta$  (Wohlert and Berglund 2011). Paracrystalline cellulose was found to exhibit intermediate mechanical stiffness between amorphous and crystalline cellulose (Kulasinski et al. 2014b). The impact of hydration on amorphous cellulose was investigated (Mazeau 2015). Dynamical and mechanical properties of amorphous cellulose show a noticeable change at 10% moisture content, which is explained by the occurrence of percolation separating the adsorption process into two regimes (Kulasinski et al. 2014a). In addition to mechanical behavior, the diffusion of water molecules in cellulose and hemicellulose polymers was investigated. The motion of water exhibits a “stop and go” stepwise movement, where both the bound time and frequency of such steps decrease with increasing moisture content (Kulasinski et al. 2015b).

In addition to the mechanical behavior of cellulose crystals, their interface behavior is also relevant to the mechanical performance of composites reinforced by cellulose. The traction-separation behavior of an interface formed by two cellulose crystals was investigated. A stick-slip motion is found to be dependent on the surface morphology and energy landscape. Interfacial water increases the separation of energy through forming a capillary bridge (Sinko and Keten 2015). Adsorption between microfibrils is carried out, showing that the direct interaction is more likely to occur between polar surfaces and that limited direct adsorption happens between the non-polar surfaces (Oehme et al. 2015). The role of hydrogen bonding and the presence of water on the strength of the interface has yet to be elucidated.

### **2.3.2.2 Hemicellulose: glucomannan and xylan**

The study of konjac glucomannan reveals that water stabilizes the structure through hydrogen bonds (Wang et al. 2010; Jian et al. 2011). Molecular simulations show that GGM of arabidopsis seed mucilage binds stably to cellulose microfibrils (Yu et al. 2018). MD simulation of oligo-glucomannan and xylan shows that glucomannan backbone is stiffer than the backbone of xylan (Berglund et al. 2016). The volumetric strain of GGM during sorption is found to be linearly related to the porosity, indicating that the swelling is directly induced by the space created by the water molecules. The decrease in the number of hydrogen bonds correlated with mechanical weakening and swelling (Kulasinski et al. 2015d). In a study of GGM laid around a CC, an excess of water adsorption is found at the crystalline-amorphous interface, explained by the lower energy penalty at the interface than in the bulk material (Kulasinski et al. 2015c).

Several papers have reported MD studies of xylan, yet mainly focused on the xylan-cellulose interaction. Mazeau and Charlier studied small xylan fragments, having five skeletal xylosyl residues, in presence of crystalline cellulose by MD. These small chains preferentially orient themselves to be parallel with the cellulose chain axis (Mazeau and Charlier 2012). The binding pattern of xylan on cellulose suggested that xylan is stable on the hydrophilic faces of crystalline cellulose fibrils (Busse-Wicher et al. 2014, 2016b).  $\alpha$ -1,2-substitutions are shown to stabilize xylan-cellulose interactions, regardless of the type of substitution (Pereira et al. 2017). Xylan substituted by lauroyl side chains was investigated and the substitution showed a considerable

effect on the polymer chain flexibility. Native xylan is semi-flexible whereas the modified xylan behaves as a flexible coil (Mazeau et al. 2005). MD simulations of xylan-cellulose shows that the xylan forms an extended conformation along the fibril axis (Falcoz-Vigne et al. 2017). The most prevalent softwood xylan, namely AGX, still lacks physical and mechanical characterization.

### **2.3.2.3 Condensed and uncondensed lignins**

Lignin is relatively less studied, compared to cellulose. The main obstacle is the complex 3D linking structure of cross-polymerized lignin imposing great difficulty from a modeling point of view. Lignin is found to associate with cellulose, especially the hydrophobic surface of the crystalline phase, in aqueous solution, suggesting a supporting role of lignin to the recalcitrance of crystalline cellulose to hydrolysis (Lindner et al. 2013; Vermaas et al. 2015). The dynamical analysis of lignin shows that hydration and heating affect lignin in similar ways (Vural et al. 2018a, b). Through ReaxFF, a correlation between lignin-cellulose coupling energy and Young's modulus of the lignin is found (López-Albarrán et al. 2017). Lignin aggregates are simulated by MD and an invariant surface fractal dimension is found under the scale ranging from 1 to  $10^3$  Å. The extensive water penetration is also revealed (Petridis et al. 2011a).

Recently, lignin topological libraries have been developed to simulate the various sizes and linkages of isolated lignin samples (Yanez et al. 2016; Dellon et al. 2017). Very recently, a lignin builder based on these libraries was developed, to transform the chemical structure into initial configurations used for molecular simulations (Vermaas et al. 2019a). Together with the optimization of the existing lignin force field (Vermaas et al. 2019b), these works make more accessible the molecular modeling of heterogeneous lignins and lignocellulosic complex structures. More investigations of complex crosslinked lignins can be expected in the near future.

### **2.3.2.4 Wood cell wall composite**

MD investigations of S2 layer-inspired systems considered systems of increasing complexity and undergoing different physical phenomena, mostly in dry state. In terms of composition and geometry, simplification of the number of polymers and of their layout is usually performed, mainly due to limited computation capacity and modeling difficulty.

Kulasinski et al. presented the currently most advanced molecular simulation of a wood cell wall S2 layer, consisting of CC microfibrils embedded in GGM and surrounded with a low DP LGN (Figure 2-14a). Hydration is shown to strongly impact various thermodynamic and mechanical properties of the constructed system (Kulasinski et al. 2017). As adsorption and swelling proceed, mechanical weakening of the composite is observed (Figure 2-14b). The anisotropy of the S2 layer model is mainly attributed to the orientation of CC. Their atomistic model selected four square crystals, one hemicellulose and a low DP condensed lignin.

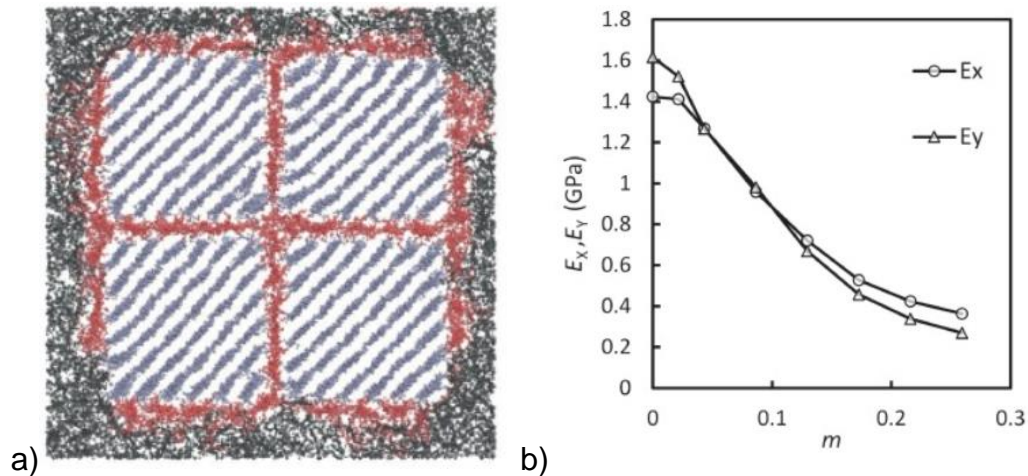


Figure 2-14 a) Wood cell wall S2 layer model. Grey, red and black color denote cellulose, hemicellulose and lignin, respectively. b) Moisture-induced weakening of Young's moduli of the S2 layer (Kulasinski et al. 2017 with permission).

There are several studies performed on S2-inspired composite systems without consideration of hydration. Assemblies of cellulose crystal/xyloglucan and cellulose crystal/lignin were studied using MD simulations, where nonspecific bonding was observed between cellulose and xyloglucan/lignin (Besombes and Mazeau 2005; Hanus and Mazeau 2006). Bamboo cell wall has also inspired MD investigations. Bamboo possesses cellulose, hemicellulose and lignin, similar to wood, while bamboo has higher content of small molecule components, e.g. alkaline extractives. The normal and shear stresses are found to dominate the separation of hemicellulose and lignin, respectively (Hao et al. 2018). A study of the interface of matrix-cellulose fibril was carried out with different binding modes of hemicellulose chains between cellulose, i.e. bridge, loop and random, the so-called "tethered model". The contact area and hydrogen bonds are found to be determining the strength of the interface (Zhang et al. 2015). Finally, a molecular model of bamboo fiber consisting of lignin, hemicellulose, LCC and cellulose fibrils was developed. The particularity of this work was the inclusion of an amorphous section along the cellulose microfibril. This amorphous region along the cellulose fibril is found to have the weakest adhesive interaction energy (Youssefian and Rahbar 2015).

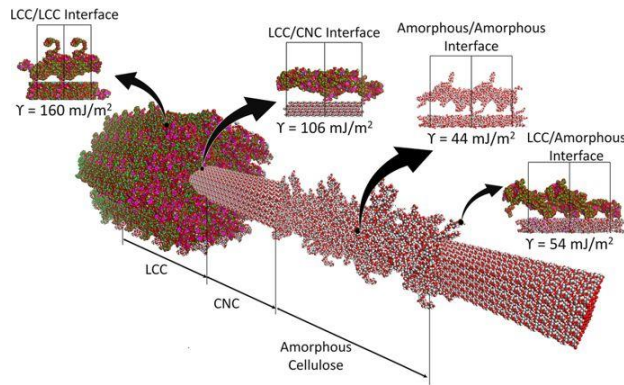


Figure 2-15 Adhesive interaction energy at the different interfaces of bamboo fiber (Youssefian and Rahbar 2015 with permission).

S2 inspired systems were used to study the behavior under large deformation, until loss of integrity of the systems. It is unclear how such studies actually relate to loading in wood, but they provide interesting insight. Hence the effect of MFA on the deformation and failure behavior of wood cell wall layer was studied. It was shown that the failure starts with fibril local buckling/kinking, according to both experiments (Da Silva and Kyriakides 2007) (Figure 2-16a) and simulation (Figure 2-16b), although it should be noted that the two systems were at totally different scales. Water was shown to cast a strengthening effect on systems with low MFA ( $<35^\circ$ ) (Deng et al. 2012). An S2 cell wall interface model built by (Jin et al. 2015) was tested under shear loading. An initial elastic deformation was followed by plastic deformation. The plastic regime consists of two sub-regimes: yielding of the matrix and relative sliding of the matrix along with cellulose (Figure 2-17).

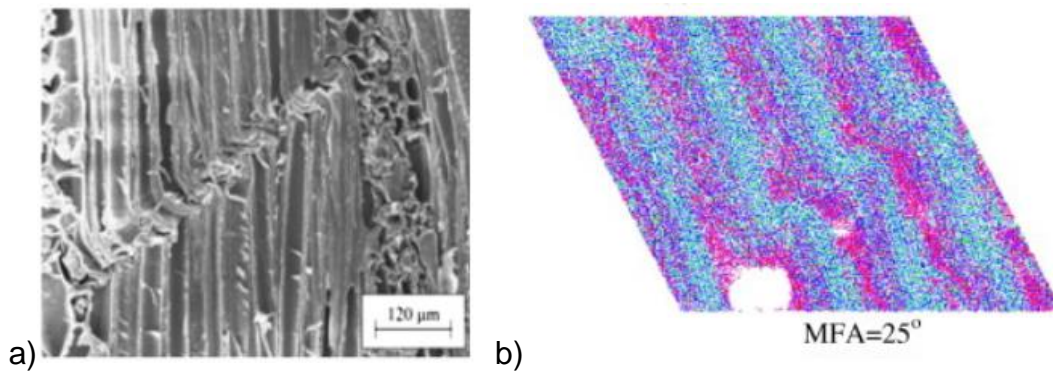


Figure 2-16 Compression failure of wood cell wall composite a) experiment (Da Silva and Kyriakides 2007 with permission), b) molecular simulation model with MFA=25° (Deng et al. 2012 with permission).

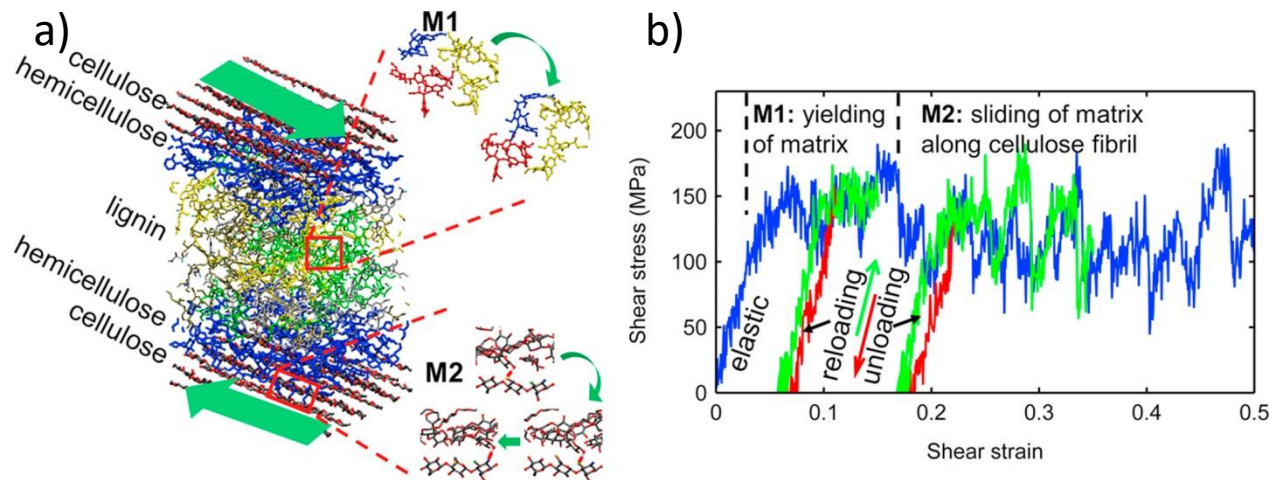


Figure 2-17 a) Cell wall composite model, b) stress-strain result under shear loading (Jin et al. 2015 with permission).

Finally, for the sake of completeness, the few works that have explored the use of coarse-graining are presented here. A coarse grain model, also named “mesoscale model”, of wood cell wall, consisting of cellulose microfibrils embedded in a polymer matrix of hemicelluloses and lignin, was built (Tam and Lau 2016) based on the methodology developed by (Adler and Buehler 2013), where the polymers were represented by beads with mass and the system total energy consists of the axial strain energy, the bending energy and the weak interactions. This mesoscale model can be seen as a mixture of coarse grain and micromechanical model, as the material mechanical properties harvested from molecular simulations are included in the form of 27 mesoscopic parameters in the total energy formulation. The polymer is represented as beads as large as  $1 \text{ nm}^3$ . Another study of such a mesoscale model is carried out in the same research group, where the temperature effect on the polymer-wood interface is discussed (Tam et al. 2017). The next challenge along this approach is the proper modeling of the effect of hydrogen bonds, especially in hydration. In this thesis, this avenue was not explored but was deemed worthwhile to be briefly mentioned.

## 2.4 Challenges and research needs

Computational studies of wood cell wall S2 layer has only recently achieved success in the understanding of the mechanical behavior of this complex multiscale material. New insights at molecular and nanometer scales are brought through atomistic modeling, including information on hydrogen bonding, chain dynamics, etc. Larger scale continuum models also contribute to the mechanical understanding of material arrangement, impact of wall thickness, elastic constants, moisture content etc. This topic is still in its infancy and there are still many gaps to fill in the future.

For material engineering, as well as for continuum modeling, the mechanical properties of individual wood cell wall components need to be known. Most of the available experimental reports are based on the study of isolated wood polymers, which chemically and mechanically differ from the ones in situ state. For example, one of the major hemicelluloses is softwood AGX, which can be used in packaging applications (Escalante et al. 2012), however experimental reports of its physical and mechanical properties are still rare. Molecular simulations can be expected to provide the missing information.

The complex mechanical behavior of the secondary cell wall including viscoelasticity, viscoplasticity and hygromechanical deformation, is speculated to originate from the matrix behavior at lower scales (Cosgrove and Jarvis 2012). Contrary to cellulose fibrils, the mechanical role of the cell wall matrix in such behavior is missing and there is a lack of structure-property relationships (Burgert and Keplinger 2013).

In wood cell wall S2 layer, there exist interfaces formed between crystalline cellulose and the amorphous materials (Kulasinski et al. 2015c), which are critical to the overall mechanical performance of the cell wall composite. Currently, it is generally assumed that non-covalent bonded intermolecular interactions, e.g. hydrogen bonding, dominate the cellulose fibril interface (Esker et al. 2009). The behavior of the interface depends strongly on the number of hydrogen bonds, which in nature shows fluctuations. Excess adsorption of moisture at the interface is shown to emerge (Kulasinski et al. 2015c), which will fundamentally change the mechanical behavior of the interface and composite. The deformation and displacement happening at the interface still need to be better characterized. Moreover, recent experimental observation shows the possibility that cellulose fibrils form direct contacts, the so-called “mechanical hotspots” (Cosgrove 2014). The possible role of this structural feature needs to be investigated and predicted. There are molecular studies of wood cell wall composite material, yet most of them lack the discussion on moisture-induced phenomena, or lack some major components of cell wall composite material, e.g. cross-linked lignin (Mazeau and Heux 2003; Charlier and Mazeau 2012; Jin et al. 2015; Kulasinski et al. 2015c; Zhang et al. 2015).

There is a need to couple continuum and discrete models to form a multiscale modeling framework to study specifically the hygromechanical behavior of components and of the cell wall. Discrete models are limited by their computational costs. Continuum methods require reliable component hygromechanical characterization. The combination of the discrete and continuum methods could offer a possibility to offset their individual disadvantages and provide a powerful numerical framework for the study of cell wall mechanical behavior. One example is the moisture-induced shape memory effect. The mechanism of this effect remains mysterious, and modeling studies trying to solve the puzzle require a good grasp of the mechanical properties of cell wall material as functions of moisture content, which are at the moment mainly only accessible through MD simulations. However, the scale of wood cells and growth rings is in the order of micro- and millimeters meter scale and can only be modeled through continuum methods. The coupling of the

continuum and discrete modeling is expected to open new gateways in multiscale modeling of wood.

## 2.5 Conclusion

This chapter summarizes the state of the art research on wood cell wall hygromechanics, an intriguing issue with many open questions. The most advanced structural information is presented, though many aspects of the structure of wood cell wall, such as composition and shape of cellulose crystalline fibril, distribution of different materials within the cell wall layer and lignin crosslink bonding, remain to be clarified, most of which arise due to limitations in experimental techniques resolution. Necessary hypotheses must be made based on experimental evidences.

The moisture-induced behavior of wood cell wall layer is reviewed, including the sorption, deformation, weakening and shape memory effects. Being a hygroscopic nanoporous material, the cell wall layer adsorbs water and shows a type II sorption isotherm. Its sorption and deformation are found strongly coupled. Critical issues such as the general picture of moisture sorption and the mechanism for weakening and shape memory effect need to be elucidated. Better understanding of these issues will not only benefit the wood research but also the general research on biopolymers and their composites.

Experimental methods are of limited resolutions which are insufficient of dealing with the nanoscale structures of wood cell wall. Moreover, wood material characterizations are normally done after extraction from raw wood which inevitably introduce chemical alteration. All these experimental difficulties call for numerical surrogates. This chapter reviews the computational studies of wood cell wall, including continuum methods, such as homogenized model, composite model and poromechanical model, and discrete methods, such as atomistic and coarse-graining simulations. The various continuum methods demand micromechanical properties of wood components which can, aptly, be extracted from molecular modeling, a research topic in its infancy.

This thesis strives to model the wood cell wall S2 layer using a multiscale computational framework. Important individual components of softwood as well as composites and interfaces are studied under the full hydration range with molecular modeling. The atomistic information is then implemented into a continuum model, to study larger scale moisture-induced phenomenon, shape memory effect. Finally, the fruitfulness of the discrete information of the S2 model, probed by rule of mixture investigations, is beautifully exhibited. The endeavor starts with the exploration of the hygromechanical behavior of the hemicellulose xylan in next chapter.

## Chapter 3 Moisture-Induced Crossover in the Thermodynamic and Mechanical Response of a Hydrophilic Biopolymer: Softwood Xylan

This chapter focuses on the hygro-thermo-mechanical behavior of an important hemicellulose of softwood, arabinoglucuronoxylan or AGX, which thermodynamic and mechanical properties lack experimental characterization. Using a prototypical polymer material allows presenting a general picture of the hydrophilic polymer-moisture relationships determined by molecular dynamics. The results show that, as adsorption proceeds, the water molecules first create new spaces and surfaces by separating the polymer chains and, after reaching a moisture content of 30 %, further insertions of water mainly happen in water clusters in the hydrated material. This transition point is referred to as the moisture-induced crossover point which is reflected in the thermodynamic and mechanical properties of this prototypical biopolymer, such as the heat of adsorption, heat capacity, thermal expansion and elastic moduli. Investigating the microscopic structure of the confined water molecules and the polymer-water interfacial area, the molecular mechanism responsible for this crossover is identified to be the formation of a double-layer adsorbed film along the amorphous polymeric chains. In addition to this moisture-induced crossover, the properties of the hydrated biopolymer are found to obey simple material models, based on which the properties of the two layers of water can be derived. On top of elucidating the general picture of sorption induced phenomena in hemicellulose and the microscopic mechanism at play, the results in this chapter will be utilized as material parameter inputs for the composite models in later chapters.

The core content of this chapter is published in Zhang, C., Coasne, B., Guyer, R., Derome, D., & Carmeliet, J. (2020). Moisture-induced crossover in the thermodynamic and mechanical response of hydrophilic biopolymer. *Cellulose*, 27(1), 89-99.

### 3.1 Introduction

As introduced in Chapter 2, one of the main components of softwood that lacks investigation is AGX which represents 5~10 % of softwood by mass and is known to be closely associated with lignin. AGX and lignin constitute the matrix situated between cellulose microfibril aggregates in wood cell walls (Salmén and Burgert 2009). AGX has diverse applications in a range of industries, such as packaging of cosmetic or medicinal products (Escalante et al. 2012), biomedical products (Li et al. 2011), plastic additives (Ünlü et al. 2009) and in bio-refinery processes (Sedlmeyer 2011). Despite its versatility and usage potential, its wide use is hindered since a number of important material properties of xylan, such as adsorption heat, heat capacity, thermal expansion coefficient and moisture-dependent elastic moduli are unknown, mainly due to the difficulty of isolating xylan from biological sources without altering it chemically (Ahlgren and Goring 1971; Barakat et al. 2007; Stevanic et al. 2014). These properties need to be investigated as they correlate with the stability and durability of this material. Mechanical properties of wood polymers are particularly relevant to industry and elastic constants at lower moisture content ( $m < 0.3$ ) are of special interest since this hygroscopic range corresponds to the range of ambient conditions. Moisture has a strong



influence on the mechanical properties of biopolymers, such as dimensional stability, stiffness (Harper and Rao 1994), glass transition (St. Lawrence et al. 2001) and crystallinity (Tanner et al. 1991). Unfortunately, there is a dearth of measured water sorption related properties of AGX (Escalante et al. 2012). This chapter will fill the gap through molecular simulations as the first objective of this work is to determine the hydromechanical properties of AGX. Molecular Dynamics (MD) has shown its capability of simulating cellulosic materials, such as cellulose and xylan, in agreement with existing experimental studies (Zhao et al. 2014; Kulasinski et al. 2016, 2017; Derome et al. 2018; Chen et al. 2018) and to unravel the molecular mechanisms at play in e.g. sorption hysteresis of deformable nanoporous materials (e.g. amorphous cellulose) (Chen et al. 2018). Such molecular simulations can provide detailed information about the state of water molecules. Experimental work has led so far to the indirect determination of the water state, with the use of a loose terminology, bound/unbound or free (Gezici-Koç et al. 2017) or unfreezable/freezable water (Li et al. 1998). To access to the microscopic information differentiating the states of water in hydrated polymer systems forms the second objective of this chapter.

In this chapter, MD is employed to investigate the role of intermolecular interactions, i.e. hydrogen bonds (HBs), explaining the microscopic mechanisms leading to the coupling between the polymer mechanical and hygric behavior. Here AGX, one of the most abundant hemicelluloses of softwood (Reid 1997), is chosen as a prototypical model of the hydrophilic biopolymers in wood. The work consists of the systematic investigation of various mechanical and thermodynamic properties of AGX at different moisture contents.

## 3.2 Materials and Methods

### 3.2.1 Chemical structure and atomistic modeling of arabinoglucuronoxylan

AGX, the most common type of xylan in softwood (Reid 1997), is formed by a backbone of  $\beta$ -1,4-linked  $\beta$ -D-xylopyranose units, partially substituted at O-2 by 4-O-methyl- $\alpha$ -D-glucopyranosyluronic acid and at O-3 by  $\alpha$ -L-arabinofuranose (Reid 1997), as shown in Figure 3-1. The degree of substitution depends on botanic sources and on extraction methods (Den Haan and Van Zyl 2003)). For the current study, a random polymer consisting of 67% xylose, 20% glucuronoacid-xylose and 13% arabinoxylose is used.

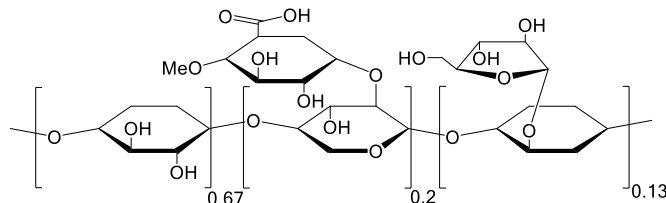


Figure 3-1 Chemical structure of AGX consisting of 67% xylose (left), 20% glucuronoacid-xylose (middle) and 13% arabinoxylose (right).

The three types of monomers are constructed using Material Studio 8.0 and randomly polymerized into chains with a degree of polymerization of 100 (Gorshkova et al. 2012). Gromacs 2016 software (Berendsen et al. 1995; Abraham et al. 2015) and Gromos 53a6 force field (Oostenbrink et al. 2004) are used for the MD simulations. The force field parameters of the monomers are obtained from an automated topology builder (Malde et al. 2011). Long-range coulombic interaction is treated using the particle-mesh Ewald method. Five chains of AGX are inserted randomly within a periodic box, with periodic boundary conditions in the three directions to avoid finite-size effects. The system is relaxed using a Nose-Hoover thermostat and a Parrinello-Rahman barostat. The temperature and the pressure are set to 300 K and 0 Pa, respectively. The thermostat and barostat coupling time constants are both 0.5 ps. Relaxation is carried out for 20 ns with an integration time step of 1 fs. Both the total energy and the system density converge within 1 ns and the system finally reaches a size of about  $5 \times 5 \times 5 \text{ nm}^3$  and a density of  $1.3 \text{ g/cm}^3$ . The density is in accordance with the literature, as measured for a xylan powder extracted from corn cobs (Verbeek 2012). Following the same procedure, two more systems are prepared and then investigated to improve the statistics and to obtain data more representative of disorder in real systems. The three repetition systems differ in their orientation and arrangement of chains but are all isotropic.

### **3.2.2 Simulation of water sorption**

Gromos force field is designed to work with the single point charge (SPC) and SPC extended (SPC/E) (Berendsen et al. 1987) water models. SPC is chosen because it reproduces better the saturation vapor pressure (4400 Pa at 300 K) than SPC/E does (1010 Pa at 300 K) (Errington and Panagiotopoulos 1998). Water adsorption is simulated at room temperature (300 K). Starting with the dry system, water molecules are inserted randomly one after another into the simulation box, avoiding overlap with the polymer and the previously inserted water molecules. Each insertion is followed by an energy minimization and then a relaxation of 100 ps. Due to computational cost, results are reported at 20 moisture content levels. A series of snapshots of hydrated polymer systems at different moisture contents is shown in Figure 3-2.

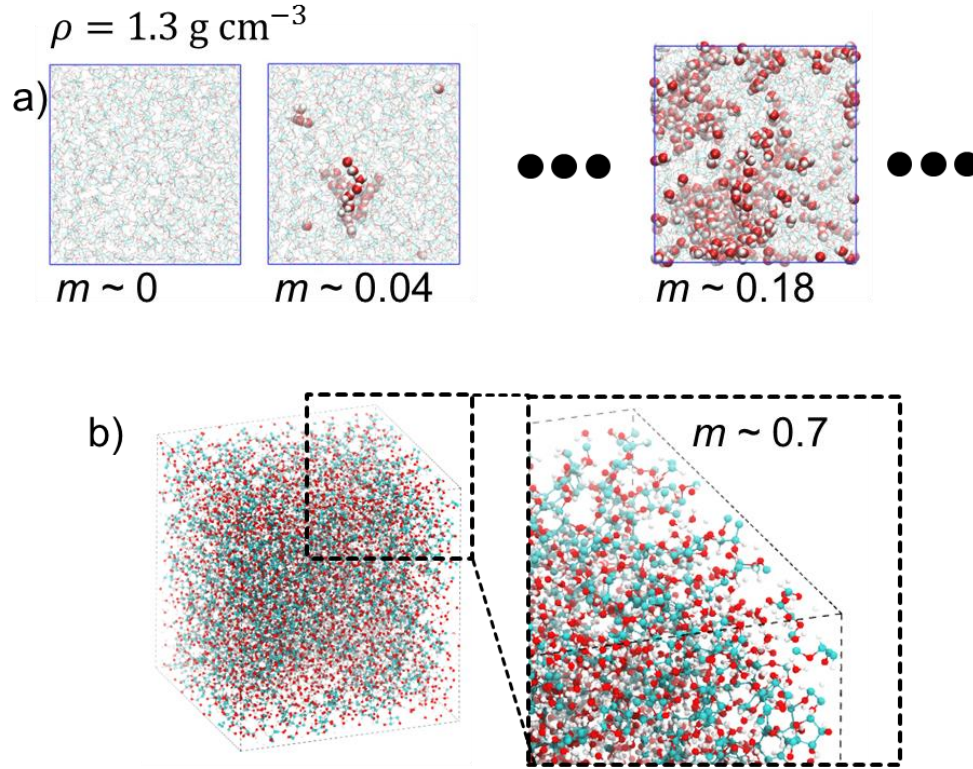


Figure 3-2 a) Orthogonal projection of polymer system in dry and hydrated states at  $m \sim 0.04$  and  $0.18$ , for systems of  $5 \times 5 \times 5 \text{ nm}^3$ , b) 3D view of system at  $m \sim 0.7$  with zoomed view. Carbon atoms in cyan, oxygen atoms in red and hydrogen atoms in white.

### 3.2.3 Material properties measurement

#### 3.2.3.1 Uniaxial swelling strain

In this study, swelling strain is reported as uniaxial swelling strain instead of volumetric swelling strain, in accordance with most available experimental reports where most samples are made in the form of thin films. The systems are equilibrated in isothermal-isobaric (NPT) ensemble for 20 ns ( $P=0 \text{ Pa}$ ,  $T=300 \text{ K}$ ). All the thermodynamic variables, such as energy, temperature, pressure and volume, reach equilibrium in the first 1 ns. The uniaxial swelling strain is defined as:

$$\epsilon_x(m) = \frac{x(m) - x(0)}{x(0)} \quad (3-1)$$

where  $x(m)$  is the length of the system at moisture content  $m$ , and  $x(0)$  is the size of the system in dry condition using a Lagrangian approach. The uniaxial swelling strains in the three orthogonal directions ( $\epsilon_X$ , where  $X=x, y, z$ ) of the three repetition samples are measured and the average value ( $\epsilon$ ) is reported.

### 3.2.3.2 Chemical potential and relative humidity

The one-step perturbation (OSP) method is used to calculate the free energy as per Equation (3-2), which is needed to determine the chemical potential as given in Equation (3-3) and, from there, the relative humidity as in Equation (3-4). OSP was shown to successfully predict solvation free energies of a number of small polar and nonpolar solutes in water with sub- $k_B T$  accuracy and significantly greater efficiency than the traditional stepwise calculation (Pitera and van Gunsteren 2001). It has also been used to determine the adsorption isotherm of amorphous cellulose (Kulasinski et al. 2014a).

The systems at different moisture contents are simulated in the NPT ensemble for 20 ns ( $P=1$  Pa,  $T=300$  K). Then, the equilibrium of the system is perturbed by removing one water molecule while all the other molecules remain. The potential energy difference of the states before and after the perturbation is calculated. The time average of the free energy difference  $\langle \Delta F_i \rangle_t$  is estimated according to the Zwanzig formula:

$$\langle \Delta F_i \rangle_t = -RT \ln \left\langle e^{-\frac{\Delta V_i(t)}{RT}} \right\rangle_t \quad (3-2)$$

where  $R$  is the gas constant,  $T$  is the temperature, and  $\Delta V_i(t)$  is the potential energy difference induced by removing the  $i$ -th water molecule.

The chemical potential,  $\mu$ , is the entity average of time-averaged free energy:

$$\mu(m) = \frac{\partial F}{\partial N} = \frac{1}{N(m)} \sum_{i=1}^{N(m)} \langle \Delta F_i \rangle_t \quad (3-3)$$

where  $N$  is the total number of water molecules in the system and  $m$  is the moisture content. The relative humidity (RH) is related to the chemical potential as follows:

$$\text{RH} = e^{\frac{\mu - \mu^*}{RT}} \quad (3-4)$$

where  $\mu^*$  is the saturation chemical potential which is taken as the chemical potential at maximum moisture content (Gröndahl et al. 2003, 2004). Moisture content is increased up to 0.7.

### 3.2.3.3 Integral heat of adsorption

Adsorption is an exothermic process and the enthalpy released by adsorption is a significant variable describing the interaction between adsorbate and adsorbent. There exist several definitions for the heat of adsorption. Here the integral heat of adsorption of water vapor is used, which is the total heat released by water vapor being adsorbed, normalized by the total adsorption amount. Measurements are carried out in NPT ensemble ( $P=1$  bar,  $T=300$  K). The heat of adsorption, at a specific moisture content  $m$ , involves three contributions, i.e. dry polymer ( $p$ ), water vapor ( $wv$ ) and the composite system ( $c$ ) formed by water being adsorbed on the polymer. The integral heat of adsorption is defined as:

$$Q(m) = (H_p + H_{wv} - H_c)/n_{water} \quad (3-5)$$

where  $H_p$ ,  $H_{wv}$ ,  $H_c$  and  $n_{water}$  are the enthalpies of dry polymer, water vapor, composite and the amount of water in mole, respectively. Since the deformation of pure polymer induced by adsorption is generally neglected for simplicity, in this study, the dry polymer is obtained by removing all water molecules in the composite system while freezing the configuration of the polymer.  $H_p$  and  $H_c$  are calculated with the definition of enthalpy  $H = U + PV$ , where the internal energy  $U$ , pressure  $P$  and volume  $V$  are directly measurable from MD. As the water vapor can be considered an ideal gas with acceptable error (Israel Urieli 2018),  $H_{wv}$  equals to  $4n_{water}RT$ , because the internal energy of water vapor in ideal gas state can be approximated by the equipartition theorem and equals  $\frac{6}{2}n_{water}RT$  (three translational and three rotational degrees of freedom), and the  $PV$  term estimated by the equation of state of an ideal gas is  $n_{water}RT$ . Usually, the heat of adsorption is reported as the heat released per kilogram of adsorbed water, therefore the unit of  $Q$  is converted from kJ/mol into kJ/kg by the factor of the molar mass of water (0.018 kg/mol). The integral heat of adsorption of the three repetition systems are collected, and the average and standard deviation values are reported.

### 3.2.3.4 Uniaxial thermal expansion coefficient

Thermal expansion is evaluated with a series of 2ns NPT simulations, with  $P=0$  Pa and nine different temperatures, i.e. 296 K, 297 K, 298 K, 299 K, 300 K, 301 K, 302 K, 303 K and 304 K. All temperatures are in the vicinity of room temperature (300 K). The uniaxial thermal expansion coefficient as a function of moisture content  $m$  is defined as:

$$\alpha_{x,T_0}(m) = \frac{1}{x(T_0, m)} \left. \frac{dx(T, m)}{dT} \right|_p \quad (3-6)$$

where  $x(T, m)$  is the length of the system along one of the three principal axes at temperature  $T$  and  $T_0 = 300$  K. A line is fitted through the data points to calculate  $\left. \frac{dx(T, m)}{dT} \right|_p$ .  $\alpha_x$  is measured in three orthogonal directions for all three repetition systems and the average value is reported.

### 3.2.3.5 Heat capacity

As performed for the determination of the thermal expansion coefficient, heat capacity is determined by a series of 2ns NPT simulations with  $P=0$  Pa and nine different temperatures, i.e. 296 K, 297 K, 298 K, 299 K, 300 K, 301 K, 302 K, 303 K and 304 K. The total energy  $U(T, m)$  and volume  $V(T, m)$  are recorded and the heat capacity at a specific moisture content is defined as:

$$c_{p,T_0}(m) = \left. \frac{dU(T, m)}{dT} \right|_{p,T_0} + p \left. \frac{dV(T, m)}{dT} \right|_{p,T_0} \quad (3-7)$$

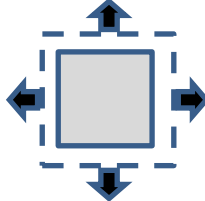

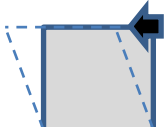
where  $c_p$  is the heat capacity,  $T_0 = 300$  K,  $P=0$  Pa. A line is fitted through the data points to calculate  $\left. \frac{dU(T, m)}{dT} \right|_{p,T_0}$ . The heat capacities of the three repetition systems are collected and averaged.

### 3.2.3.6 Elastic constants and Poisson's ratio

The elastic constants are determined from the slope of the linear regime of stress-strain curves at room temperature. To construct the stress-strain curve for bulk ( $K$ ), Young's ( $E$ ) and shear moduli ( $G$ ), tensile volumetric, uniaxial and shear strains are applied respectively and the resulting stresses are collected. The stresses are referred to as pressure in MD and are computed from the kinetic energy and the virial (details in Abraham et al. 2015). In the simulation results, the linear regime usually spans until a strain of 4%.

Although in principle the deformation rate does not play a significant role as will be explained below, it is chosen as low as possible, namely  $3.66 \times 10^{-5}$  nm/ps,  $5 \times 10^{-5}$  nm/ps and  $3.66 \times 10^{-5}$  nm/ps, for bulk, Young's and shear moduli measurements, respectively, in order to eliminate rate effects. The strain rate, therefore, is in the order of  $10^8$  s<sup>-1</sup>. Stepwise strains are applied to a given structure with each step straining around 0.01% of the initial dimension. Every step is followed by a relaxation run of 100 ps to allow molecular rearrangement. The relaxation conditions for bulk, Young's and shear moduli are different. For bulk moduli, the strained structure is relaxed in the NVT ensemble. For Young's and shear moduli, the structure is relaxed with the strained dimension fixed and the other dimensions coupled to the barostat ( $P=0$  Pa). For example, in a Young's modulus measurement, for a sample undergoing uniaxial strain in  $x$ -direction, the relaxation will be carried out with the  $x$  coordinates fixed while the  $y$  and  $z$  coordinates are coupled to a barostat to allow fluctuation. Due to the stepwise straining and the following relaxation, the influence of strain rate is minimized. The disadvantage of this method is the much higher computational cost comparing with the static approach (Theodorou and Suter 1986) where the entropic contribution is neglected. The loading conditions of the mechanical tests are summarized schematically in Table 3-1.

Table 3-1. Schematic of mechanical tests.

| Property  | Bulk modulus  | Young's modulus  | Shear modulus   |
|-----------|---|--|---|
| Test      | volumetric tension  | uniaxial tension   | shear   |
| Schematic |  |  |  |

In addition, the Poisson's ratio and the shear modulus assuming isotropy can be predicted by using the measured bulk  $K$  and Young's moduli  $E$  according to:

$$\nu = \frac{3K - E}{6K} \text{ and } G = \frac{3KE}{9K - E} \quad (3-8)$$

The number of water molecules is constant during loading so that the measurements are conducted at constant moisture content, therefore the measured elastic constants correspond to the undrained ones. For Young's and shear moduli, the moduli measured in three orthogonal straining directions are collected and averaged. The moduli and Poisson's ratios of the three repetition systems are collected and averaged.

### 3.2.3.7 Percolation

Percolation of water is the configuration achieved where one large water cluster crosses from one side to the other side of the polymeric system. Two water molecules that are located within 0.6 nm distance are considered to be in the same water cluster. The value 0.6 nm refers to the second minimum of the radial distribution function of bulk water. Percolation probability is defined as the time span during which percolation is occurring divided by the total simulation time span. In MD simulations, the time span is discretized and represented by time frames with a fixed interval of 1 fs. Therefore, the percolation probability is the number of time frames where percolation is present divided by the total number of time frames. The percolation probability is determined in function of moisture content.

### 3.2.3.8 Hydrogen bonds

As HBs are playing a significant role in the hygromechanical behavior of the polymer, their occurrence and distribution are tracked. The criteria for HB are defined by the configuration of the donor-hydrogen-acceptor triplet:

$$R \leq 0.35 \text{ nm and } \alpha \leq 30^\circ \quad (3-9)$$

where  $R$  is the distance between the donor oxygen atom and the acceptor oxygen atom, and  $\alpha$  is the angle of acceptor oxygen atom – donor oxygen atom – donor hydrogen atom. The criteria are illustrated in Figure 3-3.

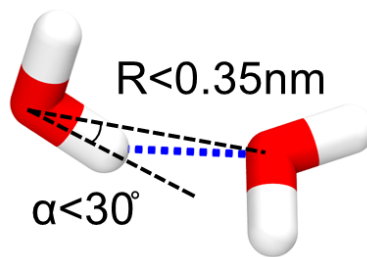


Figure 3-3 Illustration of hydrogen bond criteria. The blue dashed line denotes the hydrogen bond formed.

The interoxygen distance criterion of 0.35 nm refers to the first minimum of the radial distribution function of SPC water (Soper and Phillips 1986; Luzar and Chandler 1993). The angle of 30° is approximately the amplitude of rotational vibrations that break HBs (Teixeira and Bellissent-Funel

1990). There are three types of HBs that are tallied in the hydrated systems, i.e. polymer-polymer, polymer-water and water-water.

### 3.2.3.9 Cohesive energy density

The cohesive energy is the interaction energy between molecules. It is measured by the difference between the internal energy of the whole system and the summation of internal energy of individual systems (Hansen 2007) and is reported as cohesive energy density, as shown below:

$$CED = \left( \sum_{i=1}^N U_{molecule\ i} - U_{whole} \right) / V_{whole} \quad (3-10)$$

### 3.2.4 Validation of the atomistic model

MD introduces several levels of simplification of molecular interactions, such as assuming harmonic bond, Lennard-Jones potential, etc. The validation of the numerical models, and especially comparisons with existing experimental data, is therefore necessary. Due to the fact that the properties of AGX suffer from a dearth of experimental reports, properties like density, isotropy, the adsorption isotherm and the swelling strains are retained for validation. It is already mentioned that the density of the material corresponds well with experiments.

#### 3.2.4.1 Isotropy

Wide-angle X-ray scattering (WAXS) experiments show that spruce xylan is isotropic under different humidity conditions (Escalante et al. 2012). In MD, the Hermans orientation function (HOF) which corresponds to the nematic order parameter is used to characterize isotropy (Hermans and Platzek 1939). It is defined as:

$$HOF = \frac{3\langle \cos^2 \theta \rangle - 1}{2} \quad (3-11)$$

where  $\theta$  is the angle between the axis of interest and the direction of a polymer monomer and the angular bracket denotes the entity average over all monomers in the system. Our simulation results show that HOF remains  $0 \pm 0.015$  regardless of moisture content, thus confirming the isotropy of the models at all moisture contents, which is in agreement with the WAXS results of (Escalante et al. 2012).

#### 3.2.4.2 Adsorption isotherm and swelling

Using the methods described above for water sorption, the sorption isotherm and swelling strain of AGX are determined. Experimental sorption curves of different xylans, unfortunately not including AGX, are reported (Gröndahl et al. 2003, 2004; Kulasinski et al. 2016), but only (Kulasinski et al. 2016) reports swelling. Two adsorption branches of sorption isotherms of glucuronoxylan isolated from aspen wood are shown in Figure 3-4a with white triangles (Gröndahl et al. 2003) and squares (Gröndahl et al. 2004). In terms of hygroscopic range and sigmoidal shape, our simulation results agree well with the experimental results. Many factors, in MD such as exact chemical composition and the degree of substitution, and in measurement errors, can affect the measured sorption



isotherms and may explain the slight differences observed in Figure 3-4a. A perfectly dry state is always a challenge to achieve experimentally, which might make the value of measured moisture content slightly lower than reality. This could also explain the experimental isotherms having slightly lower moisture content under the same RH than the MD results.

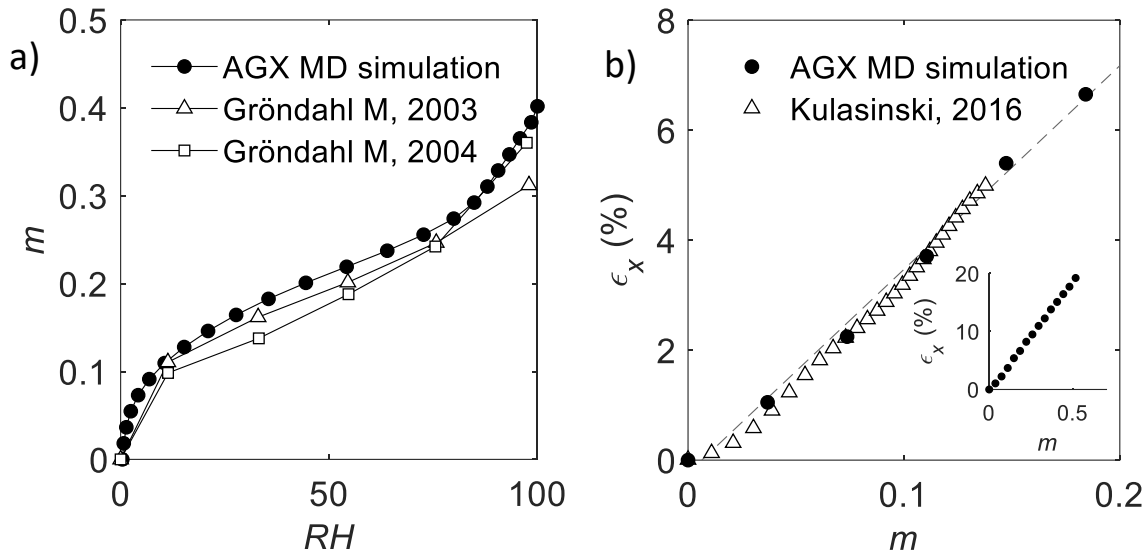


Figure 3-4 a) Sorption isotherms of xylan from MD simulation (black dots) compared with two experimental studies (triangles (Gröndahl et al. 2003) and squares (Gröndahl et al. 2004)). b) Uniaxial swelling strain versus moisture content  $\epsilon_x(m)$  (black circles) compared with experimental results of rye arabinoxylan for  $m < 0.15$  (white triangles) (Kulasinski et al. 2016). The dashed line is a linear fit of the simulation data. The inset shows MD results for  $\epsilon_x(m)$  for a broader range of moisture content, i.e.  $m = 0 \sim 0.5$

The maximum moisture content in Figure 3-4a is  $\sim 0.4$ . In theory, when RH approaches 100%, the sorption isotherm becomes steep and the corresponding equilibrium moisture content tends to reach high values. In this study, the maximum moisture content being discussed is 0.7.

Swelling is a frequent co-occurrence of moisture adsorption for biopolymers. Black dots in Figure 3-4b represent the uniaxial swelling strain, the arithmetical average of three repetition samples on three principal directions. The swelling strain is practically the same in all three principal directions which means that AGX swells isotropically. The grey dashed line is the linear fitting of black dots in the moisture content range of 0 to 0.2. The white triangles are the experimental swelling strain results for rye arabinoxylan (Kulasinski et al. 2016), which agree well with our simulation. Given that the sample is in the form of a film, the experiment only covers  $m < 0.15$ , as at higher moisture contents wrinkling occurred. The swelling strain over a broader range of moisture content is solely measured through MD and shown in the inset of Figure 3-4b. At very low moisture content, the swelling coefficient is lower than the overall swelling coefficient. This initial non-linearity is

frequently observed in biopolymers and well explained, i.e. some of the initially adsorbed waters can first fill the existing pores of the polymeric material, instead of displacing it (Kulasinski et al. 2015d). This is supported by the pore size distribution results (Figure 3-5). For dry AGX, there exist pores as large as  $\sim 0.7$  nm, which are much larger than the size of a water molecule.

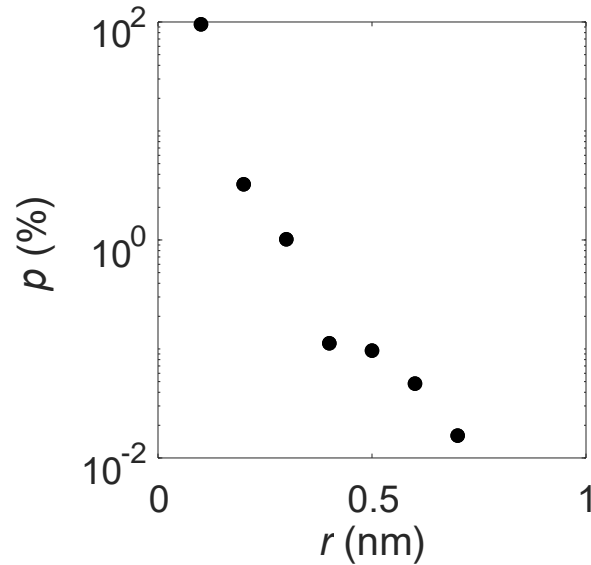


Figure 3-5 Pore size distribution of dry AGX.

### 3.3 Results and discussions

#### 3.3.1 Properties as a function of moisture content and occurrence of moisture-induced crossover

The integral heat of adsorption  $Q(m)$  is shown in Figure 3-6. The dots are the average of three different models while the shaded areas denote the standard deviation (a similar mode of representation is used for Figure 3-7, Figure 3-8 and Figure 3-9). At low moisture content, the heat of adsorption is close to that measured using MD for amorphous cellulose (AC),  $\sim 3620$  kJ/kg (Kulasinski 2015). At high moisture content, the heat of adsorption gradually approaches the value of bulk water,  $\sim 2260$  kJ/kg (Murphy and Koop 2005). Interestingly, two different linear regimes can be identified, one for a lower moisture content range and another for a higher moisture content range. The transition separating the two regimes occurs around  $m \sim 0.3$ .

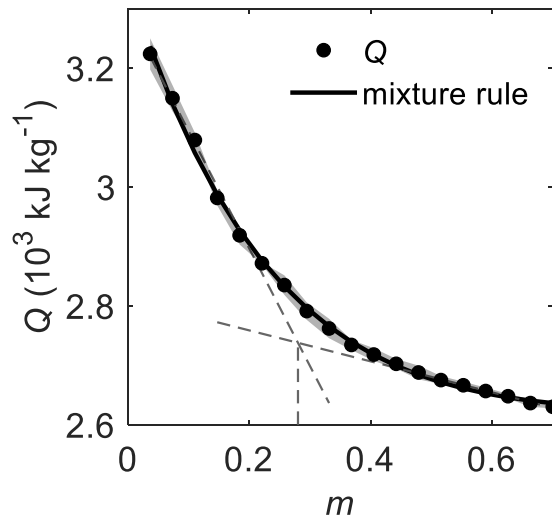


Figure 3-6 Heat of adsorption  $Q(m)$  as a function of moisture content at room temperature 300 K.

The uniaxial thermal expansion coefficient of AGX is shown in Figure 3-7. As moisture increases, the thermal expansion coefficient of AGX approaches the value of pure SPC water indicated by the solid line with asterisks. At 300 K, the uniaxial thermal expansion coefficient of SPC water is  $\alpha_{X,300K,SPC} = 2.3 \times 10^{-4} \text{ K}^{-1}$ , which is larger than the experimental value  $\sim 7.9 \times 10^{-5} \text{ K}^{-1}$  (a known imperfection of the SPC water model (Jorgensen and Jensen 1998)). As observed for the heat of adsorption, a transition occurs around 0.3 moisture content.

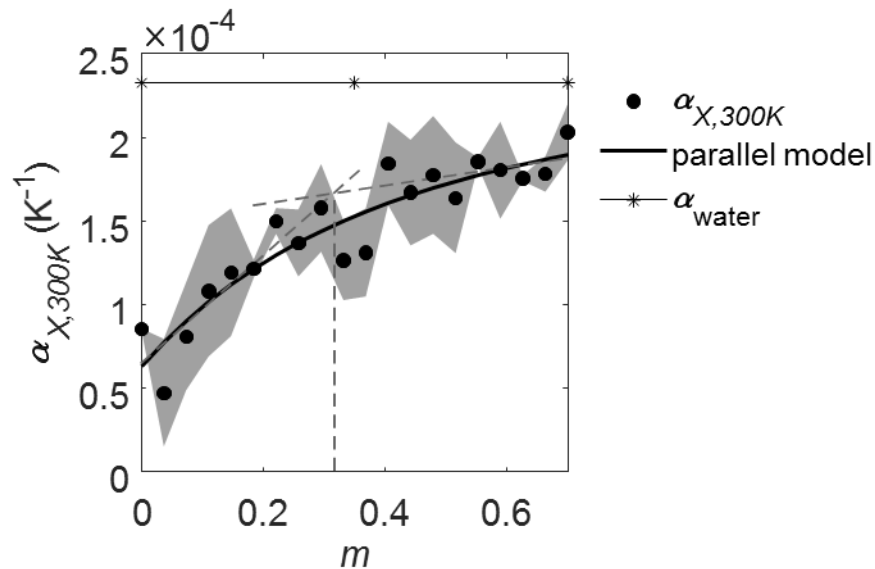


Figure 3-7 Uniaxial thermal expansion coefficient  $\alpha_{X,300K}(m)$ .

The heat capacity of AGX is shown in Figure 3-8. With increasing moisture content, the heat capacity approaches the value of pure SPC water. At 300 K, the heat capacity of SPC water is  $C_{p,300K} = 4.594 \text{ kJ}/(\text{kg K})$ , which agrees well with the experimental value of  $4.186 \text{ kJ}/(\text{kg K})$  (Chase Jr. 1998). Once more, a transition is noted to occur around 0.3 moisture content.

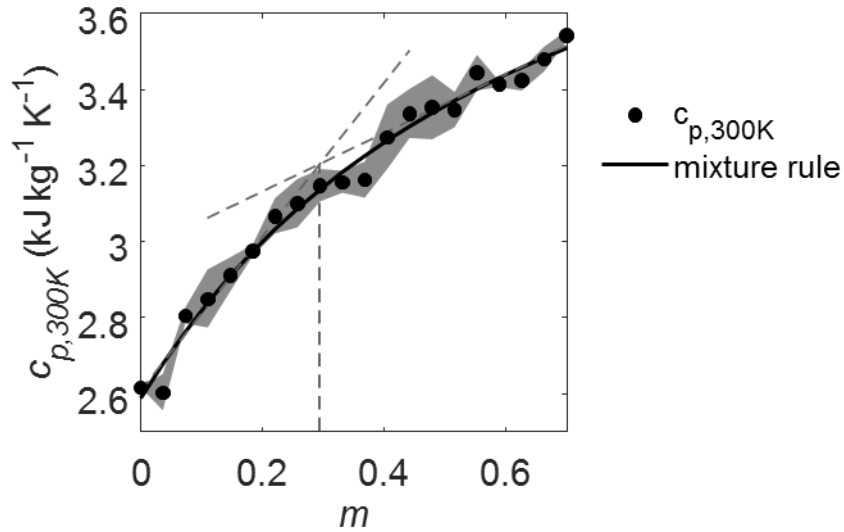


Figure 3-8 Heat capacity  $C_{p,300K}(m)$ .

The bulk, Young's and shear moduli and Poisson's ratio of AGX are shown as solid dots in Figure 3-9a and b. The Poisson's ratio is calculated based on bulk and Young's moduli using equations (3-8). The bulk and shear moduli are difficult to measure experimentally, as samples are usually prepared in the form of thin films (Chang et al. 2018). Available reports, mostly only of Young's moduli at  $27^\circ\text{C}$  and 50% RH, agree well with our simulation which is about 2.5 GPa under similar temperature and moisture content (Gröndahl et al. 2004; Höjje et al. 2005; Escalante et al. 2012). For all these simulated mechanical properties, there is also a transition happening around  $m \sim 0.3$ .

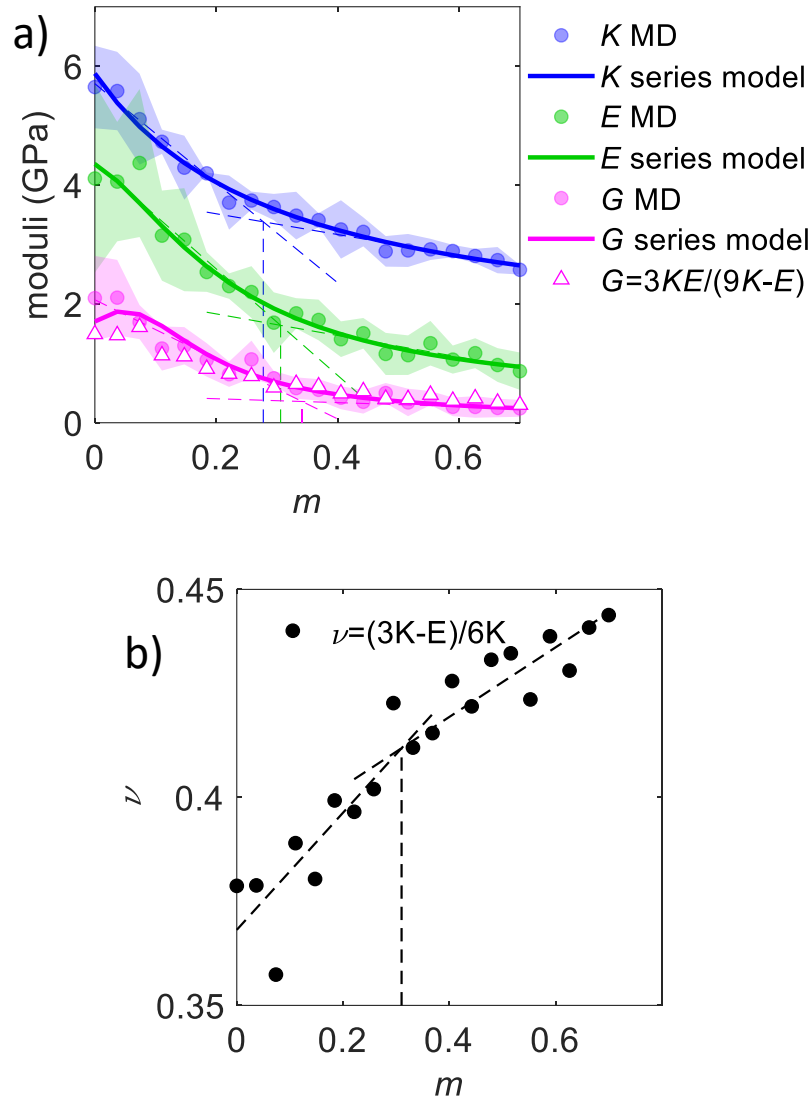


Figure 3-9 a) Elastic constants, i.e. bulk, Young's and shear moduli as functions of moisture content. b) Poisson's ratio calculated based on bulk and Young's moduli.

For an isotropic material, like AGX, as shown in the previous section, shear moduli can be predicted from bulk and Young's moduli using Equation (3-12). The predicted values represented by white triangles in Figure 3-9a agree well with the shear moduli measured by MD in pink dots.

$$G = \frac{3KE}{9K - E} \quad (3-12)$$

All the above mentioned thermodynamic and mechanical properties are rescaled to the range of 0~1 by using the following equation:

$$\widetilde{X}(m) = \frac{X(m) - X(m_{max})}{X(0) - X(m_{max})} \quad (3-13)$$

where  $X$ ,  $X(0)$  and  $X(m_{max})$  are properties at  $m$ , dry and saturated moisture condition, respectively.

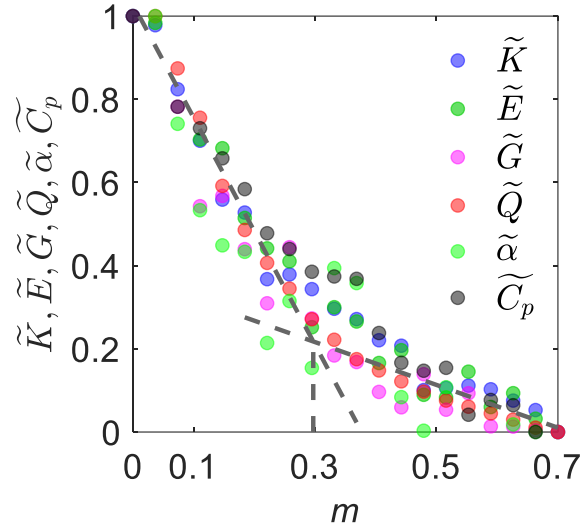


Figure 3-10 Rescaled properties of AGX versus moisture content.

As described earlier, all the rescaled properties show a transition also called crossover happening around  $m \sim 0.3$ . It should be noted that the transition, like most physical transitions, is not an abrupt change. Rather the transition gradually happens over a range and the transition point is taken as the center of this zone.

### 3.3.2 Mechanisms of moisture-induced transition

To explain the transitional behavior observed around  $m \sim 0.3$ , three possible mechanisms, i.e. percolation, breakage of hydrogen network and multiple layers of adsorption, are discussed in this section.

#### 3.3.2.1 Percolation

Given that, at percolation, a water cluster crosses the system, this occurrence influences diffusion-related phenomena, such as water transport (Kulasinski et al. 2014a) or electron conductivity (Wessling 1991). This effects is due to the percolating water cluster allowing water molecules to travel along a path with minimized interaction with the polymer. It is thus plausible that percolation could coincide with the transition of material properties observed above. The percolation probability versus moisture content is shown in Figure 3-11. The inset, a colored illustration, is a snapshot of the hydrated polymer system at  $m \sim 0.14$ , where the blue and red clusters refer to the isolated and percolating water clusters, respectively.

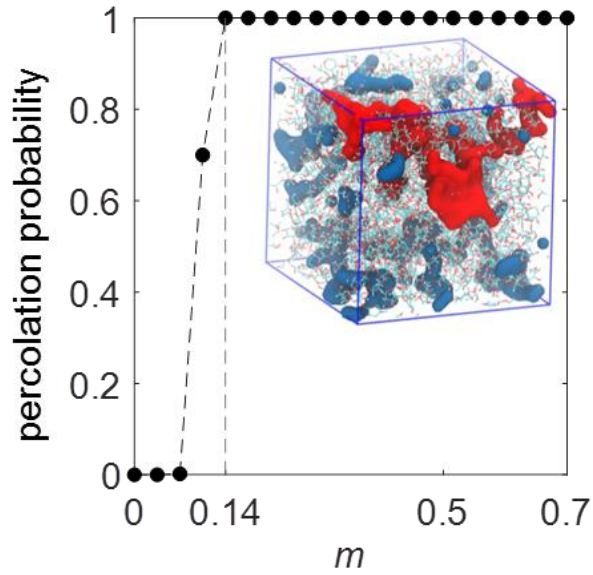


Figure 3-11 Probability of occurrence of percolation versus moisture content. Inset is a snapshot of the hydrated polymer system at  $m \sim 0.14$ .

Simulation trajectories show that, at low moisture content, water molecules tend to attach themselves to the hydroxyl sites of the polymer chains. These water molecules diffuse but are also for some time bonded by HBs where their movement is confined in a small region. As moisture content increases, formerly separated water regions connect, eventually forming water regions that percolate across the whole system. There is a critical range, from  $m \sim 0.11$  to  $0.14$ , where the percolation probability abruptly increases from 0% to 100%. However, the general transition depicted in Figure 3-10, which happens at  $m \sim 0.3$ , cannot be explained by percolation, as percolation already saturates at  $m \sim 0.14$ . There should be another mechanism explaining the behavior at higher moisture content.

### 3.3.2.2 Density of polymer-polymer and polymer-water hydrogen bonds

Since percolation could not explain the transition, another possible mechanism, i.e. the hydrogen bond network and water distribution in the hydrated AGX, is now probed. The HBs between polymer chains play a central role in the moisture-induced effects of hydrophilic polymeric material, such as mechanical weakening (Kulasinski et al. 2015d) and sorption hysteresis (Chen et al. 2018). The establishment of HBs is judged by applying the criteria presented above. The number of HBs is normalized by the initial dry material volume  $V_0$  to obtain the density of polymer-polymer HBs ( $\#HB/V_0$ ). Both  $\#HB/V_0$  for AGX-AGX and AGX-water – shown in black and white dots respectively in Figure 3-12 – remain constant after  $m > 0.18$ , which is below the transition point of  $m \sim 0.3$ . Thus, the number of HBs, either as polymer-polymer and polymer-water interactions, cannot explain the crossover.

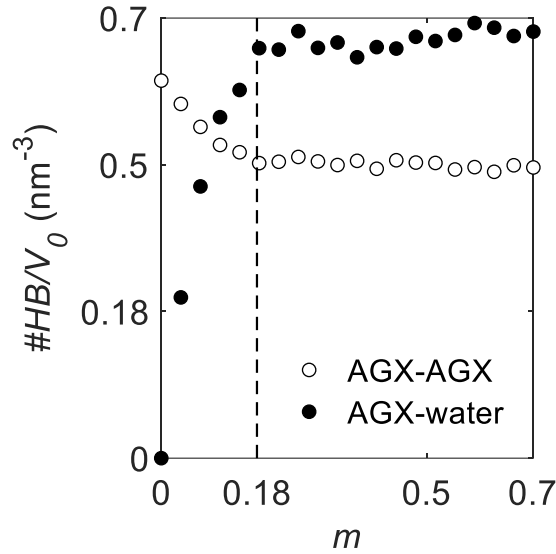


Figure 3-12 Density of hydrogen bonds between AGX-AGX (white) and AGX-water (black), versus moisture content.

In previous work, for another wood polymer, AC, a linear relationship between the number of polymer-polymer HBs and the mechanical moduli was found. The breakage of HBs was then understood to be the main mechanism of the mechanical weakening of AC (Kulasinski et al. 2015). Following the Equation (3-13), the bulk moduli and number of HBs can be rescaled, as shown in Figure 3-13. It is noted that at dry state the number of HBs equals 1, while the number decreases from 1 to 0.1 in a moisture range of 0 to 0.18.

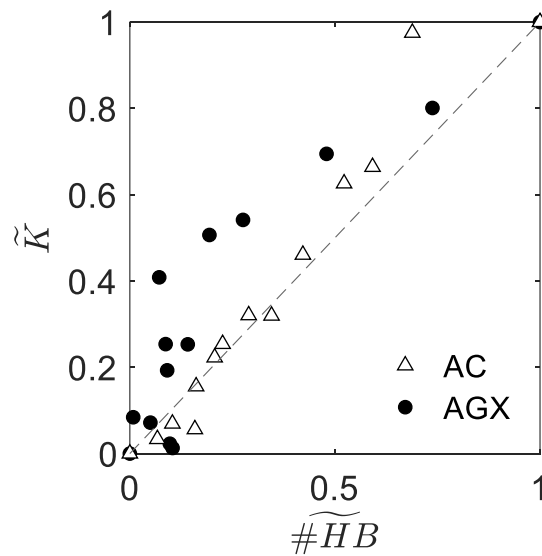


Figure 3-13 Rescaled bulk moduli of AGX and AC versus normalized number of polymer-polymer hydrogen bonds.



In the present study, within the range of 0 ~ 0.18 moisture content, moduli also scale linearly with the HBs breakage. However, for higher moisture contents, i.e.  $m > 0.18$ , further decrease of moduli is seen to occur without further breaking of HBs. The mechanical weakening behavior of AGX for  $m > 0.18$  due to the loss of HBs cannot explain the transition happening around  $m \sim 0.3$ . This indicates that there must be another mechanism explaining the mechanical weakening behavior of AGX for  $m > 0.18$ , and the transition happening around  $m \sim 0.3$ .

### 3.3.2.3 Double layer adsorption

Another possible mechanism inspired by experimental observations is that moisture-induced mechanical weakening occurs also at the appearance of “free water”. As mentioned above, water in the material has been considered to experience two possible states (Hodge et al. 1996b; Li et al. 1998; Brouillet-Fourmann et al. 2002), i.e. “bound” or “unfreezable” in the counterpart of “free” or “freezable”. Thanks to MD, the trajectories of individual water molecules can be tracked, yielding a statistical description of adsorption layers, where the polymer-water distance  $d_{pw}$  is defined as the distance between the oxygen atom of water and its nearest polymer neighbor atom. The water population  $N_{water}(m, d_{pw})$  is the time average of the number of water molecules at a specific moisture content  $m$  and polymer-water distance  $d_{pw}$ . The water population along the polymer chains is given as a function of two parameters, polymer-water distance and moisture content, and is shown as a surface plot in Figure 3-14. At lower moisture content, there is only one peak centered at 2.8 Å. At higher moisture content, practically for  $m > 0.3$ , at least two major peaks, centered at 2.8 Å and 5.6 Å, can be identified.

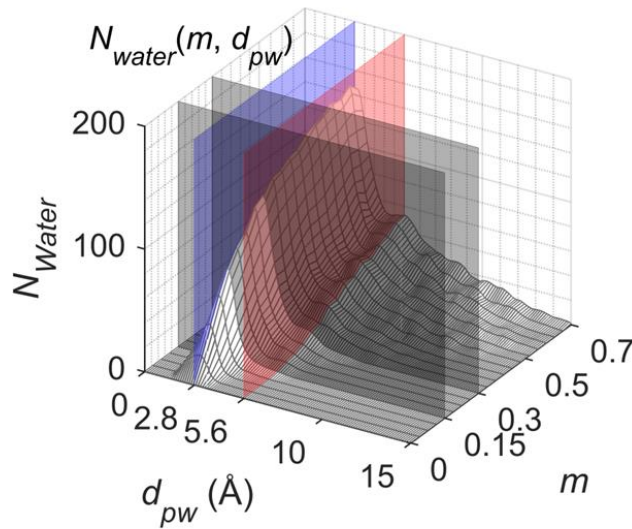


Figure 3-14 Water population as a function of moisture content and polymer-water distance  $N_{water}(m, d_{pw})$  shown as a 3D surface. The four cut planes, i.e. in red and blue,  $d_{pw} = 5.6$  Å and 2.8 Å, and in grey  $m = 0.15$  and 0.3, refer to graphs of Figure 3-15 and Figure 3-16.

Considering the water population versus distance at two moisture contents, as shown in Figure 3-15, the first peak is clearly identified at  $m = 0.15$ , while the second peak is starting to show up at  $m = 0.3$ . Between the two peaks, there is a “valley”, i.e. a local minimum, at  $4.5 \text{ \AA}$ . The water population is practically zero for  $d_{pw} > 15 \text{ \AA}$ . The water that resides within  $4.5 \text{ \AA}$  of the polymer chains is defined as the 1<sup>st</sup> adsorbed water layer and the water lying at more than  $4.5$  but less than  $20 \text{ \AA}$  from the chains as the 2<sup>nd</sup> adsorbed water layer. In this study, given the presence of these two peaks, the water molecules are assumed to form two layers. The water population can be described by the summation of two Gaussian distributions, as shown by the dashed lines calculated from the double Gaussian decomposition (DGD). The DGD captures the main trend of the curve, however not without a small misfit, e.g. at  $5.6 \text{ \AA}$  for  $m = 0.3$ . The occurrence of double-layer adsorption is also supported by the sigmoidal shape of the AGX sorption isotherm (type II isotherm) (Ergun et al. 2010).

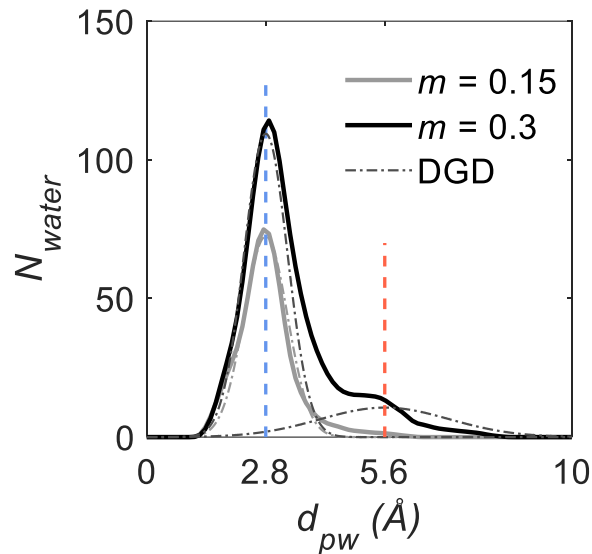


Figure 3-15 Water population as a function of polymer-water distance at  $m = 0.15$  and  $0.3$ , respectively. The black dashed curves are double Gaussian decomposition (DGD) of water population.

The blue and red cut planes in Figure 3-14 denote the center location of the 1<sup>st</sup> and 2<sup>nd</sup> adsorbed water layers, respectively, and the corresponding graphs are given in Figure 3-16. The solid curves are the water population at  $d_{pw} = 2.8 \text{ \AA}$  and  $5.6 \text{ \AA}$ . The linear growth of the water population at  $d_{pw} = 2.8 \text{ \AA}$  slows down from  $m = 0.3$ , indicated by the divergence of the solid blue curve below the dashed line fitted over the range of low moisture content. The water population at  $d_{pw} = 5.6 \text{ \AA}$  starts to grow from  $m = 0.3$ .

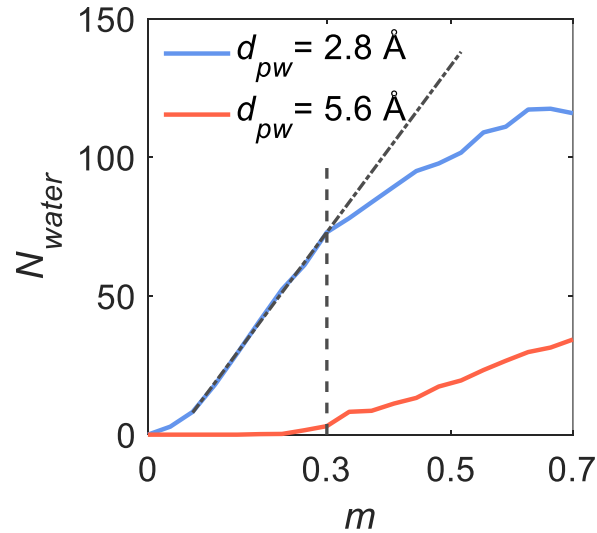


Figure 3-16 Water population as a function of moisture content  $N_{water}(m)$  at the polymer-water distance of 2.8 Å and 5.6 Å.

Figure 3-17 shows the snapshots of the hydrated polymer system at  $m = 0.15$  and  $0.3$ , respectively. The polymer chains, the 1<sup>st</sup> and the 2<sup>nd</sup> layers of water are shown in color thick sticks, blue and red surfaces, respectively. The 2<sup>nd</sup> layer of water is present only at  $m = 0.3$ . The average side length of the system increases from 5.1 nm for  $m = 0.15$  to 5.4 nm for  $m = 0.3$  indicating swelling of the system.

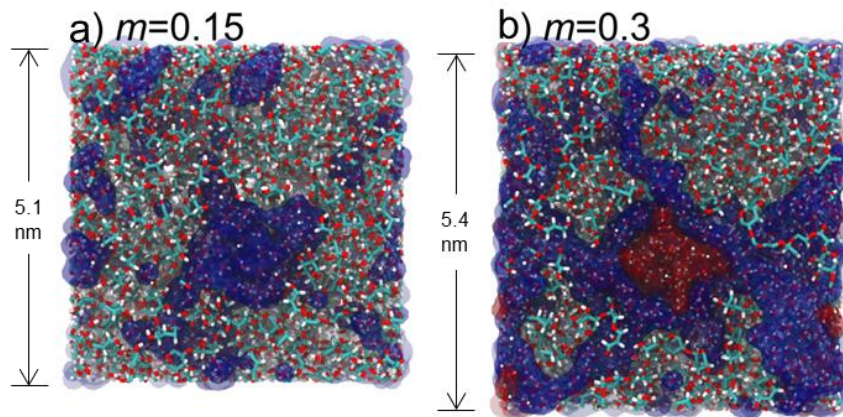
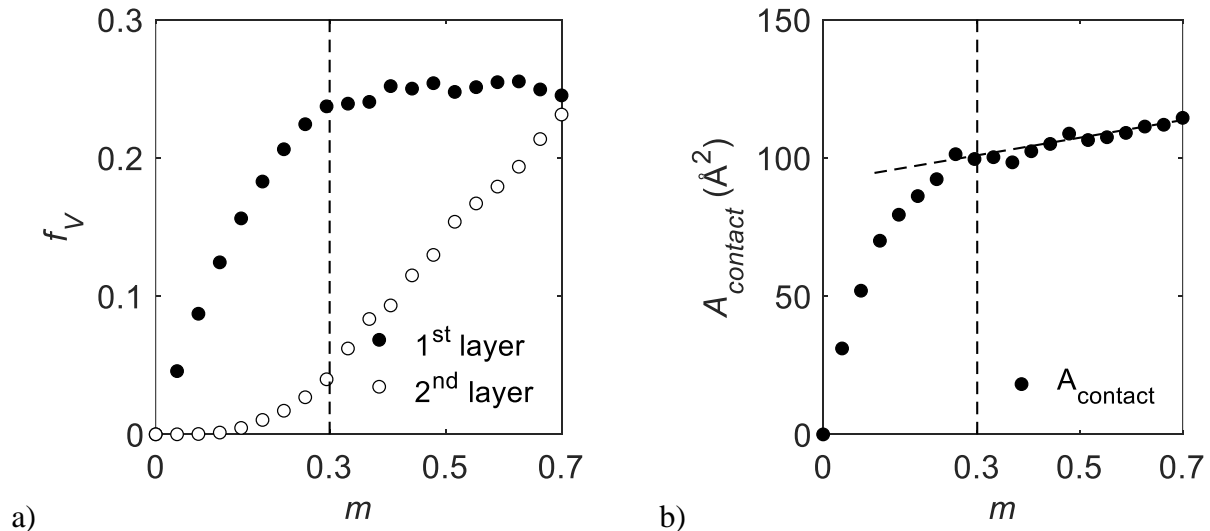


Figure 3-17 Snapshots of hydrated polymer system at (a)  $m = 0.15$  and (b)  $0.3$ , respectively. The polymer chains, the 1<sup>st</sup> and 2<sup>nd</sup> layer of water are shown in color thick sticks, blue and red surfaces, respectively.

Figure 3-18a shows the volume fraction of the 1<sup>st</sup> and 2<sup>nd</sup> water layers as a function of moisture content. The volume fraction of the  $i$ -th water layer is defined as follow:

$$f_{v,i} = \frac{\frac{mass_i}{\rho_{water}}}{\frac{mass_{water}}{\rho_{water}} + \frac{mass_{polymer}}{\rho_{polymer}}} \quad (3-14)$$

where the density of water  $\rho_{water}$  and polymer  $\rho_{polymer}$  are assumed to have a constant value of  $1 \text{ g cm}^{-3}$  and  $1.3 \text{ g cm}^{-3}$ , respectively. The volume fraction of the 1<sup>st</sup> layer undergoes a steep increase from dry state to become  $\sim 0.25$  at  $m \sim 0.3$ , from which point the growth of 1<sup>st</sup> layer saturates. The volume fraction of the 2<sup>nd</sup> water layer, which starts to appear at around  $m \sim 0.2$ , grows steadily with increasing moisture content after  $m \sim 0.3$ . The saturation of the 1<sup>st</sup> water layer is supported by the analysis of the contact area between polymer and water shown in Figure 3-18b. The water-polymer contact area is defined as  $A_{contact} = A^{polymer} + A^{water} - A^{system}$ , where  $A^{polymer}$ ,  $A^{water}$  and  $A^{system}$  are the surface areas of the polymer, water and full systems, respectively. These surface areas are measured by the so-called rolling ball algorithm (Shrake and Rupley 1973), using a ball of a specific radius, here  $1\text{\AA}$ , to roll along the surface of interest, namely the surfaces made by the van der Waals surface of the atoms. The plane defined by the center of the ball as it rolls is the calculated surface area. As shown in Figure 3-18b, within the moisture range of  $0 \sim 0.3$ , water adsorption generates new contact surface. This means that the newly adsorbed water molecules bind to the polymer. However, for  $m > 0.3$ , the contact area somewhat saturates, which means that the newly adsorbed water molecules attach themselves to the formerly adsorbed water rather than to the polymer.



a) Figure 3-18 a) Volume fraction of 1<sup>st</sup> (black) and 2<sup>nd</sup> (white) layers of water. At  $m = 0.3$ , the 1<sup>st</sup> layer saturates while the 2<sup>nd</sup> layer starts to quickly grow. b) Contact area between polymer and water.

As the 1<sup>st</sup> and 2<sup>nd</sup> water layers are located each at a different distance from the polymer chain, their interactions with the polymer are also different. This induces different dynamics and mobility for these two populations (Li et al. 1998; Zhao et al. 2019). The transition from 1<sup>st</sup> to 2<sup>nd</sup> water layer

is likely to influence the properties of the hydrated polymer and to induce a transition, i.e. a crossover, in thermodynamic and mechanical properties of the polymer.

### 3.3.2.4 *Properties of polymer, first and second layers of water predicted by material models*

Having identified the main mechanisms for transition or crossover, the results of heat of adsorption are revisited as shown in Figure 3-6. The figure shows that the adsorption of the first water molecules releases more heat than the adsorption of those of the 2<sup>nd</sup> layer. After  $m > 0.3$ , the 2<sup>nd</sup> layer of water quickly grows and starts to dominate the heat of adsorption. The heat of adsorption approaches the latent heat of liquid water as moisture increases, indicating that the fast-growing 2<sup>nd</sup> water layer resembles bulk water. Similarly in the case of heat capacity, thermal expansion coefficient, elastic constants and Poisson's ratio, the saturation of the 1<sup>st</sup> layer of water and the quick growth of the 2<sup>nd</sup> layer of water induces the crossover. The differentiation of two layers of water enables us to decompose properties into the contributions of different types of water. Hence, three simple material models, i.e. mixture rule, parallel and series models, are used to predict the mechanical and thermodynamic properties, which are seen as the summation of the contributions of three major types of materials involved: polymer, 1<sup>st</sup> and 2<sup>nd</sup> layers of water. The constitutive equations for these models read as:

$$\text{Mixture rule/Parallel} \quad X_c = f_{v,p}X_p + f_{v,w1}X_{w1} + f_{v,w2}X_{w2} \quad (3-15)$$

$$\text{Series} \quad 1/X_c = f_{v,p}/X_p + f_{v,w1}/X_{w1} + f_{v,w2}/X_{w2} \quad (3-16)$$

where  $X_c$ ,  $X_p$ ,  $X_{w1}$ ,  $X_{w2}$  are the properties of composite, polymer, 1<sup>st</sup> and 2<sup>nd</sup> layers of water and  $f_{v,p}$ ,  $f_{v,w1}$  and  $f_{v,w2}$  are the volume fractions of polymer, 1<sup>st</sup> and 2<sup>nd</sup> layers of water, respectively. From simulations, the values of  $X_c$ ,  $f_{v,p}$ ,  $f_{v,w1}$  and  $f_{v,w2}$  can be directly extracted, however the properties of the polymer, and the 1<sup>st</sup> and 2<sup>nd</sup> layers of water  $X_p$ ,  $X_{w1}$  and  $X_{w2}$  can only be determined indirectly. The mixture rule and the parallel model share the same mathematical equations, but they differ in their interpretation. The mixture rule represents the composite behavior of scalar properties such as heat of adsorption and heat capacity, while mechanical properties, such as Young's, bulk, shear moduli and thermal expansion coefficient, are tensorial properties represented by the parallel or series models.

The mechanical moduli, i.e. bulk, Young's and shear moduli, are found to correspond to the series model, the heat of adsorption and heat capacity correspond to the mixture rule, and the thermal expansion coefficient corresponds to the parallel model. Figure 3-6 to Figure 3-9 give the data obtained by MD and the fitted models (solid curves). A list of values for  $X_p$ ,  $X_{w1}$  and  $X_{w2}$  are summarized in Table 3-2. It is found that  $X_{w2}$  correspond relatively well with the value of bulk water. Under the same context, it is reasonable to speculate that  $X_{w1}$  represents the properties of the 1<sup>st</sup> layer of water, which are difficult to measure both numerically and experimentally.

Finding that the material properties like heat of adsorption and heat capacity follow a mixture rule model is logical since these are scalar properties. Our findings show that the polymer material, the first and second adsorbed water layers act as a layered composite material loaded mainly normally to the layers as in a series model. Since the thermal expansion corresponds to a parallel model, it shows that the polymers, as well as layers of water, mainly expand along their longest direction which is along the layer direction as in a parallel model. The properties of the second layer of water resemble that of bulk water as listed in Table 3-2. According to all these analyses, the conclusion is that the saturation of the 1<sup>st</sup> water layer and the development of the 2<sup>nd</sup> water layer is the mechanism inducing the crossover occurring around  $m \sim 0.3$ , as seen in heat of adsorption, thermal expansion coefficient, heat capacity, elastic moduli and Poisson's ratio.

Table 3-2 Predicted properties of the polymer, first and second layers of water\*

|  | <b>polymer</b>       | <b>first layer<br/>water</b> | <b>second layer<br/>water</b> | <b>bulk water</b>     | <b>unit</b> |
|--|----------------------|------------------------------|-------------------------------|-----------------------|-------------|
| <b>bulk moduli <math>K</math></b>                            | 5.9                  | 1.9                          | 1.5                           | 1.7                   | GPa         |
| <b>young's moduli <math>E</math></b>                         | 4.6                  | 1.1                          | 0.32                          | 0                     | GPa         |
| <b>shear moduli <math>G</math></b>                           | 1.9                  | 0.6                          | 0.068                         | 0                     | GPa         |
| <b>adsorption heat <math>Q</math></b>                        | 3340                 | 1110                         | 2660                          | 2260                  | kJ/kg       |
| <b>thermal expansion<br/>coefficient <math>\alpha</math></b> | $6.4 \times 10^{-5}$ | $3.7 \times 10^{-4}$         | $2.9 \times 10^{-4}$          | $2.33 \times 10^{-4}$ | 1/K         |
| <b>heat capacity <math>C_p</math></b>                        | 2.6                  | 4.6                          | 4.4                           | 4.594                 | kJ/kg/K     |

\*Bulk, Young's and shear moduli are inferred by the series model. Adsorption heat and heat capacity are inferred by the mixture rule. Thermal expansion coefficient is inferred by the parallel model.

### 3.3.2.5 Cohesive energy density

As shown in the previous section, although AC and AGX are both hydrophilic polysaccharides, they behave differently. In our opinion, this difference between AC and AGX could originate from their different intensity of intermolecular interaction, a hypothesis that is verified by evaluating their cohesive energy density (CED), as listed in Table 3-3.

Table 3-3 Cohesive energy density of AGX, AC and water

|                       | CED MD (cal cm <sup>-3</sup> ) | CED Exp. (cal cm <sup>-3</sup> ) |
|-----------------------|--------------------------------|----------------------------------|
| Arabinoglucuronoxylan | 80.90                          | -                                |
| Amorphous cellulose   | 122.99                         | 161.54 (Haynes W. M. 2017)       |
| Water                 | 542.67 (SPC with PME)          | 546.29 (Hansen 2007)             |

The CED quantifies the volumetric contribution of intermolecular interaction to the internal energy of a substance in condensed state. To our knowledge, the CED of arabinoglucuronoxylan has not been reported yet. As shown in Table 3-3, the CEDs of AC and water measured by MD agree with experimental results. Comparing with the CED values, AC is closer to that of water than that of AGX is, indicating the better miscibility of AC to water (Hansen 2007). This explains that, at high moisture content (e.g.  $m > 0.18$ ), HB breakage is saturated for AGX, but not yet for AC as shown in Figure 3-13. Generally speaking, polymers and solvents with similar CED tend to dissolve each other (Hansen 2007), such as AC and water.

### 3.3.3 The general picture of moisture adsorption

Following the above results and discussions, the adsorption process in AGX can be briefly summarized. The dry material possesses initial pores that are large enough to accommodate water molecules, as supported by the pore size distribution (Figure 3-5). The first water molecules enter the existing pores in the polymeric system, inducing low swelling strain. As more and more water is adsorbed, the polymer chains are separated, polymer-polymer HBs break and new porosities are created. Concurrently, the polymer-polymer HB number lowers (Figure 3-12) and the polymer-water contact surface area increases (Figure 3-18). Percolation water cluster starts to form at  $m \sim 0.11$  (Figure 3-11) and the breakage of polymer-polymer HB plateaus at  $m \sim 0.18$  (Figure 3-12). The first layer of water adsorption saturates at  $m \sim 0.3$ , as supported by the water population analysis (Figure 3-14). The later adsorbed waters attach themselves to the existing water clusters and do not form new contact surfaces with polymer chains. This layering behavior of water molecules in first and second layers is seen as the mechanism elucidating the crossover of the thermodynamic and mechanical properties of AGX.

This new insight fills a gap for the full understanding of the structure-property relationship of polymers, which may interest many research fields and industries. For example, in the plastic, adhesive, hydrogel and food industries, the states and molecular structures of the water within polymers matrix have an important impact on the material properties where crossover might come into play (Hodge et al. 1996a; Li et al. 1998; Brouillet-Fourmann et al. 2002). Another example is that, in classic linear poromechanics (Coussy 2003), the energy terms of the strain and chemical potential are quadratic terms, while the coupling energy term is written as the linear product of strain and chemical potential. This means that the poroelastic properties, e.g. bulk modulus, moisture capacity and coupling coefficient are constants independent on strain (or stress) and chemical potential (or moisture content), which might lead to wrong predictions. This study shows

that two modes, separated by a transition zone, exist in the moisture-material interactions. This physics could provide guidance on the proper modeling of thermodynamic and mechanical properties of polymeric porous media, thus facilitating the improvement of existing poromechanical models.

Interestingly, in experiments, similar saturations around  $m \sim 0.3$  have been also found for other materials. Li et al. (Li et al. 1998) were able to differentiate “unfreezable” water, which creates strong interaction with starch polymer either energetically bounded or kinetically retarded, to “freezable” water by using differential scanning calorimetry (DSC). They found that the saturation of “unfreezable” water happens at 0.3 moisture content. Brouillet-Fourmann et al. (Brouillet-Fourmann et al. 2002) revealed a similar saturation of bound water at 0.3 moisture content in a hydrated starch system also by DSC. Hodge et al. (Hodge et al. 1996a) found a saturation of “nonfreezing water” for water concentration greater than 0.3 in polyvinyl alcohol.

### 3.4 Conclusion

There is considerable interest in understanding the thermodynamic and mechanical responses of hydrophilic plant biopolymers upon moisture adsorption. In particular, such understanding could allow better utilization of plant-based sustainable resources. In this study, molecular dynamics simulation is used to investigate the influence of moisture on the properties of a prototypical hydrophilic polymer: softwood xylan. The heat of adsorption, heat capacity, thermal expansion, elastic moduli and Poisson’s ratio are documented as functions of moisture content.

All the mechanical and thermodynamic properties show a transition occurring around  $m \sim 0.3$  moisture content, which cannot be explained by the alteration of the hydrogen bond network which plateaus at  $m \sim 0.18$ , nor by the occurrence of percolation. A study of water population distribution and polymer-water contact area leads to the identification of a double-layer adsorption. The saturation of the first adsorption layer and the growth of the second adsorption layer of water are identified as the main mechanism of the moisture-induced transition and crossover. This decomposition of two types of water also enables a further material model study, where properties of the composite can be attributed to the contributions of the three major components, i.e. polymer, first and second layers of water. Whether the crossover observed in the current study is actually occurring universally in similar systems still requires further investigation. Nevertheless, the simulation framework and the statistical analysis of the layering structure of water could be extended to other material systems potentially explaining phenomena associated with it. These new insights provide an important piece of information towards the full understanding of the structure-property relationship of polymers, which may interest many research fields and industries. Mechanical properties of wood polymers are particularly important to the industry, where practice suffers from the lack of knowledge of individual components.

The computational results of this chapter fill the gap of experimental characterization of AGX material. Here, a general picture of the adsorption process is presented. In contrast, the next chapter



inquires into the microscopic mechanisms of moisture-induced weakening effects from both dynamical and thermodynamical points of view. These two chapters together form an integrated understanding of hydration impact on biopolymer mechanics, while offering novel characterizations on two of the most important components of softwood S2 wall layer matrix, namely AGX and uLGN.

## Chapter 4 Disentangling Heat and Moisture Effects on Biopolymer Mechanics: A Case Study of Softwood Lignin

In the previous chapter, the impact of moisture on the thermodynamics and mechanics of biopolymers was discussed using softwood xylan as the prototypical polymer. It is important to distinguish the mechanisms by which heat and moisture impact biopolymer mechanics, which is the aim of this chapter. Heat and moisture are known to have important mechanical effects on polymers such as hygric swelling, thermal expansion and mechanical weakening. A common approach when investigating such effects is to assume the effects of heat and moisture to be similar – the so-called time-temperature-moisture superposition. This molecular dynamics study evaluates the extent of similarity in the effects of moisture and heat on the hygric swelling, thermal expansion and mechanical weakening of a biopolymer: an uncondensed type of lignin, one of the most abundant polymers in the plant regime. A microscopic metric, the local stiffness of the polymer skeleton ( $T/\langle u^2 \rangle$ ), temperature divided by the amplitude of segmental motion ( $\langle u^2 \rangle$ ), is introduced to analyze the mechanisms of mechanical effects of heat and moisture. The local stiffness of the polymer skeleton and the overall stiffness of the composite material are shown to be strongly correlated, with a Pearson correlation coefficient of 0.96. Under the assumptions of harmonic vibration and isotropy, an explicit equation relating bulk moduli and the local stiffness is derived, yielding theoretically predicted moduli in good agreement with MD measurements. The thermal expansion and weakening are shown to be interrelated and both dependent on the local stiffness. The analysis of the potential energy further points out that heating weakens both primary and secondary bonds of the polymer skeleton, while hydration only affects the secondary bonds. This major difference is thought to be at the origin of the different impacts of heat and moisture on biopolymer mechanics, offering a revised view on the time-temperature-moisture superposition principle.

The main content of this chapter is published in Zhang, C., Shomali, A., Guyer, R., Keten, S., Coasne, B., Derome, D., & Carmeliet, J. (2020). Disentangling Heat and Moisture Effects on Biopolymer Mechanics. *Macromolecules*, 53(5), 1527-1535.

### 4.1 Introduction

The systematic understanding of the coupled physics of moisture and heat is important for the effective utilization of many natural and synthetic polymeric materials. One approach for considering the effects of heat and moisture is based on the widely acknowledged time-temperature superposition principle (TTSP), also named as the thermo-rheologically simple postulate, which assumes that an increment in temperature is equivalent to an increment of time of observation. For example, the time-elastic modulus curves at different temperatures resemble each other when horizontally shifted. In addition to temperature, a number of other shifting factors are known, such as moisture content, diluent concentration, blend ratios. Thus, jointly varying moisture content and temperature creates a “doubly shifted” master curve, based on which a number of experimental

reports have proposed the so-called time-temperature-moisture superposition principle (TTMSP) of polymers (Onogi et al. 1962; Emri and Pavsek 1992; St. Lawrence et al. 2001; Patankar et al. 2008; Silberstein et al. 2011; Fabre et al. 2018; Suarez-Martinez et al. 2019). This master curve also suggests that the influence of heat and moisture can be treated using mathematical forms similar to the Williams-Landel-Ferry (WLF) equation (Williams et al. 1955; Emri and Pavsek 1992; Chaléat et al. 2008), though it is reported that the TTMSP may not hold at low moisture content (Harper et al. 1997). The moisture content is sometimes referred to as “apparent temperature”, where an increment in moisture content is taken as an equivalent of rise in temperature (Parodi et al. 2018). The current justification of TTMSP is based on macroscopic and phenomenological observations but lacks observations of the mechanisms at play at the microscale. Similarity of the effects of heat and moisture on polymers elastic behavior has yet to be analyzed and the mechanism at its origin elucidated.

In this chapter, the heat and moisture effects are analyzed and discussed in terms of their similarities, as inspired by TTMSP, but also their differences, the latter a topic rarely touched in literature. Molecular dynamics (MD), a simulation method widely used in bio-physics or materials science, is the main tool of investigation of this thesis. Applying proper force field parameters and potential equations, MD allows capturing the trajectories of atoms at femtosecond time resolution giving microscopic information. Based on such microscopic movements of atoms, macroscopic variables such as temperature, pressure, enthalpy can be harvested using statistical thermodynamics, making MD a powerful tool for investigating physical and mechanical aspects. Here the focus is on the instantaneous elastic response of a model polymeric material, while the study of viscoelastic is out of the scope of this investigation. The detailed MD information is then used for an attentive analysis of the differences and similarities.

There are few papers discussing the combined influence of heat and moisture on the mechanical behavior of polymers using MD. Xin and Han show that both heat and moisture decrease the mechanical properties of cross-linked epoxy (Xin and Han 2013). Vural et al. find a similar effect of either heat or moisture on polymer segmental relaxation (Vural et al. 2018b). Suarez-Martinez et al. show that both temperature and moisture affect in a similar way the dynamics of a polyelectrolyte chain, supporting the time–water–temperature superposition principles (Suarez-Martinez et al. 2019). However, the different effects of heat and moisture on the mechanical properties of biopolymer has yet to be interrogated with MD.

As prototypical polymer, this study focusses on the behavior of the uncondensed type of lignin (uLGN), lignin being one of the most abundant biopolymers on Earth. Uncondensed lignin is a linear polymer, not to be confused with condensed lignin also present in plants which is randomly cross-polymerized. The uLGN is known to be moderately hydrophilic thus serving as a complement to other frequently studied hydrophilic polymeric materials, such as nylon (polyamide) (Valentin et al. 1987), polyvinyl acetate (PVAc) (Emri and Pavsek 1992) and polyvinyl alcohol (PVA) (Onogi et al. 1962). There have been several MD studies focused on various properties of

lignin. Petridis et al. study the temperature-dependent structure and dynamics of randomly branched lignin, i.e. condensed type of lignin, and observed that temperature rise enhances dynamics and the polymer transforms from compact to extended conformations (Petridis and Smith 2009; Petridis et al. 2011b). Vural et al. combine MD and experiments, namely neutron scattering and dielectric spectroscopy, and found that dilatation is hysteretic in heating and cooling (Vural et al. 2018a). Buehler et al. investigated the influence of lignin structure on the deformation of wood cell walls in dry state (Jin et al. 2015). Beste et al. used the ReaxFF force field to investigate the thermal decomposition in oxygen environment of the most common linkages in softwood, which included condensed lignin (Beste 2014). Despite these works, there is a lack of a comprehensive study of the mechanics of lignin under various temperatures and moisture contents. Extraction of lignin, a common pretreatment called the delignification process, is of significant economic impact due to its ubiquitous presence in the pulp and paper production. Thus, a better understanding of the microscopic mechanisms of the combined impact of heat and moisture could help to improve the delignification process. In general, the existing experimental characterization of lignin is based on its chemically heterogeneous structure, i.e. randomly branched. A study of the mechanical properties of linear lignin under a series of temperature and moisture content fills the experimental gap.

In this chapter, the study aims at understanding the microscopic mechanisms of hygric swelling, thermal expansion and mechanical weakening under hygric and thermal loadings. Using MD, the local stiffness of the polymer skeleton for different amounts of adsorbed water is determined. The amplitude of segmental motion, sometimes referred to as the Debye-Waller factor, is used as a microscopic metric. The macroscopic elastic moduli derived from a theoretical model are compared with MD measurements. The objective is to provide an explanation for the similarities and differences between the effects of heat and moisture on the fundamental thermodynamic and mechanical behavior of this polymer, lignin, taking into account the molecular mobility and energetics.

## **4.2 Materials and Methods**

### **4.2.1 Preparation of the hydrated lignin system**

Lignins may have different compositions. The lignin in S2 spruce wall layer has one monomer, coniferyl alcohol. Thus, the modeled uLGN consists of a linear chain of  $\beta$ -O-C4 linked coniferyl units (the  $\beta$  carbon is linked with the oxygen atom connected to C4), with degree of polymerization estimated to be around 100 (Pettersen 1984). The modeled lignin unit is shown in Figure 4-1. The C2, C5 and C6 positions of the monomer are free of substitution while the C3 position is substituted with a methoxyl group (Dorrestijn et al. 2000). There is a lack of experimental characterization of pure uLGN material, caused by the difficulties of its extraction without chemical alteration. Although the exact structure of lignin in plants is still ongoing investigation due to its complex nature, the polymer uLGN is understood to be of rather linear type. The molecular model here contains five chains with a degree of polymerization 100.

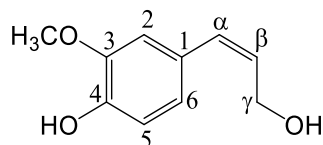


Figure 4-1 Chemical structure of the monomer of uncondensed lignin, coniferyl unit. The  $\beta$  carbon is linked with the oxygen atom connected to C4, forming the so-called  $\beta$ -O-C4 linkage.

The initial chemical structure is built in Material Studio 8.0. For MD simulations, Gromacs 5.0 (Abraham et al. 2015) software and Gromos 53a6 (Oostenbrink et al. 2004) force field are applied. The Gromos 53a6 force field is chosen because of its unique feature that it is based primarily on reproducing the free enthalpies of hydration and apolar solvation for a range of compounds, which fits the investigations about biomolecule hydration, solvation and association (Oostenbrink et al. 2004). The automated topology builder (ATB) server is used to carry out the parameterization and the primary geometry optimization (Malde et al. 2011; Canzar et al. 2013; Koziara et al. 2014). The single chains of uLGN are energy minimized. Then, five relaxed chains are placed in one simulation box with full periodic boundary conditions. The system is further relaxed for 20 ns in NPT using a Nose-Hoover thermostat and a Parrinello-Rahman barostat with temperature and pressure being 300 K and 0 Pa, respectively. The equilibrated system attains a density of  $1.33 \text{ g/cm}^3$ , which is in accordance with the experimental result of  $1.36 \text{ g/cm}^3$  (Terashima et al. 2009). The density measured under 0 Pa pressure is close to that measured under standard pressure (0.101 MPa). The Herman's orientation function of the equilibrated structure has a value of  $0 \pm 0.02$  which verifies that the simulated material is actually isotropic. The hydroxyl groups of lignin are evenly distributed in space, meaning that no hydrophobic or hydrophilic pores are formed. All production simulations are carried out under NPT ensemble. In most simulations, the pressure is set to 0 Pa, except for the bulk modulus measurements for which the system is tested under a specific mechanical loading. The cut-off distances of both Coulombic and van der Waals interactions are set to 1 nm and the long-range Coulombic interactions are calculated by particle mesh Ewald summation. The covalent bonds with hydrogen atoms are constrained with the LINCS algorithm. The time step of integration is 1 fs.

The GROMOS force field is designed to work with the single point charge (SPC) model. This study focuses on the thermodynamic equilibrium state without consideration of water diffusion process. The SPC model predicts well the density, heat of vaporization and isothermal compressibility of pure water. However, this model yields a value for the thermal expansion coefficient (TEC), of  $\sim 10^{-3} \text{ K}^{-1}$  at 298 K, which is relatively larger than that measured in experiments,  $\sim 2.5 \cdot 10^{-4} \text{ K}^{-1}$  at 298 K (Jorgensen and Jenson 1998). Water molecules are introduced to the system through the random insertion of water molecules, followed by energy minimization and 10 ps of equilibration. To reduce the computational costs, 8 moisture content levels are chosen for further studies. For each moisture content level, an extra 20 ns of equilibration is applied to ensure equilibrium is reached. The distribution of water molecules, quantified by the radial distribution function of the oxygen

atoms of water, is seen to remain stable after 10 ns, confirming that 20 ns of equilibration time is sufficient to let the system reach equilibrium. The polymer carbon atoms radial distribution functions are also checked in a similar way. In fact, extended simulations as long as 1000 ns are carried out and give radial distribution function results similar to the one of the 20 ns results (Figure 4-2a and b). A snapshot of the hydrated polymer system at  $m \sim 0.3$  is shown in Figure 4-2c.

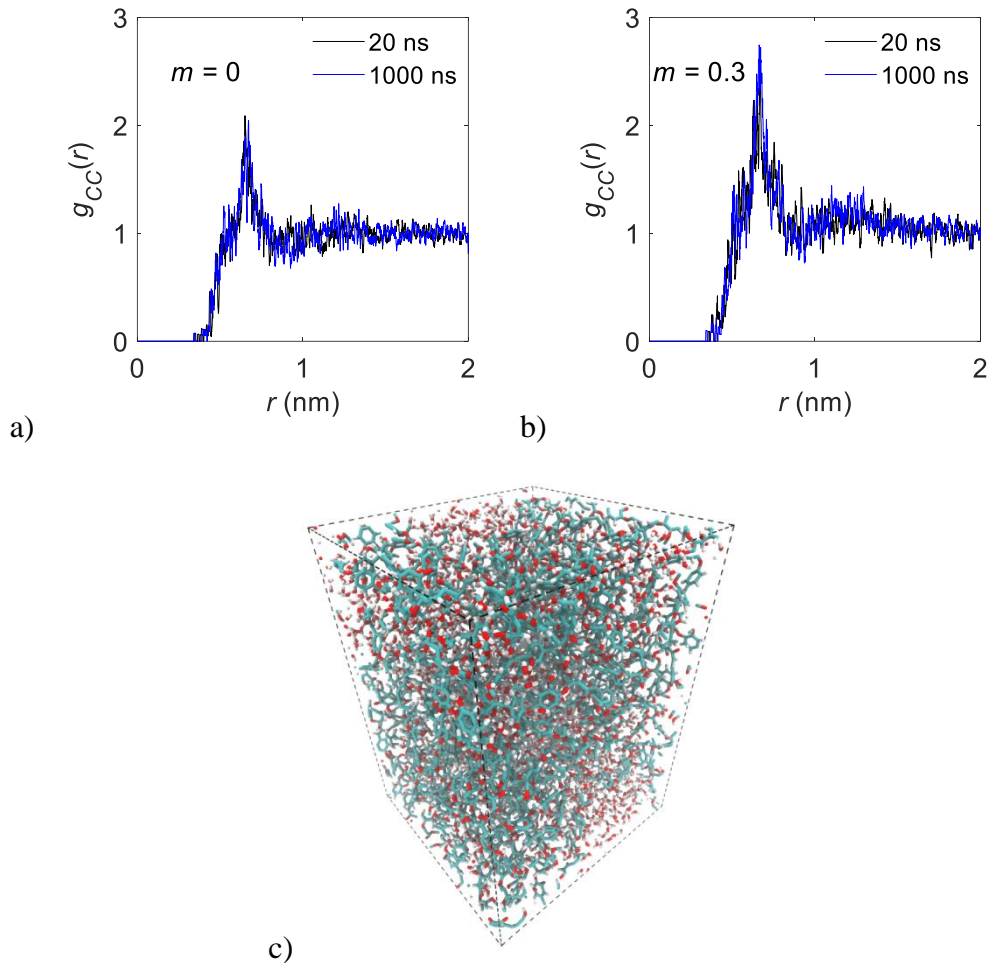


Figure 4-2 Radial distribution function plot of carbon atoms of lignin polymer at a)  $m=0$  and b)  $m=0.3$ . c) Snapshot of hydrated uLGN at  $m \sim 0.3$ .

The studied moisture content range covers  $0 \sim 0.3$ , with an increment of 0.04, in mass of water per mass of dry polymer. The investigated temperature range is 283~373 K, with an increment of 10 K. These ranges are broader than the ranges of common ambient conditions of wood usage to allow a more in-depth investigation. It is noteworthy that, in the temperature range of investigation, no major change of chemical or physical properties, such as pyrolysis of polymer and temperature-induced phase change of water, occurs. The pyrolysis temperature of lignin ( $\sim 600$  K) (Yang et al. 2006) is much higher than the maximum temperature studied here. Water molecules confined in porous media have a lower freezing point ( $< 273$  K) (Jackson and McKenna 1990) and higher

boiling point ( $>373$  K) (Roduner) than bulk water due to the Gibbs-Thomson effect. This ensures that, in this work, water molecules do not experience a phase change such as freezing or evaporation, but only adsorption and desorption.

Three repetition systems are prepared following the same modeling process above. They differ by their polymer chain orientations and initial water insertion locations. All the repetition systems are then tested under the same protocol as described below. The obtained results are averaged and their standard deviation calculated. This study only concerns the bulk properties of the bulk material without discussing surface properties, which would require special arrangement of materials and introducing a vacuum to form a surface. The focus is on mechanical properties and their dependence on temperature and moisture content, disregarding transport properties like water diffusion.

#### 4.2.2 Evaluation of the free strain

The volume of the system, denoted as  $V(m, T)$ , is measured as the time average volume over a 0.5 ns production run that followed a 1.5 ns equilibration run in the NPT ensemble ( $P = 0$  Pa). The volume is measured under a series of different moisture content and temperature conditions allowing free deformation. The system reaches its stable state within the first 0.1 ns of the equilibration run. The volumetric strain  $\epsilon_V(m, T)$  due to changes in moisture content and temperature is determined as the relative difference with respect to the volume at  $m = 0$  and  $T = 283$  K:

$$\epsilon_V(m, T) = \frac{V(m, T) - V(0, 283 \text{ K})}{V(0, 283 \text{ K})} \quad (4-17)$$

Volumetric strain is referred to as swelling strain when the moisture content is increased, or as thermal expansion strain when the temperature is increased. In this work, volumetric strain is referred to as free strain.

#### 4.2.3 Evaluation of the bulk modulus

The bulk modulus is measured by compression test. The system is first equilibrated in NPT ( $P = 0$  Pa) for 20 ns to obtain the equilibrium volume  $V(m, T)$  in the free stress state. Then equal pressure in x, y and z direction is applied, where the system is simulated in NPT (compression  $P = \sigma = 0.05$  GPa) for 2 ns to obtain the equilibrium volume in the loaded state  $V^\sigma(m, T)$ . The system equilibrium is reached within the first 0.1 ns of the run, which is much shorter than the total relaxation time given to the system of  $\sim 2$  ns. The bulk modulus is calculated as (Kulasinski et al. 2014a):

$$K(m, T) = -V \frac{\partial \sigma}{\partial V} = \sigma \left| \frac{V(m, T)}{V^\sigma(m, T) - V(m, T)} \right| \quad (4-18)$$

The load value  $\sigma$  of 0.05 GPa is chosen large enough to suppress sufficiently fluctuations of the system volume and to guarantee that the resulting strain ranges from 2% to 4%.

There are multiple methods to measure bulk modulus of a material. The advantage of the method retained to determine the bulk modulus by imposing a pressure is its low computational cost, which is important considering the large number of samples in this study. In this method, a hydrostatic pressure is applied and the responding volumetric strain is collected. A more rigorous yet more expensive method of measuring elastic modulus would have been straining materials at a low rate meanwhile collecting the responding stress. As information, this more rigorous method is used in other parts of this thesis, such as the bulk modulus of uLGN, as function of the moisture content ranging from 0 ~ 0.3 at room temperature 300 K presented in Chapter 8.

#### 4.2.4 Evaluation of the density of the polymer-polymer hydrogen bonds

As presented in Chapter 3, the criteria for hydrogen bond are defined by the configuration of the donor-hydrogen-acceptor triplet:

$$r \leq 0.35 \text{ nm and } \alpha \leq 30^\circ \quad (4-19)$$

where  $r$  is the distance between the donor oxygen atom and the acceptor oxygen atom, and  $\alpha$  is the angle of acceptor oxygen atom – donor oxygen atom – donor hydrogen atom. It should be noted that the first minimum of the radial distribution function of SPC water is positively proportional to the temperature (arrows indicated in the Figure 4-3).

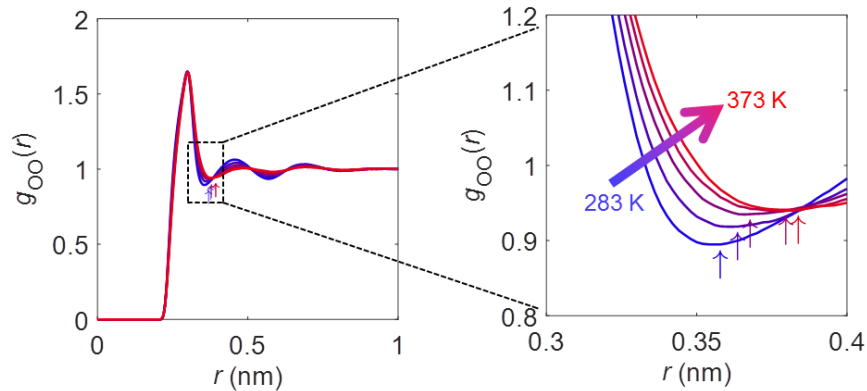


Figure 4-3 Radial distribution function of SPC water oxygen atoms, with zoom-in shown on the right side.

In this chapter not only polymer-polymer hydrogen bonds are presented, because of their determining role in polymer mechanics, but also polymer-water and water-water hydrogen bonds are included. The number of hydrogen bonds is normalized by the sample volume at  $m = 0$  and  $T = 283 \text{ K}$ , resulting in a Lagrangian density of polymer-polymer hydrogen bonds with units of  $\text{nm}^{-3}$ . The average value of the three repetition systems is reported.

#### 4.2.5 Evaluation of the local stiffness

In this chapter, the local stiffness is used as a metric at microscale. The local stiffness is defined as the quotient of temperature  $T$  and the  $\langle u^2 \rangle$  factor. The  $\langle u^2 \rangle$  factor indicates the average



displacement of atoms at picosecond time scales and is related to the mechanical properties. An inverse proportionality is frequently assumed between the  $\langle u^2 \rangle$  factor and the local elastic properties, e.g. high-frequency modulus  $G_\infty$  (Riggleman et al. 2010), derived on the basis of the simple Maxwell model of liquids (van Zanten and Rufener 2000). The  $\langle u^2 \rangle$  is also referred to as the Debye-Waller factor (Debye 1913; Waller 1923), a property of material that can be measured by neutron scattering experiments (Price and Fernandez-Alonso 2013) and molecular simulations (Xia et al. 2017).

The  $\langle u^2 \rangle$  factor can be understood as follows. At molecular level, a chain segment displaces within a temporary cage formed by its surrounding segments, as schematized in the left part of Figure 4-4a. The mean square displacement (MSD) of the chain segment increases, shown as stage 1 in the MSD-time plot of Figure 4-4b, until the movement of the segment is restrained by the boundary of the cage and bounces back. A plateau in the MSD-time plot emerges when such rebounds happen, shown as stage 2, where the corresponding time scale is called the caging time and the corresponding MSD,  $\langle u^2 \rangle$ , indicates the size of the molecular cage. Beyond the caging time, the chain segments will show diffusive behavior and escape from the cage, as shown in the right part of Figure 4-4a and in Figure 4-4b stage 3.

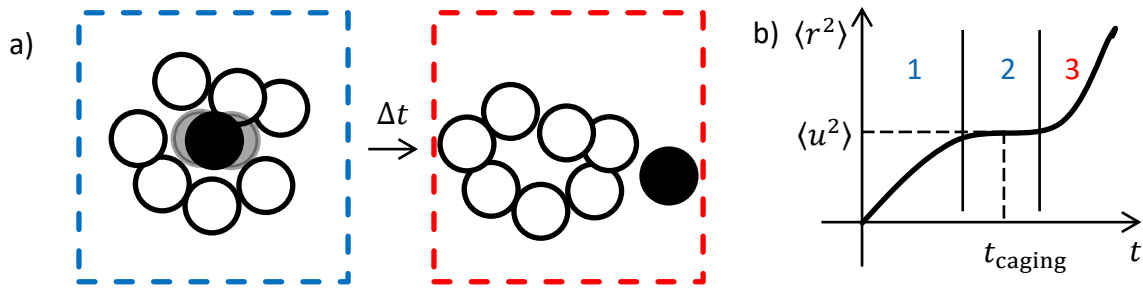


Figure 4-4. a) Schematic representation of caging effect, blue and red squares corresponding to caged and diffusive states, respectively. b) Mean square displacement curve of chain segments versus time. Stages 1 and 2 correspond to the blue state while stage 3 to the red state.

If the chain segment is assumed to be confined to its equilibrium location by a harmonic spring, the energy of the chain segment movement can be expressed as  $k\langle u^2 \rangle$ , where  $k$  stands for an presumed local spring constant. In the present work, each monomer is taken as a polymer segment and the MSD of its center of mass is measured. Comparing with the MSD of single atoms, the MSD of the center of mass of the monomer eliminates the contribution of rotations of this monomer to MSD. Within the moisture content and temperature range of investigation, the MSD of uLGN polymer plateaus after  $\sim 10$  ps, due to the confinement of the cage formed by the surrounding atoms of the chain segment. As per ref. (Xia et al. 2017), the  $\langle u^2 \rangle$  factor in this study is defined as the average mean MSD of polymer segments at 10 ps, the caging time of uLGN. The  $\langle u^2 \rangle$  factor for water is measured similarly, by assessing the average MSD of the center of mass of water molecules. Higher temperature increases both the caging time and  $\langle u^2 \rangle$ . Nevertheless, within the ranges of temperature and moisture content in this investigation, caging time stays around  $\sim 10$  ps.

## 4.3 Results

### 4.3.1 Macroscopic results: heat and moisture-induced free strain and mechanical weakening

Figure 4-5a shows the volumetric swelling strain, referred to as free strain as a function of both temperature and moisture content, using a green to yellow scale in addition to contour lines. As moisture content and temperature increase, the free strain increases from 0 at  $T = 283$  K and  $m = 0$ , to more than 0.4 at  $T = 373$  K and  $m = 0.3$ .

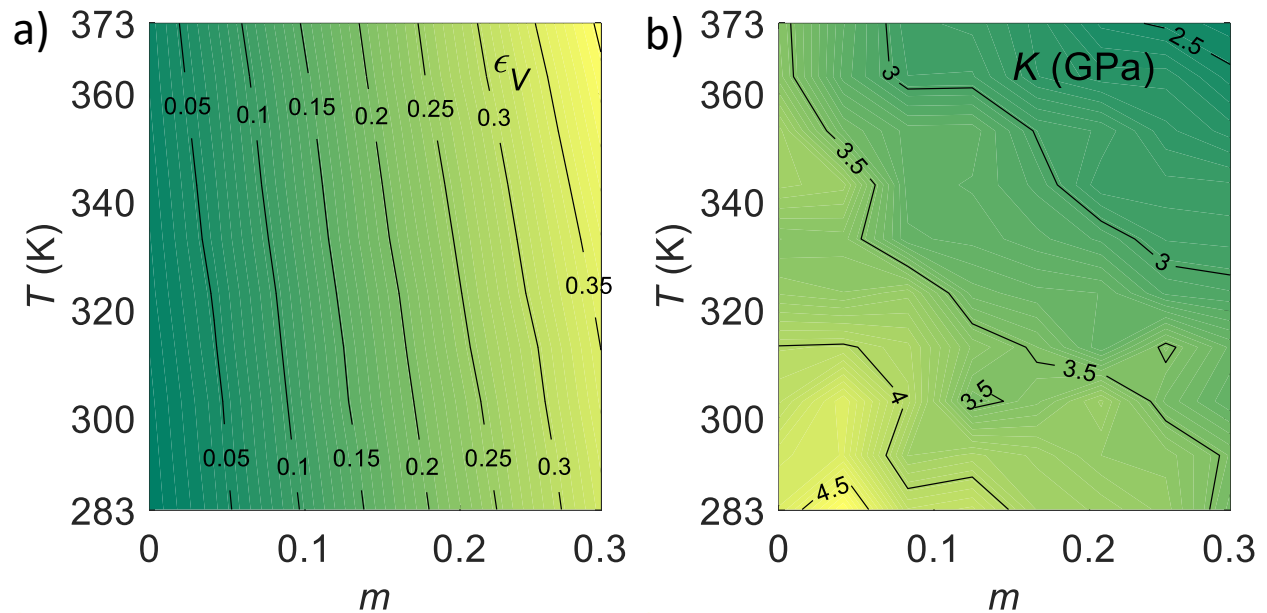


Figure 4-5 a) Free strain as a function of temperature and moisture content. b) Bulk modulus as a function of temperature and moisture content, contour line units are in GPa.

The bulk modulus of uLGN as a function of temperature and moisture content is shown in Figure 4-5b. The higher moduli are denoted by yellow and the lower by green colors. As temperature and moisture content increase, the bulk modulus decreases from more than 4.5 GPa to less than 2.5 GPa indicating a mechanical weakening of the material. Due to scattering, the contour lines are not as smooth as those for free strain shown in Figure 4-5a. The rather diagonal lines indicate that the increases of temperature and moisture content both induce mechanical weakening.

### 4.3.2 Microscopic results: weakening and straining explained by local stiffness

Figure 4-6 gives the local stiffness  $T/(u^2)$  of the polymer skeleton and of water as a function of temperature and moisture content, respectively.

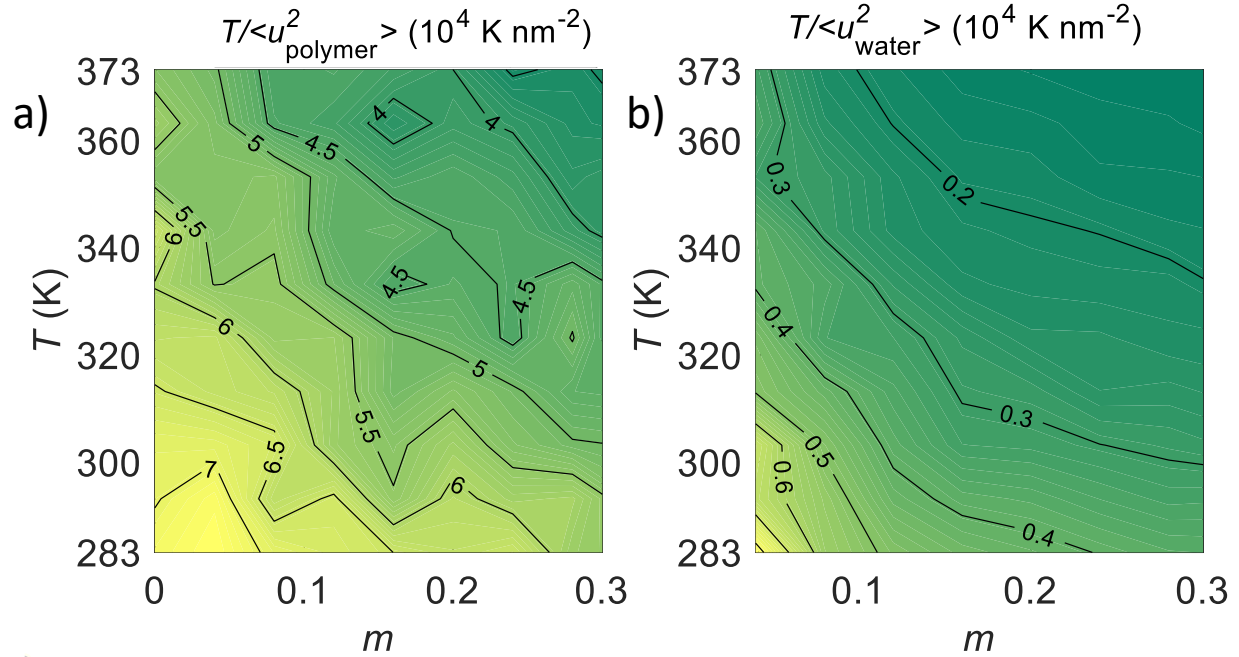


Figure 4-6 a) Local stiffness  $T/\langle u^2 \rangle$  of the polymer skeleton as a function of moisture content  $m$  and temperature  $T$ . b) Local stiffness  $T/\langle u^2 \rangle$  of water as a function of moisture content  $m$  and temperature  $T$ . The unit of the contour lines is  $10^4 \text{ K nm}^{-2}$ .

As shown in Figure 4-6,  $T/\langle u^2 \rangle$  for both the polymer skeleton and water decreases with increasing temperature and moisture content. In terms of absolute value, the local stiffness of polymer, ranging from  $3.0 \sim 7.4 \cdot 10^4 \text{ K nm}^{-2}$ , is around 10 times higher than that of water, ranging from  $0.13 \sim 0.83 \cdot 10^4 \text{ K nm}^{-2}$ . This indicates that the stiffness of the hydrated uLGN system is dominated by the stiffness of the polymer chains rather than by the stiffness of the adsorbed water. In fact, the local stiffness of the polymer skeleton (Figure 4-6a) resembles the overall stiffness of the composite material (Figure 4-5b), which will be further supported by correlation analysis in the following section.

### 4.3.3 Link between microscopic and macroscopic results

The correlation plot of the measured bulk moduli and the local stiffness of the polymer skeleton is shown in Figure 4-7. The dots form a line indicating a strong correlation. The Pearson correlation coefficient of 0.96 indicates that  $T/\langle u^2 \rangle$  can serve as an indicator for the macroscopic stiffness of the material. The circles denote the average values of the three repetition tests, and the error bars denote the standard deviation. With the increment of moisture content or temperature, the deviation decreases. In order to indicate the hygrothermal state of each point of the graph, the color of the circles gradually changes from black to red denoting the increase in temperature from 273 to 373 K, while the color of the edges of the circles changes from black to blue denoting the increase in moisture content from 0 to 0.3.

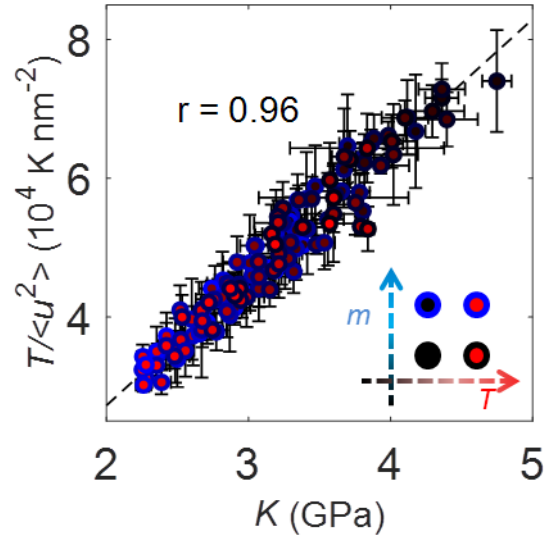


Figure 4-7 Correlation of local stiffness and measured bulk moduli. Error bars indicate the standard deviation of the repetition samples. The Pearson correlation coefficient is 0.96. Marker face color changes from black to red denoting increasing temperature, and the marker edge color changes from black to blue denoting increasing moisture content.

Based on the observation above, there is a linear relation between the local stiffness  $T/\langle u^2 \rangle$  at the microscale and the macroscopic bulk modulus  $K$ , which is derived in the following. The bulk modulus  $K$  measured above under NPT at different temperatures and moisture contents is referred to as isothermal bulk modulus. The time scale studied in this section is in the order of several picoseconds. Therefore time effects can be neglected. The thermal energy, i.e. the translational kinetic energy, of a chain segment equals  $\frac{3}{2}k_B T$ . As this chain segment is assumed to be confined to its equilibrium location by a harmonic spring, the energy of the chain segment movement can be expressed as  $k\langle u^2 \rangle$ , where  $k$  stands for an assumed local spring constant. The maximum potential energy stored in the spring should equal the kinetic energy of the segment:

$$\frac{1}{2}k\langle u^2 \rangle \cong \frac{3}{2}k_B T \quad (4-20)$$

The intrinsic vibration frequency of a harmonic spring is  $\omega_0 = \sqrt{k/a\lambda}$ , where  $a$  is the size of the segment and  $\lambda$  the line density of the polymer chain. Therefore, the wave speed  $c$  in the material is:

$$c = \omega_0 a = \sqrt{ka/\lambda} \quad (4-21)$$

The longitudinal wave speed in the material is related to the adiabatic bulk modulus. Assuming that the isothermal and bulk modulus are equal, which holds for a number of solid materials (Grimvall 1999), the wave speed is given by:

$$c = \sqrt{\frac{K + \frac{4}{3}G}{\rho}} \quad (4-22)$$

with  $G$  the shear modulus and the density of the material given by  $\rho = \lambda a/a^3$ .

For an isotropic material, the bulk and shear moduli are related by Poisson's ratio through:

$$G = \frac{3K(1-2\nu)}{2(1+\nu)} \quad (4-23)$$

Combining equations (4-20) to (4-23), the bulk modulus of the dry polymer can be predicted from the local stiffness  $T/\langle u^2 \rangle$  by:

$$K = \frac{(1+\nu)k_B T}{(1-\nu)a\langle u^2 \rangle} \quad (4-24)$$

This equation shows that the bulk modulus at the macroscale is directly related to the amplitude of segmental motion  $\langle u^2 \rangle$  or local stiffness  $T/\langle u^2 \rangle$  at microscale.

Continuing further, the Young's and shear moduli for an isotropic material can also be derived from the bulk modulus and Poisson's ratio:

$$E = \frac{3(1+\nu)(1-2\nu)}{1-\nu} \frac{k_B T}{a\langle u^2 \rangle} \quad \text{and} \quad G = \frac{3}{2} \frac{1-2\nu}{1-\nu} \frac{k_B T}{a\langle u^2 \rangle} \quad (4-25)$$

The equations (4-24) and (4-25) are strikingly simple, considering that only two assumptions, i.e. harmonic vibration and isotropy, are introduced. The relation between the amplitude of segmental motion  $\langle u^2 \rangle$  and shear or Young's moduli was shown in (Zaccai 2000), but, in this study, explicit equations are provided for bulk, Young's and shear moduli as functions of  $\langle u^2 \rangle$ . For most polymers, the Poisson ratio varies between  $0.35 < \nu < 0.45$ . A standalone MD test shows that, at 300 K and  $m = 0$ , the Poisson's ratio of pure uLGN is  $\sim 0.37$ , in accordance with experiments (Salmén 2004).

Using equation (4-24), the bulk modulus of the dry polymer as a function of temperature can be predicted knowing the local stiffness  $T/\langle u^2 \rangle$  at microscale. Reminding that the chain segment is defined as a lignin monomer and that 500 monomers occupy a volume of around  $104 \text{ nm}^3$ , where  $500 * a^3 = 104 \text{ nm}^3$ , the size of the chain segment is on average  $a \sim 0.59 \text{ nm}$ . There is no strict way of determining the chain segment size and other approaches could give slightly different values of chain segment size. As shown in Figure 4-8, the predictions of the bulk modulus based on the local stiffness  $T/\langle u^2 \rangle$  agrees well with MD measurements of the bulk modulus though the absolute predicted values are lower than the measured ones. The difference between these two sets of values may be attributed to the simplifications made in the derivation of equation (4-24), such as assuming elasticity, isotropy and homogeneity, the validity of harmonic confinement assumption, the way of determining the chain segment size and the accuracy of the method of bulk moduli measurement. To what extent these assumptions affect the predicting power of equation (4-24) might be the topic of future investigations. Also noteworthy, as  $\langle u^2 \rangle$  can be measured by neutron scattering

experiments (Price and Fernandez-Alonso 2013), equations (4-24) and (4-25) might be examined in future through experimental studies.

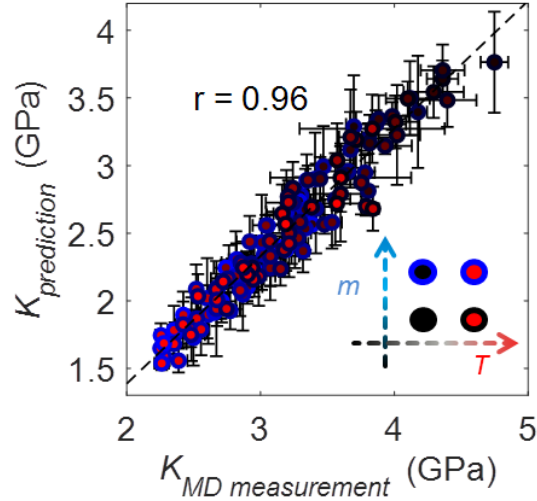


Figure 4-8 Comparison of the bulk moduli directly measured by MD and predicted through the equation (4-24). Marker face color changes from black to red denoting the rise of temperature, and the marker edge color changes from black to blue denoting the rise of moisture content.

As suggested by the form of local stiffness, i.e.  $T/\langle u^2 \rangle$ , moisture content and temperature influence this mechanical property in different ways. Temperature enters both numerator and denominator, since  $\langle u^2 \rangle$  depends on the temperature, while moisture content alters only the denominator by  $\langle u^2 \rangle$ . Though phenomenologically heat and moisture both induce macroscopic weakening of material, they impact the molecular mechanics differently.

To look into these phenomena, a relation is derived between thermal expansion and local stiffness of the material. In Gruneisen theory (Grüneisen 1912; Tabor 2013), based on the existence of an asymmetrical potential energy curve in terms of the distance between atoms, a simple relationship between the thermal expansion coefficient and the bulk modulus at the macroscale is derived:

$$\alpha = \frac{\gamma_G C_V}{VK} \quad (4-26)$$

where  $\alpha$ ,  $\gamma_G$ ,  $C_V$ ,  $V$ ,  $K$  are the volumetric thermal expansion coefficient, Gruneisen parameter, specific heat under constant volume, volume and isothermal bulk modulus, respectively. The Gruneisen parameter is defined as the rate of change of vibrational frequency with thermal expansion. The Gruneisen theory was originally developed for crystals where atom movements are restricted. Thus, as the lignin systems can be seen as chain segments moving around their equilibrated location within a time span of several pico-seconds, it is deemed reasonable to extend the theory to this polymer. The thermal expansion coefficient  $\alpha$  is related to thermal strain  $\varepsilon_V =$

$\alpha \Delta T$ . Combining equation (4-24) and (4-26), a relation is found between volumetric thermal strain  $\varepsilon_V$  and the local stiffness  $T/\langle u^2 \rangle$ :

$$\varepsilon_V = \frac{1 - \nu \gamma_G C_V \alpha \langle u^2 \rangle}{1 + \nu} \frac{1}{V k_B T} \quad (4-27)$$

This equation shows that thermal strain increases with the decrease of local stiffness of the material, which depends on both temperature and moisture content. Equation (4-27) also shows that several other material properties, including Poisson's ratio, Gruneisen parameter, heat capacity, and temperature, determine the thermal expansion of the material. These observations could encourage further work investigating how these material properties are related to each other. Also, a further elaboration of equation (4-27) into a simpler form could be a future research topic.

#### 4.4 Discussion: Beyond the similarity of heat and moisture

The results above have shown that both heat and moisture have a similar effect on expanding/swelling and on mechanical weakening of the material. It was also shown that the hygric swelling, thermal expansion and mechanical weakening are all related to the increase of the amplitude of segmental motion on the microscale. Looking beyond the similarities, the differences between the effects of heat and moisture are now discussed.

##### 4.4.1 Free strain - the difference between the impacts of moisture and heat

The data of the free strain  $\varepsilon_V(m, T)$  dependent on temperature  $T$  and moisture content  $m$  in Figure 2a is further used to study the combined effect of heat and moisture. To do so, three different models are introduced. A first model, called the "1<sup>st</sup> order independent model" assumes that the free strain is linearly correlated with temperature and moisture content, where the term "independent" refers to the fact that the contributions of heat and moisture are additive. In a second model, called the "2<sup>nd</sup> order independent model", second-order terms in temperature and moisture content are added, without considering a coupling between temperature and moisture content. Finally, in the coupled model, a linear coupling term in temperature and moisture content  $m \cdot T$  is added to the first-order independent model. The results of these models are shown in Table 4-4, where the sum of squared errors (SSE) is used to evaluate the quality of each model. Comparing the SSE of the different models, the coupling model provides by far the best results, indicating that the coupling between temperature and moisture content is essential in describing the heat-moisture dependence of free strain. This coupling effect between heat and moisture is a first indication that both factors are not just additive, but that there is an interaction between the two factors.

It was shown above that heat facilitates the segmental motions of the polymer chains. Moisture is known to reside as water molecules in between the polymer chains and to interact with the intermolecular interactions between the polymer chains leading to a weakening of the material. As an example of such intermolecular actions, Figure 4-9 gives the density of the polymer-polymer hydrogen bonds as a function of temperature and moisture content. In the low moisture content range ( $m < 0.1$ ), with increasing moisture content, a sharp decrease is observed in the number of

hydrogen bonds indicating the breakage of hydrogen bonds between the chains, which are replaced by water-polymer hydrogen bonds, leading to a mechanical weakening of the material. This weakening of the material by intermolecular interactions of the water molecules in between the polymer chains, i.e. breaking of polymer-polymer hydrogen bonds, will, in turn, facilitate lowering the local stiffness and, as such, water molecules in between the chains may be seen as an activator of segmental motions of the chains. This means that the fundamental mechanisms of heat and moisture are different, where moisture must be seen as an activator, while heat is a direct cause for the segmental motions. This will be further elaborated in the next section. The polymer-water and water-water hydrogen bonds are included for completeness.

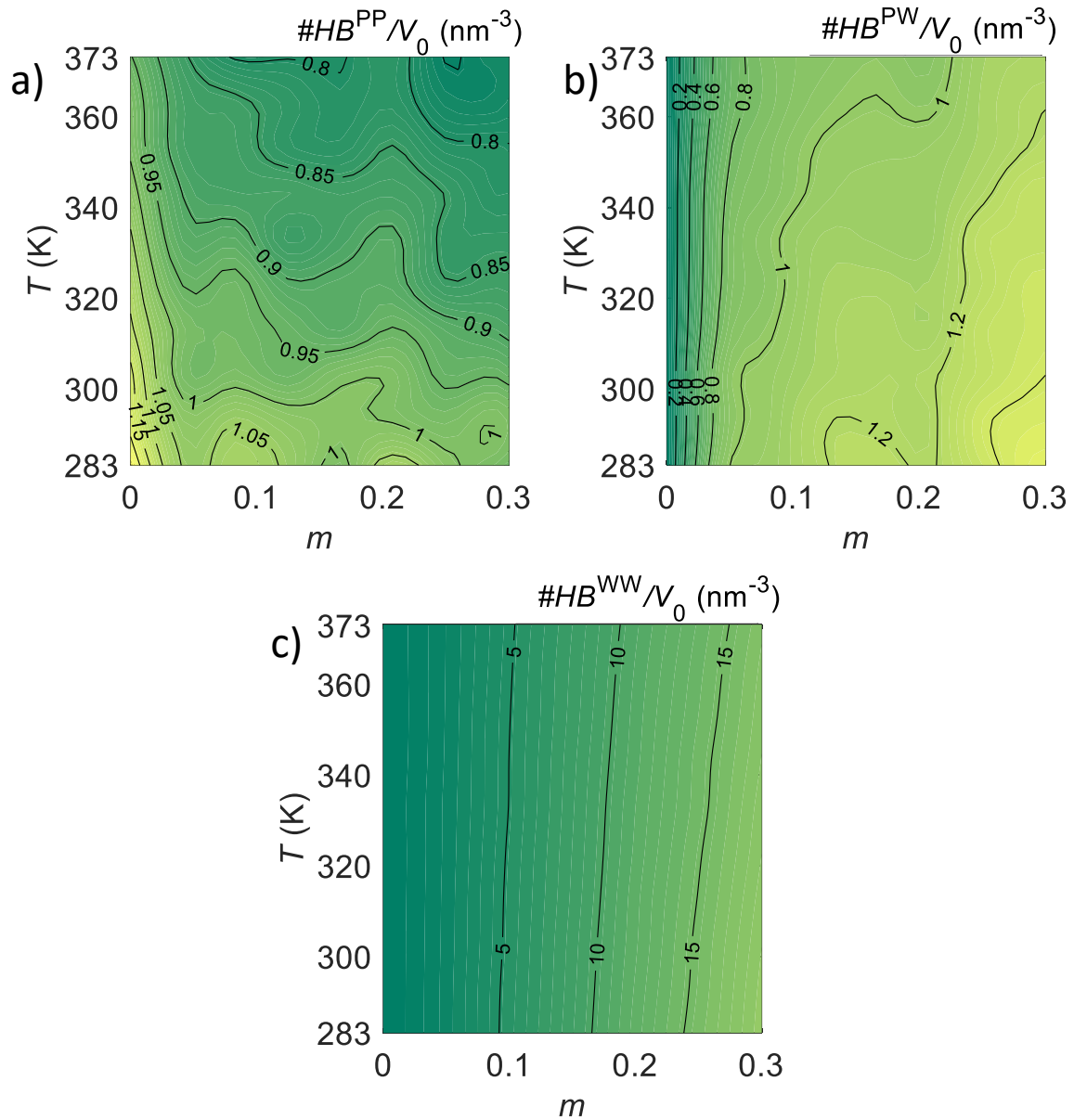




Figure 4-9 Density of a) polymer-polymer, b) polymer-water and c) water-water hydrogen bonds as a function of temperature and moisture content. Units are in nm<sup>-3</sup>.

Table 4-4 Different models for free strain as a function of temperature and moisture content.

| Type of model                           | Fitting of $\epsilon_V(m, T)$                         | SSE    |
|---|---|--------|
| 1 <sup>st</sup> order independent model | $1.2m - 7.6E^{-4}T - 0.24$                            | 0.0075 |
| 2 <sup>nd</sup> order independent model | $1.2m - 4.3E^{-4}T + 0.055m^2 + 1.8E^{-6}T^2 - 0.048$ | 0.0071 |
| coupled model                           | $0.72m + 3.7E^{-4}T + 1.4E^{-3}mT - 0.12$             | 0.0011 |

#### 4.4.2 Primary and secondary bond energy - different impacts of moisture and heat

Finally, this last section presents the analysis of the energetic aspects of the uLGN polymer skeleton as temperature and moisture content increase. The energy terms are obtained through the calculation of potential energy of the polymer skeleton, which is the system consisting only of polymer chains after removing all the water molecules.

The potential energy of the polymer skeleton consists of two parts: the primary bond energy and the secondary bond energy. The primary bond energy includes all the chemical-bond related energies or the so-called “bonded interaction energy” in MD, i.e. bond energy, angle energy, dihedral energy. The secondary bond energy includes all the intermolecular interaction energies or the so-called “non-bonded interaction energy” in MD, i.e. van der Waals and Coulombic interaction energy. The primary and secondary bond energies of the polymer skeleton are shown in Figure 4-10a and b, respectively, where higher and lower values are denoted by yellow and green colors. The primary energy is zero when the bonds are at exactly their equilibrium location. Any displacement from this location causes an energy increase. Therefore the primary energy values are positive. In contrast, the zero point of secondary energy is defined as molecules at infinite separation. When atoms are at finite distance from each other, the secondary energy goes to negative values. An increase in potential energy indicates a weakening of the interactions. As shown in Figure 4-10a, the primary bond energy of polymer skeleton increases mainly with temperature. The contour lines are almost horizontal, indicating an almost negligible influence of moisture content on primary bond energy.

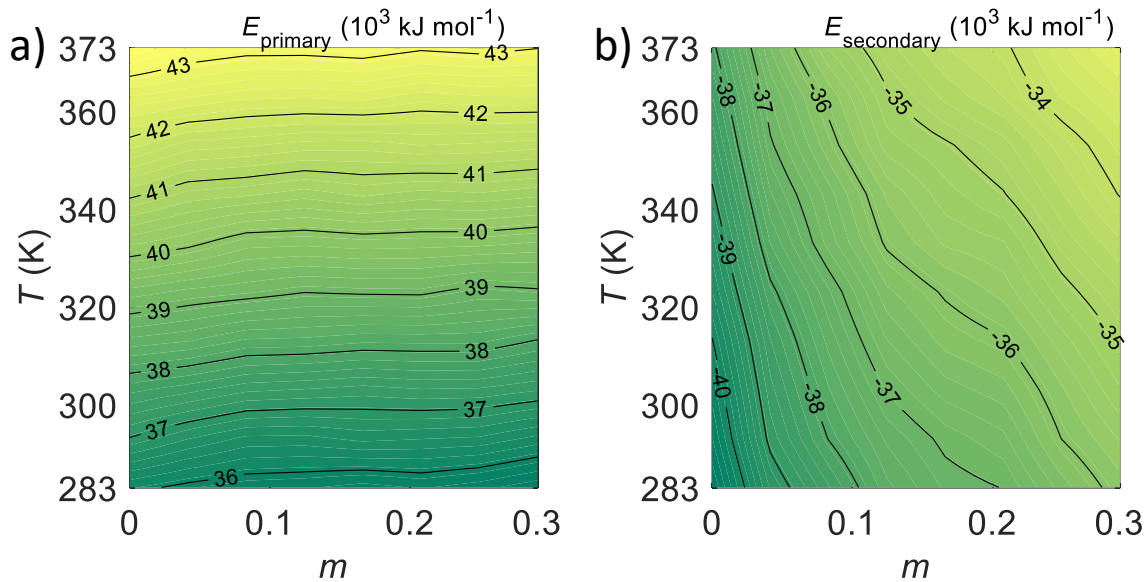


Figure 4-10 Potential energy of polymer skeleton: a) primary bond energy; b) secondary bond energy.

Figure 4-10b shows the secondary bond energy. In contrast with the previous graph on primary bond energy, moisture strongly influences the secondary bond energy. The density contour lines of the secondary bond energy get looser when moisture content increases, indicating that the influence of moisture is getting weaker as hydration proceeds. This means that the first adsorbed water molecules have a more important impact on the potential energy, as indicated with the smaller spacing between the counter lines. The temperature also influences the secondary bond energy, but to a less extent than moisture content does, while moisture has only a negligible effect on primary bond energy. This implies that water molecules intervene only with intermolecular interactions, e.g. hydrogen bonds, and can hardly affect chemical bond interactions. This agrees with the former report that water relaxes the charged assemblies by interrupting the attraction between oppositely charged groups of the polymers (Zhang et al. 2018).

Although some similarities between the impact of heat and moisture on free strain and stiffness are observed, similarities which are in line with the time-temperature-moisture superposition principle proposed by various experimental studies (Onogi et al. 1962; Emri and Pavsek 1992; St. Lawrence et al. 2001; Patankar et al. 2008; Silberstein et al. 2011; Fabre et al. 2018), the effects of heat and moisture have different origins. Heat affects both primary and secondary bonds, while moisture only alters secondary bonds. This fundamental difference between heat and moisture effects highlights also the different mechanisms induced by heat and moisture on the polymeric systems. Considering the important role of primary and secondary bonds on the stiffness of material (Soboyejo 2002), our findings may have important implications. To mention one example, for thermosetting polymers, where chains are cross-linked into networks and primary bonds play the dominant role, excessive heat could cause the severance of the primary bonds and consequently

weakening (Callister Jr 2000), while the impact of moisture could be limited. The potential of this hypothesis could be the object of future studies.

## 4.5 Conclusion

To address the fundamental issue of heat and moisture effects on polymers hygro-thermo-mechanical behavior, this study investigates the prototypical lignin polymer at various temperature and moisture levels using molecular dynamics simulations. In line with previous reports, thermal expansion, hygric swelling and mechanical weakening of material occur concomitantly with the increment of temperature and moisture content. The detailed analysis suggests the important role of the coupling between heat and moisture for the hygric swelling of lignin polymer. To explain the weakening effect, a quantity called local stiffness  $T/\langle u^2 \rangle$  is introduced. Under the assumptions of harmonic vibration and isotropy, an equation relating microscopic segmental motions  $\langle u^2 \rangle$  to macroscopic modulus is proposed. This equation allows one to theoretically predict the bulk moduli of material, which are in good agreement with the measurements, supporting that the local stiffness is a good indicator for macroscopic local stiffness. Combined with Gruneisen theory, thermal expansion is shown to be also related to the local stiffness. The energetic analysis of the polymer skeleton shows that, while secondary bonds are influenced by both heat and moisture, the primary bonds are affected by heat alone. This indicates the fundamental difference between moisture and heat, which influences have long been assumed to be similar, offering a different view of the so-called time-temperature-moisture superposition principle, based on molecular level inspection.

To recap, until now the dominant amorphous components of softwood cell wall S2 layer matrix, i.e. AGX (Chapter 3) and uLGN (this chapter), have been studied. The mechanical properties are characterized and found in accordance with the experimentally reported value range. The general picture and microscopic mechanism of moisture-induced mechanical effects are presented. With the work presented so far, a good understanding of homogeneous hydrated polymer system can be achieved. However, towards understanding the S2 layer composite materials, homogeneous observations are not sufficient and complementary information is required. Namely, in softwood cell wall S2 layer, there exist two types of interfaces, i.e. cellulose crystal-cellulose crystal interface and cellulose crystal-matrix interface, which have strong influence on the overall mechanical performance of S2. These interfaces will be the focus of the next two chapters.

## Chapter 5 Cellulose Nanocrystals undergoing Frictional Stick-Slip

This chapter focuses on the frictional slip-stick behavior of the interface between crystalline cellulose fibrils, one of the interfaces probably present in plant cell walls. The interface is not only interesting to plant mechanics but also more generally with regards to crystalline cellulose reinforced composites. Crystalline cellulose features exceptional physical and mechanical properties such as transparency and high tensile strength and has attracted tremendous attention due to its potential for providing sustainable solutions to a large variety of applications, e.g. cellulose nanocrystal paper. The absence of a complete understanding of the behavior of the crystal-crystal or crystal-matrix interfaces forms a bottleneck towards the improvement of the overall mechanical performance of cellulose reinforced composites. Thus, the crystal-crystal interface is the focus of this chapter, while the crystal-matrix interface is studied in the next chapter. Using atomistic simulation, this chapter reports the mechanical behavior of two cellulose-cellulose nanocrystal interfaces: one involving the hydrophilic-hydrophilic surfaces of crystalline cellulose, i.e. (110)-(110) and the other involving the hydrophilic-hydrophobic surfaces, i.e. (110)-(200). The impact of the loading direction, interfacial moisture, misalignment and surface types are systematically examined.

The core content of this chapter is published in Zhang, C., Keten, S., Derome, D., & Carmeliet, J. (2020). Role of hydrogen bonds in frictional stick-slip dynamics in shearing cellulose nanocrystals. *in preparation*.

### 5.1 Introduction

Crystalline cellulose, the load bearing component of plant cell, constitutes about half of the mass of wood cell wall. The mechanical performance of the cell wall is largely determined by the properties and organization of cellulose fibers. The interface formed by the contact of two cellulose fibers is believed to have strong implication on the mechanics of the cell wall (Park and Cosgrove 2015; Xiao et al. 2016a). Nevertheless, the cellulose-cellulose interface is a rarely explored field of research. Crystalline cellulose, due to its configuration, has two types of surface, a hydrophilic one (referred to here as 110, as explained below) and a hydrophobic one (200). Better understanding of the different interfaces should provide a necessary complement to the current knowledge of wood cell wall mechanics.

As a newly available material, cellulose nanocrystal has attracted tremendous attention in recent years for its great potential in many applications. With the annual production of natural cellulose nanocrystals being 75 ~ 100 billion tons, low-cost extraction methods have been developed and upscaled for industrial production, improving the accessibility of cellulose nanocrystals (Trache et al. 2017). In addition to extreme abundancy and sustainability, crystalline cellulose possesses other qualities, such as excellent mechanical properties, with the axial tensile stiffness in the range of 120~160 GPa (Sakurada et al. 1962; Tashiro and Kobayashi 1991; Nishino et al. 1995; Šturcová et al. 2005; Kulasinski et al. 2014b) comparable to Kevlar (Moon et al. 2011), low density,

biocompatibility, possibility of surface modification, optical light transparency and low thermal expansion. These advantages make cellulose nanocrystal a strong candidate for numerous applications, such as multifunctional paper (Nogi and Yano 2009), purification membrane (Wu and Yuan 2002), photonic film (Giese et al. 2014), electrode in green electronics (Weng et al. 2011; Zhu et al. 2013), super absorbent hydrogel (Ma et al. 2015a) and many others (Zhu et al. 2016a). In most cases, cellulose crystalline fibers are applied as a stiff scaffold or network onto which functional components are loaded (Li et al. 2013, 2016b; Kim et al. 2013; Zhao et al. 2015). Due to the high surface-volume ratio of nanocrystals, the mechanical properties of the cellulose-cellulose interface contacts may significantly influence the overall performance of the composite. However, cellulose crystal reinforced composites have been found to display mechanical properties much lower than the upper bound predicted by composite theories (Moon et al. 2011). There is a strong need for a better understanding of cellulose nanocrystals interfacial behavior, which will provide fundamental insights for composite design (Ma et al. 1998; Xia et al. 2018).

Interfacial behavior can be particularly well understood through shearing or friction experimental investigations. For considering this behavior at molecular scale, frictional experiments have so far only considered material interfaces without, or with a moderate amount of, hydrogen bonds, such as NaCl crystal (Fessler et al. 2019), graphene/gold (Kawai et al. 2016) and graphene oxide/PMMA (Dai et al. 2016). There is a lack of experimental studies on cellulose crystal interfaces or, more generally, on highly hydrogen bonded interfaces.

Computational studies of the interface behavior of crystalline cellulose have emerged to fill this gap. Using molecular simulation, Sinko and Keten (Sinko and Keten 2014, 2015) investigated the shear and tensile failures of the interfaces between cellulose nanocrystals. The hydrogen-bonded (110)-(110) interface is found to have higher tensile strength than the weaker interaction dominated (200)-(200) interface. However, under shearing test, the (200)-(200) interface contact shows a stick-slip behavior with a higher energy barrier than that what the hydrogen-bonded (110)-(110) interface contact displays. Wu et al. (Wu et al. 2013a, b) investigated also computationally the sliding at the cellulose crystal interface formed by the contact of (200)-(200) planes and focused on the effects of sliding velocity, normal load, relative angle and hydrogen bonding. They indicate that, in that type of contact, rather than hydrogen bonding, other intermolecular interactions such as van der Waals and electrostatic interactions are expectedly the determinant factors of interfacial friction behavior. Wei et al. (2018) studied surface-modified cellulose nanocrystals. The introduction of a methyl(triphenyl)phosphonium group at the interface weakens the interface at dry condition, however, the presence of moisture strengthens it. Yet, the understanding of the interfacial behavior and of the mechanisms at play between cellulose crystals is still in its infancy. Especially, the specific role of the hydrogen bond is under debate and has only been discussed qualitatively (Wu et al. 2013a, b). Moreover, composites containing cellulose crystals in a hydrophilic matrix are affected by moisture because moisture preferentially adsorbs at the cellulose-matrix interface, breaking the interfacial hydrogen bonds, increasing the porosity of the structure, resulting in a loss of mechanical stiffness (Kulasinski et al. 2015c; Chen 2019). The

interrelations between hydrogen bonding, interfacial mechanical behavior and environmental factors like ambient moisture remain to be explored. Finally, a heterogeneous interface, such as the (110)-(200) interface of cellulose, has not been simulated and characterized yet.

Thus, this chapter investigates the frictional shearing and separation of the interfaces comprised of two hydrophilic or hydrophilic and hydrophobic surfaces of crystalline cellulose, i.e. the (110)-(110) and the (110)-(200) interfaces, using atomistic simulations. The systems are interrogated to document the occurrence of stick-slip behavior, the possibility of stiffness recovery after an irreversible slip and of different behavior along opposite shearing directions. Finally the effect by hydration and/or misalignment on the shearing behavior is also documented. Density, orientation and distribution of interfacial hydrogen bonds are studied in detail as possible paths of understanding the behavior. These studies should help to, not only complement the current knowledge of wood cell wall mechanics but also, provide guidance to the design of cellulose nanocrystal reinforced composites, an attractive solution in many fields. The mechanical properties presented here are used in the upscaling study using finite element method presented in Chapter 7.

## **5.2 Material and method**

### **5.2.1 Cellulose nanocrystal structure and its molecular modeling**

Cellulose is a polymer of  $\beta$ -1-4 linked glucan organized in a 2-fold screw conformation, i.e. the glucosyl unit inverts by  $180^\circ$  with respect to its neighbor, this repeating unit indicated by dashed square in Figure 5-1a. The degree of polymerization of cellulose in wood cell wall, one of its major sources, is on the order of  $10^4$ . It is generally accepted that cellulose is present in both crystalline and amorphous phases in the cell wall, with a clear predominance of the crystalline phase (Kataoka and Kondo 1999; Newman 1999; Horikawa 2017). The stable crystal structure is an assembly of glucose chains held together via intermolecular interactions, i.e. one inter- and two intra-chain hydrogen bonds per monomer (Gardner and Blackwell 1974). The native cellulose allomorph present in wood cell wall is cellulose I $\beta$  (Figure 5-1b), as identified by near-infrared spectroscopy,  $^{13}\text{C}$  nuclear magnetic resonance and X-ray spectroscopy analyses (Kataoka and Kondo 1999; Newman 1999; Horikawa 2017). The width and length of wood cellulose nanocrystals are 3~5 nm and 100~200 nm respectively (Araki et al. 1999). The structure of cellulose crystals depends on their source. Structural details, such as the number of cellulose chains per crystal, the cross-sectional shape, the configuration of paracrystalline or amorphous regions, are still under debate, as can be seen in (Nishiyama et al. 2002; Fernandes et al. 2011; Ding et al. 2014; Kubicki et al. 2018). In this study, the focus is the behavior of cellulose crystal interfaces. The cellulose crystal structure used here, i.e. I $\beta$  form with 36 chains possessing a hexagonal cross-section, has often been retained (Delmer 1999; Mutwil et al. 2008; Habibi et al. 2010; Fernandes et al. 2011; Endler and Persson 2011), though various other forms have been suggested (Tejado et al. 2012; Jarvis 2013; Newman et al. 2013; Thomas et al. 2013; Nixon et al. 2016; Kubicki et al. 2018). A more detailed summary of current research on cellulose crystal structure can be found in chapter 2.

The initial structure of cellulose crystal is generated by the cellulose builder toolkit (Gomes and Skaf 2012) based on the crystallographic information from Nishiyama et al. (2002). The structure is then energy minimized and equilibrated following the procedure of a previous study (Kulasinski et al. 2014b). GROMACS 5.0 package (Abraham et al. 2015) and GROMOS 53a6 force field are used for the simulation. The integration time step of the equation of motion is 1 fs. The canonical ensemble (NVT) is applied, where the temperature is controlled by Nose-Hoover thermostat and is set at room temperature 300 K. The van der Waals interaction has a cut-off radius of 1.4 nm and particle-mesh Ewald summation is used to account for long-range Coulomb interactions. The mechanical properties of an infinite I $\beta$  cellulose crystal model with a square cross-section were validated by comparison with experiments, as described in a previous study (Kulasinski et al. 2014b). The hexagonal configuration retained here counts 8 planes of 3,4,5 or 6 chains, for a total of 36 chains. In longitudinal direction, the chains count 10 glucosyl units. It should be noted that, in this study, however, the crystal is of finite size in transverse direction (36 chains) with a hexagonal cross-section. The equilibrated structure of a cellulose crystal is shown in Figure 5-1b. This structure is given periodic boundary conditions, with covalent bonds across the boundary, in effect attaining an infinite length. The hydrophilic (i) and hydrophobic (o) planes, i.e. (110) and (200), respectively, of the crystal are also indicated.

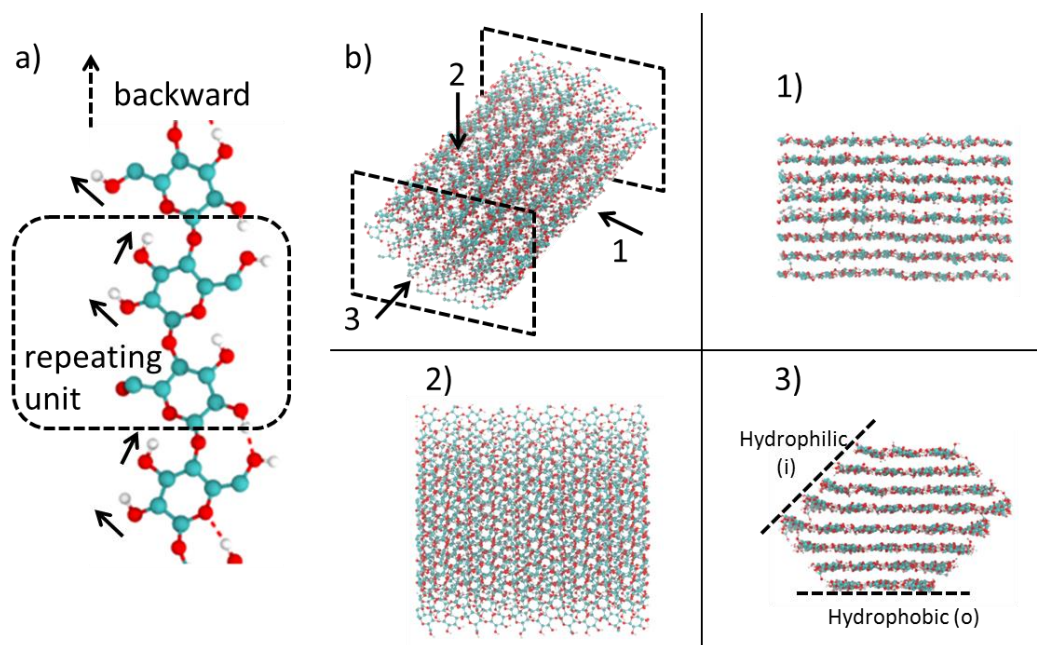


Figure 5-1 a) Snapshot of a section of a cellulose chain. The repeating unit is indicated by the dashed square. Black arrows denote the preferential orientation of the hydroxyl group. b) Snapshot of a section of I $\beta$  cellulose crystal. Top, side and front views are shown by subplots b1), b2) and b3), respectively. In the front view, the hydrophilic (110) and hydrophobic (200) planes of the crystal are indicated.

## 5.2.2 Pulling tests and boundary conditions

To study the behavior of the cellulose crystal interface, two cellulose crystals are stacked on top of each other and then relaxed. The equilibrated system is shown in Figure 5-2. Two cellulose chains from the interface are highlighted, i.e. a red chain from the upper crystal and a blue one from the lower. Periodic boundary conditions (PBC) are applied in all directions. As mentioned above, the upper crystal is 10 glucosyl units (five cellobioses) long and the periodic conditions allow mimicking an infinitely long cellulose crystal. In contrast, the bottom crystal (in blue color) is of finite length and possesses nine glucosyl units without any cross-boundary covalent bonds. An approximate 10 nm blank is left in transverse directions ensuring no influence of the periodic images in transverse directions.

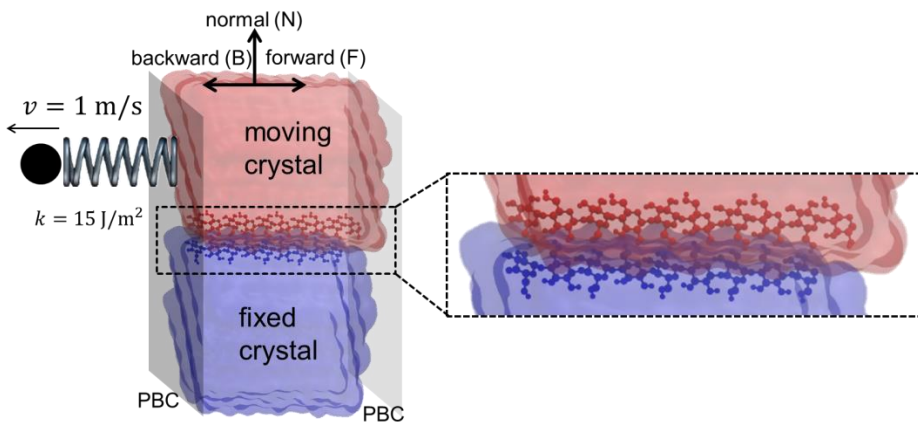


Figure 5-2 Snapshot of the system of two crystals in contact, using a see-through representation for the crystals with two cellulose chains (red and blue) at the interface shown explicitly. The atoms of the bottom crystal (blue) are constrained to their initial locations by a harmonic potential. The atoms of the top crystal (red) are connected to a virtual spring of stiffness of  $k$ . At the other end of the virtual spring, a virtual atom is moving at constant velocity  $v$ , exerting a force on the top crystal atoms.

The bottom crystal is fixed by restraining the atoms to their initial locations through a harmonic spring with high stiffness ( $\sim 3 \text{ J m}^{-2}$ ). The atoms of the upper crystal are attached individually to a virtual spring with a spring constant of  $k_{\text{pull}}$ . It is noted that it is also possible to pull only on the non-hydrogen atoms or the backbone atoms. At the other end of the spring, a virtual atom moves at a constant velocity  $v_{\text{pull}}$ . Both  $k_{\text{pull}}$  and  $v_{\text{pull}}$  affect the shearing results. As shown in Figure 5-3, increasing the pulling velocity leads to higher stick-slip peak stress and lower stress oscillation. Such a result agrees with the analytical prediction of a critical velocity at which stick-slip motion is replaced by steady sliding (Eiss and McCann 1993; Yoshizawa and Israelachvili 1993; Baumberger et al. 1994). The combination of  $k_{\text{pull}} = 15 \text{ J m}^{-2}$  and  $v = 1 \text{ m s}^{-1}$  is chosen, as these settings yield a series of clearly defined stick-slip events in the shear stress - displacement curve. The displacement is defined as the travel distance of the center of mass of the crystal in pulling direction. A more detailed study of the influence of spring constant and pulling velocity on the



frictional dynamics is out of scope of this thesis, since this chapter mainly focuses on stick-slip behavior and the influence of moisture on this behavior. In reality interface friction may be accompanied by the disintegration of cellulose crystal which is not relevant to this study. Therefore, pairwise harmonic constraints are applied to the carbon atoms to preserve the relative position of atoms, in effect making the crystals stable and that they do not break. The constant of the virtual spring of  $15 \text{ J m}^{-2}$ , meaning that we have a test setup with weak pulling spring leading to clear stick-slip events instead of steady sliding (Leeman et al. 2016). As the virtual atom moves, the virtual spring extends imposing external forces on the atoms of the top crystal (in red color). This external force increases with increasing straining of the weak spring and finally exceeds the interfacial force that maintained the crystals together, at which point the top crystal starts to move and slips.

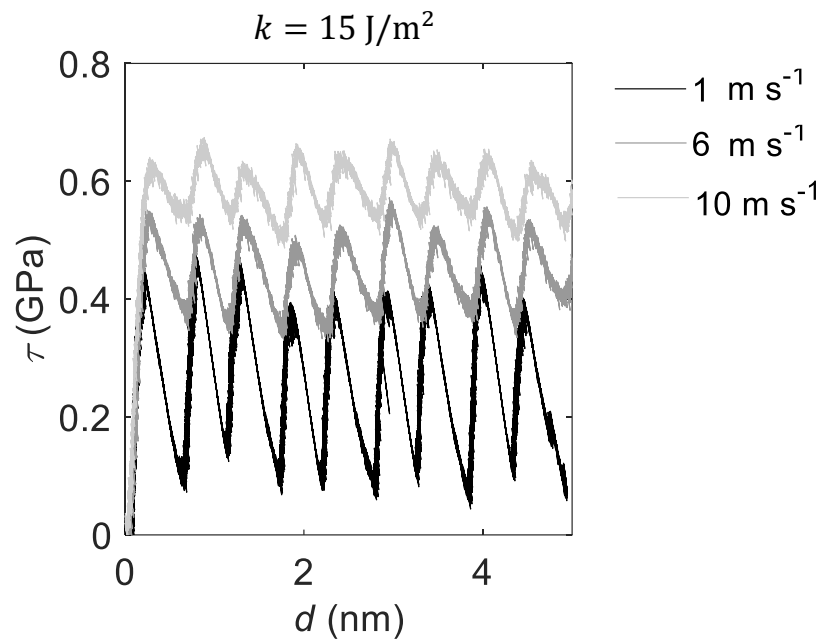


Figure 5-3 Shear stress - displacement curves for different forward pulling velocities for a hydrophilic-hydrophilic interface with a virtual spring  $k=15 \text{ J m}^{-2}$ .

Three pulling directions are considered in this study, forward (F), backward (B) and normal (N). It is known from both experiments and simulations that the interfacial hydroxyl groups preferentially orient along one direction, as indicated by black arrows in Figure 5-1a (Gardner and Blackwell 1974; Kulasinski et al. 2014b), which is defined as the backward direction in this study. The forward direction is opposite to the backward direction. The normal direction is the direction perpendicular to the contact surface, as illustrated in Figure 5-2.

As mentioned above, the hexagonal crystal displays both hydrophilic and hydrophobic surfaces. In theory, there could be three combinations of contacts, i.e. hydrophilic-hydrophilic contact (ii), hydrophilic-hydrophobic contact (io) and hydrophobic-hydrophobic (oo) contact. The “oo” contact

is not stable and, in the simulations, such contact always transforms into either “ii” or “io” (Oehme et al. 2015). Therefore, such contact is not considered in this study. However, the mechanical characterization of such “oo” contact can be found in (Wu et al. 2013b; Sinko et al. 2014), because those studies use infinite crystals. For a composite material with cellulose crystal reinforcements, e.g. wood S2 cell wall layer, it is highly possible that the longitudinal axes of the crystals are not perfectly aligned, or that moisture may be adsorbed at the interface due to the abundance of hydroxyl groups of the cellulose molecules. The systems with misalignment and moisture are denoted by “A” and “M”, respectively. In total eight different configurations are studied, i.e. ii, iiA, iiM, iiAM, io, ioA, ioM, and ioAM. The snapshots of all equilibrated systems are shown in Figure 5-4a. It can be speculated that wood cellulose fibers in S2 layer, the most important source of cellulose, are only slightly misaligned with each other (Fahlén and Salmén 2002; Keplinger et al. 2014; Casdorff et al. 2018), though there is a lack of experimental characterization of the exact angles of misalignment between the longitudinal axes of the individual crystals. Following this consideration, the misalignment angle in this study is assumed to be of a small value, namely  $10^\circ$ , as shown in Figure 5-4b. To study the influence of moisture on stick-slip behavior, water molecules, i.e. single-point charge (SPC) water models, are introduced to the contact area of crystals. To build the moist system, the crystals are first separated by a distance of 0.2 nm, a length similar to the size of a water molecule, and then the SPC water molecules fill the gap with a density of  $1 \text{ g cm}^{-3}$ , in order to build up one layer of water molecules. The moist system is then energy minimized and equilibrated for 100 ps. The relaxed system (iiM) is shown in Figure 5-4c. Systems with more interfacial moisture, i.e. with a 0.3 nm gap filled with water molecules, have also been tested. It is found that, as shearing proceeds, the water layer thickness decreases to 0.2 nm and no significant difference in terms of shear stress - displacement was found, therefore results for such systems are not reported in this chapter. The pulling tests are carried out on three replica systems for better statistics.

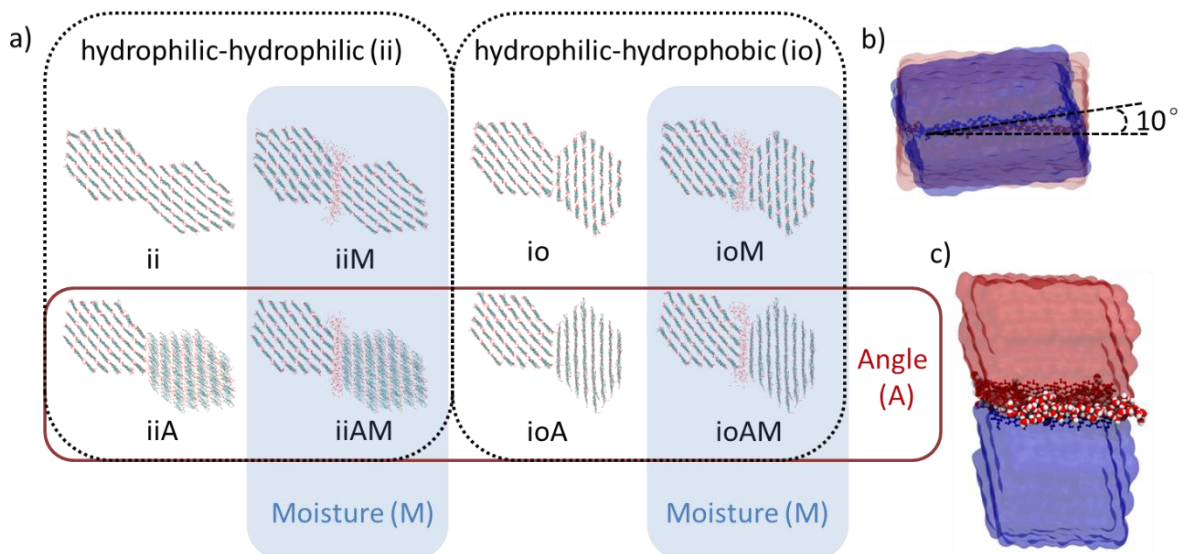


Figure 5-4 a) Snapshots of the 8 different systems studied, i.e. ii, iiA, iiM, iiAM, io, ioA, ioM and ioAM. b) Snapshot of the hydrophilic-hydrophilic contact with misalignment (iiA). c) Snapshot of the hydrophilic-hydrophilic contact with interfacial water layer (iiM).

### 5.2.3 Measurements

Molecular-level details of the interfacial mechanical behavior can be extracted from the simulations, including displacement, velocity, stress, number of hydrogen bonds, interaction energy and adhesion energy covering positional, force and energetic aspects, respectively. Measurement methods of these quantities are described below. When plotting the measured properties as functions of the displacement measured in the pulling direction, the curves usually exhibit an oscillatory shape, e.g. the shear stress - displacement curve of Fii (Forward hydrophilic-hydrophilic) system in Figure 5-5. To analyze these curves, average values, local minima and maxima (peak values) and the drop values (delta values), i.e. the difference between local maximum and minimum, are extracted.

#### 5.2.3.1 Mechanical behavior: displacement, shear stress, velocity, stress and interfacial stiffness

The displacement  $d(t)$  is defined as the displaced distance in pulling direction of the center of mass of the moving crystal at time  $t$  relative to the position at  $t_0$ . The velocity  $v(t)$  is defined as the velocity of the center of mass of the moving crystal, which is calculated using the relation  $v(t) = (d(t+\Delta t) - d(t)) / \Delta t$ . The  $\Delta t$  used here is 10 ps. It should be noted that this velocity does not necessarily equal to the velocity of the pulling virtual atom  $v_{\text{pull}}$  due to the presence of the weak spring. The force exerted on the crystal atoms, denoted by  $T(t)$ , can be calculated through Hooke's law, i.e. the product of spring constant and the extension of the spring. For forward and backward pulling tests, the shear stress is the shear force  $T$  per area of contact  $A$ , i.e.  $\tau(t) = T(t) / A$ , while for the normal pulling test, the normal stress is the normal force  $N$  divided by the contact area, i.e.  $\sigma(t) = N(t) / A$ . The interfacial stiffness is defined as the slope of the stress-displacement curve, that is the drop value of stress  $\Delta\tau$  divided by the corresponding displacement  $\Delta d$ .

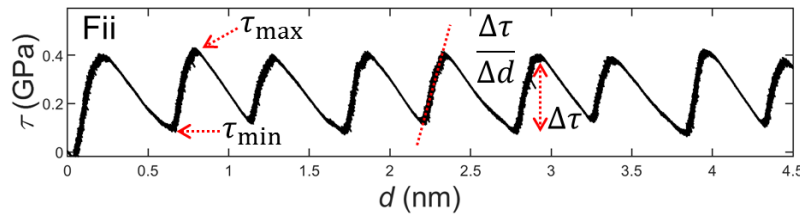


Figure 5-5 Stress-displacement curve of Fii system with sample indications of maximum minimum, drop and slope values.

#### 5.2.3.2 Hydrogen bonds

The hydrogen bonds (HB) of interest here are the interfacial cellulose-cellulose hydrogen bonds, i.e. the hydrogen bonds formed across the interface between the moving and the fixed crystals.

Interfacial hydrogen bonding is reported to strongly influence the mechanical behavior of the interface (Sinko and Keten 2014; Sinko et al. 2015, 2016). The criteria for HB are defined by the configuration of the donor-hydrogen-acceptor triplet:  $r \leq 0.35$  nm and  $\alpha \leq 30^\circ$ , where  $r$  is the distance between the donor oxygen atom and the acceptor oxygen atom, and  $\alpha$  is the angle formed by the acceptor oxygen atom–donor oxygen atom–donor hydrogen atom configuration. The interoxygen distance criterion of 0.35 nm refers to the first minimum of the radial distribution function of SPC water (Soper and Phillips 1986; Luzar and Chandler 1993). The angle of  $30^\circ$  is approximately the maximal angle of HBs (Teixeira and Bellissent-Funel 1990). The number of hydrogen bonds ( $\#HB$ ) is divided by the contact area, i.e.  $\#HB A^{-1}$ , yielding the areal density of hydrogen bonds. The average values, local minima and maxima and the drop values of the areal density of hydrogen bonds are also extracted.

### **5.2.3.3 Areal density of interaction and adhesion energy**

The interaction energy  $U_I(t)$  is defined as the difference between the potential energy of the dry system  $U_{AB}(t)$  and the summation of the potential energies of the two crystals separated  $U_A(t)+U_B(t)$ , i.e.  $U_I(t)=U_{AB}(t)-(U_A(t)+U_B(t))$ . The potential energy, either  $U_{AB}(t)$ ,  $U_A(t)$  and  $U_B(t)$ , is obtained by post-processing the trajectories of the pulling tests. Three systems are constructed and their potential energy is measured, i.e. one with both the fixed and the moving crystal  $U_{AB}(t)$ , one with only the moving crystal  $U_A(t)$  and one with only the fixed crystal  $U_B(t)$ . The energy values are divided by the contact area  $A$  giving the areal density of interaction energy  $U_I(t) A^{-1}$ . The average values, local minima and maxima and the drop values of the areal density of interaction energy are also extracted.

When pulling in the normal direction, the adhesion energy  $E_{adhe}$  is defined as the integral of the force-displacement curve which refers to the work of pulling the moving crystal away from the fixed crystal.

## **5.3 Results**

This section starts with the analysis of the periodic stick-slip behavior of dry and aligned interfaces undergoing shearing tests, where the dynamics and energetics of stick-slip events and the mechanical performance of interfaces are analyzed. Then the investigation extends to the impact of moisture and misalignment on interface behaviors, and a correlation analysis is applied to identify the determining factors of interface mechanics.

### **5.3.1 Stick-slip behavior of dry and aligned interfaces undergoing shearing tests**

The analysis of the results of the forward (F) and backward (B) shearing tests of dry and aligned interfaces, i.e. Fii, Fio, Bii, and Bio, reveals a stick-slip behavior at atomistic level. The atoms of the moving crystals are affected by two external forces: the molecular attraction force exerted by the fixed crystal and the pulling force exerted by the virtual spring being pulled by external loading. The origin of the stick-slip behavior of the interface can be seen as a competition between these

two forces. When the pulling force exceeds the frictional shear strength, slip happens. Otherwise the system sticks.

The displacement of the center of mass of the moving crystal along the pulling direction as a function of time is shown in Figure 5-6. Figure 5-6a shows the displacement over a longer time range (0~5 ns). Clear periodicity can be visually identified, and the average moving speed, calculated by the slope of the curves, is  $\sim 1 \text{ m s}^{-1}$ , corresponding to the pulling velocity. Figure 5-6b is the zoom-in of the squared region in a) and shows the displacement during a full stick-slip period. Looking more closely at one cycle, initially, the pulling force is lower than the molecular attraction force, no slip happens at the interface and the interfaces remain stuck, indicated by a plateau with moderate slope highlighted with the box with red dashed lines in Figure 5-6b. In this stick phase, the small slope indicates the small elastic deformation of the crystal. As the pulling continues, there comes a point where the attraction-pulling force equilibrium is broken and the top crystal abruptly slides to another position, a process referred to as slip. This phase shows quite vertical sections indicating fast increases in displacement as highlighted with red shaded square in Figure 5-6b. These two phases are referred to here as stick I and slip I. After the sudden release of the accumulated elastic energy, the pulling force again drops below the attraction force, causing the crystal to re-stick. The following stick and slip phases are highlighted by the green dashed square and green shaded square, respectively in Figure 5-6b. As will be explained below, a full stick-slip cycle thus consists of four phases, i.e. stick I, slip I, stick II and slip II. The total displacement for a full stick-slip cycle is about 1.06 nm, corresponding to the length of the repeating unit of crystalline cellulose (Nishiyama et al. 2002; Kulasinski et al. 2014b).

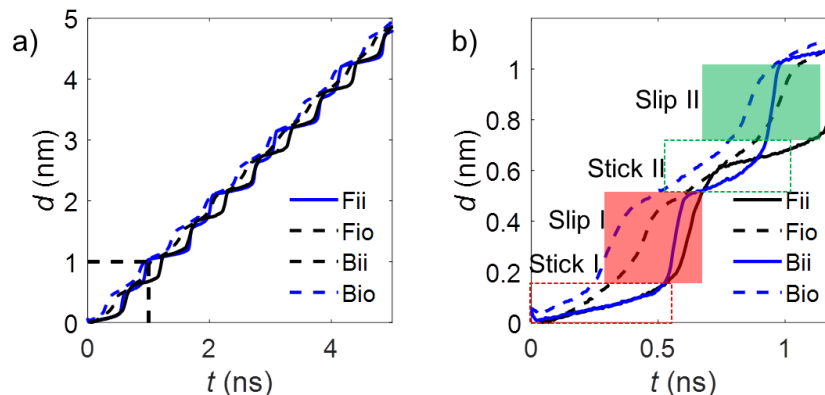


Figure 5-6 Displacement of the center of mass of the moving crystal in pulling direction as a function of time, a) displacement over a long time (0~5 ns), b) displacement over one cycle consisting of stick I, slip I, stick II and slip II.

To illustrate the dynamical process of stick-slip motion, two chains of the Bii system are used as a sample system (Figure 5-7a). The top and bottom chain belong to the moving and fixed crystal, respectively. Snapshots are taken every 10 ps and in total 50 snapshots are superimposed into one

image. One hydroxyl group on the moving chain is oversized to serve as a marker of location. The color of this marker hydroxyl group changes from red to blue denoting evolution in time. This marker hydroxyl is initially located at the equilibrium location  $d=0$  nm at  $t=0$  ns, where it sticks for some time. Then it abruptly moves to the next sticking location at  $d\sim 0.53$  nm at  $t\sim 0.57$  ns. The slip happens so fast that no image was captured during slip. Such stick and slip events repeatedly occur in a regular pattern resulting in periodicity. When analyzing the displacement and time duration of the four phases of the full cycles for the four systems, i.e. Fii, Fio, Bii, and Bio, consistency is observed as shown in Figure 5-7b where the average values and standard deviations are indicated by black dashed lines and error bars. The error bars have low values except for the Fio system. In general, the displacement of the stick-slip event corresponds to the length of the repeating unit. In Figure 5-7c, the systems resemble each other, except for the stick I phase of the system Bii being much longer than that of the other systems.

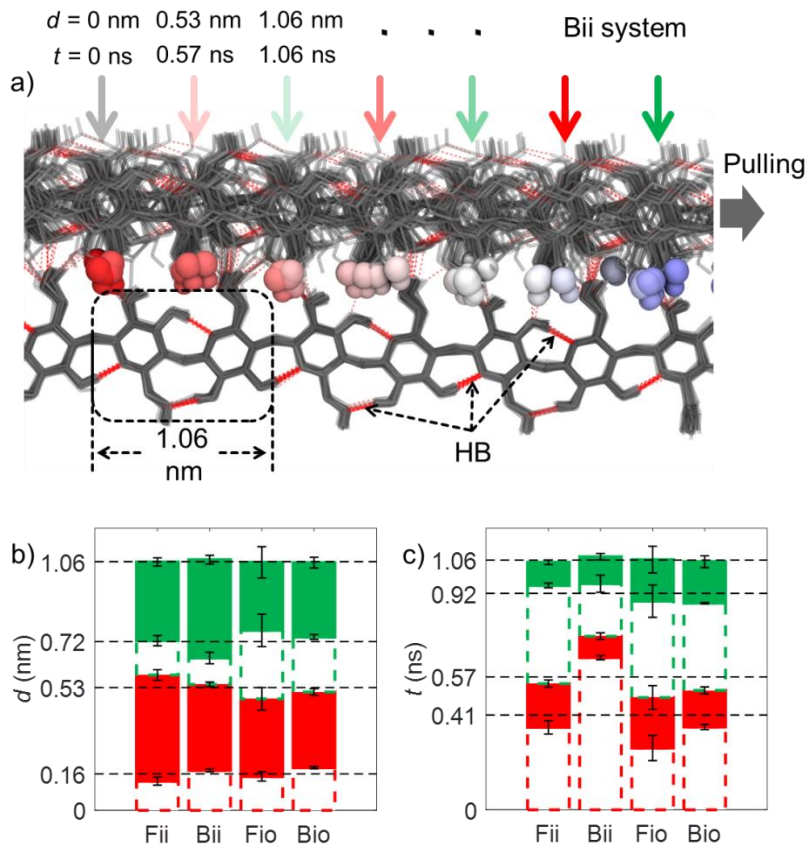


Figure 5-7 a) Different images of chains superimposed at different time frames for the Bii system interface, with color of the marked hydroxyl group from red to blue denoting evolution in time. b) Displacement and c) time duration during stick (dashed lines) and slip (colored) phases, i.e. stick I (red dashed lines), slip I (red colored box), stick II (green dashed lines) and slip II (green colored box) for the dry aligned systems, i.e. Fii, Bii, Fio, and Bio. The average values and standard deviations are indicated by black dashed lines and error bars.

To fully describe the stick-slip behavior, four critical parameters are documented. The interfacial shear stress  $\tau$ , the velocity of the moving crystal  $v$ , the interfacial hydrogen bonds areal density  $\#HB A^{-1}$  and the areal density of interaction energy  $U_I A^{-1}$  are measured for the four dry and aligned systems (Fii, Fio, Bii, and Bio), and plotted as functions of displacement  $d$ , shown in Figure 5-8. Notably, all these variables exhibit periodic profiles. In particular, the shear stress and the interfacial energy show sawtooth profiles and are synchronous with each other, indicating a regular stick-slip behavior of the system. The four properties vary at the same pace, though the peaks emerge at different displacements. The process of the periodic stick-slip motion can be generalized to consist in the four phases mentioned above, i.e. stick I, slip I, indicated in red, stick II and slip II, indicated in green, which correspond to the first stress ascending section, the first stress descending section, the second stress ascending section and the second stress descending section, respectively (Figure 5-8).

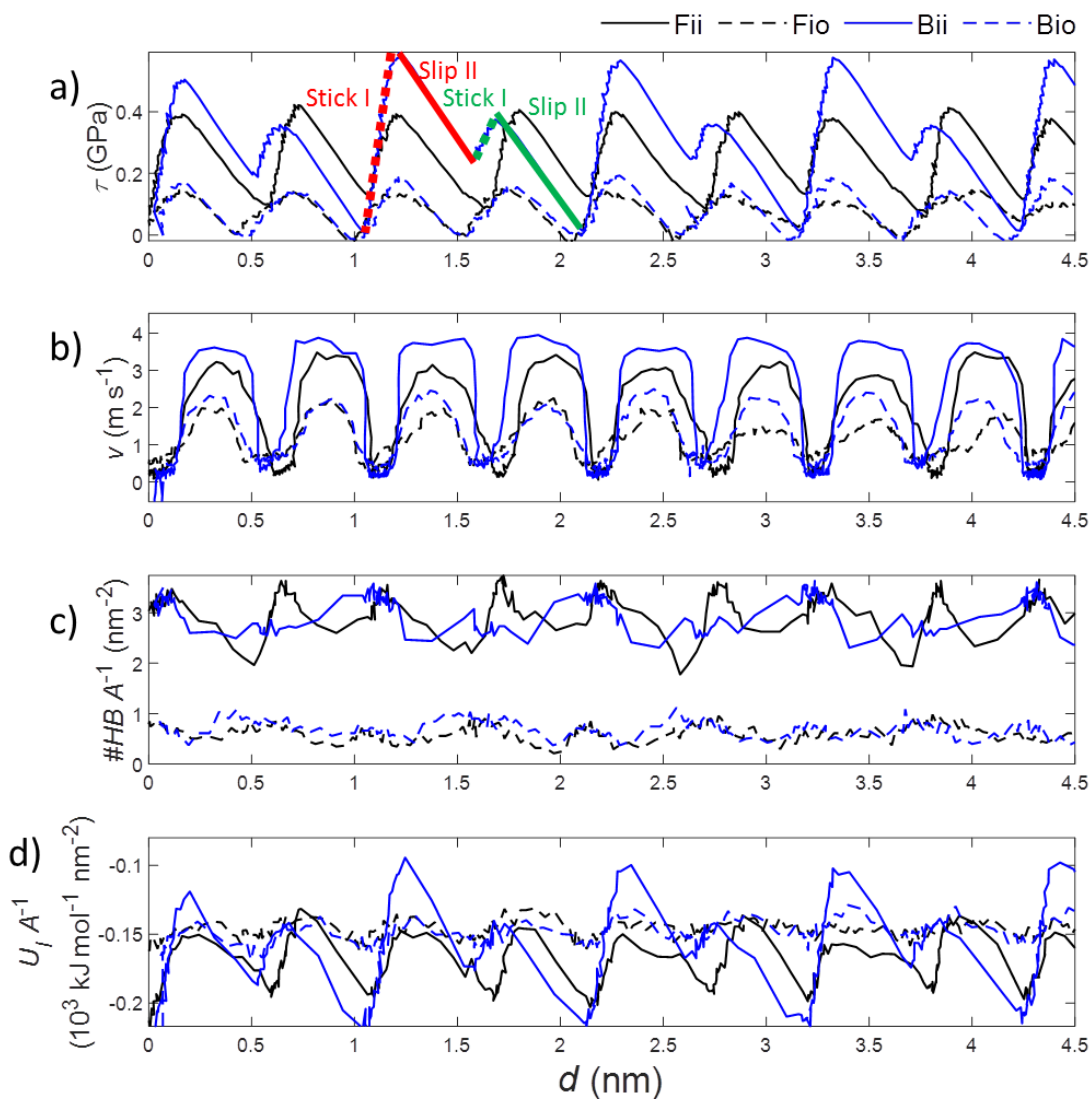


Figure 5-8 a) Interfacial shear stress  $\tau$ , b) velocity of the moving crystal  $v$ , c) interfacial hydrogen bond density  $\#HB A^{-1}$  and d) areal density of interaction energy  $U_I A^{-1}$  for the four dry and aligned systems: Fii, Fio, Bii, and Bio.

The systems Fio and Bio show lower maximum shear stress compared to Fii and Bii. This lower shear stress can be explained by the much lower density of hydrogen bonds (Figure 5-8c) in the hydrophilic-hydrophobic configuration compared to the density of hydrogen bonds in the hydrophilic-hydrophilic configuration, as the hydrophilic plane possesses a much larger number of hydroxyl groups, which are ready to form hydrogen bonds.

Figure 5-8 further shows the velocity (Figure 5-8b) and areal density of interaction energy (Figure 5-8d) for the aligned dry systems showing similar periodic/regular behavior. The velocity is lower



for the Fio and Bio systems, as correlated to the lower shear stress for these systems compared to the Fii and Bii systems. The average areal density of interaction energy of all systems has a similar value. However, the Fii and Bii show a more sawtooth behavior than the Bio and Fio systems. Rigorous discussions on the correlations between these properties are provided in the next section.

The regular pattern of interfacial shear stress versus displacement curves for different stick-slip cycles shows that the interface recovers after slipping, as displayed in Figure 5-9. The interfacial stiffness (units  $\text{GPa nm}^{-1}$ ) during the stick phases is determined as the slope of the stress-displacement curve. The error bar is relatively small demonstrating the regularity in interface stiffness recovery after the slip. The stiffness is clearly smaller for Fio and Bio systems due to the smaller hydrogen bonds areal density of these systems. The difference in stiffness between stick I and stick II and between forward and backward pulling directions is smaller.

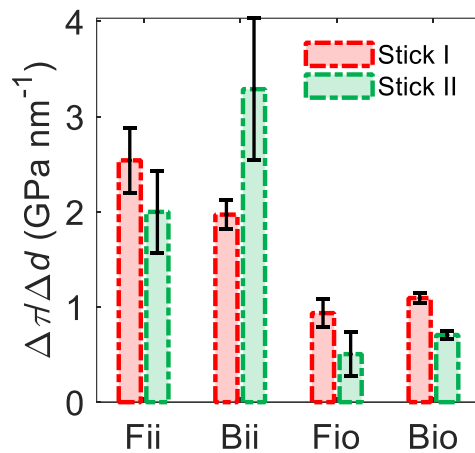


Figure 5-9 Stiffness (units  $\text{GPa nm}^{-1}$ ) during stick I and stick II for Fii, Bii, Fio, and Bio systems

For the “ii” contact, the shear behavior in forward and backward directions is different. As shown in the stress-displacement curves (Figure 5-8), the two peaks of the Fii system are of similar height, duration and interface stiffness, yet Bii presents two different types of peaks. The origin of this difference in shearing behavior depending on direction stems from the asymmetric distribution and orientation of hydrogen bonds. The hydrogen bonds areal density for the different systems during the different stick-slip phases is presented in Figure 5-10. For the Fii system, stick I and stick II phases share the same hydrogen bond areal density value, therefore Fii system possesses two similar stress peaks. For the Bii system, however, the hydrogen bond areal density of the stick I phase is abnormal and ~20% more than that of the stick II phase, as shown by the arrow in Figure 5-10a.

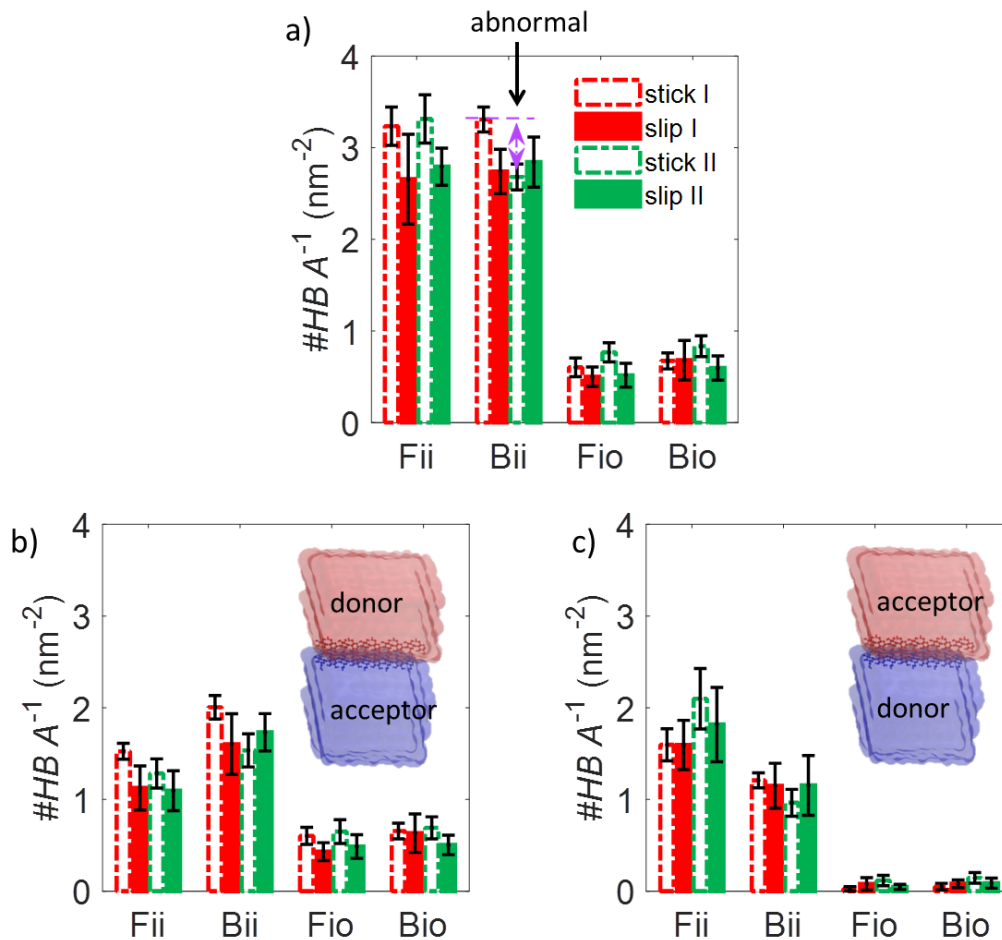


Figure 5-10 Areal density of hydrogen bond: **a)** total value, **b)** moving crystal as donor and **c)** moving crystal as acceptor.

In fact, the preferential orientation of hydroxyl groups at the interface has more implications. For the “ii” interface, when being pulled along the forward direction, the moving crystal tends to act more as hydrogen acceptor and less as hydrogen donor, Figure 5-10b and c. On the contrary, when the moving crystal is being pulled along the backward direction, the moving crystal act more as hydrogen donor. This swap of donor-acceptor pair may be at the origin of the direction-dependent behavior observed in the pulling test, as the strength of the hydrogen bond depends on the donor-acceptor configuration. For the “io” interface, regardless of the pulling direction, the hydrophilic surface mainly acts as hydrogen bond donor and the hydrophobic surface as hydrogen bond acceptor.

### 5.3.2 Impact of moisture and misalignment

In this section, the effects of the presence of moisture in the interface, *M*, and the misalignment of the interface, *A*, are discussed. Taking into account these two parameters results in the study of a total of 16 systems, i.e. Fii, FiiM, FiiA, FiiAM, Fio, FioM, FioA, FioAM, Bii, BiiM, BiiA, BiiAM,

Bio, BioM, BioA and BioAM. The curves for the dry and aligned systems were presented in Figure 5-8, while the curves of all the 16 systems are included in the Figure 5-11 to Figure 5-14. Within each figure, the pulling direction and the contact type is the same, while the impact of moisture and misalignment can be identified via comparison.

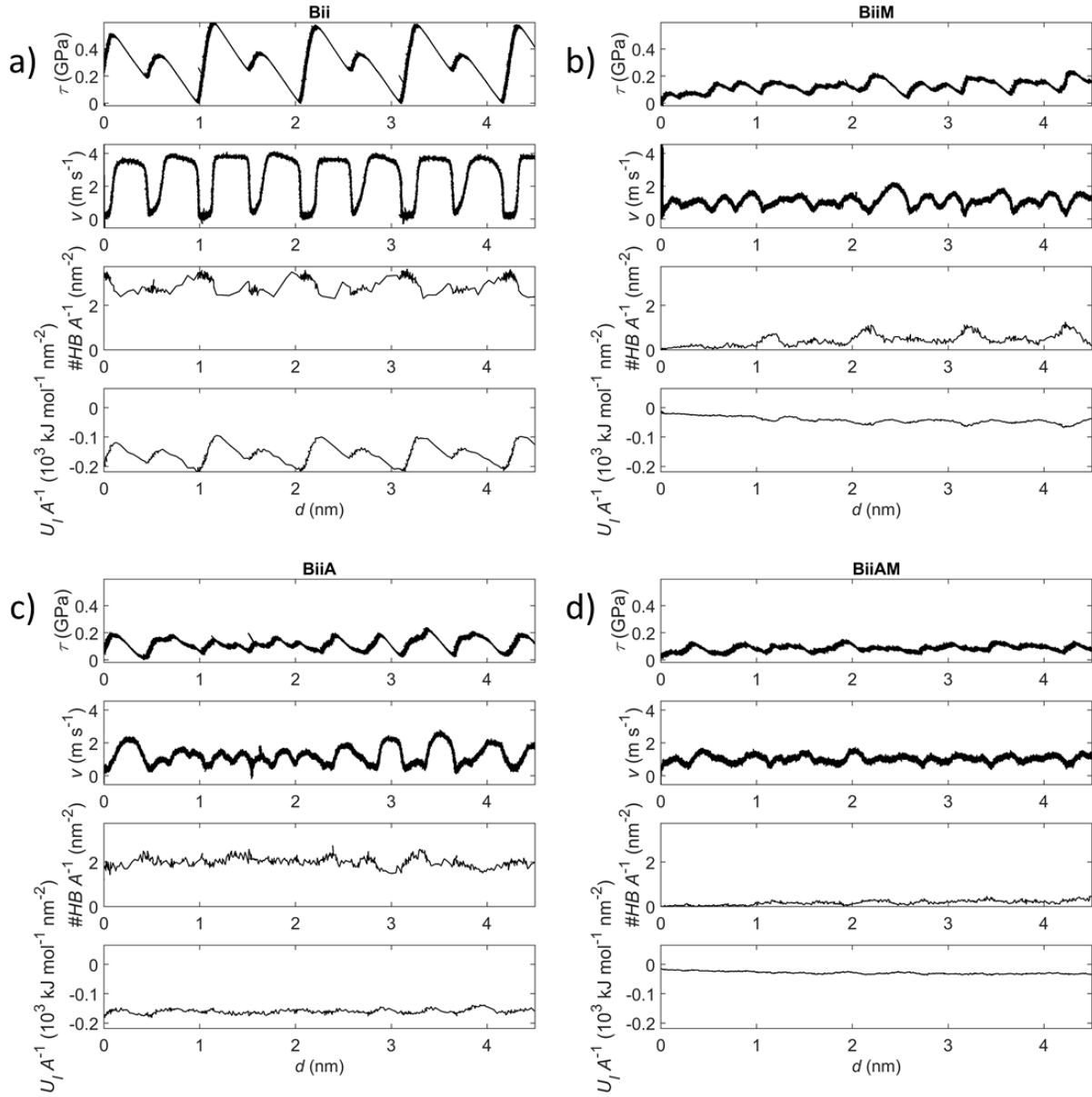


Figure 5-11 Interfacial shear stress  $\tau$ , velocity of the moving crystal  $v$ , interfacial hydrogen bond density  $\#HB A^{-1}$  and areal density of interaction energy  $U_I A^{-1}$  for the a) Bii, b) BiiM, c) BiiA and d) BiiAM systems.

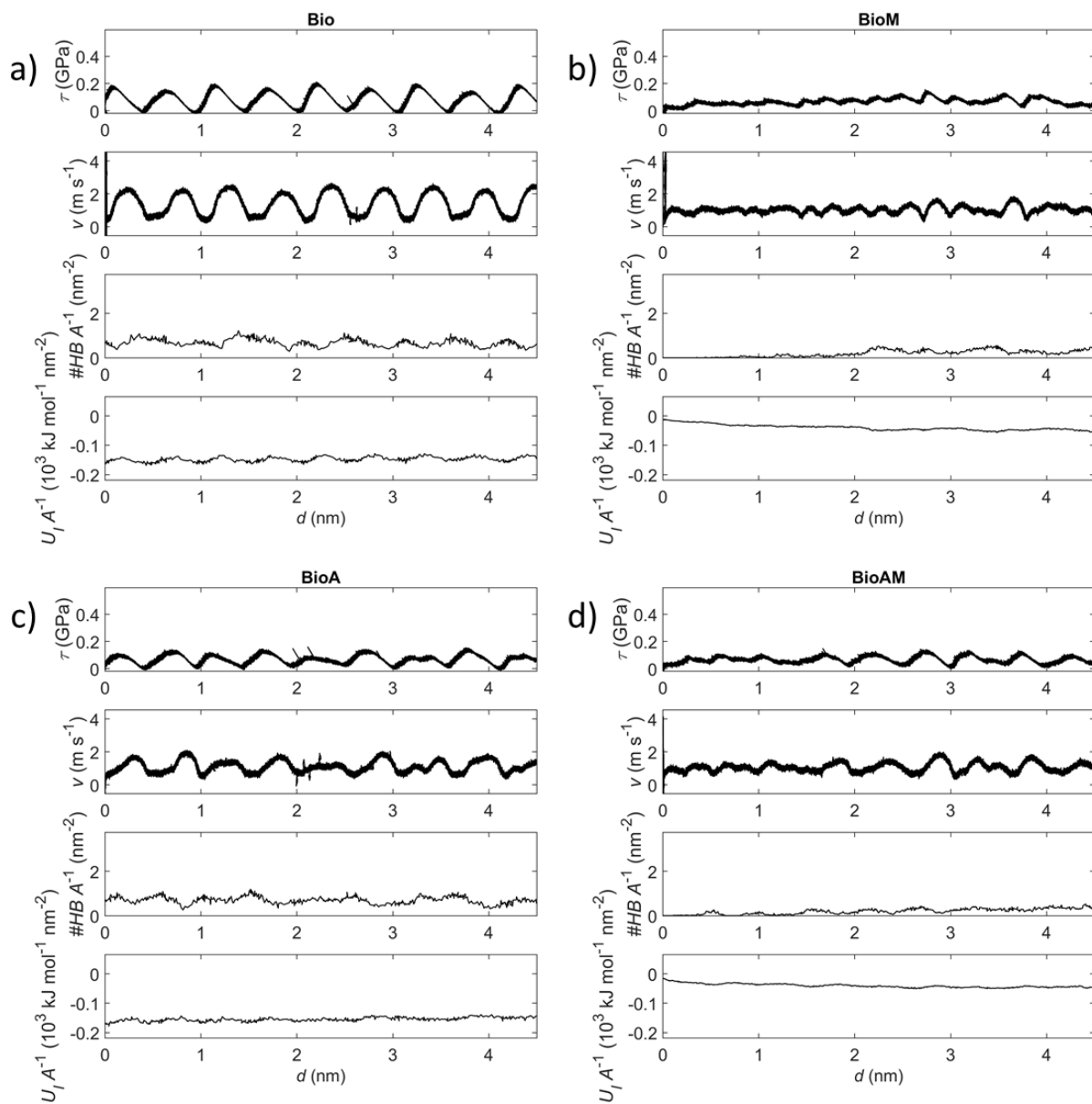


Figure 5-12 Interfacial shear stress  $\tau$ , velocity of the moving crystal  $v$ , interfacial hydrogen bond density  $\#HB A^{-1}$  and areal density of interaction energy  $U_I A^{-1}$  for the a) Bio, b) BioM, c) BioA and d) BioAM systems.

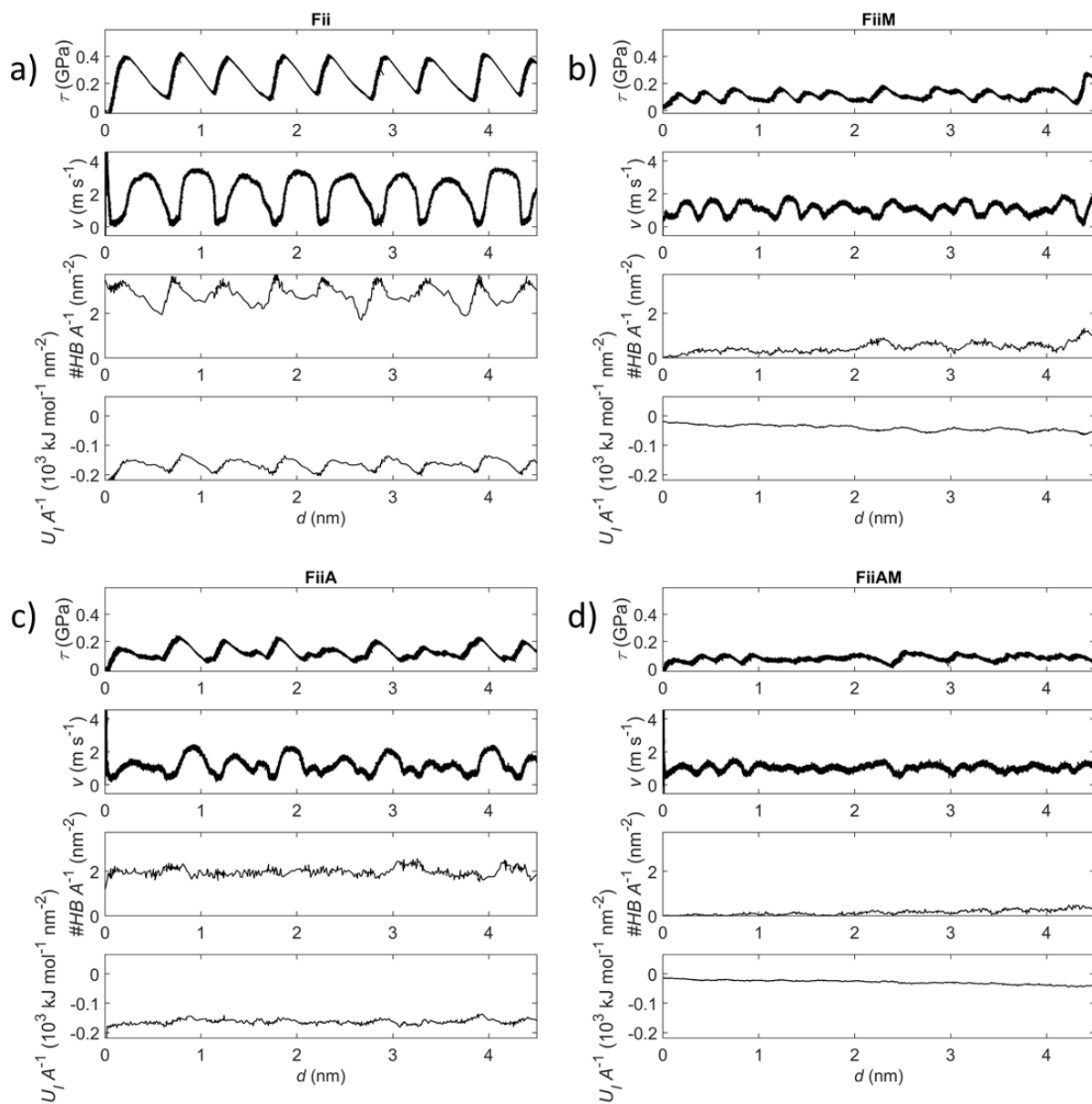


Figure 5-13 Interfacial shear stress  $\tau$ , velocity of the moving crystal  $v$ , interfacial hydrogen bond density  $\#HB A^{-1}$  and areal density of interaction energy  $U_I A^{-1}$  for the a) Fii, b) FiiM, c) FiiA and d) FiiAM systems.

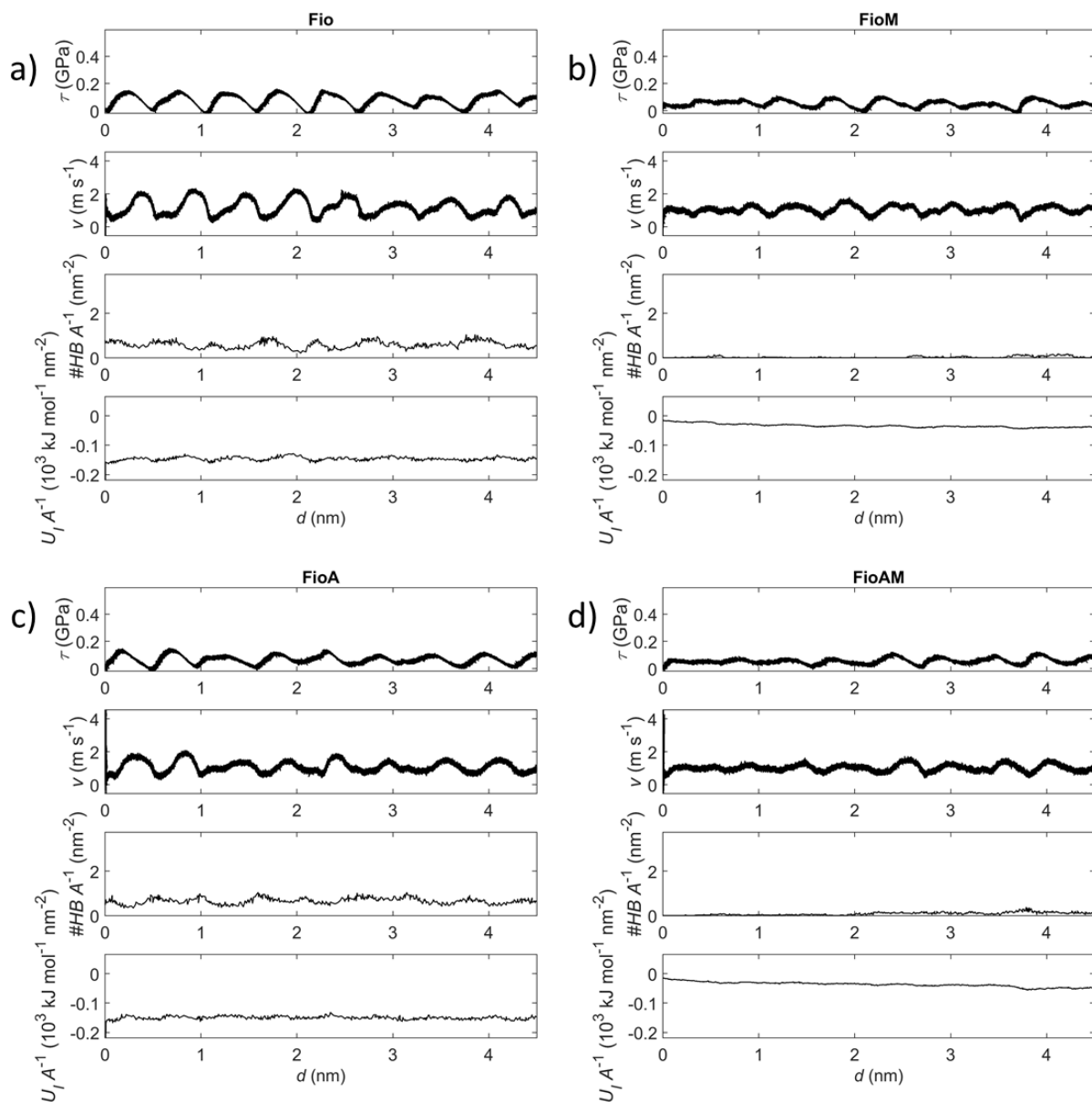


Figure 5-14 Interfacial shear stress  $\tau$ , velocity of the moving crystal  $v$ , interfacial hydrogen bond density  $\#HB A^{-1}$  and areal density of interaction energy  $U_I A^{-1}$  for the a) Fio, b) FioM, c) FioA and d) FioAM systems.

Figure 5-11 to Figure 5-14 are first discussed looking at the effect of the presence of water molecules in the interface. With the addition of the interfacial water layer, the crystal slides relatively steadily without any strong stick or abrupt slipping. The stress-displacement curves still show a weak sawtooth profile, however the periodicity vanishes, indicating that the influence of the periodic structure of the cellulose chain is lost due to the screening effect of moisture. The velocity of the moving crystal amounts to around 1 m s<sup>-1</sup> which corresponds to the moving speed

of the pulling speed, also indicating the strong weakening effect of moisture on the mechanical stiffness and strength of the interface. From the stress-displacement curves in Figure 5-11 to Figure 5-14, the peak shear stress  $\tau_{\max}$  can be extracted and summarized in Figure 5-15. It can be found that a single layer of water molecules significantly reduces the maximal shear stress.

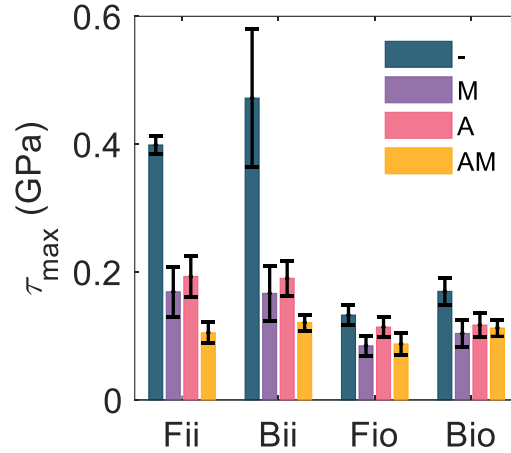


Figure 5-15 Impact of moisture and misalignment on maximum shear stress  $\tau_{\max}$ .

It is highly possible that cellulose crystals in a composite do not perfectly align with each other along the axial direction (Reising et al. 2012). From Figure 5-11 to Figure 5-14 the effect of misalignment is documented and Figure 5-15 summarizes the effect of misalignment on maximum shear stress. In general, the misalignment is found to reduce the shear stress. Misalignment displaces the contacting two crystalline surfaces from the “commensurate” state, where some of the atoms of two flat and rigid crystalline surfaces may be forced to climb uphill while the rest move downhill. This rearranging causes the effective reduction of the frictional forces and shear stress (Shinjo and Hirano 1993; Hod et al. 2018). Finally, Figure 5-15 also shows that the combination of moisture and misalignment (AM) results in a small additional reduction of the maximal shear stress.

### 5.3.3 Central role of hydrogen bond revealed by correlation analysis

For each system, several quantities are determined to characterize the 16 systems, i.e. interfacial shear stress  $\tau$ , velocity of moving crystal  $v$ , interfacial hydrogen bond areal density  $\#HB A^{-1}$  and areal density of interaction energy  $U_I A^{-1}$ . These quantities are all function of time or displacement, resulting in a large number of curves. For the sake of brevity and convenience of discussion, the information of all the curves is compacted by extracting the average value, local maxima and minima, and the drop, i.e. the difference between local maxima and minima. The original curves are included in Figure 5-11 to Figure 5-14.

The interfacial shear stress  $\tau$ , velocity of the moving crystal  $v$ , interfacial hydrogen bond density  $\#HB A^{-1}$  and areal density of interaction energy  $U_I A^{-1}$  seem to vary concertedly, as seen from Figure 5-8 and Figure 5-11 to Figure 5-14, suggesting possible correlations between the various

measurements. To quantify possible correlations, the average value, local maxima and drop of the interfacial shear stress  $\tau$ , velocity of the moving crystal  $v$ , interfacial hydrogen bond density  $\#HB A^{-1}$  are pairwise plotted with the indication of the Pearson correlation coefficients ( $r$ ), as shown in Figure 5-16. The average, maximum and drop of shear stress, velocity and hydrogen bond areal density are found to meaningfully correlate to each other with significant Pearson correlation coefficients (greater than 0.76 or less than -0.80). These strong correlations suggest a determining role played by hydrogen bonds for (110)-(110) and (110)-(200) contacts of cellulose nanocrystals. The areal density of interaction energy  $U_I A^{-1}$  does not show a meaningful correlation with the other properties, therefore it is not included in the present discussion and analyzed later. It is noted that the “ii” systems (solid black dots in Figure 5-16) are to some extent outliers which may have a great influence on the values of the Pearson correlation coefficient. A separate correlation analysis, where the “ii” cases are excluded, gives correlation coefficients greater than 0.5 or less than -0.5. This indicates that the correlations are valid though weakened.

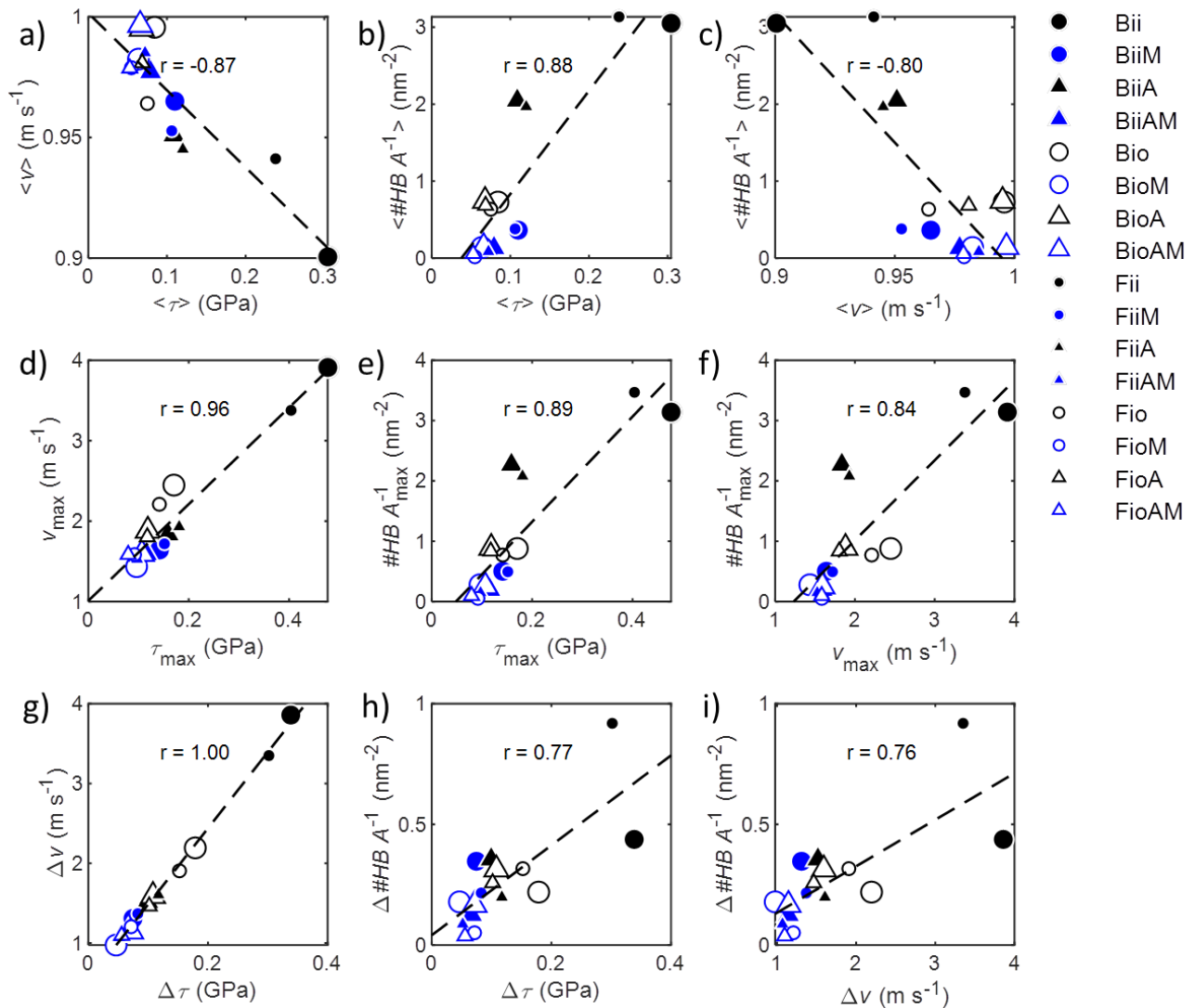




Figure 5-16 Correlation plots of three values, i.e. average value, local maxima and drop, with the three parameters, i.e. the interfacial shear stress  $\tau$ , velocity of the moving crystal  $v$ , areal density of hydrogen bond  $\#HB A^{-1}$ .

The hydrogen bond areal density and shear stress are positively correlated, as shown in Figure 5-16b, e and h. The hydrogen bonds provide the mechanical stiffness and strength of the interface. The friction force of a single cellulose-cellulose hydrogen bond  $f_{HB}$  can therefore be calculated by the ratio of friction force to the number of interfacial hydrogen bonds. For the dry cases,  $f_{HB} \sim 1.3 E^{-10}$  N. It is noted that the friction force of the single cellulose-cellulose hydrogen bond depends on the shearing speed (in this study  $1 m s^{-1}$ ).

The average velocity and shear stress are negatively correlated ( $r = -0.87$ ), whereas the peak value and drop value of velocity and shear stress are positively correlated ( $r \sim 1$ ), as shown in Figure 5-16a, d and g. Friction lowers the speed of the top crystal, which is remaining for a longer time fixed to the bottom crystal. At the same time, higher friction can increase the elastic energy stored during the stick phase and such increased energy will induce higher peak velocity when released during slip. Similar observations can be made for the effects of hydrogen bonds. A higher areal density of hydrogen bonds lowers the average velocity, whereas it increases the peak and drop values of velocity, as shown in Figure 5-16c, f and i.

The variables of dry and aligned “ii” contact (filled black circles in Figure 5-16) locate somewhat differently from the other systems. This noticeably different mechanical behavior of the “ii” contact can be seen as a result of the different number of the hydrogen bonds, as the hydrophilic planes possess a large number of hydroxyl groups that can serve as hydrogen donors and acceptors.

In addition to the plots given in Figure 5-16, more correlations can be identified as summarized in Table 5-1, where the nine different quantities, namely  $\langle\tau\rangle$ ,  $\langle v\rangle$ ,  $\langle\#HB A^{-1}\rangle$ ,  $\tau_{max}$ ,  $v_{max}$ ,  $\#HB A^{-1}_{max}$ ,  $\Delta\tau$ ,  $\Delta v$  and  $\Delta\#HB A^{-1}$ , are found to be mostly correlated with each other and so with significant correlation coefficients.

Table 5-1 Pearson correlation coefficients of the average value, local maxima (peak value) and drop (delta value) of the interfacial shear stress  $\tau$ , velocity of the moving crystal  $v$  and interfacial hydrogen bond density  $\#HB A^{-1}$ .

|             | Average                     |                    |                             | Peak values  |           |                     | Delta values |            |                     |       |
|-------------|-----------------------------|--------------------|-----------------------------|--------------|-----------|---------------------|--------------|------------|---------------------|-------|
|             | $\langle\tau\rangle$        | $\langle v\rangle$ | $\langle\#HB A^{-1}\rangle$ | $\tau_{max}$ | $v_{max}$ | $\#HB A^{-1}_{max}$ | $\Delta\tau$ | $\Delta v$ | $\Delta\#HB A^{-1}$ |       |
| Average     | $\langle\tau\rangle$        | -                  | -0.87                       | 0.88         | 0.99      | 0.92                | 0.87         | 0.90       | 0.92                | 0.73  |
|             | $\langle v\rangle$          | -0.87              | -                           | -0.80        | -0.82     | -0.72               | -0.79        | -0.70      | -0.72               | -0.53 |
|             | $\langle\#HB A^{-1}\rangle$ | 0.88               | -0.80                       | -            | 0.88      | 0.85                | 1.00         | 0.86       | 0.86                | 0.79  |
| Peak values | $\tau_{max}$                | 0.99               | -0.82                       | 0.89         | -         | 0.96                | 0.89         | 0.96       | 0.96                | 0.77  |
|             | $v_{max}$                   | 0.92               | -0.72                       | 0.85         | 0.96      | -                   | 0.84         | 1.00       | 1.00                | 0.74  |
|             | $\#HB A^{-1}_{max}$         | 0.87               | -0.79                       | 1.00         | 0.89      | 0.84                | -            | 0.85       | 0.85                | 0.81  |

|              |                     |      |       |      |      |      |      |      |      |      |
|--------------|---------------------|------|-------|------|------|------|------|------|------|------|
| Delta values | $\Delta\tau$        | 0.90 | -0.70 | 0.86 | 0.96 | 1.00 | 0.85 | -    | 1.00 | 0.77 |
|              | $\Delta\nu$         | 0.92 | -0.72 | 0.86 | 0.96 | 1.00 | 0.85 | 1.00 | -    | 0.76 |
|              | $\Delta\#HB A^{-1}$ | 0.73 | -0.53 | 0.79 | 0.77 | 0.74 | 0.81 | 0.77 | 0.76 | -    |

Hydrogen bonding consists in bonding by van der Waals and electrostatic interactions. The delta values of areal density of interaction energy  $\Delta U_I A^{-1}$  are found to correlate ( $r = 0.77$ ) with the delta values in areal hydrogen bond density  $\Delta\#HB A^{-1}$ , shown in Figure 5-17. The correlation coefficient is 0.76 after removing the outliers (solid black dots). This indicates the dominant role of hydrogen bonding in the areal density of interaction energy. It should be noted that the hydrogen bond and areal density of interaction energy being discussed here are only the cellulose-cellulose ones. The hydrogen bond and areal density of interaction energy involving water molecules are omitted because, in this way, the system with moisture can be directly compared with the dry systems.

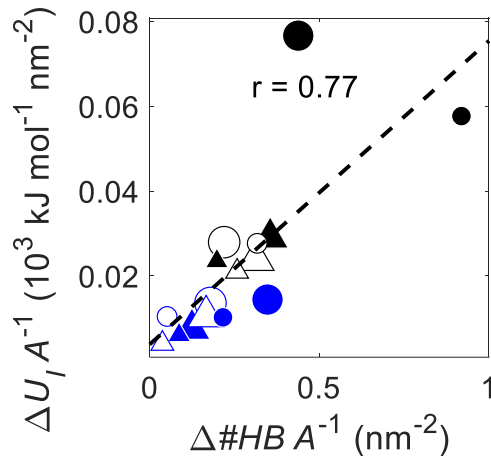


Figure 5-17 Correlation between the drop of areal density of interaction energy  $\Delta U_I A^{-1}$  and the drop of interfacial hydrogen bond density  $\Delta\#HB A^{-1}$ .

### 5.3.4 Adhesion energy of the interfaces

The above sections deal with the frictional tests where the crystals are pulled laterally. In this section, the normal pulling tests are carried out. The moving crystal is being pulled along the normal direction while the force and center of mass displacement are tracked. The pulling stress  $\sigma$  is plotted as a function of pulling displacement  $d$ , shown in Figure 5-18a. Three quantities are extracted from the curves, namely maximum stress  $\sigma_{\max}$ , the displacement corresponding to maximum stress  $d\sigma_{\max}$ , the area under the curve which is defined as the adhesion energy  $E_{\text{adhe.}}$ . The first two quantities are shown in Figure 5-18b. The dry systems show higher maximum stresses than the moist systems, indicating the weakening effect of moisture. The maximum stresses of the moist systems occur at larger displacements, which can be explained by the water bridges formed between cellulose crystals that extend the interaction distance between the crystals.

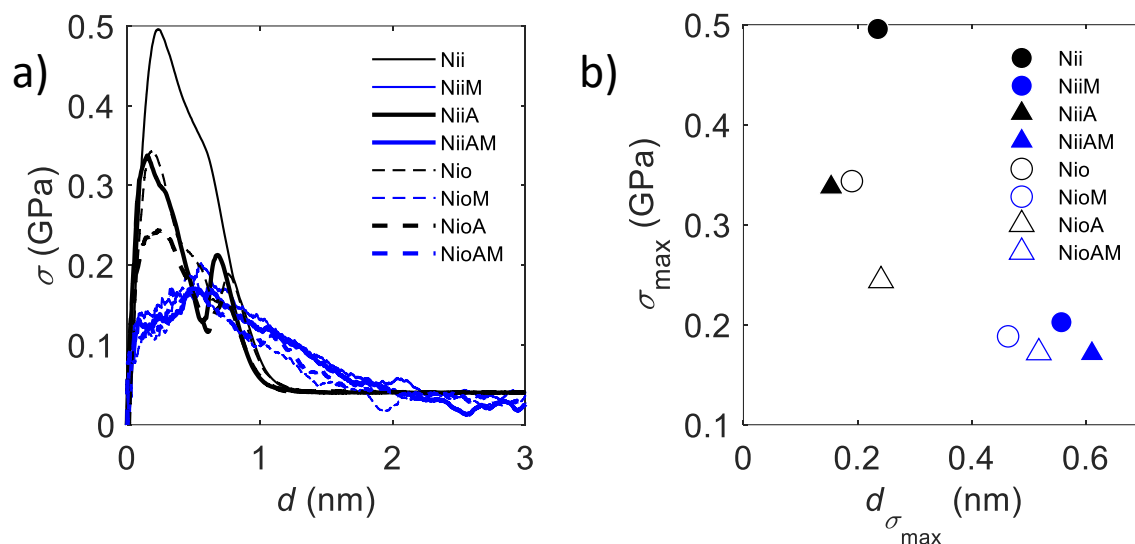


Figure 5-18 a) Stress-displacement curve of normal pulling tests. b) Maximum stress and the displacement correspond to maximum stress

The adhesion between polymer surfaces plays an important role in the interfacial behavior (Lavielle 1991). The adhesion energy can be used to quantitatively describe the energy needed to separate two crystals under different conditions. For the dry systems, after a certain distance ( $\sim 1$  nm), the adhesion energy stops to grow (Figure 5-19a), because the distance between the two crystals is beyond the cutoff distance of intermolecular interaction resulting in a zero interaction force and the consequent saturation of energy. In contrast, for the moist interfaces, the adhesion at small displacement is lower than the one of dry systems as also observed by (Xiao et al. 2016b; Wang et al. 2017). However, the adhesion energy continues to grow after 1 nm displacement. Although the direct molecular interactions between the crystals are zero, there exists a water bridge between the crystals (a snapshot of system NiiM is included in Figure 5-19b) connecting the two crystals with forces akin to capillary forces (as also seen in Sinko and Keten 2014).

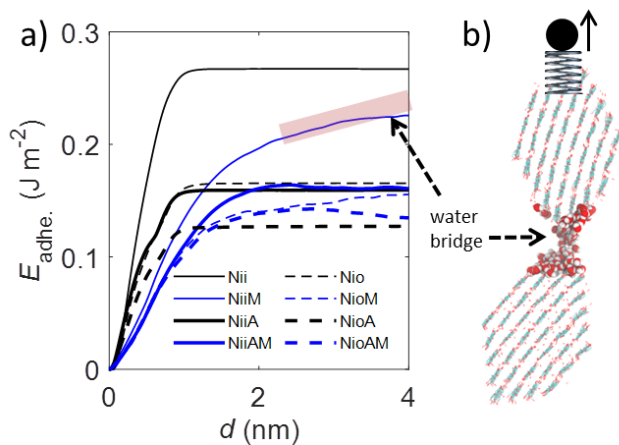


Figure 5-19 a) Adhesion energy versus displacement of various interfaces. b) Snapshot of the system with interfacial moisture and water bridge.

The misalignment reduces the adhesion energy, which can be explained by the reduced number of hydrogen bonds between the crystal interfaces. Moisture shows contrasting effects. For strongly bonded aligned interfaces, moisture reduces the adhesion (also shown by molecular simulations in Büyüköztürk et al. 2011), however, for misaligned interfaces, moisture increases the adhesion energy by forming a water bridge as also shown in Ref. (Sinko and Keten 2014). In the results presented here, the adhesion energy of Nii system is twice as large as ones of the other systems, indicating the much stronger adhesion of the dry and aligned “ii” contact. Based on these observations, if cellulose crystal is to be used as a scaffold, it is optimal to prevent moisture while promoting alignment to achieve better adhesion. The adhesion energy in this study ( $0.27 \text{ J m}^{-2}$  for “ii” contact) is lower than the previously reported value ( $3.5 \text{ J m}^{-2}$  (Sinko and Keten 2015)). This difference is attributed to the pulling conditions. The two studies use similar pulling velocity however the spring constant of (Sinko and Keten 2015) is about 200 times larger than the one used in the current study.

Experiments of dry polymer-polymer contact also showed the correlation between adhesion energy and shear stress (Lavielle 1991). This correlation is also seen in our simulations. As shown in Figure 5-20, the adhesion energy linearly correlates with the average shear stress for the dry and moist cases with a Pearson coefficient of 0.86 (0.65 after removing solid black dots).

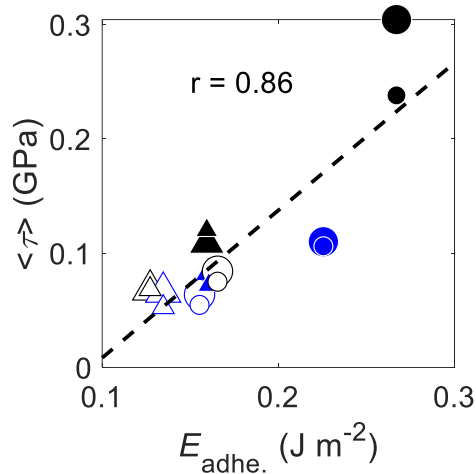


Figure 5-20 Correlation between the average stress  $\langle \tau \rangle$  and adhesion energy  $E_{\text{adhe.}}$ .

## 5.4 Discussion

This study systematically examined the impact of moisture, misalignment, pulling direction and contact surface type on the frictional behavior of cellulose crystal interface. Cyclical stick-slip behavior is revealed to have a period corresponding to the dimension of cellulose repeating unit.

This agrees with former reports from the computational study of the shear test of the CNC-CNC interface, which displayed an oscillatory periodic pattern and force peak period of  $\sim 1.04$  nm (Wei et al. 2018).

The extensive correlation analysis reveals the central role of hydrogen bonding in the mechanical performance of the interface. Interfacial shear strength, velocity profile and interface interaction are found to all strongly correlate with hydrogen bond, regardless of moisture condition, misalignment, pulling direction and type of contact surface. In another study, the MD measurement of peptide sliding over a polar surface in aqueous solution showed a similar correlation, i.e. friction force was found to be proportional to the number of hydrogen bonds (Erbaş et al. 2012). The friction force of a single hydrogen bond was estimated to be  $f_{\text{HB}} \sim 1 \text{ E}^{-10}$  N, which is in the same order of magnitude to the value stemming from the current study ( $f_{\text{HB}} \sim 1.3 \text{ E}^{-10}$  N). Such quantities can be useful. For example, the stress-displacement curve is commonly revealed by the pull-out test of single regenerated cellulose fiber (Zarges et al. 2018), whereas the concomitant hydrogen bonding is difficult to measure. The proposed single hydrogen bond friction force can be applied to infer, as a first indication, the number of hydrogen bonds.

The stress versus displacement during the stick phase is thought to be characterized by a set of hydrogen bonds which act as one-dimensional springs. These springs remain intact during displacement, but can rotate and slightly extend. However, when the displacement/rotation becomes too large, the HBs will be broken and the interface will slip. After slipping and having released the elastic energy, new HB springs will again be formed at the new equilibrium position. The velocity of the moving crystal is dependent on the amount of elastic energy being released which is determined by the density and strength of HB. The HBs are an important contributor to the interaction energy. These observations provide an explanation for the correlation between HB and friction stress, velocity and interaction energy.

Upon completing a stick-slip cycle, the mechanical properties of the interface recover. Similar observations of such recovery of material stiffness after irreversible deformation is reported on the wood cell wall level, referred to as “Velcro effect” (Keckes et al. 2003). There are multiple hypotheses trying to explain this effect (Altaner and Jarvis 2008; Salmén and Bergström 2009; Speck and Burgert 2011; Cosgrove and Jarvis 2012). The work presented here, namely the stick-slip behavior and the interface recovery after deformation at the molecular scale, may be showing a phenomenon at the root of the Velcro effect, although a more rigorous study is needed in the future.

Misalignment will mainly reduce the areal density of HBs. These HBs will break at a lower shear force. Also the drop in shear stress will be lower, due to the smaller number of acting HBs. At the macroscopic scale, such structural misfit induced by misalignment may lower the frictional forces by 1000 times, a situation referred to as “superlubricity”. However, at the nanometer scale, the superlubricity effect may break down because of the extremely high surface-volume ratio at this

scale (Ma et al. 2015c). In the current case, the hydrogen bonding between cellulose chains provides inevitably strong attraction, apparently still overriding the softening effect resulting from incommensurability.

Moisture reduces the mechanical performance by reducing the areal density of HB, acting in a way similar to misalignment. Previous studies of Sinko et al. (2014) and Wei et al. (2018) also reported on the weakening effect of moisture on the traction and separation behavior of (110)-(110) and (200)-(200) contacts of CNC fibril. They found that the interfacial adhesion and shear behavior can be drastically changed by the presence of moisture, e.g. the friction barriers are lowered by 3~4 times. For example, moisture is seen as a lubricant that is responsible for the low friction at cartilage in animal joints by forming hydration shells surrounding charges of polymers (Ma et al. 2015b). This weakening effect of moisture could serve as the mechanism of a so-called molecular switch, where the motion of crystal could be activated by the adsorption of moisture and locked by the desorption of moisture (Xiao and Hu 2016). In composite materials, the cellulose nanocrystals can form a percolated network, a stiff scaffold, through interfacial hydrogen bonding at contacting points (Shanmuganathan et al. 2010; Dagnon et al. 2012; Zhu et al. 2012). Such bonding is readily destroyed by the introduction of moisture, due to the competitive adsorption of water molecules to the hydroxyl group, resulting in a drastic softening of the composite material (Shanmuganathan et al. 2010; Dagnon et al. 2012; Zhu et al. 2012). In this way, the wetting and drying processes could reversibly switch high and low interfacial friction.

Contrary to the broad applications of crystalline cellulose in various fields, the understanding of crystalline cellulose interfacial behavior is still in its infancy. Experimental studies of this stick-slip behavior will remain a challenge in the foreseeable future, because frictional experiments, e.g. the commonly employed atomic force microscopy, face technical difficulties handling the cellulose nanocrystals. The current study focuses on the crystal-crystal interface. However, it might be interesting to look at the behavior of interface cellulose crystal - matrix, which is one of the most important factors determining the overall mechanical performance of the cellulose fiber reinforced material, which will be done in the next chapters. Besides possible experimental and computational efforts, a theoretical model of the interfacial behavior of cellulose crystal needs to be developed. The Frenkel-Kontorova-Tomlinson (FKT) model (Weiss and Elmer 1996) can be modified and further developed to serve the purpose, though a number of issues should be resolved to strengthen the predicting power of FKT model. For example, the fixed surface is assumed to have a sinusoidal potential in FKT model, which may greatly differs from the measured interaction energy  $U_I$  in this study (e.g. blue solid curve in Figure 5-8d).

This study investigated the impact of moisture and misalignment at polymeric crystal interfaces, while there are in fact much more parameters to consider when tackling real composites, such as temperature, straining rate, etc. The mechanical performance of the interface may be utterly different under another set of loading conditions, which remain to be explored in the future.

## 5.5 Conclusion

Through molecular simulation of the hydrophilic crystalline interfaces, this study provides detailed information on the interfacial mechanical behavior of cellulose nanocrystals, seen as the bottleneck towards the understanding of the hygromechanical behavior of composites. For dry and aligned interfaces, a regular stick-slip behavior is identified. A full stick-slip cycle consists of four phases, i.e. stick I, slip I, stick II and slip II, characterized by different levels of friction and displacement. A full stick-slip period corresponds to the dimension of the repeating unit. Direction-dependent behavior is found, when shearing the crystal along opposite directions, which is ascribed to the asymmetric distribution and preferential orientation of hydrogen bonds. The interface stiffness recovers after an irreversible slip, the origin of which is attributed to the re-formation of hydrogen bonding.

Systematic examinations of the impact of loading direction, misalignment and presence of moisture are conducted in hydrophilic-hydrophilic and hydrophilic-hydrophobic crystalline interfaces. The misalignment of crystal surfaces and the existence of interfacial moisture lower the interfacial friction and disturb the regular pattern of stick-slip. However, regardless of the various loading conditions, interfacial stress, shear velocity and interaction energy are shown to strongly correlate with the density of interfacial hydrogen bonds, indicating the central role of hydrogen bonding in frictional behavior. The areal density of interaction energy moderately correlates with the density of hydrogen bonds. The areal density of hydrogen bonds explains why the hydrophilic-hydrophobic contact is weaker than the hydrophilic-hydrophilic contact. Besides hydrogen bond, average shear stress is found to correlate strongly with the adhesion energy of the interface. These revealed atomistic mechanisms can help improve the design of promising cellulose nanocrystal reinforced composites and moreover contribute to the general understanding of the mechanics of hydrogen bonded interfaces.

As recent microscopy images suggested, the direct contact of cellulose fibers may exist and act an important role in cell wall mechanics (Park and Cosgrove 2012a). This chapter provides the missing piece of information on such structure. In the next chapter, a similar yet more common interface in terms of what is present in the S2 cell wall layer, namely the cellulose crystal-hemicellulose matrix interface, is discussed using similar pulling techniques. The two chapters together form a full picture of the behavior of interfaces in wood cell wall.

## Chapter 6 Mechanics of the Fiber-Matrix Interface in Wood Cell Wall

Following the discussion of the fiber-fiber interface in the previous chapter, this chapter investigates the mechanical behavior of a prevailing fiber-matrix interface in wood cell wall, i.e. the cellulose crystal-galactoglucomannan interface. Galactoglucomannan (GGM) is known to be the hemicellulose most in adjacency with crystalline cellulose (CC). The anisotropic swelling behavior of the composite is studied. Molecular simulations of the prototypical fiber-matrix system reveal the interface mechanics over the full hydration range, filling gaps in experimental studies. The existence of an interphase, the region between ‘bulk’ matrix and fiber where shear stress transfer occurs, is described and its thickness, composition and structure are analyzed. It is important to note that because of the exceptional mechanical performance of cellulose crystal, numerous studies employ this natural fiber in composites. This study provides new insights in understanding the interface mechanics between CC-GGM and beyond in the interaction fiber-matrix in wood S2 cell wall layer.

### 6.1 Introduction

Cellulose fiber extracted from plant biomass is attracting tremendous attention as an environmental-friendly replacement of synthetic fibers. The mechanics of the fiber-matrix interface, the contact region of fiber and matrix, determines to a large extent the overall performance of a composite material. In addition to its nanoscale dimension and its high strength, cellulose fiber presents the particularity of hosting a quite abundant amount of hydroxyl groups on its surface, which from one side offers a strong interaction between matrix and reinforcement, but from the other side renders the interface susceptible to moisture. There is a strong need of better grasp of the behavior of the cellulose fiber-matrix interface in composites, especially with respect to the full hydration range. In addition to the interface, the matrix adjacent to the fiber, a region acknowledged as interphase, also plays an important role in composite mechanics. Within the interphase, the stress transfers from the load-bearing fibers to the bulk matrix. A stiff interphase may enhance the overall stiffness yet reduces the toughness, and vice versa (Piggott 1989). Such transition region usually spans from nanometers to even micrometers.

Molecular interactions at the interface and within the interphase highly affects the effectiveness of stress transfer and therefore the final performance of the composite. Researchers actively seek remedies for improving the adhesion and have developed many strategies, including surface modification, coating and addition of nanoparticles (Reale Batista and Drzal 2018). Recent development of nanoindentation tests using atomic force microscope (AFM) refines the interphase study down to tens of nanometers (Lee et al. 2007; Pakzad et al. 2012). The studies on the interface and interphase region actually consist in only 30 % and 2 %, respectively, of the studies on composites (Teklal et al. 2018). The structure and the mechanical role of the interphase region remain to be elucidated. Given the hydrophilicity of the components, the role of moisture on the



composites should also be ascertained. Since molecular level details are still missing, computational studies at molecular scale are warranted to fill the gap.

This chapter examines the mechanical behavior of the prevailing fiber-matrix interface in the softwood cell wall, i.e. the CC-GGM interface with the objectives to elucidate the role of water and interphase in its interface mechanics, the interplay between hydrogen bonding and material stiffness, providing critical insights for the promising natural fiber composites. A two-component system is constructed, consisting of cellulose crystals and hemicellulose matrix, which can be considered as a surrogate modelling the main working mechanism in S2 wood cell wall layer, i.e. the mechanics of fiber-matrix interface. The structure of the composite at different moisture content, thus under swelling, is studied. The occurrence of the interphase region is probed using density profiles. Finally, the interface is characterized using pulling tests, where the matrix has either a restrained or unrestrained mobility.

## 6.2 Materials and methods

In this section, the preparation method of the atomistic model of the composite system is introduced, followed by the description of the tests of swelling and pulling and finally the measurement methods for determining material properties are given.

### 6.2.1 Preparation of the composite system

To study the mechanical behavior of fiber-matrix interface in wood cell wall, a prototypical model of cell wall made of two types of materials, one stiff cellulose fiber and a compliant hemicellulose matrix, is constructed. The schematic of the system is shown in Figure 6-1a. As the theme of the thesis is the analysis of the hygromechanical behavior of the S2 cell wall layer, the system retains the essence of the matrix-fiber as seen in wood, schematically shown in Figure 6-1b, where GGM is right next to CC while the other components, such as xylan and lignin surround the GGM. Quartz crystal microbalance and Fourier transform IR spectroscopy results supported the adjacency of GGM to CC (Salmén and Fahlén 2006). Therefore, this study takes GGM as the matrix material. In the next chapter, the S2 layer represented by CC and matrix consisting of GGM, xylan and lignin, will be analyzed.

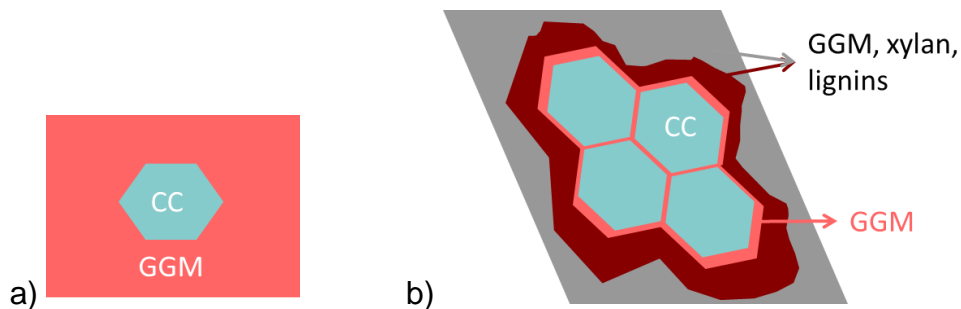


Figure 6-1 a) Schematic of fiber-matrix composite system. b) Schematic of S2 layer.

To model the composite, the amorphous and the crystalline phases are built separately. Then a hollow is made in the amorphous phase to receive the crystal. The MD approach, the building of each phase and the assembly of the composite are presented.

### 6.2.1.1 General MD parameters

GROMACS 5.0 package (Abraham et al. 2015) and GROMOS 53a6 force field (Oostenbrink et al. 2004) are used for the MD simulations. The integration time step of the equations of motion is 1 fs unless otherwise stated. For NVT simulations, the temperature is controlled by the Nose-Hoover thermostat. For NPT simulations, the pressure is controlled by the Parrinello-Rahman barostat. The Coulomb and Van der Waals interactions have cut-off radii of 1.0 nm and the particle-mesh Ewald summation is used to account for long-range Coulomb interactions.

### 6.2.1.2 Crystalline cellulose and galactoglucomannan

The chemical structure of cellulose chain is shown in Figure 6-2a. A cellulose crystal with 36 chains forming a hexagonal cross-section (Ding et al. 2014) is generated by the cellulose builder toolkit (Gomes and Skaf 2012) based on the crystallographic information from Nishiyama et al. (2002). The structure is then energy minimized using a conjugate-gradient algorithm. Equilibration is carried out in canonical ensemble (fixed volume at 300 K). The length of the cellulose is 10 monomers. The two ends of each cellulose chain are bonded using cross periodic boundary covalent bonds to achieve an infinitely long cellulose chain. The density of the CC model is 1.5 g cm<sup>-3</sup>. To avoid the equilibrated cellulose crystal from disintegrating, pairwise harmonic restraints are applied to the carbon atoms to preserve the relative positions of atoms, in both tests swelling and shearing.

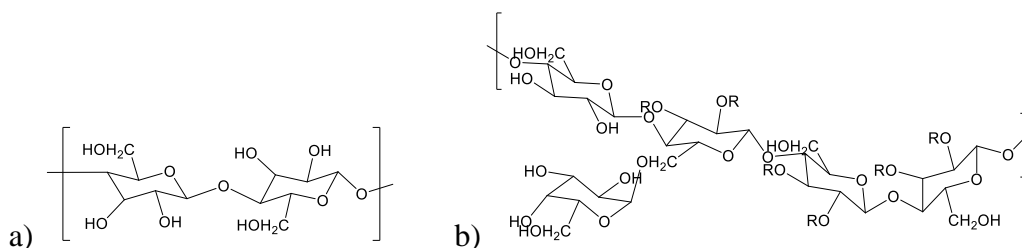


Figure 6-2 Chemical structures of a) cellulose and b) galactoglucomannan.

The initial structure of a single GGM chain is built in Material Studio 8.0. The GGM chain is formed by randomly polymerizing glucose and mannose monomers (ratio 1:4), and additionally, galactose side groups are branched on mannose units (~ 8 wt %) (Xu et al. 2010), as shown in Figure 6-2b. The length of the GGM chain is 100 monomers. Initially, 36 chains are inserted into the periodic box with random locations and orientations. The system is subjected to NPT relaxation (0 bar, 700 K) for 1 ns followed by another NPT relaxation (0 bar, 300 K) for 10 ns. The relaxed system displays a size of 15.6\*11.1\*4.8 nm<sup>3</sup> and a density of 1.2 g cm<sup>-3</sup>. It is noted that this is a large simulation system with ~54 k atoms. This significant size of the matrix is necessary to include the full interphase region.

The next section is assembling process of the two built systems. Alternatively, the GGM could have been built around the CC (as done in chapter 8), but this was not retained. Here 36 chains of DP 100 GGM are involved making insertion inefficient.

### ***6.2.1.3 Embedding crystalline cellulose fiber in galactoglucomannan matrix***

The length of CC (5.3 nm) is slightly longer than 4.8 nm, one of the lateral sizes of the GGM system. To match the two dimensions, in a first step, GGM is subjected to a slight uniaxial tension strain to match the length of the CC. After such straining, it is important to release the residual stress by applying a 10 ns NVT relaxation at high temperature and a 5 ns NPT relaxation at room temperature (0 bar on the transverse directions only, 300 K). Another 1 ns of NPT relaxation (0 bar and 300 K) guarantees that the three principal directions of the system are all relaxed to a zero pressure.

The next step is to embed the CC fiber within the GGM matrix. There are two techniques of embedding, both presenting some drawbacks. One manner is akin to wedging, i.e. by applying a force at the location that will push the polymer chains away, thus making a void throughout the GGM bulk material. This method introduces, unfortunately, unphysically high residual stresses as some chemical bonds of the displaced polymer are highly stretched. Another method is to directly remove the chains within the volume where the fiber is to be inserted, which does not introduce residual stresses but creates unnecessary porosity. In this study, the two methods are combined. First, the geometrical centerline of the GGM material along z-axis is chosen as the future axial position of the CC. Strong forces are applied along the radial direction perpendicular to the selected center axis. In this way, a hole of 6 nm in diameter is created. The chains being pushed away are unphysically stretched. Second, a steepest descent energy minimization is applied to release the stress of the unphysically stretched chains, which will cause the hole to shrink. Third, the matrix polymer chains that would overlap with future CC are removed manually. In total 6 chains of GGM are removed, and the CC is then placed into the hole, with its center axis overlapping the center line of the GGM material. Fourth, a NPT relaxation (0 bar, 300 K) of 6 ps with an integration time step of 0.01 fs is applied. The integration timestep is intentionally set to a minimal value to facilitate the convergence of the system. Fifth, a compression at high-temperature NPT simulation (1000 bar on the transverse direction, 800 K) is applied while keeping the CC atoms at the fixed location to heal the porosity created by removing chains and to help the matrix to form better contact with the newly inserted CC. Finally, another 5 ns of NPT relaxation (0 bar, 300 K) is applied, resulting in a CC fiber embedded in the GGM matrix with stress-free boundaries with a dimension of  $14.1 \times 10.1 \times 5.3 \text{ nm}^3$ . The overall density is  $1.3 \text{ g cm}^{-3}$ , a value larger than the density of GGM ( $1.2 \text{ g cm}^{-3}$ ) and lower than the density of CC ( $1.5 \text{ g cm}^{-3}$ ). A snapshot of the system is shown in Figure 6-3, where CC and GCM are shown with balls and lines, respectively. Carbon, oxygen, and hydrogen atoms are colored in cyan, red and white, respectively.

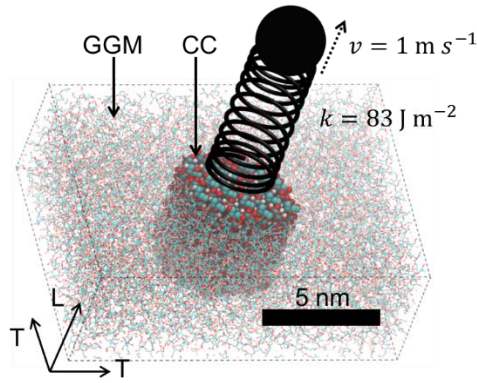


Figure 6-3 Computational system of crystalline cellulose fiber embedded in galactoglucomannan matrix.

### 6.2.2 Hydration

Moisture is introduced via a random insertion scheme, where SPC water molecules are inserted one after another in randomly chosen locations that do not overlap with existing atoms. After the successful insertion of a water molecule, a conjugated gradient energy minimization is applied, followed by an NPT relaxation (0 bar, 300 K) of 10 ps. The moisture content is defined as the ratio of the mass of water to the mass of GGM:

$$m = \frac{\text{mass of water}}{\text{mass of GGM}} \quad (6-1)$$

It should be noted that, usually in wood science, the moisture content is defined as the ratio of the mass of water to the mass of dry material. The denominator would then be here the total mass of GGM and CC. However, since CC does not adsorb water, it is found convenient to consider moisture content in reference to the mass of GGM only, which facilitates the comparison with the hygromechanical properties of GGM. Rigorously, sorption should be characterized by sorption isotherm relating relative humidity or chemical potential to the moisture content. Here these are omitted due to the large uncertainty of chemical potential measurement.

### 6.2.3 Pulling test

To study the CC-GGM interface mechanics, pulling tests are carried out recording shear stress-displacement curves. The pulling test here is distinct from the pull-out test used in other studies such as (Zarges et al. 2018), because the system has periodic boundary conditions, therefore the fiber atoms that are being pulled out of one boundary actually reenter the system at the opposite boundary.

All atoms of CC are attached to a virtual spring with a spring constant  $k_{\text{pull}}$ . At the other end of the spring, a virtual atom moves at a constant velocity  $v_{\text{pull}}$  (Figure 6-3). The combination of  $k_{\text{pull}} = 83 \text{ J m}^{-2}$  and  $v_{\text{pull}} = 1 \text{ m s}^{-1}$  is chosen so that these settings yield a series of clearly defined stick-slip

events in the shear stress - displacement curve. The displacement of the center of the mass of CC is denoted as  $d$ .

Pulling tests are carried out along the two opposite directions and the average of the results of the two cases are presented below to eliminate the influence of pulling direction.

As noted above, the pulling tests are performed for two cases of matrix deformation. In the restrained case, the matrix atoms are linked by a harmonic potential to their initial location. In the other case the matrix atoms are free to move, the unrestrained case. It should be noted that the unrestrained case is more realistic because it allows the matrix to relax as the shearing proceeds. The restrained case where matrix atoms are restrained is only presented for theoretical discussion. The difference between restrained and unrestrained case shows the impact of matrix relaxation.

## 6.2.4 Measurements

As the focus of this system is the behavior of the interface between fiber and matrix and of the interphase, i.e. the matrix in the area adjacent to the fiber, the following are documented: swelling strain, spatial density of matrix material, polymeric chain orientation, stick-slip dynamics during pulling test, and occurrences of hydrogen bond, as described next.

### 6.2.4.1 Swelling strain

The uniaxial swelling strain is defined as follows:

$$\varepsilon_X(m) = \frac{X(m) - X(0)}{X(0)} \quad (6-2)$$

where  $X(m)$  is the size of the system at moisture content  $m$ , and  $X(0)$  is the size of the system in dry condition (i.e. Lagrangian approach). The uniaxial swelling strains of three orthogonal directions ( $\varepsilon_X$ , where  $X = x, y, z$ ) are measured. In this study, the system is transversely isotropic with the  $x$  and  $y$  axes being the transverse direction ( $T$ ) and the  $z$ -axis being the longitudinal direction ( $L$ ). Therefore two uniaxial swelling coefficients will be determined, i.e.  $\varepsilon_L = \varepsilon_z$  and  $\varepsilon_T = (\varepsilon_x + \varepsilon_y)/2$ .

### 6.2.4.2 Number density of atoms

The number density of atoms ( $\rho_N$ ) is defined as the number of atoms divided by the volume the atoms occupied. It will be determined as a function of distance to the CC surface ( $d_{cc}$ ). The interface enrichment  $\Delta\rho_N$  is defined as the difference between maximum value of  $\rho_N^{\max}$  and the number density far away from the CC surface  $\rho_N^{\text{sat}}$ , i.e.

$$\Delta\rho_N = \rho_N^{\max} - \rho_N^{\text{sat}} \quad (6-3)$$

### 6.2.4.3 Herman's orientation function

Herman's orientation function (HOF) characterizes the extent of orientation of the polymer chain with respect to the axis of interest, which corresponds to the nematic order parameter (Hermans and Platzek 1939). It is defined as:

$$\text{HOF} = \frac{3\langle \cos^2 \theta \rangle - 1}{2} \quad (6-4)$$

where  $\theta$  is the angle between the axis of interest and the direction of a polymer monomer and the angular bracket denotes the entity average over all monomers in the system. The direction of polymer monomer, here mannose and glucose, is defined as the vector formed by the C1 and C1' atom, i.e. the C1 atom of the next monomer.

### 6.2.4.4 Displacement, velocity and shear stress during pulling

The displacement ( $d$ ) is defined as the distance traveled by the center of mass of CC from its initial position. The average velocity of the atoms ( $v$ ), including both CC and GGM atoms, is defined as the average displacement of the atoms divided by the time span. The shear stress ( $\tau$ ) at the interface is defined as the traction force applied to the CC fiber divided by the surface area of CC,  $\sim 88 \text{ nm}^2$  for the hexagonal 10 monomer long-36 chain cellulose crystal, as previously done in (Pitkethly and Doble 1990). The local maxima, local minima and drop values of shear stress are extracted.

### 6.2.4.5 Areal density of interfacial hydrogen bonding

The number of hydrogen bonds (#HB) formed between CC and GGM is extracted during the simulation trajectory. The establishment of hydrogen bonds is based on geometric criteria:

$$r \leq 0.35 \text{ nm and } \alpha \leq 30^\circ \quad (6-5)$$

where  $r$  is the distance between the donor oxygen atom and the acceptor oxygen atom, and  $\alpha$  is the angle of acceptor oxygen atom – donor oxygen atom – donor hydrogen atom. The interoxygen distance criterion of 0.35 nm refers to the first minimum of the radial distribution function of SPC water (Soper and Phillips 1986; Luzar and Chandler 1993). The angle of  $30^\circ$  is approximately the angle of vibrations that break HBs (Teixeira and Bellissent-Funel 1990).

The areal density of interfacial hydrogen bond, #HB  $A^{-1}$ , is defined as the number of hydrogen bonds between CC and GGM normalized by the contact area of CC and GGM. The local maxima, local minima and drop values of interfacial hydrogen bonding are extracted, following similar procedure as for shear stress.

## 6.3 Results

### 6.3.1 Swelling of the composite and the constraining effect of fiber

Swelling co-occurs with water adsorption, as is commonly observed in wood polymers. The composite is assumed to be transversely isotropic. Given the cross-sectional hexagonal configuration of CC, this assumption is a simplification, but acceptable because the difference in elastic properties between the radial and tangential direction (the transverse directions) is minute

when comparing to the difference between longitudinal and transverse directions. The uniaxial swelling strains in transverse and longitudinal directions are shown in Figure 6-4a. The longitudinal swelling remains almost around zero (red hollow circles), in accordance with experimental results of the wood cell wall (Derome et al. 2012), which is attributed to the high stiffness of the cellulose fiber and that moisture does not enter CC and therefore CC is free of swelling.

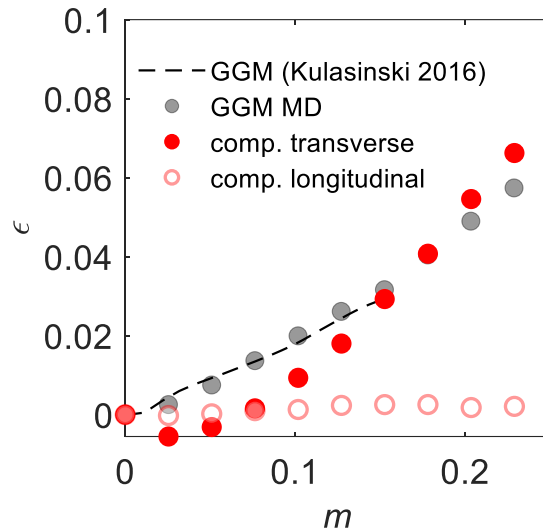


Figure 6-4 Uniaxial swelling strain of composite in longitudinal and transverse directions and of pure GGM.

The transverse direction (red dots) shows a more complex behavior. At low moisture content ( $m < 0.04$ ), the adsorption of water molecules induces a slight shrinkage. In comparison, the swelling strain for pure GGM material (gray dots in Figure 6-4, details of the measurement are described in Chapter 8) does not manifest shrinkage at the same moisture content. This difference may be explained by the fact that in the composite the water molecules are first adsorbed in the existing porosity at the interface, resulting in an additional attraction between CC and GGM and thus shrinkage. The result of the attraction induced by water adsorption is also indicated by a small increment in number density of matrix atoms at low moisture content,  $m < 0.1$  range as seen in Figure 6-5b, as discussed below. For  $m > 0.04$ , the system starts to swell with a swelling coefficient higher than that of the pure GGM. The limited longitudinal swelling is compensated by the enhanced transverse swelling.

## 6.3.2 Composition and configuration of the interphase

### 6.3.2.1 Enrichment of matrix and water atoms at the fiber-matrix interphase

As introduced in the method section, the water molecules are introduced to the system which is then relaxed to mimic the water adsorption process. After relaxation, the distribution of water molecules is determined, i.e. number density ( $\rho_N$ ) as a function of the distance to the CC surface

( $d_{cc}$ ). As shown in Figure 6-5, both the number density for matrix (solid line) and water (dashed line) starts from zero at zero distance, meaning that no penetration of water or matrix into CC fiber happens, in line with experimental reports (Frey-Wyssling 1954; Belbekhouche et al. 2011). The number density of matrix and water atoms quickly increases to a maximum value at the interphase and then reaches a plateau value at an approximate distance  $d_{cc} > 1.5$  nm. This means that the CC surface casts an influence over the distribution of matrix and water atoms, where the density of the matrix increases fast when moving from the interface to the matrix. At some distance from the interface a densification or enrichment of the matrix is seen, although the influence rapidly decays afterwards.

It should be noted that the maximal density of water molecules is slightly closer to CC than the maximal density of matrix atoms (Figure 6-5a), meaning that there is a porosity within the interphase accessible to water molecules. With increasing moisture content, the number density of matrix, both at interface and in bulk, decreases (Figure 6-5b), while the number density of water increases, meaning that the matrix is swelling and the extra porosity is filled with water molecules.

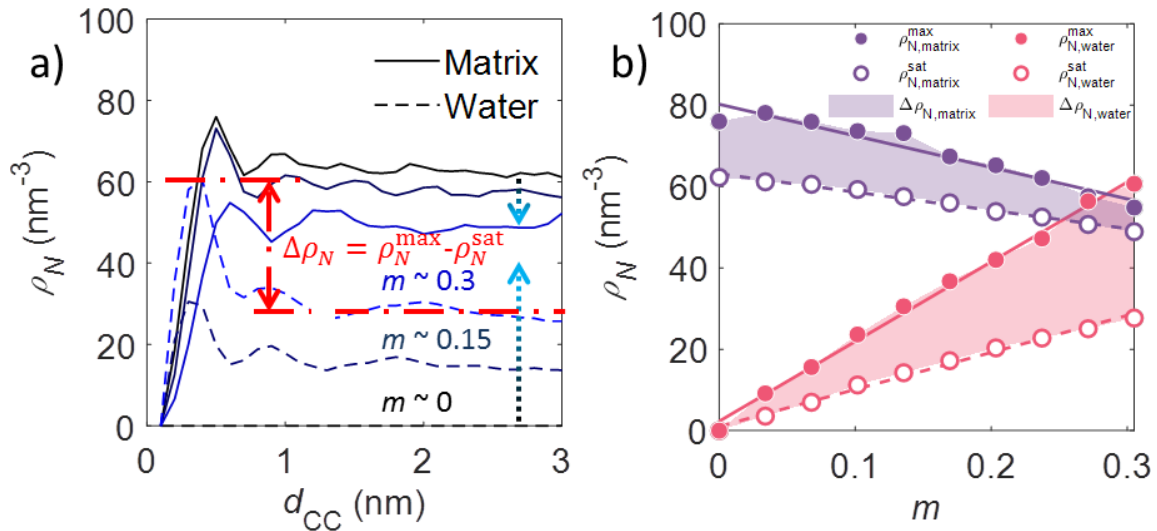


Figure 6-5 a) Number density ( $\rho_N$ ) of matrix and water atoms as functions of the distance to CC surface ( $d_{cc}$ ). b) Interface enrichment ( $\Delta\rho_N$ ) of matrix and water atoms.

The enrichment of matrix and water atoms at the interface can be quantified by a metric, the number density enrichment  $\Delta\rho_N$  at the interface which is the difference between maximum value of  $\rho_N^{max}$  and the number density far away from the CC surface  $\rho_N^{sat}$ , and is shown in shaded areas in Figure 6-5b. For the matrix, the interface enrichment of matrix slightly decreases with moisture content, while the interface enrichment of water increases strongly with moisture content. This means that, with increasing average moisture content, more and more water will relatively be located at the interface, and thus water has a stronger tendency to bind with the CC surface. The thickness of the



enrichment zone, indicated by the width of the first peak, of matrix is larger than that of the water. This is probably due to the larger molecular size of polymer. While water consists of three atoms that is free to adapt to the influence of CC, polymers consist of much larger size and therefore convey the influence of CC to a longer range.

### 6.3.2.2 Orientation of GGM chains at the interface

To characterize the orientation of GGM monomers, Herman's orientation function is used. The HOF values with respect to the three principal axes at two moisture content levels,  $m = 0$  and  $0.3$ , are shown in Figure 6-6. The  $x$  and  $y$  directions refer to the transverse directions, and  $z$  the longitudinal direction. The distance to CC surface,  $d_{CC}$ , is defined as the distance between the center of mass of a monomer to the nearest CC atom. It is noted that the HOF values of 1, 0 and -0.5 denotes perfect alignment, random oriented and perpendicular, respectively. For the monomers closer to the CC surface, the HOF values are relatively far from zero, indicating the formation of oriented and aligned structures. More specifically, the monomers are more aligned along longitudinal direction then with the perpendicular to transverse directions. This is in agreement with various experimental and modeling studies, where the hemicellulose was suggested to form ordered structures aligned to the axial direction of fiber (Åkerholm and Salmén 2001; Stevanic and Salmén 2009), due to the influence of the regular crystal structure of cellulose fiber. In contrast, further from the surface, more exactly at  $d_{CC} > 1$  nm, the HOF values remain close to zero, indicating the random orientation of monomers in the bulk matrix. It is noted that the monomers of the dry case are more aligned than those of the wet case, as the HOF values of the dry case are farther from zero. In effect, moisture weakens the matrix making the chains more flexible and also because moisture also partially screens the interaction between CC and GGM, mitigating the influence cast by CC.

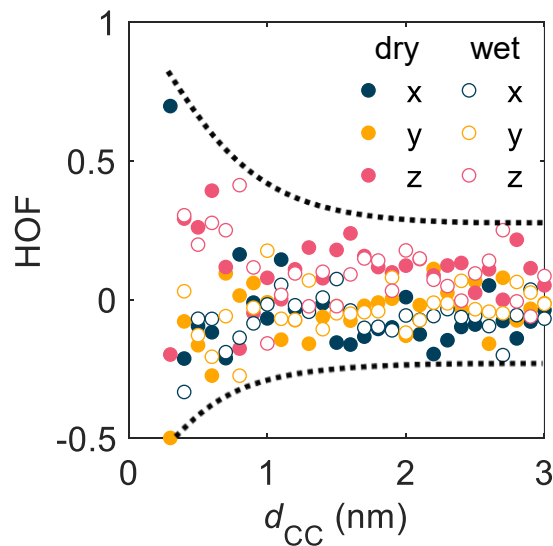


Figure 6-6 Herman's orientation function values of GGM monomers as a function of distance to CC surface.

### **6.3.3 Interface friction mechanics revealed by pulling tests**

#### **6.3.3.1 Thickness of the interphase region**

Pulling tests are employed to investigate the interface mechanics under a series of moisture content levels. The normal stress applied to CC fiber is transferred via shear stresses to the matrix. The region affected by fiber movement is referred to as the interphase and the thickness of this region is called the thickness of the interphase. To quantify the thickness, the velocity distribution of the matrix and water is shown below during pulling. Both the unrestrained (Figure 6-7a and b) and restrained cases are included (Figure 6-7c and d).

For the unrestrained case, the velocity distribution of the composite system (averaged over the first 5 ns) is shown in Figure 6-7a. The magnitude of velocity is denoted in descending order by purple-red-white-green, as displayed by the scale bar. Left and right columns correspond to the matrix atoms and water molecules, respectively. Top and bottom rows are the systems at  $m \sim 0.03$  and  $0.3$ , respectively. The isosurface of 3 nm distance to the CC surface is indicated by the black line. The swelling of the system can be observed through the comparison of the systems at  $m \sim 0.03$  and  $0.3$  in Figure 6-7a.

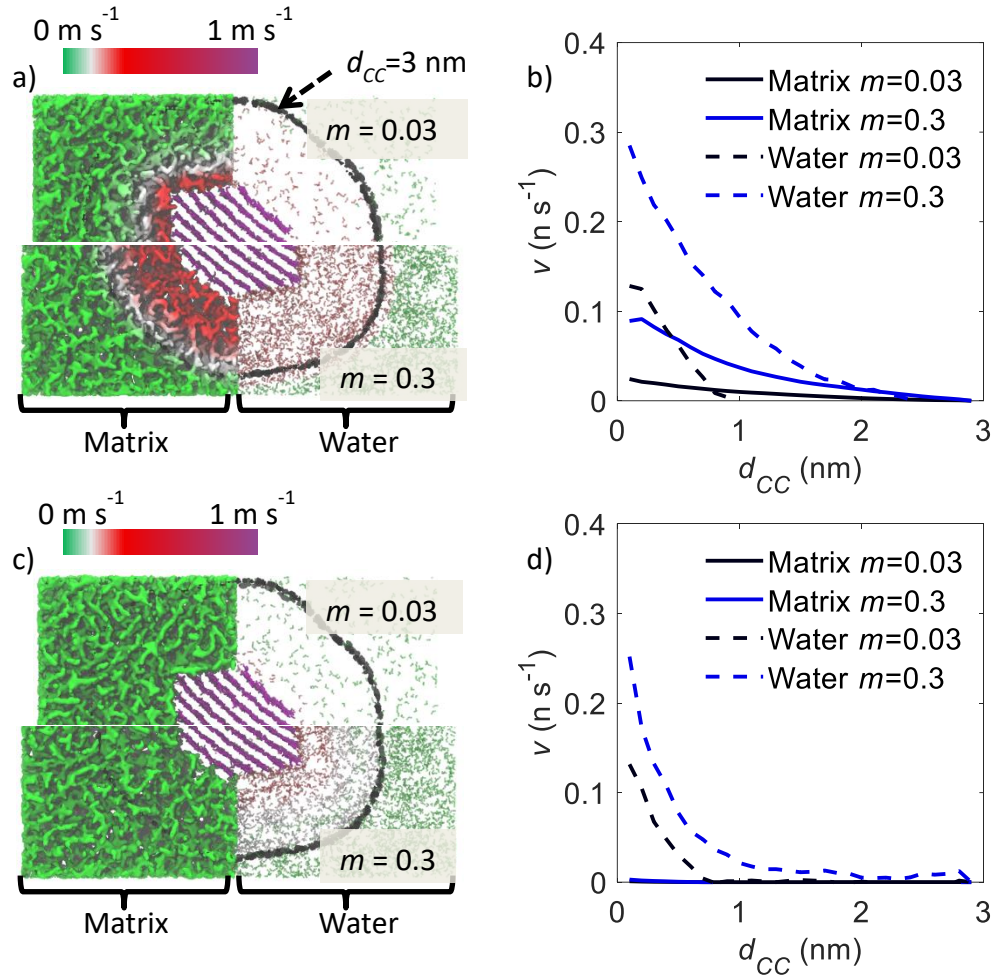


Figure 6-7 a) Velocity distribution in the composite system: CC, unrestrained matrix and water at  $m = 0.03$  (top) and  $m = 0.3$  (bottom). b) Velocity of unrestrained matrix and water atoms as functions of the distance to CC surface under two different moisture contents. c) Velocity distribution in the composite system of the matrix restrained case. d) Velocity of restrained matrix and water atoms.

The velocity distribution is averaged to a one-dimensional curve, i.e. average velocity as a function of the distance to the CC surface (Figure 6-7b). The matrix and water atoms adjacent to the CC move at velocities less than  $0.3 \text{ m s}^{-1}$ , which is slower than the CC fiber ( $1 \text{ m s}^{-1}$ ). The velocity of matrix and water decays fast with distance to the CC. Water moves faster than the matrix, because matrix atoms are restrained by the covalently bonded polymer chains and chain entanglements. For  $m \sim 0.03$ , the influence of fiber movement is confined within  $\sim 1 \text{ nm}$  distance. However, for  $m \sim 0.3$ , as the matrix is weakened by moisture and becomes more compliant, the influence reaches further, i.e.  $\sim 2 \text{ nm}$ . To achieve proper simulation of the interfacial mechanics, the size of the system should be larger than the length scale of the interphase, as is the case in this study.

For the restrained case, the matrix atoms are prevented from moving (solid curves in Figure 6-7d have zero velocity value), while the water molecules can move through the restrained polymer phase. The motion of CC results in a movement of water molecules connected to it. The influence however quickly decays. Velocity of water molecule more than 1 nm away from the cellulose crystal surface is almost zero. In comparison, the restrained case shows a thinner influencing zone than the thick interphase in the unrestrained case.

### 6.3.3.2 Interface frictional stick-slip and stress

To measure the frictional behavior at the interface, the fibers are subjected to pulling along the axial direction, and the shear stress  $\tau$  between fiber and matrix at the interface is recorded as a function of displacement  $d$  as shown in Figure 6-8. The motions of the crystal show stick-slip pattern, where, in the stick phase, the stress accumulates with little increment of displacement and, in the slip phase, the stress is released with a leap in displacement. The friction at the interface thus switches between static and kinetic.

Once again, two cases are considered, one with matrix atoms free to move (Figure 6-8a) and one with matrix atoms restrained (Figure 6-8b). The matrix restrained case corresponds to ‘pure’ interface mechanics, while the matrix unrestrained case allows for the deformation of the matrix. Comparing with the unrestrained case (Figure 6-8a), the stick-slip pattern in the restrained case (Figure 6-8b) is more regular, where the periodicity corresponds to the length of the repeating unit of cellulose chain  $\sim 1.06$  nm.

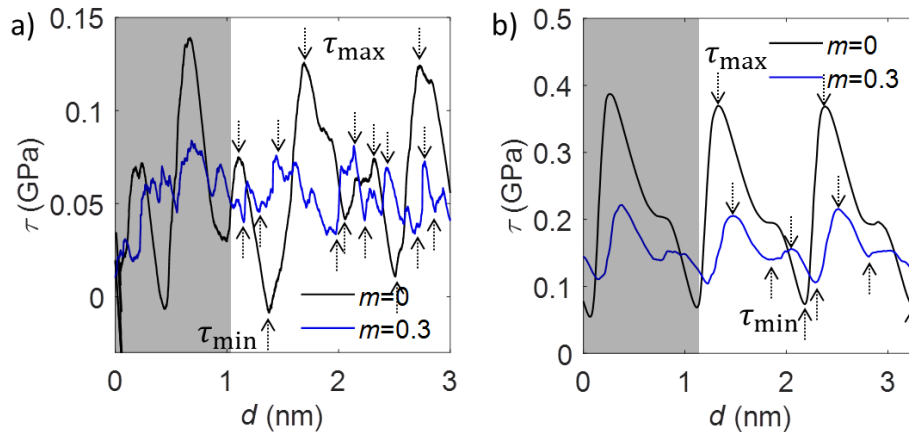


Figure 6-8 Shear stress as a function of displacement for the a) unrestrained case and b) restrained case. Black and blue curves correspond to moisture content  $m \sim 0$  and 0.3, respectively. Gray shade denotes the first cycle.

In Figure 6-8, the local maxima  $\tau_{\max}$  (down arrow) and local minima  $\tau_{\min}$  (up arrow) are annotated. The drop value in shear stress is defined as the difference between maximum and minimum shear stress value:

$$\tau_{\text{drop}}(m) = \tau_{\text{max}}(m) - \tau_{\text{min}}(m) \quad (6-6)$$

The maximum shear stress (Figure 6-9a and b), the minimum shear stress (Figure 6-9c) and their difference (Figure 6-9d), the drop value, are extracted. It should be noted that the peaks in the first cycle are not collected since this first cycle, marked by gray shade, is still influenced by the initial conditions. One dot is averaged over 1~4 stick-slip events. The restrained case corresponds to the pink dots in Figure 6-9 and the unrestrained ones in blue. The maximum shear stress that the interface can sustain is ~ 0.1 GPa in the unrestrained case and ~ 0.4 GPa in the restrained one.

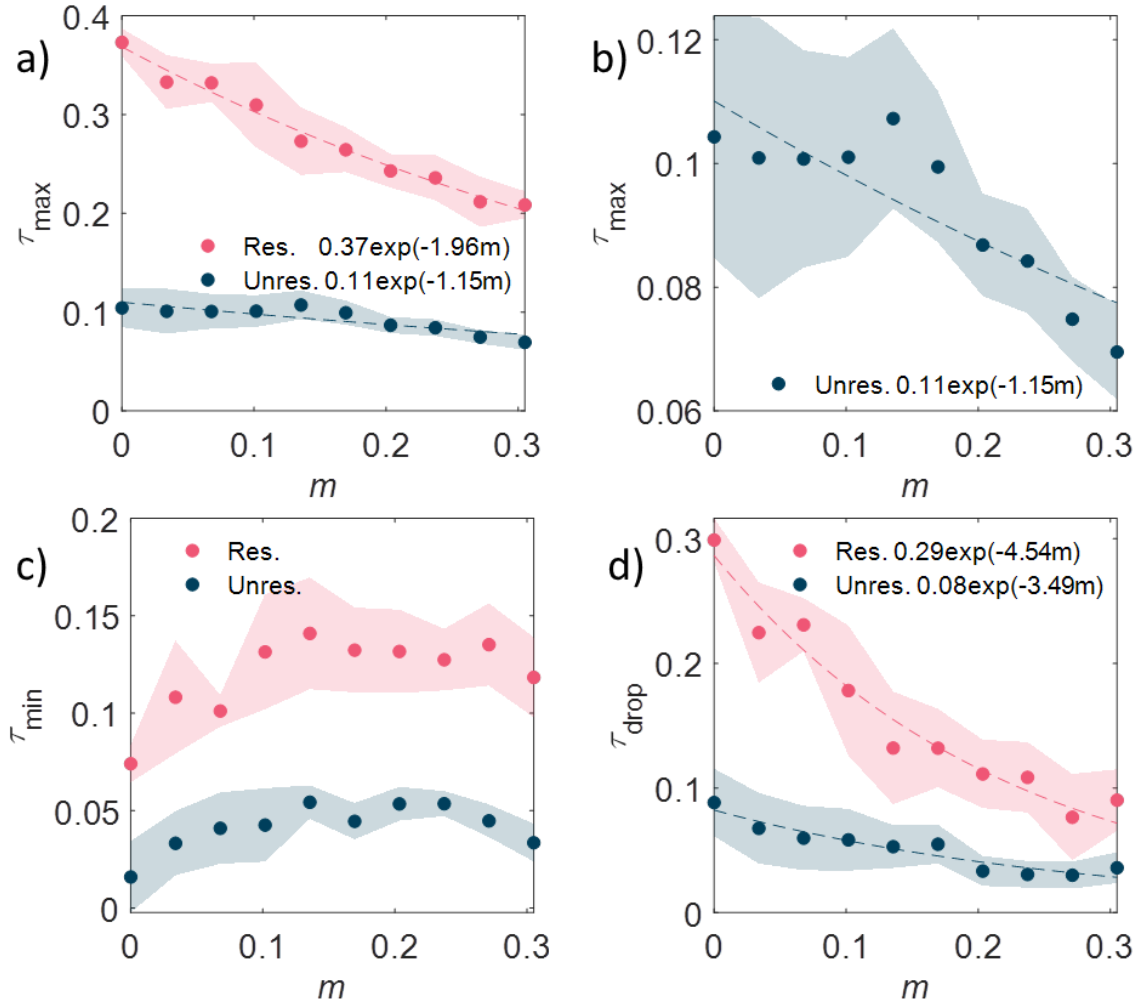


Figure 6-9 a) Maximum shear stress. b) Zoom in on the maximum shear stress for the unrestrained case. c) Minimum shear stress. d) Drop value of shear stress, i.e. the difference between maximum ( $\tau_{\text{max}}$ ) and minimum shear stress ( $\tau_{\text{min}}$ ).

The restrained cases show much higher friction (~ 4 times) than the unrestrained cases for all moisture contents. The major difference between the two cases is that the restrained matrix possesses much higher matrix stiffness than the unrestrained. The difference in maximum shear

stress between the two cases indicates the influential role played by deformation in the interphase region. When the matrix is more deformable, slip occurs at lower shear stress. The maximum shear stress and drop values decrease with increasing moisture content for both restrained and unrestrained cases. This decrease can be explained by the weakening effect by moisture on the interface behavior.

Hydrogen bonds between CC and GGM are expected to play an important role in the stick-slip behavior as well as in the determining mechanics of biopolymer systems. Similar to shear stress, here the areal density of hydrogen bond is determined as a function of displacement with local maxima, local minima and drop values extracted. The maximum shear stress is found to strongly correlate with the areal density of hydrogen bonds between CC and GGM (Pearson correlation coefficient  $r > 0.99$ ) for both unrestrained at high moisture range (Figure 6-10a) and restrained cases over the full moisture range (Figure 6-10b). With increasing moisture content, the areal density of hydrogen bonds decreases for both restrained and unrestrained cases. As mentioned above, the restrained case represents friction limited to the interface since the matrix is not deforming. The strong correlation enables estimation of single hydrogen bond force, which is defined as the slope of the dashed line in Figure 6-10b, i.e.  $f_{HB} \sim 1.4 \text{ E}^{-10} \text{ N}$ . When the interphase is deformable, the single hydrogen bond force is of much lower value, i.e.  $f_{HB} \sim 6.7 \text{ E}^{-11} \text{ N}$ , implying the importance of matrix stiffness on maximum shear stress and effective hydrogen bond force. The unrestrained case shows a transition at  $m \sim 0.13$ . With increasing number of hydrogen bonds, i.e. decrease in moisture content, the maximal shear stress increases until a limit is reached. Further increase of the number of hydrogen bonds does not strengthen the interface anymore, and the one-to-one relation between HB and maximal shear stress vanishes. The deformation of the interphase cancels out the HB contribution to increase the maximum shear stress.

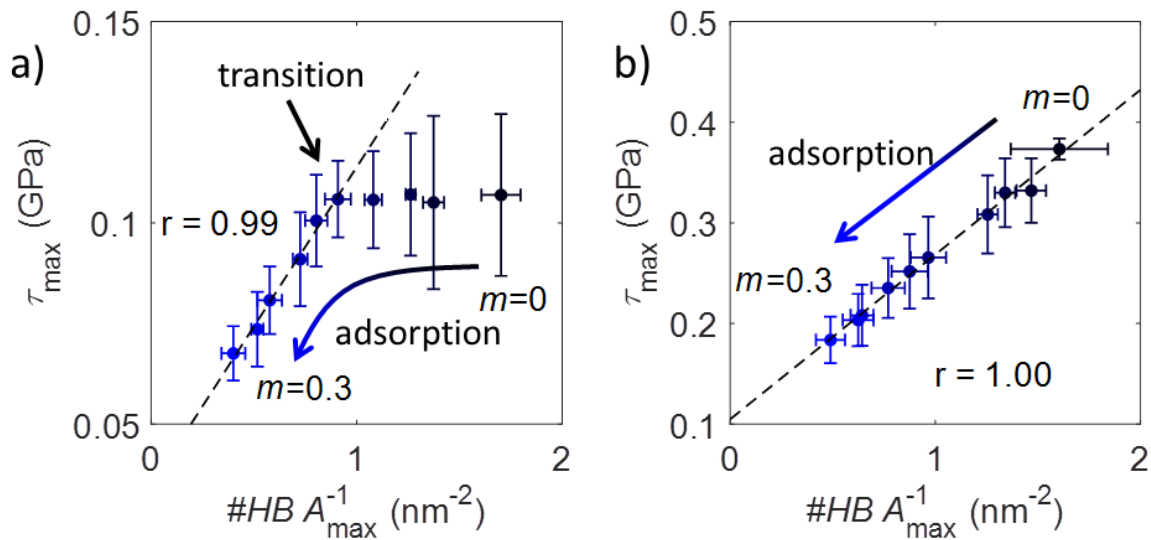


Figure 6-10 Correlation between maximum shear stress and the peak value of areal density of interfacial hydrogen bond: a) unrestrained case; b) restrained case. The gradient in blue color from dark blue to light blue denotes the increase in moisture content from  $m = 0$  to  $m = 0.3$ .

## 6.4 Discussion

The interfacial structure has a profound impact on the composite (Schlaich et al. 2016). Mean-field theory was used to establish an interpretation of the surface enrichment within a hundred nanometer, where the theoretical prediction of the distribution profile was shown to be consistent with experiments (Jones et al. 1989). The enrichment was asserted to be surface energy-driven and thus can be seen as an indication of good compatibility between fiber and matrix. The CC-GGM interaction will be further discussed in Chapter 8. The thickness of the interphase can be measured by nanoindentation tests of atomic force microscope, and is found to be linearly related to the diameter of the crystalline fiber (Pakzad et al. 2012). Cellulose nanocrystal of diameter  $\sim 4$  nm corresponds to the thickness of interphase of less than 5 nm, which is in agreement with the current study.

The CC surface is highly charged because of the abundant hydroxyl groups, and therefore atoms with counter charges will be attracted towards the surface and consequently form the surface enrichment. The thin layer of attracted counter-charges is widely acknowledged in colloidal science, termed as electric double layer (Bockris et al. 1963). The attraction is so strong that the surface-confined atoms travel together with the CC surface, which is indicated by the velocity profile Figure 6-7, where velocity of matrix (in case of unrestrained) and water is much higher close to the CC surface. As a result of the rich polar hydroxyl group of CC surface, though both matrix and water atoms enrich at the interface, the water prevails with increasing moisture content. It can be expected that, for other matrix materials more hydrophobic than GGM, e.g. polyolefin thermoplastics (John and Anandjiwala 2008), the interfacial enrichment of water at the CC surface will be more prominent. In natural composite materials featuring simultaneous high stiffness and toughness, the reinforcement and matrix take tension and shear load, respectively (Ji and Gao 2004). The load is transferred via the interface making the interface properties a critical parameter determining the overall mechanical performance of the composite. The surface enrichment of water should be reduced to improve the interface performance. One remedy is acetylation to make the CC surface less hydrophilic.

Since each hydrogen bond provides a certain amount of force, it is optimal to enhance the specific surface area, the ratio of surface area to the total mass, to achieve better mechanical performance for the same content of reinforcement. Natural reinforcements, such as mineral platelets in bones, nacre and tooth, as well as cellulose crystal in wood, are all of nanosize, a size maximizing the specific surface area.

## 6.5 Conclusion

This chapter characterizes the mechanics of the most common interface in wood cell wall composite, i.e. the interface of CC fiber to hemicellulose GGM matrix. A two-component composite atomistic model is built under full hydration range. Anisotropic swelling is identified, while the composite is much constrained along the axial direction of CC fiber and shows small swelling. Along the transverse directions, the composite first shrinks, as water fills the initial porosity exerting net attraction, and then swells. Surface enrichment of matrix and water are observed, and as the moisture content increases, water prevails against matrix indicating the stronger affinity of water to CC. Results of Herman's orientation functions reveal the ordered structure of GGM matrix in vicinity of the interface, where GGM monomers are more aligned to the axial direction of cellulose fiber, leading to the formation of an interphase with certain thickness. Such alignment is mitigated by moisture.

Pulling tests are carried out to characterize the shear strength of the interface. Stick-slip motions are found, similar to the CC-CC interfaces in the previous chapter. Moisture is shown to strongly influence the interface mechanic by interrupting the interfacial hydrogen bonding. The deformable matrix displays lower shear strength comparing with non-deformable matrix. The correlation between the number of hydrogen bonds and the interfacial friction suggests the force rendered by a single HB to be  $1.4 \text{ E}^{-10} \text{ N}$ , a value very close to what was found in the previous chapter. The restrained case, a hypothetical case with the matrix being restrained represents the case where the interface mechanics is not influenced by the deformation of the matrix. On the contrary, the unrestrained case, the matrix being deformable, represents the combined behavior of interface and interphase deformation. The restrained case shows regular stick-slip pattern with high peak stresses, whereas the regularity and peak stresses both degrades for unrestrained case. The peak stresses are lowered by the weakening effect at higher moisture contents.

Combining this and the previous chapters, two of the most important interfaces of wood cell wall S2 layer are characterized under full hydration range. The results provide vital information for the understanding of wood hygromechanics, and meanwhile contribute to the utilization of extremely promising natural fiber, cellulose crystal, reinforced material. Both CC-CC and CC-GGM interface shows moisture-dependency, i.e. water adsorption weakens the interface and lowers the shear strength for several times. Such behavior will be upscaled into a finite element model and related to the moisture-induced shape memory effect in the next chapter.



## **Chapter 7 Towards Unraveling the Moisture-Induced Shape Memory Effect of Wood: The Role of Interface Mechanics**

This chapter investigates the mechanism of moisture-induced shape memory of wood, a phenomenon that fascinated wood scientists for ages and yet not completely understood. Using finite element modeling, a possible mechanism is explored for the moisture-induced shape memory of wood cell wall stemming from the interface mechanics, a factor that has been much overlooked. The interface mechanics extracted from molecular simulations in Chapters 5 and 6 are implemented into different mechanical models solved by finite elements, representative of three configurations present in the cell wall. These models incorporate moisture-dependent elastic moduli of matrix and of the interface matrix and fiber. One configuration, named mechanical hotspot with fiber-fiber interface, is found to particularly strengthen the shape memory effect. Systematic parametric studies reveal that the interface mechanics could well be at the origin of shape memory: upon drying an interface, it becomes strong and stiff, and the deformation of the composite can be fixed, whereas, when the interface is wet and weak, the frozen deformation cannot be sustained and recovery happens. This work hints at the interface behaving as a molecular switch.

### **7.1 Introduction**

The previous chapters have investigated several important hygromechanical behaviors of wood-based polymers, such as crossover, swelling and weakening. The interfaces present in wood have also been discussed. This chapter deals with another important, yet unexplained phenomenon observed in wood, i.e. shape memory effect (SME). Finite element models are built with the constitutive relations upscaled from the atomistic investigations of the previous sections.

Shape memory effect, also referred to as hygrolock-springback (Saifouni et al. 2016; Hajihassani et al. 2018) or set-recovery (Laine et al. 2016), is one of the most intriguing mechanical effects. Wood keeps its deformed shape when being dried under maintained deformation even after the removal of the mechanical loading, called fixation, and it recovers the original shape after being wetted again, called here recovery. Wood fixation is frequently sought, for example, the shape stability of bent wood used in curved furniture. On the other hand, the tendency to recovery may pose difficulties, for example, in the case of densified wood that may recover some volume upon water adsorption and be weakened (Navi and Pizzi 2015). A better understanding of the mechanisms of SME can be helpful in inspiring the design and fabrication of nature-inspired smart materials, e.g. cell-bundle torsional actuator with memory (Plaza et al. 2013), and in improving the stability of deformed wood (Navi and Pizzi 2015).

It should be noted that SME tends to be confused with shape change effect (SCE). The shape change effect is a common phenomenon of almost all materials. Materials deform as a response to environmental stimuli, such as heat, mechanical loading, magnetic field, light, moisture etc., and the materials change back to its original shape with the removal of the incentives. A typical example

is the hygroscopic swelling of wood, where it expands due to the adsorption of water and shrinks with desorption. This reversible swelling and shrinking feature of plant cell walls is at the foundation of natural actuation, which facilitates the control of critical processes in life cycles, such as the releasing of seeds from pine cones with humidity changes (Dawson et al. 1997) or the self-planting of wheat seeds (Elbaum et al. 2008). In contrast to SCE, SME implies that the deformation of materials is maintained even after removal of the environmental stimuli, and the original shape is only recovered when certain conditions are satisfied. The SME is similar to SCE in the sense that the materials finally recover their original shapes, whereas the maintenance of the deformation at an intermediate state is the characteristic of SME.

Though the SME of wood has been discussed in numerous reports, many observations remain unexplained. The SME can be observed at different scales under different conditions. On timber level, the SME was attributed to the multi-scale hierarchical structure of wood tissue (Ugolev 2014). However, more and more evidences are implying that it is highly possible that the SME of wood originates from cell wall material. For example, Plaza et al. (2013) observed a memory effect in nano-indentation, where the indented dry middle lamella fully recovers after being wetted with a drop of water. In another example, Derome et al (2012) observed half-cell moisture-induced shape recovery after a cell was mechanically deformed. The SME can be triggered by various stimuli, such as temperature (Ugolev 2014), moisture (Ugolev 2014) and temperature-moisture combined (Navi and Heger 2004; Jakes et al. 2014). In terms of loading conditions, there are stress memory and strain memory (Ugolev 2014). It is noted that high temperature may induce a series of chemical reactions, e.g. pyrolysis, which is out of the scope of this study. Instead, this study focuses on the moisture-induced SME.

Since the late 18<sup>th</sup> century, European wood engineers actively seek to eliminate the SME to improve the dimensional stability of densified wood (Inoue et al. 1993). The vast majority of available literature covers either the practical solution of reduction of springback of densified wood or the phenomenological description of the macroscopic behavior of wood specimen, leaving the microscopic mechanism of moisture-induced SME of wood barely elucidated. For example, Colmars et al. developed a one-dimensional discrete formulation of the hygrolock model that can describe the mechanical behavior with humidity cycles (Colmars et al. 2014). The general mechanism for shape memory behavior of polymers (composites) is relatively clear, where several micro-mechanisms are essential for a material to show SME. These mechanisms are: 1. storage of potential energy for later recovery; 2. a molecular switch that kinetically locks the system at deformed state. To this day, for wood, only speculations or hypotheses address these mechanisms. A major difficulty lies in the fact that it is experimentally challenging to gather information about molecular interactions at nanometer scale for such sophisticated composite structure, from where the SME likely originates. A numerical study is warranted to complete experimental investigation by considering the system nanoscale features that could be involved in SME.

The modeling of wood cell wall material can be overwhelmingly complicated because of the multi-component, heterogenous and hierarchical structure, in addition to the rate-dependent response to mechanical loading and the coupled deformation-sorption behavior. The shape memory behavior of wood involves multiple mechanical and sorption loading/unloading steps. The possible cause of the complex behavior can be multiple. Initially, the swelling induced deformation and the alternation of hydrogen bonded state was suspected to be at the origin. When dried at the deformed state, the reformation of hydrogen bonds makes the material stiff and maintains the deformation. When wetted again, the structure swells possibly driving the shape to recover. One critical missing point is the memory. While the shape changes as a response to wetting, how should the structure know which direction to go? The information of the initial shape is stored somewhere that is not revealed. Glass transition was suspected to play a role in switching the structure between rigid and flexible states, unfortunately also not hinting at any possible explanation of the information of initial shape. The mechano-sorptive effect, i.e. the coupling between deformation and sorption, was the next subject of discussion. But the deformation induced by mechanical loading is rather elastic, meaning that with the removal of loading, the shape will immediately recover without observable fixation. These considerations lead to the rough conclusion that the matrix alone could not explain the full story of SME. The cellulose fibers then come in sight. Recent observations of plant cell wall suggest that the fiber come into contacts with each other at certain positions forming possible connected fiber meshes (Park and Cosgrove 2012b; Zhang et al. 2014, 2016; Xiao et al. 2016a). The fibers contacts can be seen as a type of interface formed between fibers, while the fiber-matrix interface prevails in cell wall material. These factors have been largely overlooked and might provide a possible mechanism for SME.

In this study, a finite element model of a prototype wood cell wall layer is built, with the hygromechanical properties of the interfaces obtained from atomistic simulations of the two previous chapters. The other mechanical parameters needed for finite element model are taken from atomistic works from literature. A loading protocol, applied to evaluate the moisture-induced SME, questions two main aspects: whether an imposed deformation in wet condition can be sustained under dry condition, and whether the original shape can be recovered when wetted again.

## **7.2 Method**

Three different systems, representing the organization of the S2 cell wall, are simulated with continuum mechanics. The computational domains, the material properties, the boundary conditions and the loading protocol are presented.

### **7.2.1 Geometry of the model**

Wood cell wall S2 layer features a complex hierarchical ultrastructure for which a definitive understanding of its material arrangement is still under debate. The S2 layer, the thickest layer of cell wall, is commonly treated as a unidirectional fiber-reinforced composite with the cellulose fibers aligned at an angle, called microfibril angle (MFA), to the axial direction of the cell, as

illustrated in Figure 7-1a (Qing and Mishnaevsky 2009). Some studies assume that hemicellulose chains connect the cellulose fiber, forming the so-called tethered network (Da Silva and Kyriakides 2007; Huang et al. 2012). Recent observations of plant cell wall suggest that the fibers are not perfectly parallel to each other but rather they may come into contacts either directly or mediated by a monolayer of hemicellulose (Park and Cosgrove 2012b; Zhang et al. 2014, 2016; Xiao et al. 2016a). The contacts of fibers have been referred to as “mechanical hotspots”, a structure that remains to be investigated.

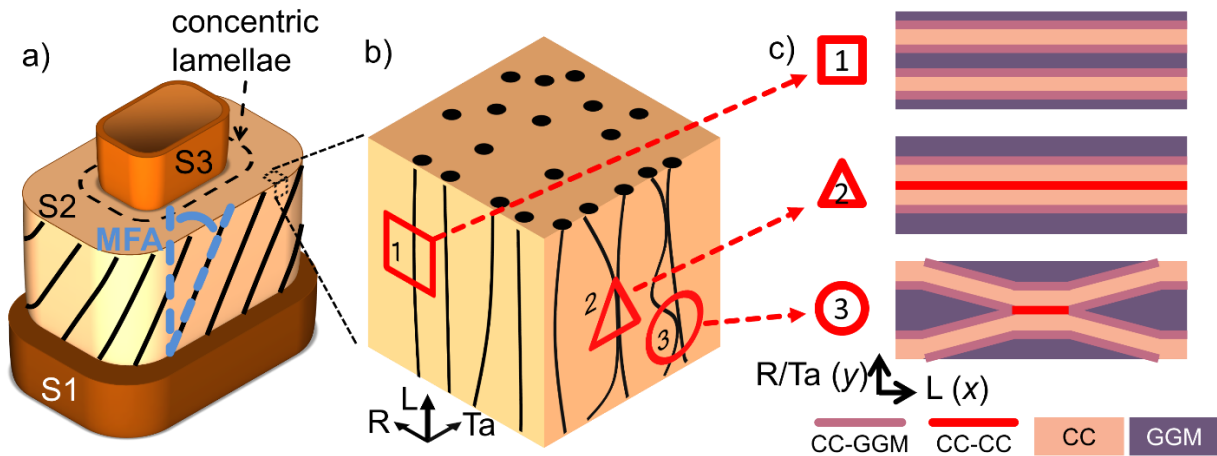


Figure 7-1 Schematic material arrangements in wood cell wall: a) secondary cell wall layers with b) close-up of S2 layer, where lines represented cellulose micro-fibrils and beige the multi-component matrix. c) Schematic representation of the models for subunits with legend for the 4 components.

It should be noted that the S2 material is different in the three directions, i.e. radial (R), tangential (Ta) and longitudinal (L). The currently widely accepted model is the so-called concentric lamella model, meaning that S2 is composed of concentric rings encircling each other, layer by layer, as indicated in Figure 7-1a. The building elements of concentric lamella are cellulose aggregates, with a thickness of ~25 nm, formed by microfibrils of approximately 3 ~ 4 nm in diameter (Fahlén and Salmén 2002; Keplinger et al. 2014; Casdorff et al. 2018). In the tangential plane, the fibers and matrix are closely connected, while in the radial direction, the connection between lamellas is weak. Therefore, it can be assumed that the mechanical hotspots may only be present in the tangential plane while, in the radial plane, the cellulose fibers mainly stay parallel to each other, as shown in Figure 7-1b. Taking these assumptions into account, three subunits are considered as basic building elements of S2 layer, as shown in the dashed square, triangle and circle regions in Figure 7-1b, covering all possible scenarios. The square subunit is cellulose fibers surrounded by matrix. The triangle subunit is where two fibers are in direct contact and are surrounded by matrix. The circle subunit is similar to the triangle one, except that the fibers are not in perfect contacts and are only in contact over a certain length. These subunits are used as the three representative geometries, namely models 1, 2 and 3, as shown in Figure 7-1c. It has to be noted that for simplicity only 2D

models are considered assuming plane stress conditions. The interfaces and materials are represented with lines and bulks, respectively. In model 3, the fibers form an undulant pattern, where the axial direction of the fiber is along the fiber principal axis and parallel to the interfaces. From now on, the longitudinal (L) and transverse (R/Ta) directions will be referred to as  $x$  and  $y$  directions, respectively. In terms of polymers, the fibers are made of crystalline cellulose. The matrix is assumed to be composed only of the hemicellulose galactoglucomannan (GGM), because experimental results suggest that galactoglucomannan is the matrix material most adjacent to cellulose fiber in wood (Salmén and Fahlén 2006).

In the full geometry, the models 1, 2 and 3 of Figure 7-1c are replicated 3 times along both  $x$  and  $y$  directions, to reduce the edge effects. The resulting geometries are shown in Figure 7-2. The total length and height of the model is  $l = 72$  nm and  $h = 36$  nm, respectively. The length chosen to stay close to the experiment report of cellulose nanocrystal length,  $\sim 100$  nm (Guo et al. 2017). The height in principle can be any arbitrary value, while here it is chosen to include 3 repetitions along  $y$  direction. As will be shown further, the size of this specimen is sufficiently large to mimick the SME effect, at the same time sufficiently small from a computational point of view.

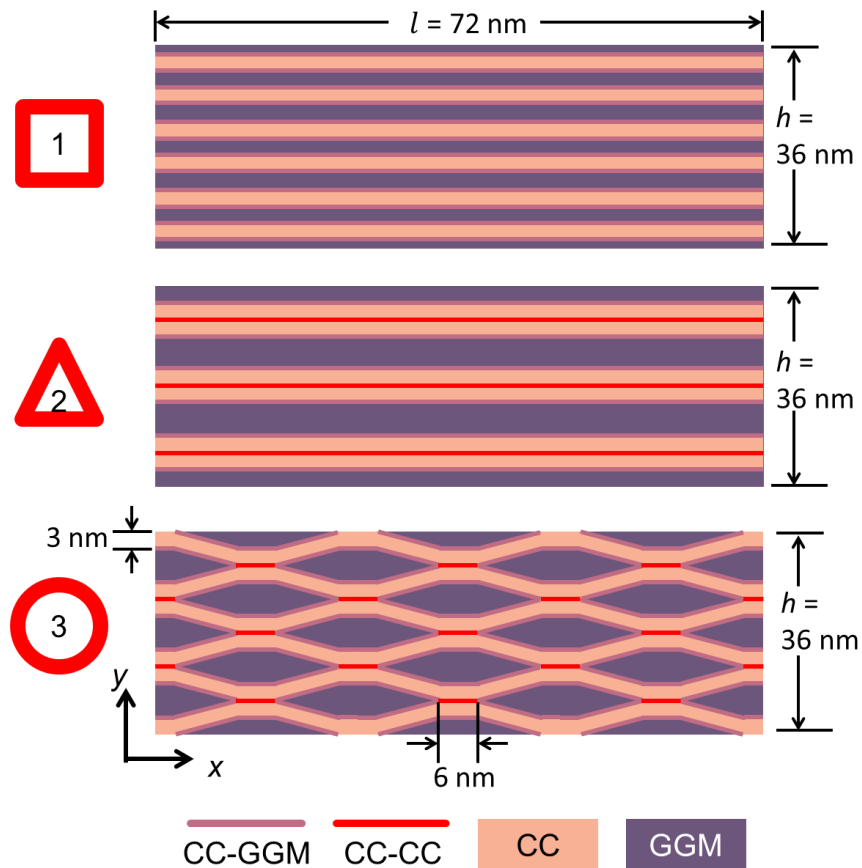


Figure 7-2 Schematic representation of the computational model geometry.

To facilitate the comparison between the three models, the models are made as comparable as possible. The mass ratio of fiber to matrix is 1:1, in line with the experimental reports (Agarwal 2006). The three models are of the same length and height. The cellulose fibers are 3 nm in height (Agarwal 2006). The CC-CC contact in model 3 is assumed to be 6 nm (Cosgrove 2014).

The meshing of model 1 is shown in Figure 7-3 as a sample. The edges are meshed with the rule that the center divisions are 10 times larger than the side divisions. In this way, the regions near the edges are finer meshed producing better accuracy, while the center coarser mesh can save computational costs. This mesh contains 7500 4-noded plane elements and 1200 2-noded contact elements. The other models are meshed similarly. Mesh sensitivity analysis is carried out by applying two times the number of divisions for all the edges resulting in total ~ 4 times more elements. It was found that the yielded results are similar to the results of the coarser mesh.

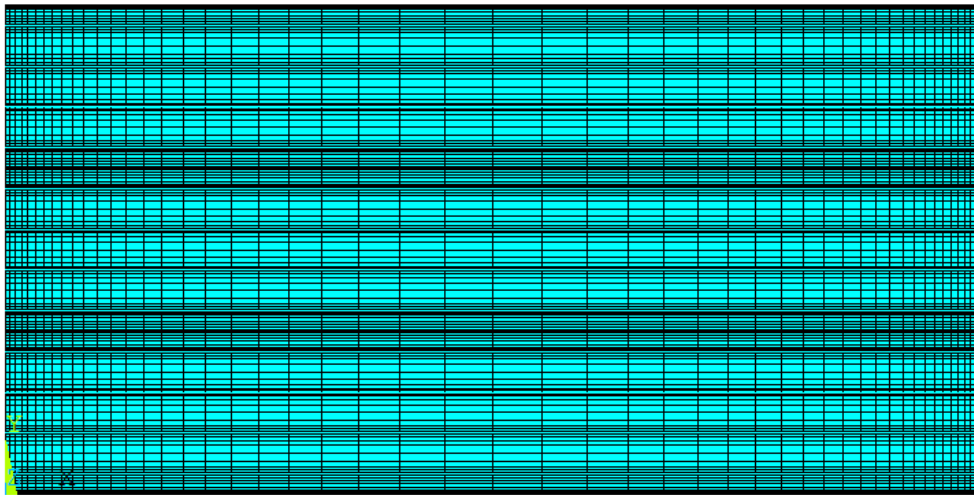


Figure 7-3 Sample meshing of model 1.

It is noted that these FE model geometries do not reproduce a realistic cell wall structure, which is three-dimensional, much more complex and irregular. These models aim at capturing the major moisture-related responses thought to be significant to play a role in SME. The models represent three basic probable configurations of what can be thought as a representative volume element of the S2. Much care is taken towards the right implementation of swelling of matrix, moisture weakening of matrix and interfaces, as described in the following section.

### **7.2.2 Constitutive laws of the components and the interfaces**

While the mechanics of wood cell wall material is complex, possibly involving rate-dependent viscoelasticity and fracture failure when subjected to load, the study of the three configurations is limited to the hygro-elastic response involving stick-slip in the interfaces, but without permanent material failure nor plastic deformation. The moisture-related mechanical features of the components and their interface are extracted from MD and inputted into FE models. The FE model here consists of two materials, namely CC and GGM, and two interfaces, namely CC-GGM and

CC-CC. The two materials are modeled by a linear elastic material model with hygroscopic swelling, as described in the following equation:

$$\varepsilon = \varepsilon_{\text{elastic}} + \varepsilon_{\text{hygroscopic swelling}} = C\sigma + \beta m \quad (7-1)$$

where  $\varepsilon$ ,  $C$ ,  $\sigma$ ,  $\beta$  and  $m$  are strain, compliance, stress, hygroscopic swelling coefficient and moisture content, respectively. The mechanical properties of CC are not dependent on moisture, as many experimental and simulation studies suggested (Frey-Wyssling 1954; Belbekhouche et al. 2011). Thus, the elastic properties of CC are fixed values (constants) independent of moisture content of the composite system and since CC does not adsorb nor swell, the hygroscopic swelling coefficient is 0. The stiffness of CC in R and Ta directions vary a lot (11.3 GPa and 72.6 GPa (Kulasinski et al. 2014b)). Since the study is in 2D, the CC is assumed to be transversely isotropic and the average of stiffness in R and Ta directions are taken as the stiffness in the transverse direction (T). The elastic behavior of a transversely isotropic fiber is described by five mechanical properties. The elastic properties are drawn from literature (Mark 1967; Nakamura et al. 2004; Kulasinski et al. 2014b; Chen et al. 2015) and listed in Table 7-1. GGM is an isotropic material that interacts with moisture and therefore can be represented by Young's and shear moduli and swelling coefficient based on the MD measurement from the previous work from our research group (Kulasinski et al. 2015d), as summarized in Table 7-1.

Table 7-1 Elastic properties of CC and GGM (Mark 1967; Nakamura et al. 2004; Kulasinski et al. 2014b, 2015d; Chen et al. 2015).

|     | Young's modulus (GPa)     |       | shear modulus (GPa)       | Poisson's ratio |            | swelling coefficient |
|-----|---------------------------|-------|---------------------------|-----------------|------------|----------------------|
|     | $E_L$                     | $E_T$ |                           | $\nu_{LT}$      | $\nu_{TT}$ |                      |
| CC  | 150                       | 42    | 4.4                       | 0.38            | 0.48       | $\beta = 0$          |
| GGM | $E(m) = 5.4 \exp(-7.2 m)$ |       | $G(m) = 1.8 \exp(-5.7 m)$ | -               |            | $\beta = 0.49$       |

With the elastic properties in the table, the other elastic properties of isotropic material can be calculated using the following equations from continuum mechanics:

$$K = \frac{EG}{3(3G-E)} \text{ and } \nu = \frac{E}{2G} - 1 \quad (7-2)$$

For transversely isotropic material, the following equations apply:

$$\frac{\nu_{LT}}{E_L} = \frac{\nu_{TL}}{E_T} \text{ and } G_{TL} = G_{LT} \quad (7-3)$$

There are two types of interfaces between the materials, namely CC-CC and CC-GGM interfaces. The interfaces can be described by a friction model where the friction exerted through the surface is a function of moisture content. In chapters 5 and 6, it is found that the interface shows a typical stick-slip behavior showing a sawtooth signature, which weakens with increasing moisture content. The study of SME, however, assumes a simplified interface model where the interface sticks, when the shear stress is below a friction threshold equal to the maximum shear stress. Sliding occurs when the shear stress at the interface equals the maximum shear stress. With increasing sliding, the shear stress remains constant equal to the maximum shear stress. The maximum shear stress is dependent on the level of moisture. Friction is assumed to be independent of the normal pressure.

Sliding along the direction parallel to the interface is permitted, but separation along direction perpendicular to the interface is not allowed. The moisture dependent interface properties are summarized in Table 7-2. These interface laws are implemented using contact elements in FEM. The finite-element software used is Ansys mechanical APDL 16.2. The bulk material is modeled using PLANE182 element. The contact elements are TARGE169 and CONTA171.

Table 7-2 Interface laws.

|        | parallel direction                    | perpendicular direction |
|--------|---------------------------------------|-------------------------|
| CC-GGM | $\tau_{\max}(m) = 0.11 \exp(-1.15 m)$ | non-separation          |
| CC-CC  | $\tau_{\max}(m) = 0.45 \exp(-3.95 m)$ |                         |

### 7.2.3 Boundary conditions and loading protocol

The three models bear the same boundary conditions and loading protocol. In wood steam bending in practice a form is used. Inspired by this, the model is shown in Figure 7-4a, where the specimen is mounted on top of a cylindrical support and a displacement or load is applied on the ends (Ugolev 2014). There exists a symmetry plane and therefore only half of this model is used as the computational domain. This setup is modeled with FEM and it is found that the results of this setup correspond to the results of the FE model with boundary conditions as shown in Figure 7-4b. Roller constraint is applied on the left edge, allowing only transverse displacement. The left bottom node is fixed, which is also used as the origin of the coordinate system. It is noted that cylinder support was also tested, and the results are identical with the point support. Vertical point load is applied by imposing a displacement  $d$  along  $y$ -axis on the free right top node. Moisture affects the system via the constitutive equations of the materials and interfaces causing swelling and weakening of the GGM as well as weakening of the interfaces.

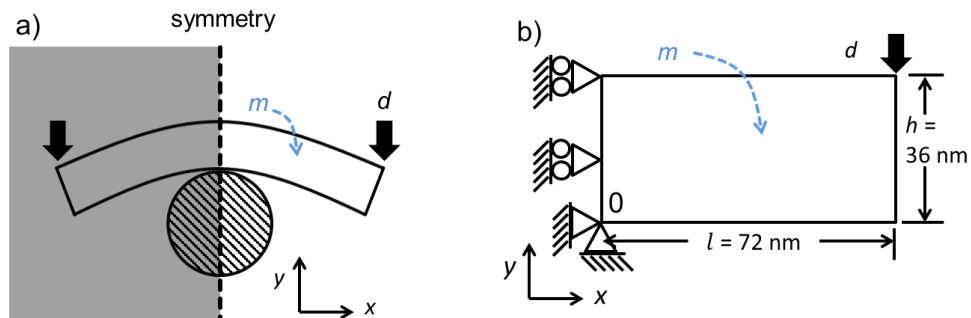


Figure 7-4 a) Schematic of loading condition. b) Boundary conditions in finite element modeling.

Based on experimental studies that demonstrated the recovery of half-cell wall from the deformed state (Derome et al. 2012) and at macroscopic timber scale (Ugolev 2014), a loading protocol is proposed. The mechanical and moisture loading protocol can be summarized as a 7-step procedure: initial state with null loading (N), uniform wet state (W), mechanical loading under wet condition imposing displacement (WS), dry while maintaining the displacement (S), remove displacement



(N'), wet again (W') and dry again (N''). The 7 steps are illustrated in Figure 7-5. In the wet states, i.e. W, WS and W', the moisture content of the system is assumed to be uniform and equal to  $m = 0.3$ . In the mechanical loaded states, i.e. WS and S, the vertical displacement applied is  $d = -7.2$  nm, corresponding to a deflection ratio  $\gamma = d/l$  of 0.1. The deflection ratio in the experimental shape memory study is usually high, e.g. close to 1 (Ugolev 2014). However, here a smaller value is used to improve convergency and keep the material deformation within the elastic range. The N, N' and N'' correspond to the initial, deformed and final states respectively. The S state is the state with the largest deformation.

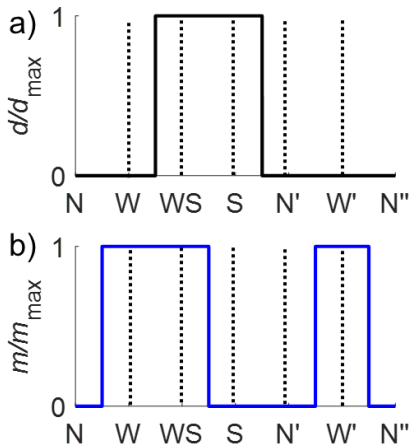


Figure 7-5 Loading protocol with co-occurring: a) displacement loading and b) moisture loading.

### 7.3 Shape memory mechanism

#### 7.3.1 Shape memory effect in the three models

The three models are subjected to the 7-step loading protocol. Qualitatively similar behaviors are observed in all the systems. First, the stress distributions and deformations in the 7 states are discussed for model 3. The results of models 1 and 2 will be described later and compared with the results of model 3.

The snapshots of the 7 states of model 3 are included in Figure 7-6, and the color denotes normal stress  $\sigma_x$  in Figure 7-6a and shear stress  $\tau_{xy}$  in Figure 7-6b. Figure 7-7 is a of the center region of Figure 7-6b. The displacements are scaled by a factor of 2 for the sake of clarity. The dashed line indicates the  $y = 0$  plane.

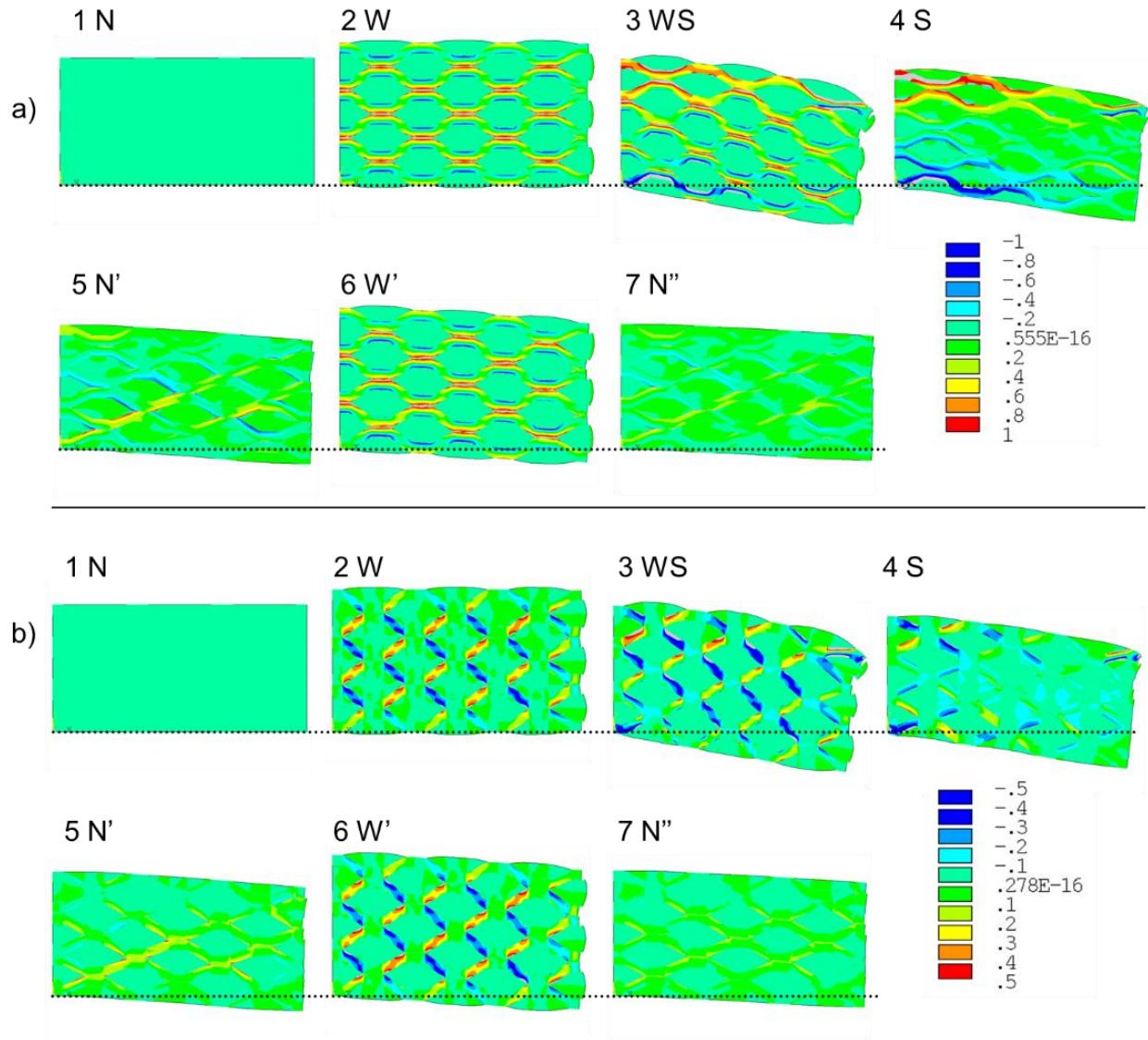


Figure 7-6 Distribution of the normal stress  $\sigma_x$  (a), shear stress  $\tau_{xy}$  (b) and deformation (a-b) of the 7 states for model 3. The color denotes the normal and shear stress level in unit of GPa.

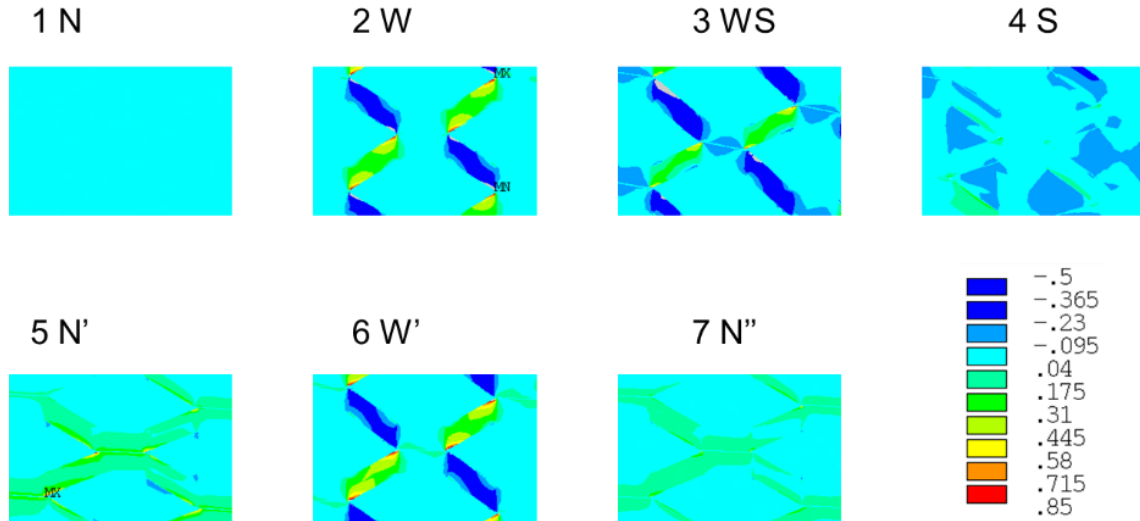


Figure 7-7 Zoom-in view of deformation and shear stress of the center of model 3. The colors denote shear stresses in unit of GPa.

It is observed that during wetting the matrix swells in state 2-W, while the CC phase does not. This differential swelling leads to internal stresses, tensile in the CC phase, compressive in the GGM matrix, and shear stresses in the material and at the interfaces. When loading in the wet state (3-WS), the normal tensile stresses increase in the top region, while compressive normal stresses at the bottom due to bending. The shear stresses also increase in the interface between CC-GGM and CC-CC, reaching the maximal shear stress at some locations where sliding occurs. CC-GGM is a weaker interface than CC-CC, so sliding will start at CC-GGM interfaces, followed by sliding at some CC-CC hot-spots. Note that the sliding at the interfaces results in a differential deformation visible at the right end of the specimen. When drying and reaching the 4-S state, the matrix shrinks and the shear stresses reduce due to a reduction in differential deformation between matrix and CC phase. When unloading to the state 5-N', some residual shear stresses and deformations remain in the specimen meaning the specimen keeps partially its deformed state, referred to as fixation. When wetting again the specimen (6-W'), the matrix swells again, and again differential stresses between CC and matrix appear, but it is observed that also the vertical deformation decreases since some slipping back may occur at the interfaces. The decrease in deformation after wetting is called recovery. Finally, when the specimen is dried again (7-N''), some residual stresses and permanent deformation may remain in the specimen.

Figure 7-8 and 9 show the distributions of the normal stress  $\sigma_x$  and shear stress  $\tau_{xy}$  and deformation for the 7 states for models 1 and 2. Recall that model 1 is composed of several layers of CC and GGM with CC-GGM interfaces. Model 2 is composed of layers of CC-CC and GGM, showing both CC-CC and CC-GGM interfaces. Models 1 and 2 show similar behavior as for model 3 over the 7 states. However, these laminated structures are much less stiff as compared to model 3 with undulating fiber mesh. As a result, the point load in models 1 and 2 to reach the same displacement

at the right end are lower than in model 3. Consequently, also the normal and shear stresses in models 1 and 2 are much lower than in model 3. Due to the lower shear stresses at the interfaces, less sliding will occur in models 1 and 2. This means that model 3 with stiff undulating fiber mesh with CC hotspots promotes the interface sliding, and as will be shown below, leads to the largest SME, while the SME in models 1 and 2 is more limited.

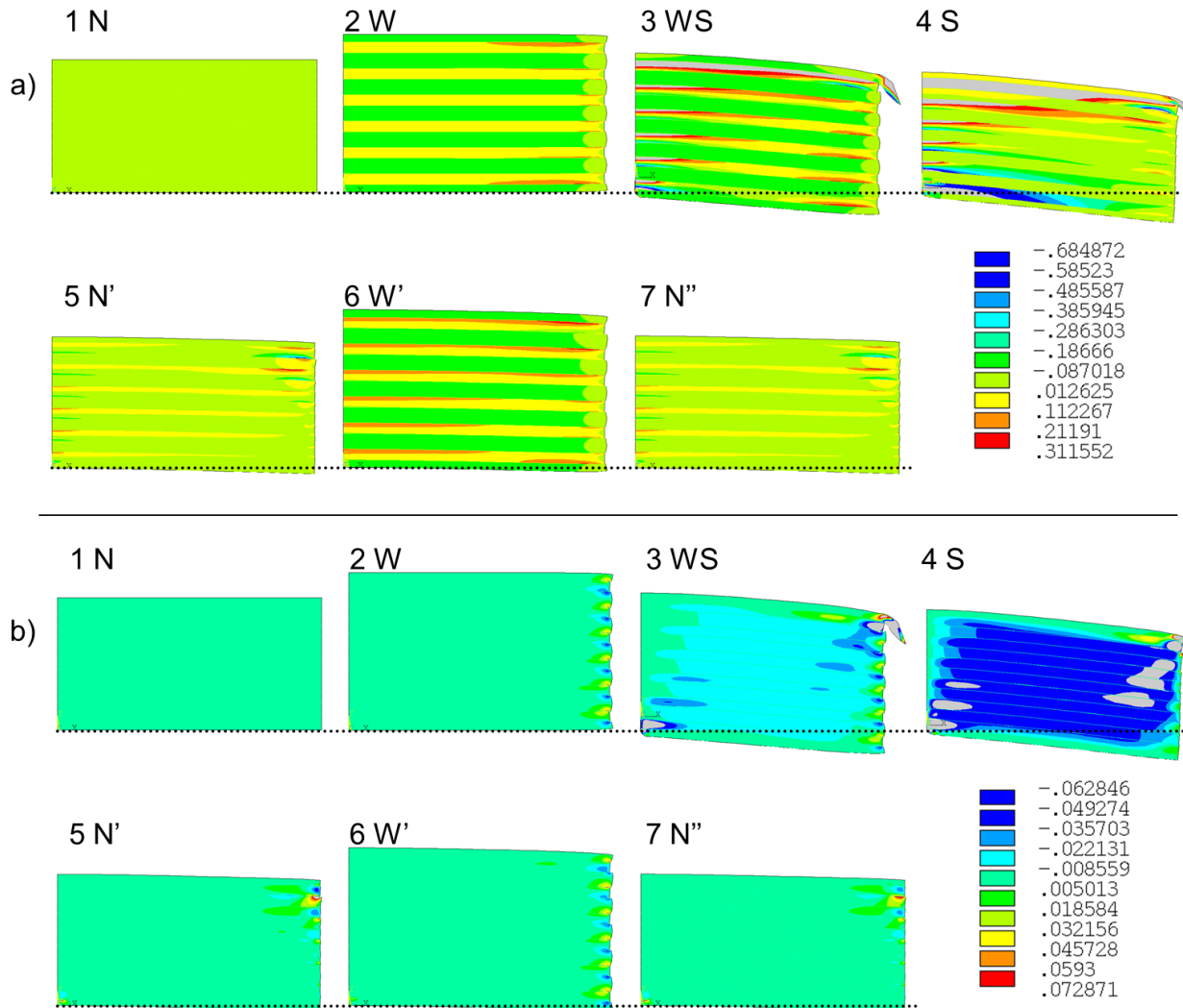


Figure 7-8 Distribution of the normal stress  $\sigma_x$  (a), shear stress  $\tau_{xy}$  (b) and deformation (a-b) of the 7 states for model 1. The color denotes the normal and shear stress level in unit of GPa.

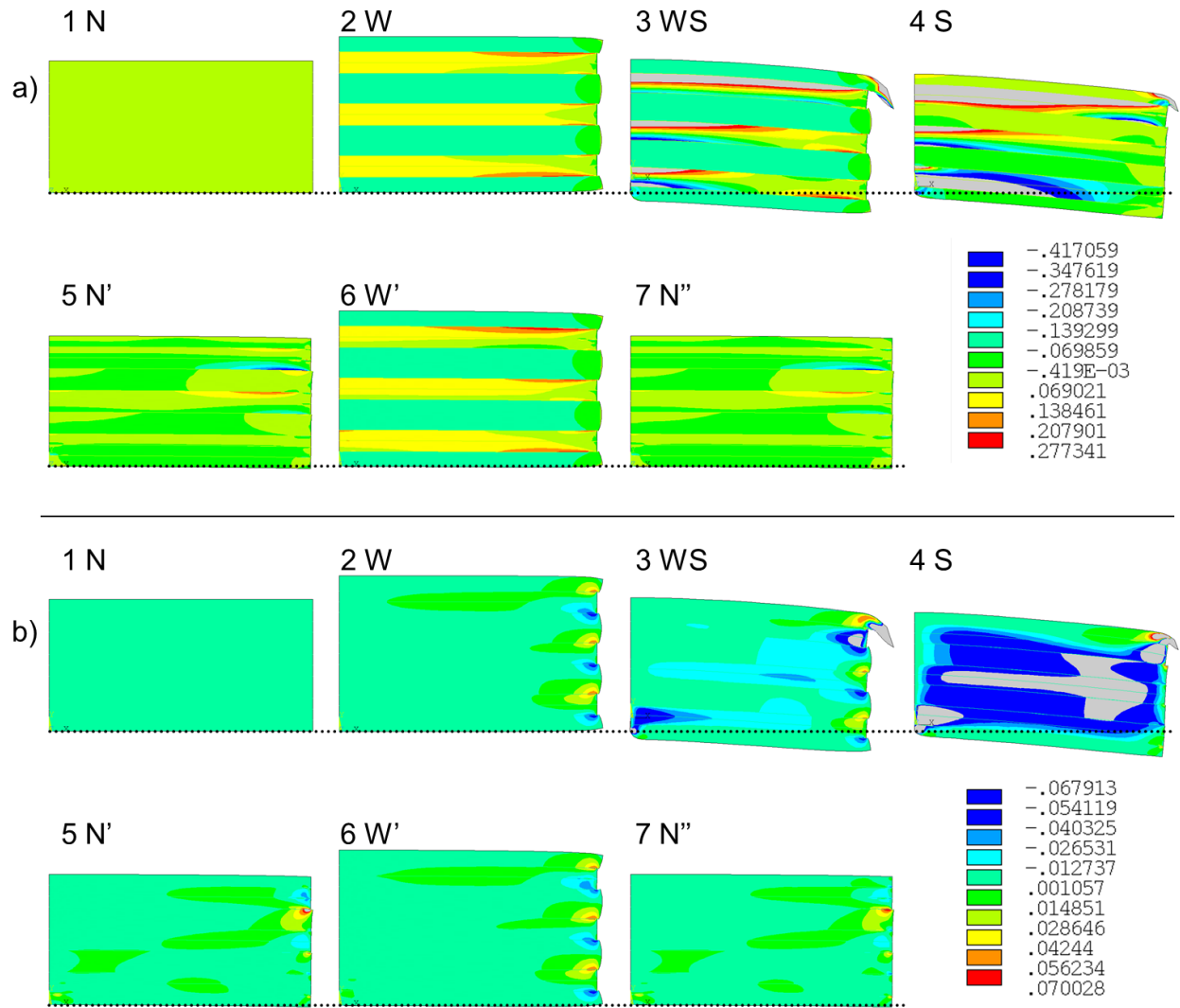


Figure 7-9 Distribution of the normal stress  $\sigma_x$  (a), shear stress  $\tau_{xy}$  (b) and deformation (a-b) of the 7 states for model 2. The color denotes the normal and shear stress level in unit of GPa.

The deformation is quantified by the deflection ratio  $\gamma$  defined as the ratio of  $y$ -displacement  $u_y$  to length  $l$ :

$$\gamma = \frac{u_y}{l} \quad (7-4)$$

It is noted that the  $y$ -displacement  $u_y$  is the difference between the  $y$ -displacement of the  $x = 0$  nm and the  $y$ -displacement of the  $x = 72$  nm. The deflection ratio is averaged along the right outer edge at  $x=72$  nm. Note that the deflection ratio is negative and absolute values are used for convenience.

The shape memory effect can be identified by the comparison of the deformations at states S, N' and N''. After being deformed by mechanical loading in the wet state, the specimen is dried reaching

the state S characterized by  $|\gamma_S|$ . After removing the mechanical load, the state N' is reached characterized by  $|\gamma_{N'}|$ . Reaching the state N' two scenarios are possible:  $|\gamma_{N'}| > 0$  and  $|\gamma_{N'}| = 0$ . For  $|\gamma_{N'}| > 0$ , the material shows a permanent intermediary deformation, meaning that a deformed shape can be maintained without external loading, referred to as partial fixation. If  $|\gamma_{N'}| = |\gamma_S|$ , the material keeps the deformation of state S, which is referred to as perfect fixation. Whereas in the case of  $|\gamma_{N'}| = 0$ , the material goes back to its initial state, meaning no fixation or shape memory occurred.

The deflection ratio  $\gamma$  of the three models over the length of the specimen is shown for the states S, N' and N'' in Figure 7-10. The three models all show partial fixation, meaning that  $|\gamma_{N'}| < |\gamma_S|$  and  $|\gamma_{N'}| > 0$ . This means that the deformed shape at S is partially maintained, which is in accordance with experimental observations (Ugolev 2014). The difference between  $|\gamma_{N'}|$  and  $|\gamma_S|$  is attributed to the decrease in elastic deformation after the mechanical loading has been removed and the specimen has been dried. Due to the release of stored elastic energy when the mechanical load is removed, the material can spring back partially, however maintaining some internal stresses and permanent deformation due to prevention of the totally slipping back at the interfaces. The system reaches an intermediate equilibrium state, while maintaining internal stresses and permanent deformation.

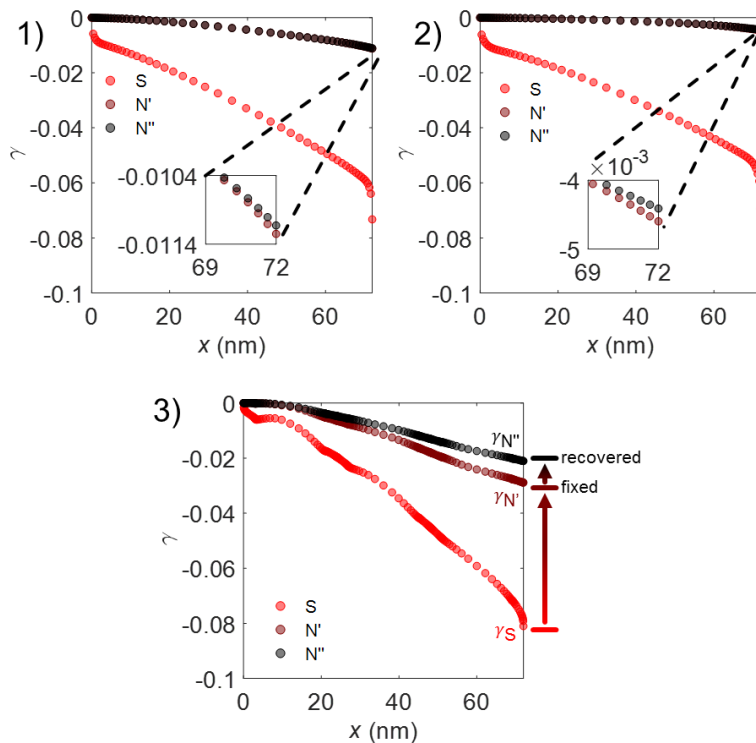


Figure 7-10 Deflection ratio of the models 1, 2 and 3 over the length of the specimen at states S, N' and N''.

Starting from the N' state, the system is again wetted and dried, reaching the final state N''. The deflection ratio  $|\gamma_{N''}|$  remains between 0 and  $|\gamma_{N'}|$ . If  $|\gamma_{N''}| = |\gamma_{N'}|$ , the material keeps its deformation of the state N', meaning no recovery occurs. The other extreme,  $|\gamma_{N''}| = 0$  indicates a full recovery to the initial state, also referred to as total shape memory effect. All three systems show recovery behavior, though the recovery of model 1 and 2 is negligible, shown in the insets of Figure 7-10. Model 3 shows a partial recovery.

The deflection ratio at the right edge  $x = 72$  nm for the states S, N' and N'' is shown in Figure 7-11. This figure is on a semi-log scale. The deformation at the state S (red color) is for all models almost the same since this state is controlled mainly by the mechanical load that was imposed at the end point to achieve a deflection ratio of 0.1 in the wet state. The fixation at state N' (brown color) is highest for model 3, while for model 2 the smallest. In the laminated model 1 and 2, the CC layers are horizontal and the mechanical load leads to shear stresses in the interface which spring back when the models are unloaded. In contrast, for model 3, the fibers are undulating and forming connected networks with CC-CC hot-spots, leading to a much more stiff structure. Since model 3 shows a much higher stiffness, the mechanical load and shear stresses will be higher leading to much larger sliding at the CC-GGM interfaces. Then, the CC-CC contacts act as constraints points to the system which prevent the spring back and contribute to the locking of the deformed shape.

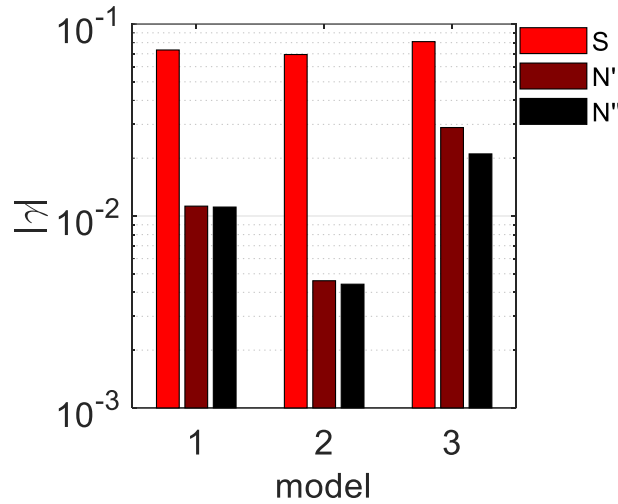


Figure 7-11 Deflection ratio at the right edge for the models 1, 2 and 3 for states S, N' and N''.

The fixation can be quantified by the fixation ratio  $R_f$ , defined as:

$$R_f = \frac{\gamma_{N'} - \gamma_N}{\gamma_S - \gamma_N} \quad (7-5)$$

In effect, this quantity represents how much the deformation is maintained at the intermediate state N' compared with the deformed state S. Remark that the initial state  $\gamma_N = 0$ . The recovery ratio is similarly defined, representing how much the deformation is maintained at the final state N'' compared to the deformed state S:

$$R_r = \frac{\gamma_{N''} - \gamma_N}{\gamma_S - \gamma_N} \quad (7-6)$$

A fixation ratio 1 means full fixation, and a recovery ratio 0 means full recovery. A fixation ratio 0 means no fixation, and a recovery ratio 1 means no recovery. When the fixation and recovery ratio are nonzero and equal to each other, there is no recovery, and almost no SME.

The deflection, fixation and recovery ratios of the three models are listed in Table 7-3. It is noted that the deflection ratios used are the values at the right edge  $x = 72$  nm. From Table 7-3, it is clear that model 3 shows the highest fixation and recovery ratios, while model 2 the lowest. Remark that the fixation and recovery ratio are almost equal for models 1 and 2, which means they show almost no recovery and thus no SME.

Table 7-3 Summary of the models: deflection, fixation and recovery ratios.

| model | $ \gamma_N $ | $ \gamma_S $ | $ \gamma_{N'} $ | $ \gamma_{N''} $ | $R_f$ | $R_r$ |
|-------|--------------|--------------|-----------------|------------------|-------|-------|
| 1     | 0            | 0.073        | 0.0112          | 0.0116           | 0.154 | 0.152 |
| 2     | 0            | 0.069        | 0.005           | 0.004            | 0.066 | 0.064 |
| 3     | 0            | 0.081        | 0.029           | 0.021            | 0.356 | 0.260 |

### 7.3.2 The origin of shape memory effect: fixation and recovery mechanisms.

The moisture induces three changes to the system, namely the swelling of the matrix, the weakening of the matrix, and the weakening of the interfaces. These three effects can be turned on and off by tweaking the constitutive relation. To turn off matrix swelling, the swelling coefficient of the matrix can be set to 0. To turn off the weakening of the matrix and interfaces, the parameter  $m$  in their controlling functions can be set equal to 0. In total  $2^3 = 8$  different cases can be generated by switching the three effects on and off. It is found that fixation and recovery are only dependent on the interface mechanics, and not on the swelling and weakening of the matrix.

In addition to model 3, a model 4 is built by turning off the weakening of the interfaces of model 3. The fixation ratio of model 4 is zero. This means that after the removal of external displacement, the system fully regains its original shape and no fixation is present. By eliminating the interface weakening, fixation and SME is eliminated. In other words, the interface weakening and strengthening, the so-called molecular switch, is at the origin of the moisture-induced shape memory effect. On the molecular level, the interfaces switch between hydrogen-bonded and non-hydrogen-bonded states controls the fixation and recovery of the system.

The molecular switch can be viewed from the aspect of sliding distance. The average sliding distance  $d_{\text{slid.}}$  of the models is shown in Figure 7-12a. The two interfaces are shown in separate groups: CC-GGM for all models and CC-CC for model 2 and model 3. It is observed that model 3 shows much larger sliding distances compared to the other models. Model 1 shows small sliding distances in CC-GGM interfaces, while model 2 shows that it mainly slides in its CC-CC interfaces. It is reminded that model 2 has to lowest fixation, followed by model 1, while model 3 shows the



highest fixation and recovery. All models show a sliding in the final N'', meaning there is no full sliding back and thus no full recovery.

Now the model 3 is discussed more in detail. The CC-GGM interface shows larger sliding than the CC-CC interface, which is because CC-GGM is weaker than CC-CC interface. For both interfaces, the state N'' after wetting again the specimen has a lower value of sliding distance than N', when the load is removed in dry state. At state N', the interface is at the strong dry state and is prevented in slipping back at the interfaces, which also prevents the spring back of the specimen. During the wetting again of the specimen (N'-W'-N'' steps), the interface is weakened by the moisture and can slip back releasing part of the deformation, until the point where shear stress is in equilibrium with friction provided by the wet weak interface. The elastic energy stored in the material is the driving force for the recovery. The equilibrium of forces at the interface is at the core of fixation and recovery. In contrast, when the weakening of the interface is turned off in model 4, the slide distances are negligible, shown in Figure 7-12b, and therefore the mechanism of SME is incapacitated. The comparison between model 3 and 4 clearly indicates the determining role of the molecular switch and the consequent sliding in shape memory effect.

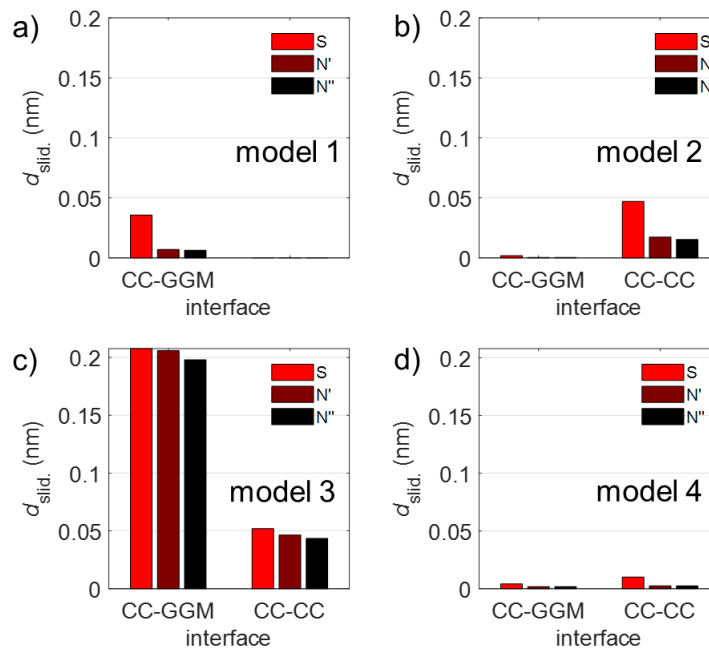


Figure 7-12 Sliding distance of the interfaces: a) model 1, b) model 2, c) model 3 and d) model 4.

Following the discussion above, the moisture-induced shape memory effect can be summarized as shown in Figure 7-13:

1. N, the initial state without deformation and stress. The interfaces are strong achieved by rich hydrogen bonding. The molecular switch is off, i.e. resistant to deformation.

2. W, the material is wetted and swells. The hydrogen bonds are broken weakening the interfaces. The molecular switch is on, i.e. prone to deform.
3. WS, the vertical load is applied on the wet material. Materials slide against each other at the interfaces, forming a new material configuration.
4. S, the moisture is removed with the loading kept at place. The hydrogen bonds are regained strengthening the interface. The molecular switch is off, locking the material configuration.
5. N', the external loading is removed. Most of the deformation is kept by the locking of the interfaces, referred to as fixation. Part of the deformation is lost due to the release of elastic energy. The shear stress at the interface is in equilibrium with the strength of dry interface.
6. W', the material is wetted again. The interface is weakened, and thus losing the ability to keep the deformed shape and recovery occurs. The deformation retained in state N' reduces. A part of the deformation remains due to the non-negligible friction provided by the weak interface. The shear stress at the interface lowers to the level of the strength of the wet interface.
7. N'', the material is dried again. Compared with the initial state N, there is residual deformation.

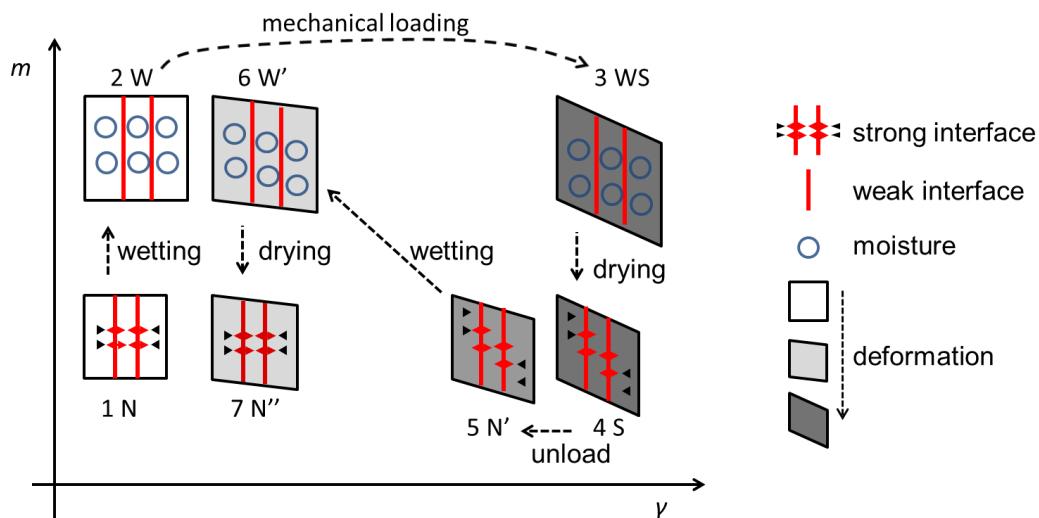


Figure 7-13 Schematic of the moisture-induced shape memory effect.

### 7.3.3 At the core of interface-controlled shape memory effect

Through the comparison between the cases with and without interface sliding, it is shown that the interface mechanics is at the core of shape memory effect, at least for the model systems presented here.

A more abstract and conceptual representation of shape memory effect can be elucidated in terms of an energy landscape involving reduction of potential energy and energy barriers that may block changes.

The potential energy of the system is denoted by  $\Gamma$  which is a function of the location of the system in the phase space denoted by a variable  $q(\gamma, d_{\text{slid.}})$ , that combines the influence of  $\gamma$ , the deflection ratio, and  $d_{\text{slid.}}$ , the sliding distance. Therefore the state of the specimen is characterized by its loading state  $q$  and energy state  $\Gamma$ .

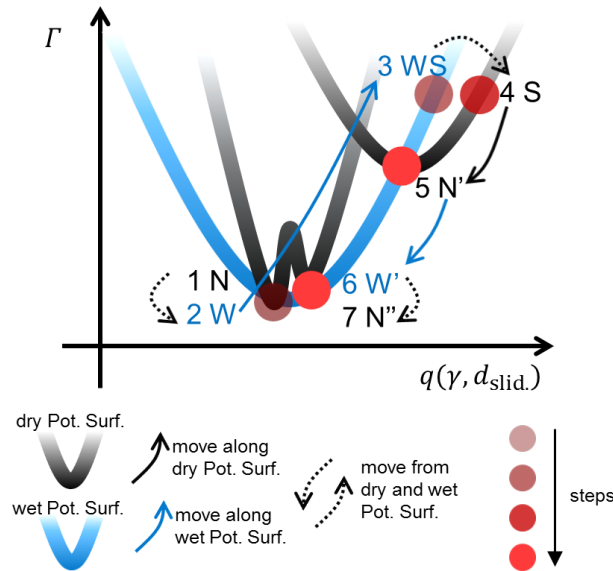


Figure 7-14 Schematic potential energy profile of the shape memory effect.

The 7-step loading protocol can be shown in terms of potential energy profiles. The system starts at the initial state 1-N located at the minimum of the dry potential surface. When wetting to state 2-W, the molecular switch is on and the system moves from the dry to the minimum of the wet potential surface. It is noted that the potential energy change induced by drying and wetting are omitted for simplicity. When mechanically loaded, the system moves away from the minimum on the wet potential energy surface to state 3-WS. When drying to state 4-S, the system moves from wet to the dry potential energy surface, remaining at high energy state since the mechanical loading is still present. When mechanically unloading to state 5-N', the system follows the dry potential energy surface to its minimum, remaining at a certain potential energy level due to fixation (molecular switch off). When wetting again (molecular switch on) to state 6-W', the system moves again to the wet potential energy surface, but energy is lost, and the system moves down on the wet energy surface. Remark that state 6-W' is located right of and above state 1-N, meaning there is still some deformation and energy stored in the system. Finally, the system is dried to state 7-N'.

The two energy minima correspond to the fixation and recovered states, while moisture acts as the activator. Through the wet potential energy surface, the system can migrate from the surface of high potential energy to the low energy surface.

For any material to show shape memory effect, there has to be at least two energy local minima/stable states. Under the activation of external stimuli, e.g. moisture in this case, the energy barrier between the two states are lowered, and therefore the kinetically locked potential energy will be released, and the system reaches a more thermodynamically stable state.

#### **7.4 Discussion and perspectives**

The shape memory effect of wood is a complex phenomenon, involving multiple scales and a wide range of physical and chemical sub-mechanisms. This chapter presents a possible mechanism of moisture-induced shape memory effect of wood cell wall composite material. Unlike most of the existing studies, where SME is attributed to bulk properties, such as crystallization, glass transition and chemical bonding, this chapter aims to show that the interface mechanics may play an important role, a factor largely overlooked. It is demonstrated that, with the moisture-dependent interface mechanics, the material is able to exhibit SME including fixation and recovery. While the removal of such moisture dependency eliminates SME.

It should be noted that this study is focused on the possible shape memory effect of wood cell wall material. Up to now, the finest scale experiment is the half-cell study (Derome et al. 2012), where cellular structure, the so-called honeycomb, may play a role on that scale which is beyond the scope of the current study. It is possible that the shape memory effect of wood is of multi-scale origin, where tissue and cell structures and nanoscopic material arrangements are each involved, which could be the topics of future research.

Although the composite in this study is able to capture the major moisture-related behaviors of cell wall composite, it differs from the realistic cell wall material in several important aspects: 1. the materials being considered are CC and GGM, whereas the other hemicelluloses and lignins are not included. 2. Materials are assumed to act elastically which might be true under small deformation and short timescale.

Based on these considerations, future studies can be expected to include the following features: 1. more components of cell wall to be introduced into FE model. 2. Adding non-linear material laws, such as mechano-sorptive effects described by poromechanics (Carmeliet et al. 2013) and time-dependent visco-elastic effect and moisture transport through diffusion, etc. 3. Three-dimensional models can be used, which may present a more obvious shape memory effect.

#### **7.5 Conclusions**

This chapter probes into one of the possible mechanisms of shape memory effects (SME) of wood cell wall composite material, i.e. moisture-controlled molecular switch based on interface mechanics.

This prototypical system proposes a mechanism of SME that is dominated by the stick-slip behavior of the interface: first, the breakage and reformation of hydrogen bonding at the fiber-

matrix interface serve as the molecular switch responsible for shape fixation and recovery; second, the elastic energy stored in the fibril serves as the driving force of shape recovery.

The atomistic insights from previous chapters are used as constitutive laws of materials and interfaces which are implemented into finite element models. Three representative models are built covering some possible material arrangements in wood cell wall. Under the 7-step loading protocol, all the models show fixation, but only some show large SME, where mechanical hotspots strengthen both fixation and recovery. The fact that the removal of moisture dependency of the interface eliminates the shape memory effect clearly indicates the deterministic role of interface mechanics in moisture-induced shape memory. The shape memory steps are also explained from the view of energetics. For any material to show shape memory effects, there have to be at least two sub-stable states, here corresponding to the different moisture conditions.

While this study uses two-component composite as the prototype and successfully reproduces one possible mechanism of the moisture-induced shape memory effect, the real wood cell wall composite is much more complex with many types of hemicelluloses and lignins. The next chapter endeavors to build a reality-mimicking atomistic model wood cell wall S2 layer composite material. The individual components, as well as their mixtures, are mechanically characterized providing the missing micromechanical properties that are vital to wood modeling.

## **Chapter 8 Mechanics of Softwood Cell Wall Layer Studied with Molecular Simulations**

In the previous chapters, wood cell wall S2 layer components and their interfaces are investigated with molecular simulation, and the shape memory effect could be explained based on a simplified S2 model. The challenging yet feasible final step is to build an atomistic model for a composite assembly resembling more closely the S2 layer. Thus, in this chapter, a state-of-the-art atomistic model of softwood S2 layer is constructed using a bottom-up approach, taking great care to reflect the state of knowledge of the molecular structure of this cell layer. Individual polymer components, including cellulose, hemicelluloses namely glucomannan and xylan and two types of lignin, as well as two mixtures of hemicelluloses and lignins and different interfaces are built and mechanically characterized in separate simulations, gathering a complete set of micromechanical properties, including hydrogen bonding, swelling and weakening, over the full hydration range. Predictions of the behavior of the mixtures and the S2 composite are made using the rule of mixture and are shown to be in accordance with the simulation measurements, while providing further insights on the MD data. The determined hygromechanical properties fill the gap of previously unknown micromechanical parameters critical for modeling wood cell wall. This extensive atomistic model leads to a better insight into the impact of intermolecular interactions induced by components forming the composite and allows to identify the role of different components and their interactions. The most important factors that determine wood mechanics at the nanometer scale are thus highlighted.

### **8.1 Introduction**

Along the endeavor of this thesis to provide a view into the behavior of wood cell wall nanocomposites, the last piece of work reported in this chapter is strongly inspired by wood, one of the most used natural materials. Several features of wood are particularly attractive. Wood has outstanding mechanical properties, e.g. a stiffness-to-density ratio higher than steel. Wood interacts strongly with moisture because the cellulosic and hemicellulosic polymers of wood feature multiple hydroxyl groups on their repeating units, strongly attracting water molecules. The presence of water induces physical and mechanical changes, such as swelling, mechanical weakening, diminution of adsorption heat, etc. In fact, most aspects of the moisture-induced behavior are nonlinear and involve intricate molecular interactions originating from the atomistic scale. The understanding and eventually the control of this hygromechanical behavior are needed as moisture plays an essential role in several wood-based applications. Despite the rich literature on the mechanical aspects of wood-moisture relationship, the fundamental microscopic mechanisms at play are still not fully elucidated.

As introduced in Chapter 2, this thesis chooses wood cell wall S2 layer as the system of investigation for its dominating role in the mechanical behavior of wood. The S2 layer itself can be considered as a fiber-reinforced composite where the cellulose crystals are the stiff fibers, of

diameters around 3 nm, surrounded by the compliant mixture of hemicelluloses and lignins, which thickness varies from 3 to 14 nm. The cellulose fibers are roughly aligned and this alignment forms an angle, called microfibril angle (MFA), with the longitudinal direction of tracheid cells. The oriented cellulose fibers endow the S2 layer with excellent stiffness, reaching 60 ~ 100 GPa along the longitudinal direction. The relatively regular atomistic arrangement of cellulose crystals is detectable in experiments, e.g. using X-ray diffraction. In contrast, the delineation of the amorphous matrix is much more difficult as the access of such molecular-level information is beyond the resolution limit of current imaging instruments. Recent atomic force microscopy (AFM) results offered a theoretical resolution of 4 nm per pixel (Casdorff et al. 2017) which is unfortunately still not enough for the inference of matrix material arrangements in the plane of investigation, not to mention their complex three-dimensional structures. Numerous reports have speculated on the ultrastructure of the S2 layer based on indirect experimental evidences, through several spectroscopy means, and proposed manifold hypotheses that remain to be verified.

To fill the experimental gaps, different paths of computational studies, including continuum and discrete methods, could enable the exploration of the nanoscopic structural hypotheses and lead to the understanding of the microscopic mechanisms of moisture-induced phenomena. For continuum models, constitutive laws of constituents and their interfaces are needed as input. The currently known mechanical properties of cell wall materials are summarized in Chapter 2. Clearly, data is lacking regarding the full hydration range, a dearth that is hindering the predicting power of continuum models.

There is a small number of molecular dynamics (MD) studies that have investigated the impact of moisture on plant cell wall systems such as wood and bamboo. However, as mentioned in Chapter 2, only Kulasinski et al (2017b) have used the current most advanced molecular simulation to look at the impact of moisture on a S2 layer surrogate system, consisting of CC microfibrils embedded in galactoglucomannan (GGM) and surrounded with a low polymerization degree lignin (LGN). A more realistic model of softwood S2 layer is expected to consist of the hemicelluloses xylan and galactoglucomannan and both condensed and uncondensed types of lignin, as performed in this study.

With the aim of modeling the S2 layer, its components and sub-units atomistically, this study systematically presents molecular models of S2 layer-related materials, interfaces and mixtures, and finally builds a S2 composite whose chemical composition and material arrangements comply with the most recent knowledge in this field. The encompassed systems are crystalline cellulose (CC), galactoglucomannan (GGM), arabinoglucuronoxylan (AGX), uncondensed lignin (uLGN), condensed lignin (cLGN), M1 (AGX mixed with uLGN), M2 (GGM mixed with cLGN) and finally a S2 composite system comprising CC, GGM, AGX, uLGN and cLGN. These choices of wood polymers refers to softwood, given its dominance in the northern hemisphere including northern Europe, North America and Russia (Rennel and Dillén 2001) and for its widespread use in construction.

The objectives of this study are the following: 1. To present an atomistic model of S2 cell wall layer that complies with the most recent experiments; 2. To offer a complete set of hygro-mechanical data of S2-related polymers and their mixtures; 3. To investigate the impact of intermolecular interactions between components; 4. To identify the most important factors of S2 mechanical performance; 5. To characterize the structural, physical and mechanical responses of wood cell wall to hydration, especially at the fibril-matrix interface.

This chapter starts with the methodology of material modeling. The numerical framework of building the investigated systems, especially the polymers that may not be adequately modeled by previous studies, are described in detail. The strategy of constructing the S2 composite atomistic model follows. Characterizations such as distribution of components and adhesion energies are presented, serving as the necessary justifications of the complex assembling procedure of this unprecedented composite model. The metrics used to probe the systems are introduced, including hydrogen bonding, swelling strain, elastic moduli and interface shear stress. The results section starts with the mechanical characterization of S2-related material systems and covers hygroscopic swelling and mechanical weakening. A rule of mixture rule analysis is used to identify the impact of molecular interactions between components induced by mixing. Finally, a specific section is dedicated to the S2 composite, addressing its unique aspect, i.e. the fibril-matrix interface.

## **8.2 Materials and Methods**

This section describes the retained material systems, including five components (CC, GGM, AGX, uLGN and cLGN), two mixtures (M1 and M2) and one composite (S2). Their chemical structures are explained, first reviewing the chemical structures as reported by literature, then presenting the decisions taken towards the atomistic model used for MD simulation, including the different steps in building the systems. Finally, the hydration process and mechanical characterization methods are presented.

### **8.2.1 Preparation of dry polymer systems**

#### **8.2.1.1 General MD parameters**

GROMACS 5.0 package (Abraham et al. 2015) and GROMOS 53a6 force field (Oostenbrink et al. 2004) are used for the MD simulation. The integration time step of the equations of motion is 1fs. The temperature is controlled by the Nose-Hoover thermostat. For NPT simulations, the pressure is controlled by the Parrinello-Rahman barostat. The Coulomb and Van der Waals interactions have cut-off radii of 1.0 nm and the particle-mesh Ewald summation is used to account for long-range Coulomb interactions.

#### **8.2.1.2 General procedure for preparation of amorphous systems**

The procedures to obtain equilibrated molecular structures are the same for GGM, AGX, uLGN, mixture 1 and 2, not including cLGN which is special due to cross-linkages. As summarized in Figure 8-1, generally, the chains are inserted into a very large periodic box with random location



and orientation. Then the box is subjected to a high compression pressure,  $\sim 1$  GPa, at 300 K. The system is then relaxed at an elevated temperature (800 K) without any pressure applied to allow the release of internal stresses induced by the initial compression. Finally, the structures are equilibrated at room temperature at 0 pressure.

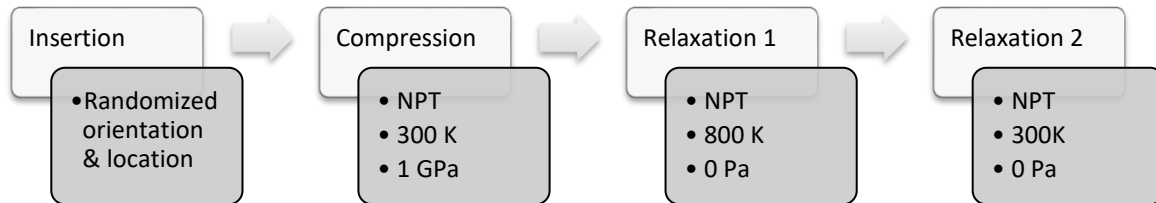


Figure 8-1 General procedure for the preparation of a bulk or mixture material system of polymer chains.

### 8.2.1.3 Cellulose crystal

Though cellulose comprises about half of the mass of cell wall layers and is studied the most among all wood polymers, some basic facts about cellulose are still not clear, such as the number of cellulose chains in a microfibril, the location of amorphous cellulose, the shape of fiber cross-section, etc. as summarized in Chapter 2.1.2. Most frequently, researchers assume the number of cellulose chains in a cellulose nanocrystal, the reinforcement phase of the wood cell wall, to be multiples of 6, based on the fact that six cellulose synthase proteins form a cellulose synthase complex subunit (Delmer 1999; Mutwil et al. 2008). Under this premise, researchers propose models comprised of 18, 24 and 36 chains based on different indirect measurements (Ding et al. 2014). In this study, the widely accepted 36 chain model is chosen. However, it is known that the arrangement of the 36 chains is subject to debate, not only in number of chains, but also in configuration. In MD studies, popular models are crystalline structures with square and hexagonal cross-sections.

In order to support the decision process, these two types of models are compared here in terms of the most stable structure, thus most likely to occur. The equilibrated single-crystal structures of hexagon and square cross-sections are shown in Figure 8-2a and b. The initial structure of each cellulose crystal is generated using the cellulose builder toolkit (Gomes and Skaf 2012) based on the crystallographic information from Nishiyama et al. (2002). The canonical ensemble (NVT) is applied, with the temperature set to 300 K. The structure is then energy minimized and equilibrated in NPT at  $10^5$  Pa and 300 K (Kulasinski et al. 2014b). The length of the cellulose chains is 10 monomers and the two ends of a cellulose chain are bonded using cross periodic boundary covalent bonds to achieve an infinitely long cellulose chain.

From the surface to the core, there are four layers in the hexagon layout, for a total of eight, and six layers in the square layout, for a total of eleven layers, as indicated by Arabic numbers on Figure 8-2a and b. The stability of the two structures is evaluated based on the adhesion energy of each

layer. To calculate the adhesion energy of layer  $i$ , the crystal is divided into two parts, one consisting of layer 1 to  $i$ , another consisting of the rest layers. The adhesion energy of layer  $i$  is defined by the summation of the potential energy of the two separate parts subtracted from the potential energy of the whole crystal. The adhesion energy of each layer for both configurations is shown in Figure 8-2c. It is noted that the 6<sup>th</sup> layer of the hexagon being at the core position, no adhesion energy corresponds for this position. Generally speaking, the hexagon crystal shows a better stability than the square crystal, as indicated by the larger adhesion energy of layers 2 and 3. Thus, the hexagonal 36 chain crystal is retained as the model used in this chapter.

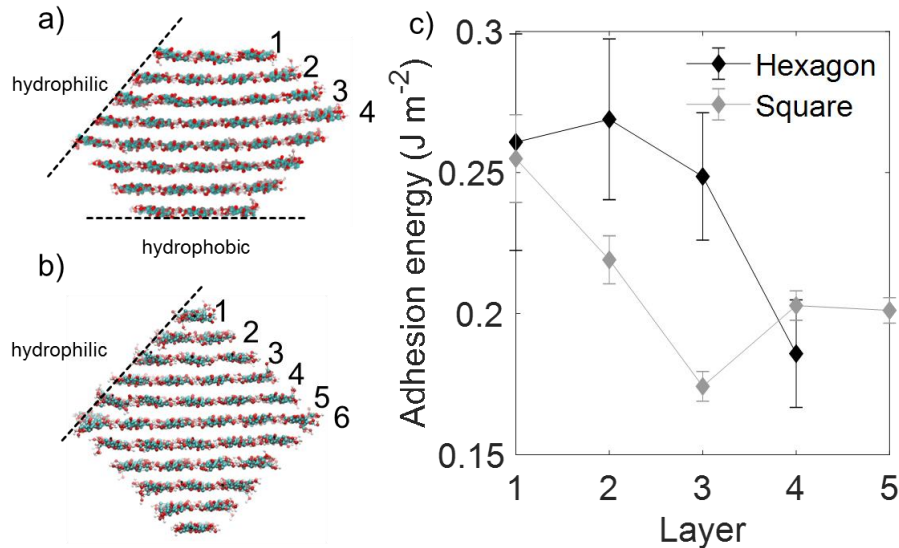


Figure 8-2 Two different arrangements of cellulose crystals consisting of 36 cellulose chains. a) Hexagonal arrangement, exposing hydrophilic and hydrophobic planes. Four layers from the edge to the core are indicated by Arabic numbers. b) Square arrangement, exposing only hydrophilic planes. Six different layers from edge to core are indicated by Arabic numbers. c) Adhesion energy of different layers for the two configurations.

In the S2 cell wall layer, it is speculated that cellulose crystals may be in close association with some amorphous cellulose regions based on the observation that rod-like cellulose crystals can be extracted from cellulose fibrils through hydrolysis (Moreau et al. 2015; Liu et al. 2017). There are multiple models for the location of amorphous cellulose. It is currently widely acknowledged that the amorphous regions are distributed along the fibril as kinks, formed by strain distortion and twisting during cell formation (Rowland and Roberts 1972; Fernandes et al. 2011; Ding et al. 2014). However other reports attribute the existence of kinks to sample processing, as indicated by the non-Gaussian distribution of kink angles of cellulose fibrils (Usov et al. 2015). In this study, amorphous regions of cellulose are not specifically included due to the uncertainty of their presence but also to the need to limit computation costs by controlling the size of the computation domain. Nevertheless, some less perfect crystalline cellulose is present as the cellulose chains at the surface of cellulose nanocrystals are less ordered than the ones at the core.

#### 8.2.1.4 Hemicelluloses: galactoglucomannan and arabinoglucuronoxylan

The atomistic models of hemicelluloses used in the current study, i.e. GGM and AGX, have been used previously in the studies reported in Chapters 3, 6 and 7. Similar to cellulose, the detailed chemical structures of these hemicelluloses are still under debate, as explained in Chapters 2 and 3, but the retained systems are described below.

The validation and characterization of AGX can be found in Chapter 3 and ref. (Zhang et al. 2020). It is reminded that the composition of AGX, has three types of monomers, i.e. 67% xylose, 20% glucuronoacid-xylose and 13% arabinoxylose, which are randomly polymerized, shown in Figure 2-4a. Force field parameters are obtained from the automated topology builder (Malde et al. 2011). For the simulation of pure AGX, the AGX system contains five chains of 100 monomers. When AGX is used in mixture or in S2, a total of four chains of 50 monomers are used for the sake of saving computational costs.

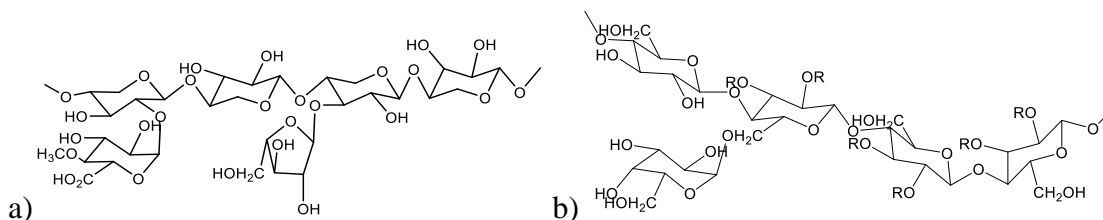


Figure 8-3 Chemical structure of a) arabinoglucuronoxylan and b) galactoglucomannan.

For GGM, two types of monomers, i.e. glucose and mannose, comprise the backbone with a ratio of 1:4, and galactose side groups are branched on mannose (~ 8 wt. %) units, shown in Figure 2-4b. The GGM model is constructed following ref. (Kulasinski et al. 2015d). The GGM system consists of four chains of 80 monomers. When GGM is used in mixture, three chains of 100 monomers, or in S2, a total of 58 chains of 10 monomers are used. The chain length of GGM in S2 is shortened for the ease of modeling, as shorter chains are easier to disperse randomly in the simulation box of limited size.

The initial structures of these two polymers are built with Material Studio software 8.0 based on the chemical structure indicated above.

#### 8.2.1.5 Lignins: condensed and uncondensed types of lignin

Lignin has been investigated extensively by experiments, and its chemical structure is known to be tridimensionally complex without a well-defined organization (Gellerstedt 2015). Softwood lignin mainly comprises coniferyl units. Depending on the chemical bond types, there are mainly two types of lignin, a more linear type (uncondensed, uLGN) and another more branched type (condensed, cLGN).

For uLGN, the linkages between monomers are all  $\beta$ -O-4, and the polymer chain is linear. The initial structure is built in Material Studio 8.0. The force field parameters for the lignin monomer

are built in the automated topology builder (Malde et al. 2011). The polymer chains are assembled into bulk material through the procedure shown in Figure 8-1. Five chains of uLGN with a degree of polymerization of 100 are first placed in a periodic box and equilibrated at 300 K and 0 bar. For the mixture and S2, four chains of 50 monomers are used.

For cLGN, the most common covalent linkage is  $\beta$ -O-4 (40~60%), followed by  $\beta$ -5', 5-5',  $\beta$ - $\gamma$ ,  $\beta$ - $\beta'$  and 4-O-5' linkages (Åkerholm and Salmén 2003; Higuchi 2014). Due to the inherent complexity in cLGN structure, a more sophisticated modeling path, referred to as random branching, must be taken. Based on the uLGN structure above, crosslink bonds are added. For force field simplicity, only 5-5' bonds are considered in this study. When two C5 atoms from two monomers are within 6 Å of each other, a crosslink bond is formed. For 5-5' bond, an equilibrium bond length of 0.149 nm and bond constant  $1.4 \times 10^7$  kJ mol<sup>-1</sup> nm<sup>-2</sup> are used. Through these steps, a highly bonded system is built. This highly bonded system is used as a template of the initial structure of cLGN. To get the final cLGN, the next step needed is the random removal of some of the linear linkages and/or cross-linkages, thus achieving a randomly branched lignin polymer with the desired ratio of linear- to cross-linkages. Then the structure is energy minimized with steepest descent and conjugate gradient algorithms and equilibrated in NPT ensemble with 300 K and 0 bar. The resulting cLGN is quite heterogeneous and possesses a distribution of degree of polymerization. In total, the cLGN system consists of 136 cLGN molecules where the number of monomers per molecule ranges from 1 to 43. The Herman's orientation function of the cLGN system shows a value around 0 indicating the isotropy of the built system (Hermans and Platzek 1939). The cLGN in mixture 2 consists of 19 molecules of DP ranging from 1 to 43. The cLGN in S2 consists of 57 molecules of DP ranging from 2 to 15. For all these systems the ratio of linear- to cross-linkages is 2:1 (Åkerholm and Salmén 2003; Higuchi 2014).

Due to the complexity of cLGN structure and the ensuing difficulty in modeling and force field construction, cLGN is seldom studied with molecular simulation, especially in the GROMOS force field. It is worthwhile to note that, concurrently with this study, a convenient tool to model the complex 3D structure of lignin in the CHARMM force field was recently developed (Vermaas et al. 2019a), but unfortunately, given the different force field used, this new tool could not benefit this study. Advantages of this method, if applicable here, would have greatly relieved the burden of manually setting up the coordinates and force fields files.

#### **8.2.1.6 Mixtures 1 and 2**

The structural arrangement of the cell wall matrix is still subject to debate. Chemical analysis and immunolabelling results reveal that GGM and cLGN are in close proximity to the cellulose fibers, while AGX and uLGN are somewhat further (Ruel and Joseleau 2005; Lawoko et al. 2005). The different components in the cell wall are in a mixture state (Salmén and Burgert 2009), which necessitates the modeling of mixtures of the different types of polymers chains.

Mixture 1 is composed of AGX and uLGN, mass ratio of 1:2. Mixture 2 is composed of GGM and cLGN, mass ratio 7:4. The mass ratios comply with experimental observations of the S2 layer, as summarized in Table 8-1.

Starting from the chains built in the previous sections, the bulk material is prepared through the procedure shown in Figure 8-1. Different chains are inserted with random locations and orientations to the simulation box and to be then successively compressed and relaxed. Molecules of all types may traverse a boundary and have cross-linkages across the periodic boundaries.

### 8.2.1.7 S2 composite

Softwood cell wall S2 layer is composed of cellulose (~ 45% mass ratio), hemicelluloses (~ 27%) and lignins (~ 28%). There could also be some tiny portion (< 3 %) of pectins, ions and extractives that are omitted here due to their reported insignificant roles in mechanics. The mass ratio of different polymers is chemically analyzed and summarized in Table 8-1.

Table 8-1 Chemical composition of the constructed softwood cell wall S2 layer atomistic model.

| component category | component polymer | exp. mass ratio         | MD model mass ratio | # monomers per chain | # chains |
|--------------------|-------------------|-------------------------|---------------------|----------------------|----------|
| C                  | CC                | 27.5% ± 2% <sup>1</sup> | 44.10%              | 10                   | 36 * 4   |
|                    | AC                | 17.6% ± 8% <sup>1</sup> |                     |                      |          |
| HC                 | GGM               | 18.6% ± 9% <sup>2</sup> | 20.90%              | 10                   | 38 + 20  |
|                    | AGX               | ~8% <sup>2,3</sup>      | 7.54%               | 50                   | 4        |
| LGN                | cLGN              | ~12% <sup>1,4</sup>     | 12.08%              | 2~15                 | 57       |
|                    | uLGN              | ~15% <sup>1,4</sup>     | 15.39%              | 50                   | 9        |

Experimental data: 1 (Dinwoodie 2000), 2 (Pettersen 1984), 3 (Scheller and Ulvskov 2010), 4 (Hon and Shiraishi 2013).

Softwood S2 layer can be seen as a fiber-reinforced composite where crystalline cellulose is embedded in a multi-component matrix. The various aforementioned components of S2 need to be positioned in certain arrangements corresponding to the structure of the S2 layer of wood. The exact structural details of each component and their arrangement within the S2 layer are the object of ongoing research, with many critical issues remaining to be clarified (Terrett et al. 2019). The state-of-the-art atomistic model of the S2 layer is constructed following the steps described below. As come across situations that required to make assumptions, these are explained.

Four crystalline celluloses, each consists of 36 chains of 10-monomer chain forming hexagonal cross-sections as shown in Figure 8-2, are first placed in the simulation box separated from each other by at least 1.5 nm (Figure 8-4a). The void spaces are filled in the later assembling steps by the insertion of the other polymers. The periodic box is shown with gray lines in Figure 8-4a. A non-orthogonal periodic boundary condition is used, where the two base vectors in the transverse

plane have an angle of  $65^\circ$ . The depth of the periodic box, i.e. the dimension along the longitudinal direction, is 5.3 nm corresponding to the length of the 10-monomer cellulose chain.

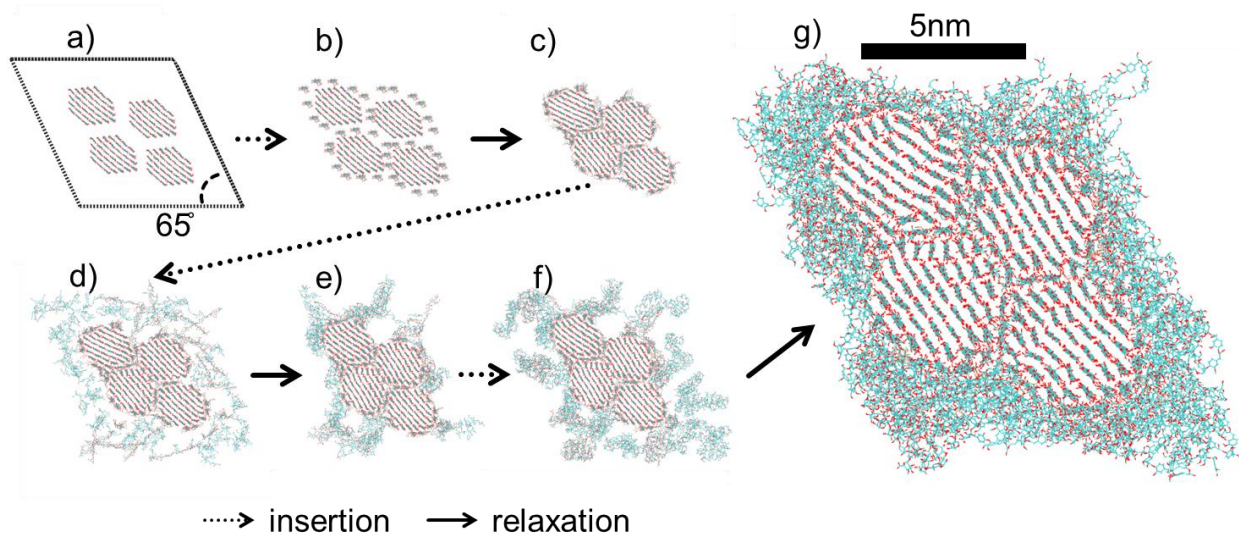


Figure 8-4 Assembling procedure of S2 layer model.

Studies have suggested that hemicellulose is the intermediate polymer joining crystalline cellulose and lignin together (Takeichi et al. 2013). Quartz crystal microbalance and Fourier transform IR spectroscopy indicated that crystalline cellulose is closely associated with GGM (Salmén and Fahlén 2006). Accordingly, in the MD model, GGM chains are the first to be deposited on the crystalline cellulose surfaces, i.e. 38 chains of GGM inserted next to the surface crystalline cellulose with relatively even distribution (Figure 8-4b). From the 38 molecules, 10 are predominantly between two crystals and the rest surrounds the four crystals. It should be noted that the length of the GGM is relatively short, i.e. 10 monomers per chain. As GGM is adjacent to cellulose crystals and enters inter-crystal space, forming the so-called microfibril, which is a bundle of crystalline cellulose glued together by GGM, the feasible size of the GGM chain is limited, hence the chosen degree of polymerization of 10. Seven steps of energy minimization and relaxation follow: steepest descent energy minimization, 100 ps relaxation in NVT (300 K) with cellulose fixed, another 100 ps relaxation without constraining cellulose, conjugate gradient energy minimization, 100 ps relaxation in NVT (300 K), 100 ps relaxation in NVT with high temperature (800 K), 100 ps relaxation in NVT at room temperature and stress-free state. The cellulose atoms are constrained during the high temperature relaxation to avoid unphysical decrystallization.

Along with GGM, cLGN is also speculated to stay relatively close to cellulose (Salmén and Fahlén 2006; Salmén and Burgert 2009), which is supported by the observation that cLGN, similar to GGM, forms an ordered structure aligned to the fiber axis (Atalla and Agarwal 1985; Terashima 1990; Åkerholm and Salmén 2003). As intermolecular forces are short-range forces, the distance between cLGN and cellulose should be close enough to ensure that the crystalline cellulose can

cast an influence over cLGN. Therefore, as the next step of assembling, a mixture of 20 GGM chains and 57 cLGN molecules, mass ratio 3:5, are inserted randomly around the previously built system of cellulose enveloped in GGM (Figure 8-4d). Five steps of energy minimization and relaxation are launched: steepest descent energy minimization, conjugate gradient energy minimization, 100 ps relaxation in NVT (300 K), 100 ps relaxation in NVT (800 K) and 100 ps relaxation in NVT (300 K). Also in these steps, cellulose atoms are restrained with a strong harmonic potential to prevent the introduction of unphysical defects of the crystal when subjected to high-temperature relaxation. After relaxation, the system reaches the state shown in Figure 8-4e. As a point of clarification, mixture 2 studied on its own is a mixture of 58 GGM chains and 57 cLGN molecules, mass ratio 7:4. In the S2 model, the same amount of GGM chains is used, i.e. 58, however it is noted that 10 of these molecules are mostly located between crystals, slightly changing the amount of GGM in contact with cLGN.

The uLGN and AGX components are then introduced to the system (Figure 8-4f), forming the matrix between cellulose microfibrils, as suggested by (Salmén and Burgert 2009). In total 9 chains of uLGN and 4 chains of AGX, each with 50 monomers per chain, are inserted to the system with a randomly chosen initial location, referred as mixture 1 with ratio 1:2 above. The chains chosen are relatively long here, as an attempt to stay as close as possible to the experimentally reported degree of polymerization (100~200) (Pettersen 1984; Gorshkova et al. 2012). The energy minimization and relaxation steps are as follows: steepest descent and conjugate gradient energy minimization, relaxation in NVT (300 K) for 100 ps, relaxation and densification (3000 bar of pressure on the transverse direction with stress-free on axial direction) in NPT at elevated temperature (400 K) for 1 ns and another relaxation in NPT (300 K, 0 bar) for 1 ns. In the last step of relaxation, the system gradually recovers from the densified status, and the density is seen to be decreasing and then approaching equilibrium after 0.4 ns. The final state is shown in Figure 8-4g. It is noted that Figure 8-4g shows only one periodic cell, whereas in other plots, e.g. Figure 8-5, more periodic images are presented. This does not mean any structural change and is merely a different style of visualization.

The material distribution of the dry S2 system is shown in Figure 8-5, using color to identify the polymers. In general mixture 2, in red, locates nearer to the CC, in cyan, surface than mixture 1, shown in gray. As shown schematically in Figure 8-5b, the GGM covers the surface of CC, while the rest of mixture 2 covers the CC aggregated glued together by GGM.

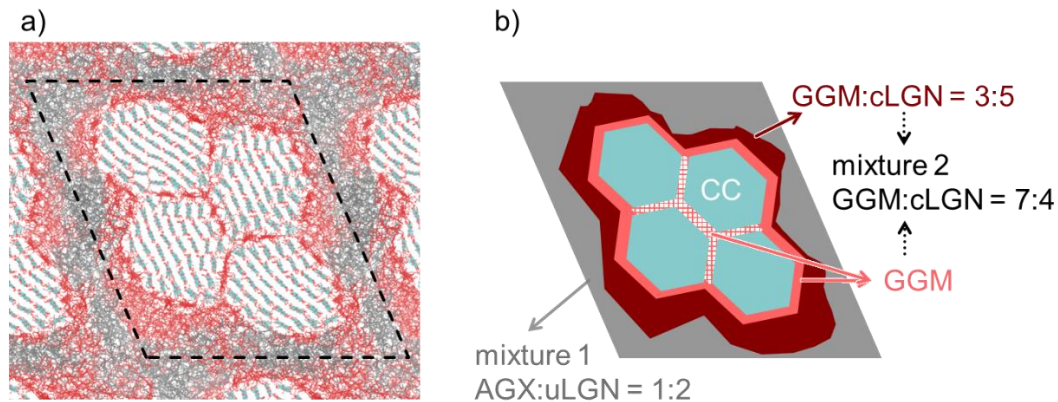


Figure 8-5 a) Material distribution of S2 with CC, mixture 1 and mixture 2 shown in cyan, red and gray, respectively. b) Schematic of the same material distribution of S2.

### 8.2.2 Hydration

The systems are characterized in dry state and at different moisture contents. As mentioned in previous chapters, in MD, there are various models of water molecule. GROMOS force field is designed to work with either the SPC or SPC/E water models (Berendsen et al. 1987). The SPC is chosen in this study because its saturation vapor pressure is closer to the value of experiments than the one of SPC/E (Errington and Panagiotopoulos 1998).

Regarding obtaining hydrated systems, intuitively, the process of hydration itself could have been modeled with water molecules in a reservoir diffusing into the material. However, such approach would be computationally expensive. Instead, in this study, as done in previous chapters, water molecules are inserted manually one after another, to randomly chosen locations that do not overlap with existing atoms of polymers nor previously inserted water molecules in the system. Following the successful insertion of each water molecule, steepest descent, conjugate gradient energy minimizations, and an equilibration run of 10 ps are carried out. All the polymer systems, except for CC which is not affected by moisture, are subjected to this hydration process.

Take the S2 composite system as an example of the hydration protocol. The initial locations of each inserted water molecule, for a total of 5200, are superimposed and shown in Figure 8-6a. As locations of water molecules are chosen randomly, positions within the cellulose crystal are also filled with water, although water is expected to only access the cellulose crystals surfaces and not core (Frey-Wyssling 1954; Belbekhouche et al. 2011). Therefore, water molecules inserted within the cellulose crystal cores are discarded. The system is then subjected to NPT relaxation at 0 bar and room temperature for 20 ns. A snapshot of the equilibrate system of  $m \sim 0.3$ , i.e. with 4947 water molecules, is shown in Figure 8-6b. It is clear that the water molecules have been attracted to the more hydrophilic regions close to the crystalline cellulose surface. As the crystals are observed to relax and lose some of their ordered structure, a few water molecules manage to enter the cellulose crystal probably due to the imperfection or disordered structure of surface chains.



With this example, the manually inserted water molecules have first to land in an empty location and, afterwards, move to locations that resemble the natural adsorption.

Once equilibrated, the moisture content ( $m$ ) is defined as the ratio of the mass of water to the mass of the polymers, except for the mass of crystalline phase. This definition of  $m$  is chosen for ease of comparison of the results of the component/mixture systems with the results of S2. Thus, the moisture content of S2 model is defined as the ratio of the mass of water to the mass of the matrix, excluding CC. Multiplying any reported moisture content by the mass of amorphous polymers and dividing with the mass of S2 model yields the moisture content in the full S2 system, which could be useful e.g. for comparison with wood studies.

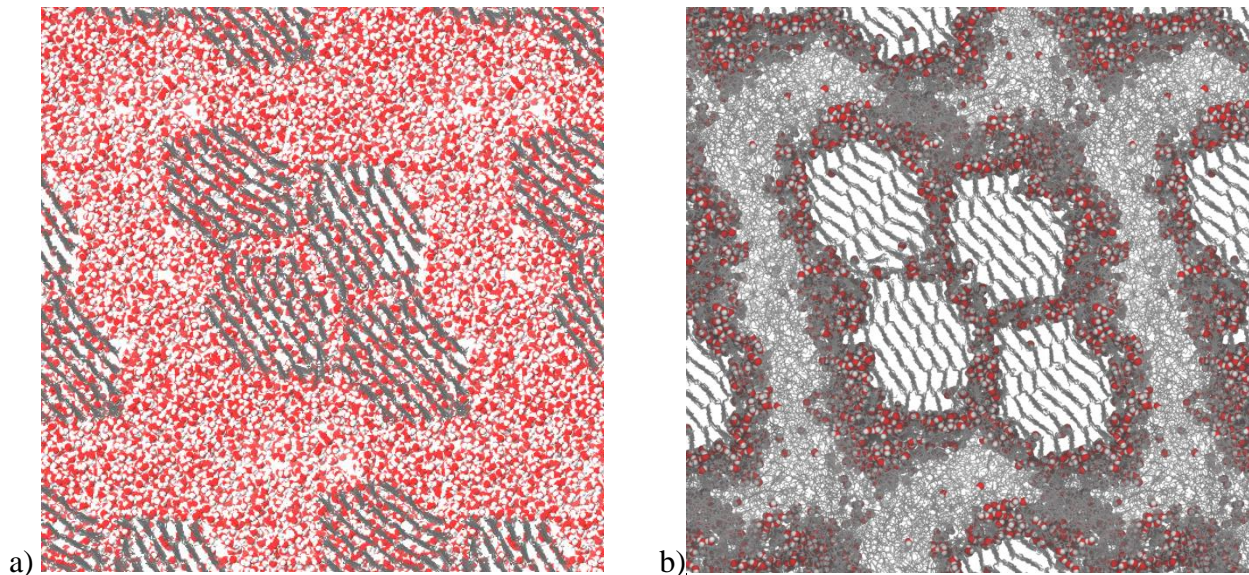


Figure 8-6 a) Schematic representation of all locations probed by water molecule insertions in the S2 system, celluloses are shown in dark grey, and all the other polymers are omitted for clarity. b) Snapshot of one state of the system equilibrated at  $m \sim 0.3$ , with all the polymers shown in gray and water in red and white.

Sorption is characterized by sorption isotherms that describe the relation between chemical potential or relative humidity and moisture content. Due to the uncertainty of chemical potential determination in MD, the isotherms are not included in this work.

### 8.2.3 Characterization

Hydrogen bond, swelling strain, elastic moduli and Poisson's ratio are characterized for the systems including individual polymers, their mixtures and composite. For the heterogeneous S2 model, the density distribution of water and matrix and the interface shear stress are additionally characterized. All systems are tested in the moisture content range of  $0 \sim 0.3$  with an interval of  $\sim 0.02$ .

### 8.2.3.1 Hydrogen bond

As performed in previous chapters, the establishment of hydrogen bonds is based on geometric criteria:

$$r \leq 0.35 \text{ nm and } \alpha \leq 30^\circ \quad (8-1)$$

where  $r$  is the distance between the donor oxygen atom and the acceptor oxygen atom, and  $\alpha$  is the angle of acceptor oxygen atom – donor oxygen atom – donor hydrogen atom. The interoxygen distance criterion of 0.35 nm refers to the first minimum of the radial distribution function of SPC water (Soper and Phillips 1986; Luzar and Chandler 1993). The angle of  $30^\circ$  is approximately the angle of vibrations that break HBs (Teixeira and Bellissent-Funel 1990). All the systems are tested in the moisture content range of 0 ~ 0.3.

### 8.2.3.2 Swelling strain

Swelling strain refers to the uniaxial swelling strain instead of volumetric swelling strain, unless otherwise stated. The uniaxial swelling strain is defined as:

$$\epsilon_X(m) = \frac{X(m) - X(0)}{X(0)} \quad (8-2)$$

where  $X(m)$  is the length of the system at moisture content  $m$ , and  $X(0)$  is the size of the system in dry condition using a Lagrangian approach. The uniaxial swelling strains in the three orthogonal directions ( $\epsilon_X$ , where  $X=x, y, z$ ) of are measured. The volumetric swelling strain  $\epsilon_V$  is defined similarly except for replacing lateral size  $X$  with the volume  $V$ . All the systems are tested in the moisture content range of 0 ~ 0.3.

### 8.2.3.3 Elastic constants and Poisson's ratio

For isotropic systems, including GGM, AGX, uLGN, cLGN, mixture 1 and mixture 2, the elastic constants are determined from the slope of the linear regime of stress-strain curves at room temperature. To construct the stress-strain curve for bulk ( $K$ ), Young's ( $E$ ) and shear moduli ( $G$ ), volumetric tensile, uniaxial tensile and shear strains are applied respectively, and the resulting stresses are collected. The stresses in MD are computed from the kinetic energy and the virials, as detailed in Abraham et al. (2015). Stepwise strains are applied to a given structure with each step straining around 0.01% of the initial dimension. Every step is followed by a relaxation run of 100 ps to allow molecular rearrangement. The relaxation conditions for bulk, Young's and shear moduli are different. For bulk moduli, the strained structure is relaxed in the NVT ensemble. For Young's and shear moduli, the structure is relaxed with the strained dimension fixed and the other dimensions coupled to the barostat ( $P=0$  Pa). For example, in Young's modulus measurement, for a sample undergoing uniaxial strain in the  $x$ -direction, the relaxation will be carried out with the  $x$  coordinates fixed while the  $y$  and  $z$  coordinates are coupled to a barostat to allow fluctuation. Due to the stepwise straining and the following relaxation, the influence of the strain rate is minimized. For Young's and shear moduli, the moduli measured in three principal straining directions are collected and averaged. The Poisson's ratio is defined as:

$$\nu_{ij} = -\frac{\epsilon_j}{\epsilon_i} \quad (8-3)$$

with subscripts  $i$  and  $j$  referring to orthogonal directions.

For the S2 composite, the system is orthotropic due to the crystalline cellulose fiber, where the elastic relation can be expressed as:

$$\begin{bmatrix} \epsilon_{xx} \\ \epsilon_{yy} \\ \epsilon_{zz} \\ \gamma_{yz} \\ \gamma_{zx} \\ \gamma_{xy} \end{bmatrix} = \begin{bmatrix} \frac{1}{E_x} & -\frac{\nu_{yx}}{E_y} & -\frac{\nu_{zx}}{E_z} \\ -\frac{\nu_{xy}}{E_x} & \frac{1}{E_y} & -\frac{\nu_{zy}}{E_z} \\ -\frac{\nu_{xz}}{E_x} & -\frac{\nu_{yz}}{E_y} & \frac{1}{E_z} \\ & & & \frac{1}{G_{yz}} \\ & & & & \frac{1}{G_{zx}} \\ & & & & & \frac{1}{G_{xy}} \end{bmatrix} \begin{bmatrix} \sigma_{xx} \\ \sigma_{yy} \\ \sigma_{zz} \\ \tau_{yz} \\ \tau_{zx} \\ \tau_{xy} \end{bmatrix} \quad (8-4)$$

where  $\epsilon$ ,  $\gamma$ ,  $E$ ,  $G$ ,  $\nu$ ,  $\sigma$  and  $\tau$  denote normal strain, shear strain, Young's modulus, shear modulus, Poisson's ratio, normal stress and shear stress, respectively.

In the composite, the  $z$ -axis denotes the longitudinal direction (L). Here the  $x$ - $y$  plane is assumed to be isotropic making the composite transversely isotropic, and both  $x$  and  $y$  axes are denoted as transverse direction (T). In the transverse plane, the following relations are thus established:

$$E_x = E_y, \nu_{xz} = \nu_{yz}, \nu_{zx} = \nu_{zy}, G_{TT} = \frac{E_T}{2(1+\nu_{TT})} \quad (8-5)$$

According to the symmetry of stress and strain tensors, the following relations hold:  $\frac{\nu_{zx}}{E_z} = \frac{\nu_{xz}}{E_x} = \frac{\nu_{yz}}{E_y}$ ,  $\nu_{xy} = \nu_{yx}$ . To conclude, for S2 composite model, five independent mechanical parameters are needed to describe the constitutive relation:  $E_z = E_L$ ,  $E_x = E_y = E_T$ ,  $G_{xz} = G_{zx} = G_{yz} = G_{zy} = G_{TL} = G_{LT}$ ,  $G_{xy} = G_{yx} = G_{TT}$ ,  $\nu_{zx} = \nu_{zy} = \nu_{LT}$ .

#### 8.2.3.4 Spatial density distribution of S2 composite

Spatial density distribution shows the density of matrix or water at a certain location with coordinates  $(x, y, z)$ . To obtain this distribution, the periodic box is partitioned into a number of cubes of identical volume  $V_i$ , volume which equals to the ratio of total volume  $V$  of the periodic box to the number of cubes. The center of the cube is  $(x, y, z)$ . The density of cube  $i$  equals the mass of the atoms within that cube divided by the cube volume  $V_i$ :

$$\rho_i(x, y, z) = \left\langle \frac{\text{mass}(x, y, z, t)}{V_i(x, y, z, t)} \right\rangle_t \quad (8-6)$$

where the bracket denotes time-averaging, over 10 ns of simulation, a time span sufficiently long that spatial fluctuations can be averaged out.

### 8.2.3.5 Interface frictional mechanics of S2 composite revealed by pulling tests

To measure the interface frictional mechanics, a study is performed along the lines of the study presented in Chapter 5 and 6, i.e. the CC is pulled along the longitudinal and the stress is extracted. The atoms of CC are attached to a virtual spring of constant  $k = 83 \text{ J m}^{-2}$ , which is in the weak spring stiffness case. The other end of the spring is moving at a constant velocity  $v = 1 \text{ m s}^{-1}$  along longitudinal axis of CC, as shown in Figure 8-7a. The shear stress is defined as the force acting on the virtual spring divided by the surface area of the four CCs, i.e.  $353 \text{ nm}^2$ . A sample of the stress vs. time curve of the dry S2 system is shown in Figure 8-7b.

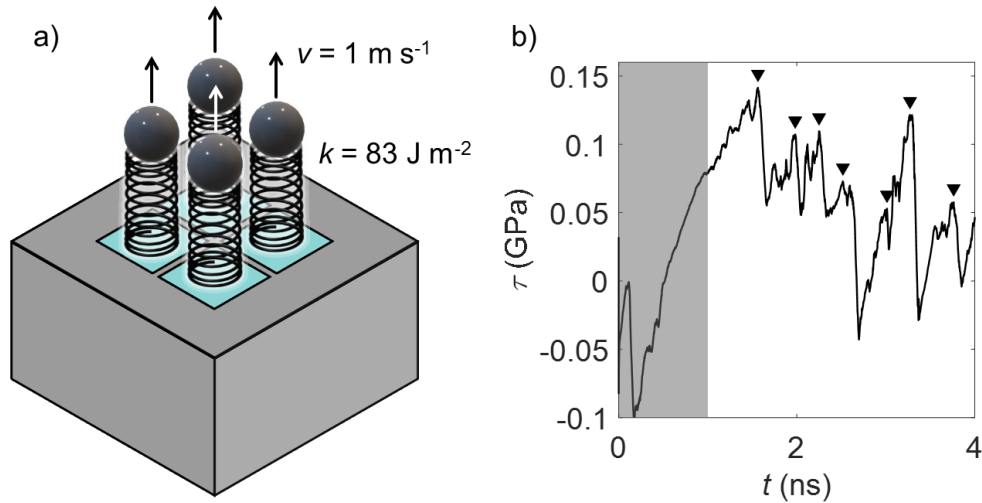


Figure 8-7 a) Schematic of pulling test setup. b) Interfacial stress as a function of time of dry S2 system, where the maximum shear stresses associated each with a displacement event are marked with triangles.

From the curve, the maximum shear stress  $\tau_{\max}$ , shown in Figure 8-7b) as the peak values marked with triangles, are collected and their averages are reported, following a protocol similar to the ones used in Chapters 5 and 6, as they define the shear strength of the interface. The average value and standard deviation are collected. Pulling tests along two opposite directions (+z and -z) are carried out and the  $\tau_{\max}$  values are averaged. The system is tested in the moisture content range of  $0 \sim 0.3$ .

## 8.3 Results

### 8.3.1 Hygromechanics of S2-related materials and composites

This section presents the hygromechanical characterization, including hygroscopic swelling and moisture-induced mechanical weakening of S2-related materials and composites, namely components AGX, GGM, uLGN, cLGN, mixtures M1, M2 and composite S2.

#### 8.3.1.1 Hygroscopic swelling

The hygroscopic swelling is characterized as the uniaxial swelling strain as a function moisture content, as shown in Figure 8-8. Such swelling is generally linear except for some initial non-linearity explained by initial porosity filling mechanism (Kulasinski et al. 2017). The studied materials systems are of nanometer sizes and show nanoporous porosity. Water molecules first enter these existing pores explaining the lower swelling, and then new pore space between the polymeric chains is created and filled by water molecules resulting in swelling.

For the studied systems, at  $m \sim 0.3$ , the uniaxial swelling strain is  $\sim 0.1$ , agreeing well with experimental reports on wood cell wall of Douglas fir (Murata and Masuda 2006). More recent X-ray tomographic study of wood cell wall micropillar reported the average of uniaxial swelling of  $\sim 0.08$  at RH  $\sim 85\%$  (Rafsanjani et al. 2014). The swelling of wood cell wall material is found to be considerably larger than that of the wood, since the free swelling at cellular wall level is hindered by the other cell walls, namely S1 and S3 and, at higher scales, by the presence of rays and growth rings (Rafsanjani et al. 2014).

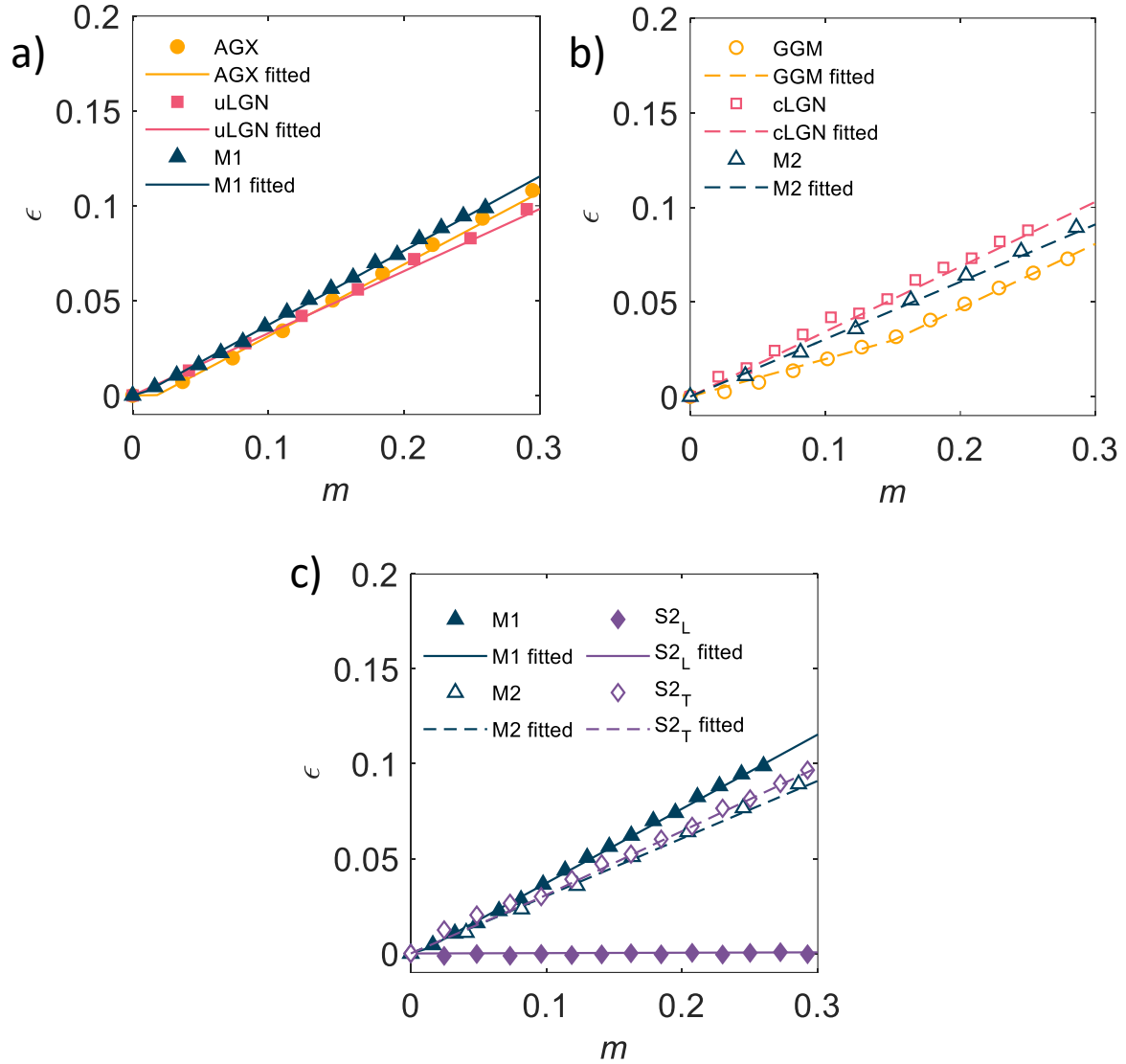


Figure 8-8 Uniaxial hygroscopic swelling strain of the systems as a function of moisture content, with MD measurements are represented by symbols and the fit by lines.

To fit the swelling curves, a piece-wise linear function is proposed:

$$\varepsilon = \begin{cases} \beta_A m, & m < m_A \\ \beta_B(m - m_A) + \beta_A m_A, & m \geq m_A \end{cases} \quad (8-7)$$

The swelling coefficient is  $\beta_A$  for  $m < m_A$ , and is  $\beta_B$  for  $m \geq m_A$ . The incremental form of the equation (8-3) is:

$$\Delta\varepsilon = \begin{cases} \beta_A \Delta m, & m < m_A \\ \beta_B \Delta m, & m \geq m_A \end{cases} \quad (8-8)$$

Following these forms, the swelling curves are fitted, and shown as lines in Figure 8-8. The fitting parameters are summarized in Table 8-2:

Table 8-2 Fitting parameters of uniaxial swelling strain as a function of moisture content.

| <b>material</b> | <b><math>\beta_A</math></b> | <b><math>m_A</math></b> | <b><math>\beta_B</math></b> |
|-----------------|-----------------------------|-------------------------|-----------------------------|
| AGX             | 0.010                       | 0.018                   | 0.379                       |
| GGM             | 0.198                       | 0.150                   | 0.340                       |
| uLGN            | -                           | 0                       | 0.328                       |
| cLGN            | -                           | 0                       | 0.343                       |
| M1              | 0.214                       | 0.011                   | 0.391                       |
| M2              | -                           | 0                       | 0.303                       |
| S2 <sub>L</sub> | -                           | 0                       | 0.002                       |
| S2 <sub>T</sub> | 0.308                       | 0.096                   | 0.336                       |

The parameter  $m_A$  indicates the moisture content extent of the initial nonlinear region. S2 transverse direction shows a high  $m_A$  value with a swelling coefficient  $\beta_A$  slightly lower as the swelling coefficient  $\beta_B$ , which can be understood as the higher volume of initial pores caused by structural mismatch between the crystalline fiber and amorphous matrix to be filled by water causing less swelling.

The parameter  $\beta_B$  is seen as the main swelling coefficient that describes the swelling in the higher moisture content range. Hemicelluloses generally swell more than lignin which can be explained by the higher hydrophilicity of hemicelluloses due to the larger density of hydroxyl groups. It is interesting to find that M1, which consists of AGX and uLGN shows higher swelling than its components, whereas M2 swells less than its components, namely GGM and cLGN. The mixing of AGX and uLGN somehow causes effective "repulsion" that enhances the swelling, while the mixing of GGM and cLGN results in effective "attraction" for  $m > 0.15$ . The swelling of S2 is assumed transversely isotropic and described by longitudinal and tangential swelling coefficients. In the longitudinal direction, the swelling is  $\sim 170$  times less than in the tangential direction. This is caused by the stiff fibers that do not swell and restrain the composite in longitudinal direction from swelling. The tangential swelling of S2 is comparable to the swelling of the other components and mixtures M1 and M2.

The volumetric swelling of isotropic and transversely isotropic materials can be expressed as:

$$\begin{aligned} \varepsilon_V &= (1 + \varepsilon_x)(1 + \varepsilon_y)(1 + \varepsilon_z) - 1 \\ &= \begin{cases} (1 + \varepsilon)^3 - 1, & \text{isotropic} \\ (1 + \varepsilon_L)(1 + \varepsilon_T)^2 - 1, & \text{transversely isotropic} \end{cases} \end{aligned} \quad (8-9)$$

In these polymer systems, where swelling is accompanied with the creation of new pore space, the porosity  $\varphi$  is a function of the volumetric swelling strain:

$$\varphi = \frac{\varepsilon_V}{1 + \varepsilon_V} \quad (8-10)$$

The porosity will be used in the later sections, to model to moisture dependence of elastic properties.

### 8.3.1.2 Moisture-induced weakening

Elastic moduli, namely bulk, Young's and shear moduli, are measured in the full hydration range and all display a weakening trend upon hydration, as shown in Figure 8-9. Generally, hemicelluloses show higher mechanical stiffness than lignins and stiffnesses of the two mixtures locate roughly in between the ones of their hemicellulose and lignin components.

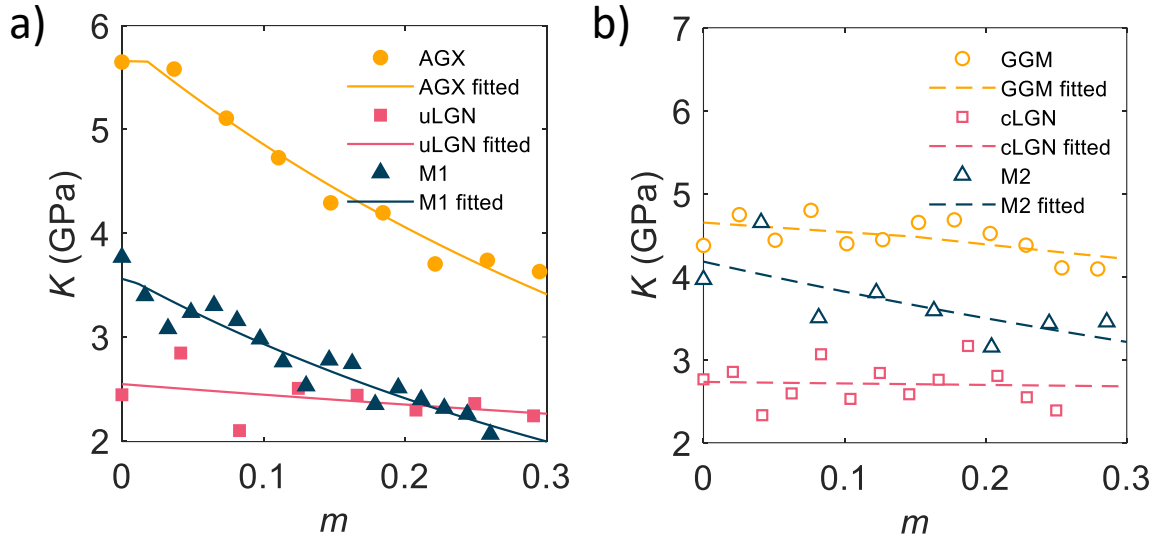


Figure 8-9 Bulk moduli as a function of moisture content. a) M1 and its components AGX and uLGN. b) M2 and its components GGM and cLGN. MD measurements are represented by symbols and fitted with equation (8-13) represented by lines.



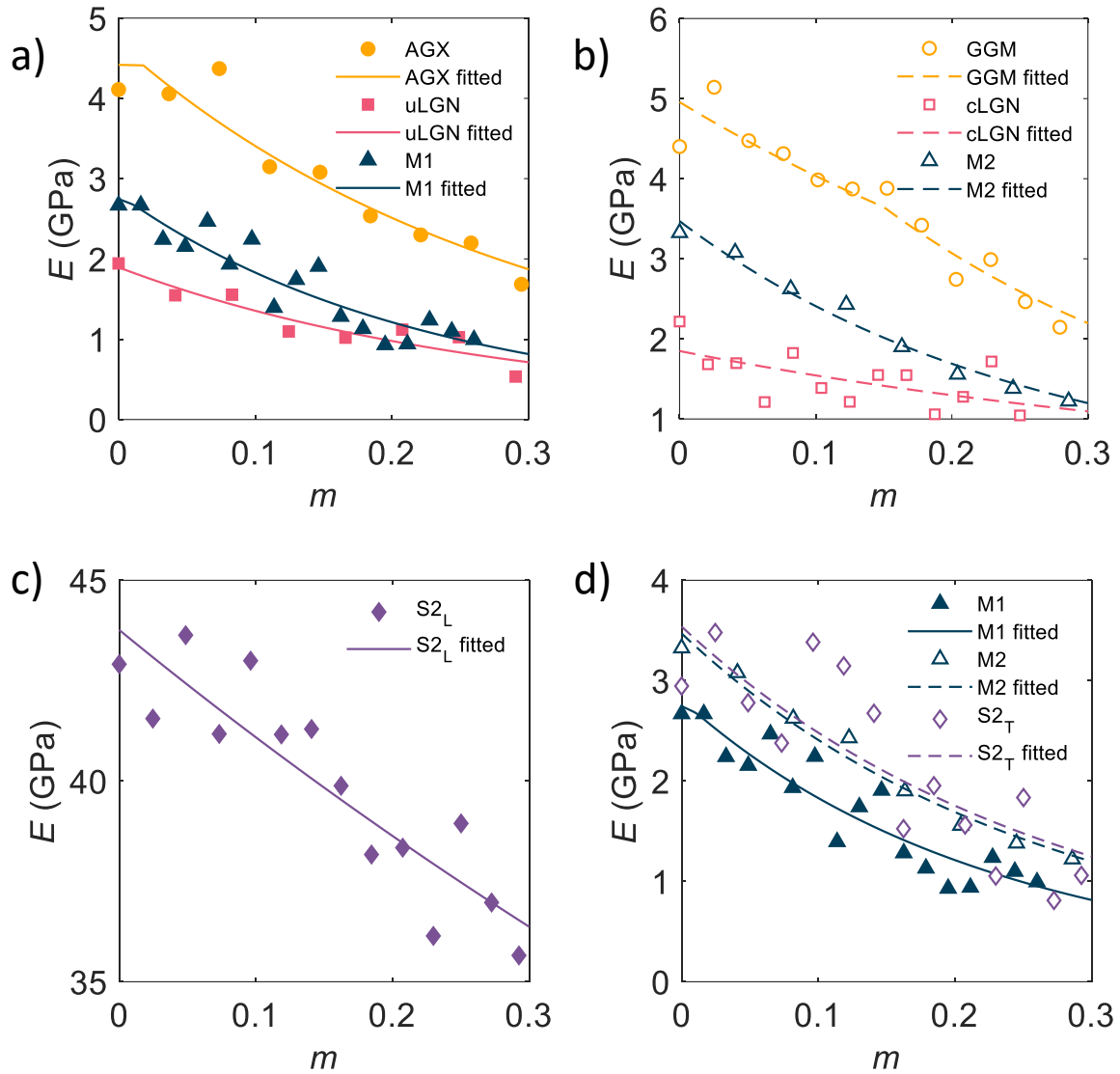


Figure 8-10 Young's moduli as a function of moisture content a) M1 and its components AGX and uLGN. b) M2 and its components GGM and cLGN. c) S2 longitudinal. d) S2 transverse and mixtures M1 and M2. MD measurements are represented by symbols and fitted with equation (8-13) represented by lines.

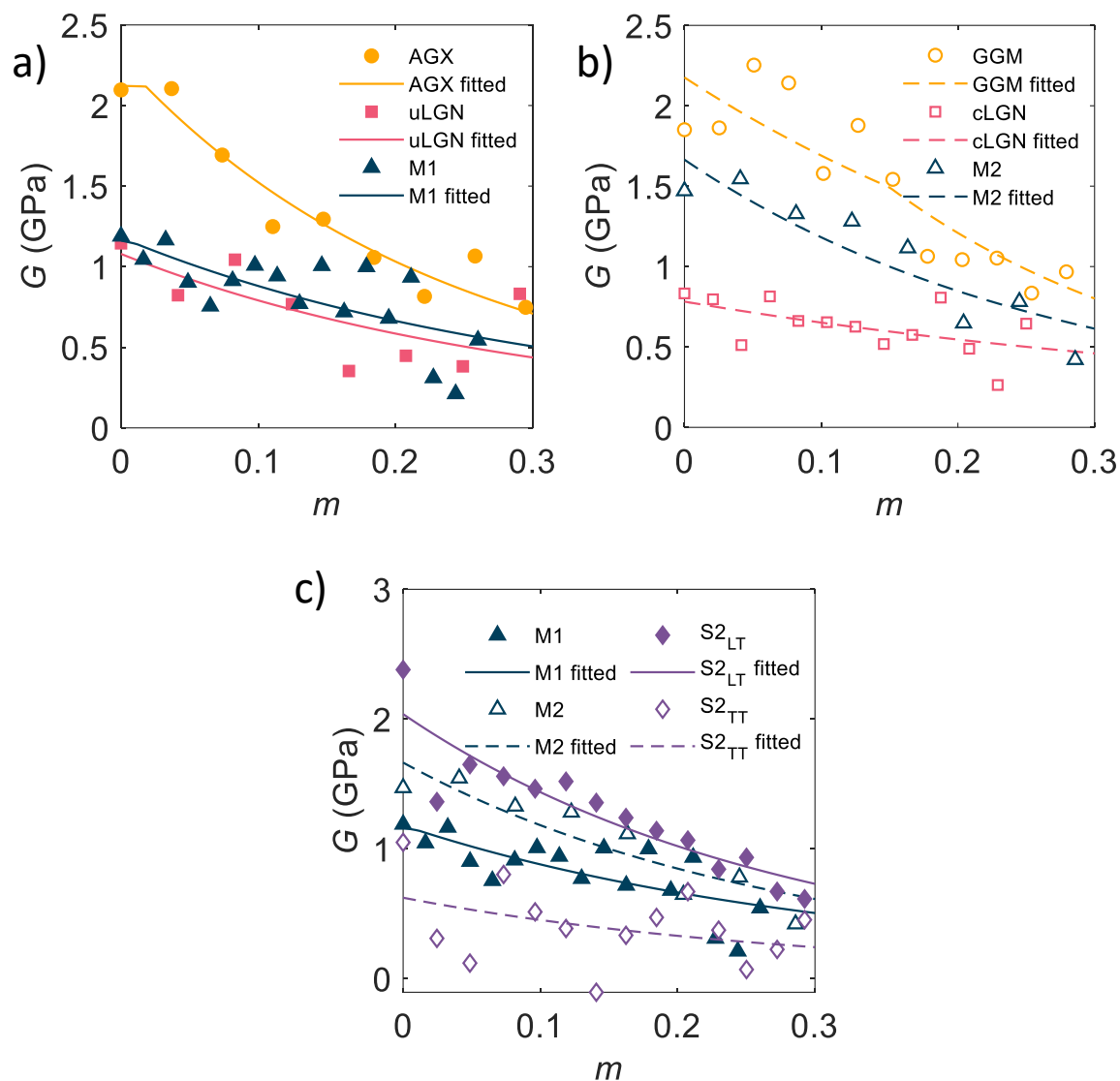


Figure 8-11 Shear moduli as a function of moisture content. a) M1 and its components AGX and uLGN. b) M2 and its components GGM and cLGN. c) S2 longitudinal, transverse and mixtures M1 and M2. MD measurements are represented by symbols and fitted with equation (8-13) represented by lines.

The MD measured moduli are in accordance with the available literature data, most of which is Young's modulus, as summarized in Chapter 2. In brief, the Young's moduli of xylan and glucomannan range from 1.8 ~ 5.4 GPa (Höije et al. 2005; Escalante et al. 2012; Kulasinski et al. 2016) and 2.5 ~ 4.3 GPa (Kulasinski et al. 2016), respectively. The reports on lignin Young's modulus gave 2.8 ~ 6.7 GPa (Cousins et al. 1975; Cousins 1976, 1977), which is higher than the MD results here. This is possibly due to their specimen preparation, where lignin powder was molded into rods where the pressurizing treatment densifies and stiffens the material.

The S2 composite exhibits a longitudinal Young's modulus of 36 ~ 44 GPa depending on the moisture content. Recent nanoindentation measurement suggested a similar range 26 ~ 40 GPa (Muraille et al. 2017). The longitudinal Young's modulus of S2 composite is ~ 10 times of the transverse one, which can be explained by the strong reinforcement effect by CC fiber. The axial Young's modulus of the CC fibrils is determined in MD by removing the matrix materials and then applying the protocol identical to the determination of the modulus of S2. It yields a value of 90 GPa, which is lower than the range, i.e. 100 ~ 160 GPa, suggested by the large number of mechanical characterizations of crystalline fibril, including experiments and simulations (Sakurada et al. 1962; Tashiro and Kobayashi 1991; Nishino et al. 1995; Šturcová et al. 2005; Rusli and Eichhorn 2008; Wu et al. 2014). The cellulose fibril in this study is weaker because the crystal here is not perfectly crystalline. More specifically, the chains at the surface of CC fibril moderately deviate from perfect crystal configurations as a consequence of relaxation and interaction with matrices, and therefore the CC fibril is weakened.

For homogeneous and isotropic materials, the bulk, Young's and shear modulus and Poisson's follow the relations:

$$G = \frac{3KE}{9K-E} \text{ and } \nu = \frac{3K-E}{6K} \quad (8-11)$$

It is confirmed by comparing all MD results, that the material systems, namely AGX, GGM, uLGN, cLGN, M1 and M2, comply with this relation. In other words, the shear moduli and Poisson's ratio can be well predicted using equation (8-11).

For transversely isotropic materials, the equation (8-12) holds. The S2 composite is found to comply roughly with this equation as shown in Figure 8-12.

$$G_{TT} = \frac{E_T}{2(1 + \nu_{TT})} \quad (8-12)$$

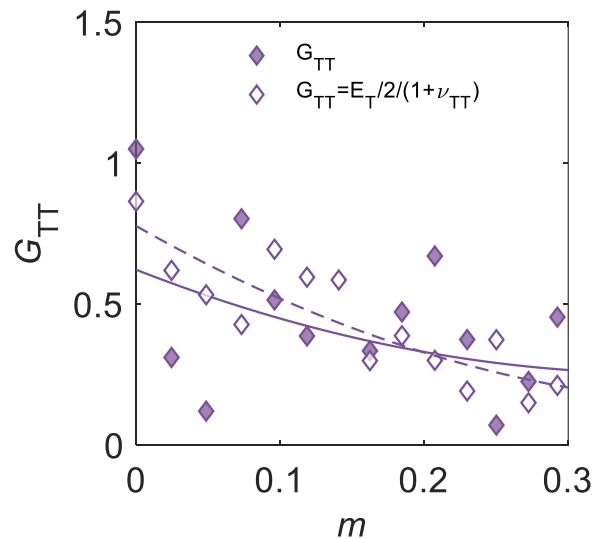


Figure 8-12 Shear modulus of S2 composite in the TT plane, comparison between MD measurement (solid symbol and line) and the prediction made by Young's modulus and Poisson's ratio (open symbol, dashed line).

MD results show that the elastic properties depend on moisture content. In this work, such moisture dependence is modeled by a dependence on porosity, as often done in literature (Nielsen 1984), a quantity related to swelling strain as defined in equation (8-10). The following power laws are used:

$$K = K_0(1 - \varphi)^{A_K} , \quad E = E_0(1 - \varphi)^{A_E} , \quad G = G_0(1 - \varphi)^{A_G} \quad (8-13)$$

where  $K_0$ ,  $E_0$  and  $G_0$  are the elastic properties at zero moisture content, and  $A_K$ ,  $A_E$  and  $A_G$  are fitting parameters. The lines in Figure 8-8 to Figure 8-11 are the fitting results and the parameters are summarized in Table 8-3.

Table 8-3 Fitting parameters of elastic moduli as a function of moisture content. The units of  $K_0$ ,  $E_0$  and  $G_0$  are GPa.

| material | $K_0$ | $A_K$ | $E_0$  | $A_E$ | $G_0$ | $A_G$ |
|----------|-------|-------|--------|-------|-------|-------|
| AGX      | 5.658 | 1.660 | 4.418  | 2.818 | 2.122 | 3.598 |
| GGM      | 4.653 | 0.420 | 4.957  | 3.497 | 2.176 | 4.291 |
| uLGN     | 2.546 | 0.423 | 1.896  | 3.475 | 1.079 | 3.217 |
| cLGN     | 2.734 | 0.067 | 1.875  | 1.791 | 0.791 | 1.789 |
| M1       | 3.561 | 1.772 | 2.747  | 3.709 | 1.162 | 2.541 |
| M2       | 4.182 | 1.007 | 3.470  | 4.071 | 1.665 | 3.818 |
| S2L      | -     | -     | 43.764 | 0.931 | 2.038 | 5.164 |
| S2T      | -     | -     | 3.540  | 5.242 | 0.624 | 4.753 |

The exponents  $A_E$ ,  $A_G$  and  $A_K$  indicate the decay rate of moduli with increasing hydration. The hemicelluloses are found to show the most severe weakening compared to the lignins. The transverse Young's modulus of S2 is also strongly influenced by hydration. In contrast, the longitudinal Young's modulus of S2 is the least weakened, which is due to the strong reinforcement of cellulose fibrils whose mechanical properties are independent of moisture content.

### 8.3.2 Mixture rule analyses

The compilation of hygromechanical data of wood polymers paves the way for comprehensive mixture rule analyses, allowing to reveal which mixing effect is at play. In this section, rule of mixture (RoM) analyses of density, swelling and weakening curves are presented. The RoM taking into account an interphase, representing interaction between the different components apart from simple mixing, is found to reproduce the MD measurements with good agreement.

#### 8.3.2.1 Density

Density is an important property of material. As shown by Kollmann (1975), the mechanical properties of wood polymers were shown to be related to their densities. The density of M1, M2 and S2 can be predicted by the fraction and density of each component. More specifically, with the

knowledge of the volume fraction of component  $f_{vj}^0$ , weight coefficient  $w_j^0$ , and density  $\rho_j$ , of component  $j$ , the compound density  $\rho'_M$  can be estimated by the following RoM:

$$\rho'_M = \sum_j f_{vj}^0 \rho_j \quad (8-14)$$

The prime symbol denotes prediction instead of MD measurement. The subscript  $M$  denotes the compound, i.e. M1, M2 or S2. The subscript 0 denotes the case where no interphase is present, showing the values before mixing. The volume fraction of component  $j$  is estimated by the weight coefficient  $w_j^0$  and density  $\rho_j$  of component  $j$  using the following equation:

$$f_{vj}^0 = \frac{w_j^0 / \rho_j}{\sum_j w_j^0 / \rho_j} \quad (8-15)$$

where  $\frac{1}{(\sum_j w_j^0 / \rho_j)}$  is the density of the compound system. The MD measured densities and the estimated volume fractions according to equation (8-15) are summarized in Table 8-4.

Table 8-4 Densities measured by MD and volume fractions.

| material | $\rho$ (g cm <sup>-3</sup> ) | $f_{vj}^0$ |      |
|----------|------------------------------|------------|------|
| AGX      | 1.30                         | 0.361      | } M1 |
| uLGN     | 1.22                         | 0.639      |      |
| GGM      | 1.24                         | 0.615      | } M2 |
| cLGN     | 1.30                         | 0.385      |      |
| M1       | 1.28                         | 0.242      | } S2 |
| M2       | 1.24                         | 0.360      |      |
| CC       | 1.50                         | 0.398      |      |
| S2       | 1.28                         | -          |      |

The RoM results are shown in Figure 8-13 by the orange bars. For all the compound systems, the RoM prediction without interphase is higher than the MD measurement. This difference stems from the mixing assuming no interaction between components and must be corrected. In polymer blends, in addition to the simple mixing of components, interactions between the components may occur. In general, a mixing rule may include, beside the contributions of each component, as well as an additional interaction term. In these blends, the different components may connect along their main chain with themselves leading to a local self-concentration effect (Lodge and McLeish 2000). On the other hand, there may be also connections between different components. These concentration and interaction effects lead to fluctuations in concentration of the components over the blend and as a result also in its density. The local fluctuations are not considered. Only the three phases, namely component 1, component 2 and the interphase between the two components, are considered.

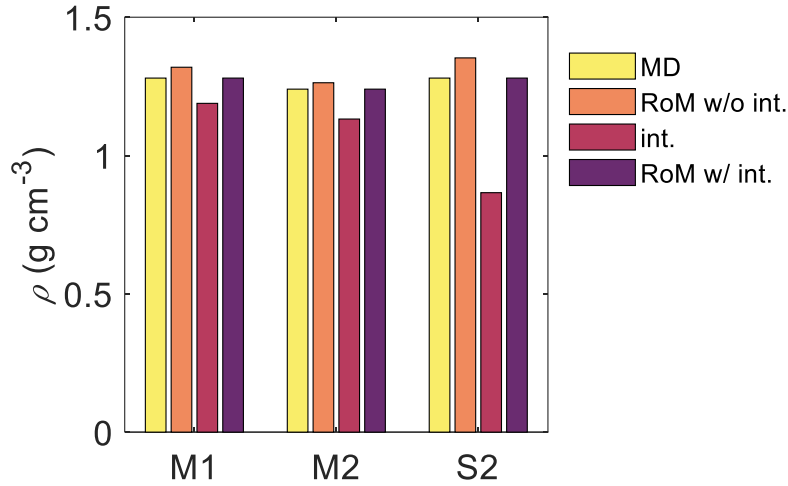


Figure 8-13 Density of compounds predicted by mixture rules.

An indication for the local self-concentration may be the number of hydrogen bonds formed between the component itself, while the number of hydrogen bonds formed between the two components is an indication of the interaction between the two components. The region where two components are affected by each other showing properties different from either party is referred to as the interphase. The interphase is included in the RoM as an individual component. In other words, in the equation (8-14) which describes the RoM without consideration of interphase, an extra interphase component term denoted by subscript  $i$  is added:

$$\rho'_M = f_{vi}\rho_i + \sum_j f_{vj}\rho_j \quad (8-16)$$

Here the volume fraction of the interphase  $f_{vi}$  is taken as the relative fraction of number of hydrogen bonds formed between the different components at dry condition  $\hat{\delta}$ :

$$f_{vi} = \hat{\delta} = \frac{\sum_{j \neq k} \#HB_{jk}}{\sum_j \sum_k \#HB_{jk} + \sum_j \#HB_{jj}} \quad (8-17)$$

where  $\#HB_{jk} = \#HB_{kj}$  denotes the number of hydrogen bonds formed between component  $j$  and  $k$ , while  $\#HB_{jj}$  are the hydrogen bonds within the component  $j$ . Consequently, the volume fractions of the other components are  $(1-\hat{\delta})$  times the value when no interphase is present and simple mixing applies:

$$f_{vj} = (1 - \hat{\delta})f_{vj}^0 \quad (8-18)$$

The relative fraction of number of hydrogen bonds formed between the different components  $\hat{\delta}$  for M1, M2 and S2 at dry state equal  $\hat{\delta}=0.210$ ,  $\hat{\delta}=0.176$  and  $\hat{\delta}=0.156$ , respectively. Details are shown in Table 8-5.

Table 8-5 Density of hydrogen bonds #HB/ $V_0$  ( $\text{nm}^{-3}$ ) in M1, M2 and S2 at dry condition.  $\hat{\delta}$  denotes the fraction of number of hydrogen bonds formed between the different components.

| M1             | #HB/ $V_0$<br>( $\text{nm}^{-3}$ ) | M2             | #HB/ $V_0$<br>( $\text{nm}^{-3}$ ) | S2             | #HB/ $V_0$<br>( $\text{nm}^{-3}$ ) |
|----------------|------------------------------------|----------------|------------------------------------|----------------|------------------------------------|
| total          | 2.34                               | total          | 5.43                               | total          | 8.50                               |
| AGX-uLGN       | 0.49                               | GGM-cLGN       | 0.96                               | CC-M1          | 0.02                               |
| AGX-AGX        | 1.14                               | GGM-GGM        | 4.15                               | CC-M2          | 1.01                               |
| uLGN-uLGN      | 0.72                               | cLGN-cLGN      | 0.32                               | M1-M2          | 0.30                               |
| $\hat{\delta}$ | 0.210                              | $\hat{\delta}$ | 0.176                              | CC-CC          | 5.37                               |
|                |                                    |                |                                    | M1-M1          | 0.37                               |
|                |                                    |                |                                    | M2-M2          | 1.43                               |
|                |                                    |                |                                    | $\hat{\delta}$ | 0.156                              |

The interphase density  $\rho_i$  is determined by substituting the MD measured compound density  $\rho_M$  into equation (8-14) and solving for the interphase density  $\rho_i$ . As shown by the red bars in Figure 8-13, the interphase densities are lower than the densities of the compounds, which may be the result of either structural mismatch or immiscibility. The mismatch is less in mixture M2 compared to the one in mixture M1, which is in accordance with the observations about the swelling coefficient, where it is found that the mixing of AGX and uLGN somehow causes effective "repulsion". Compared with M1 and M2, the interphase density of S2 is significantly lower than its composite overall density, which can be explained as the result of the structural mismatch at the cellulose crystal fiber and amorphous matrix interface, resulting in an increase in porosity. This aspect will be discussed in more detail below.

### 8.3.2.2 Sorption isotherms

The moisture content of the different components in a compound differs with each other. In the previous sections the mechanical properties of wood-related systems are reported as functions of moisture content. A more rigorous way is using relative humidity (water activity) or chemical potential as governing variable of the hygroscopic behavior instead of using moisture content. Wood polymers adsorb water following sorption isotherms, showing moisture content versus relative humidity (RH) or water activity ( $a_w$ ). As adsorption isotherms are used, in this work hysteresis between adsorption and desorption is neglected. Due to the large uncertainty in determining the chemical potential by MD, the isotherms of xylan, glucomannan and lignin from literature (Muraille et al. 2015) are retained to represent the sorption isotherms of AGX, GGM, cLGN/uLGN.

The Guggenheim-Anderson-de Boer (GAB) model has been shown to successfully describe the experimental sorption isotherms of cellulosic materials. The GAB model is written as follows:

$$m = C_m \frac{C_G K_{GAB} a_w}{(1 - K_{GAB} a_w)(1 - K_{GAB} a_w + C_G K_{GAB} a_w)} \quad (8-19)$$

where  $C_m$  corresponds to the concentration of the adsorbed monolayer (dry basis);  $C_G$  is the Guggenheim constant that is related to the heat of sorption of the monolayer;  $K_{GAB}$  is related to the heat of sorption of the intermediate layer. The parameter  $a_w$  denotes water activity or RH. The parameters for AGX, GGM, LGN and their mixtures are summarized in Table 8-6. The uLGN and cLGN uses the same set of parameters as LGN.

Table 8-6 GAB model parameters for AGX, GGM, LGN and their mixtures (Muraille et al. 2015).

| <b>material</b> | <b><math>C_m</math></b> | <b><math>C_G</math></b> | <b><math>K_{GAB}</math></b> |
|-----------------|-------------------------|-------------------------|-----------------------------|
| AGX             | 0.065                   | 24                      | 0.98                        |
| GGM             | 0.085                   | 30                      | 0.8                         |
| LGN             | 0.043                   | 17                      | 0.76                        |
| AGX:LGN = 1:1   | 0.053                   | 35                      | 0.91                        |
| GGM:LGN = 1:1   | 0.059                   | 22                      | 0.83                        |

It is noted that the mixtures in Ref. (Muraille et al. 2015), films made of AGX:uLGN = 1:1 and GGM:cLGN = 1:1 (mass ratio), are different from the M1 and M2 in terms of mass ratio. To construct the sorption isotherm for M1 and M2, the following mixture rule using weight coefficients is applied:

$$m(\text{RH}) = \sum_j w_j^0 m_j(\text{RH}) \quad (8-20)$$

The sorption isotherm of binary blend AGX:LGN=1:1 and GGM:LGN=1:1, measured by (Muraille et al. 2015) and predicted by equation (8-20), are shown by the dots in Figure 8-14. The mixture rule predictions are found to be in good agreement with the experimental measurements of mixtures, except for a slight overshooting at high RH for AGX-LGN blend. Therefore, it is concluded that the sorption isotherms of mixtures can be reliably predicted from the isotherms of their components using equation (8-20).



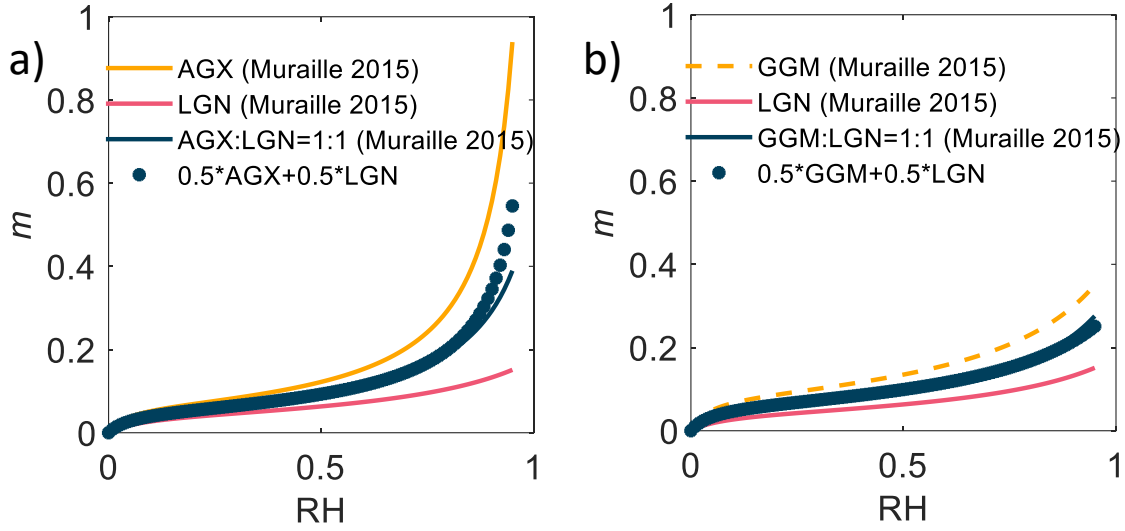


Figure 8-14 a) Sorption isotherms of GGM, LGN, GGM:LGN=1:1 (Muraille et al. 2015) and the prediction of mixture rule. b) Sorption isotherms of AGX, LGN, AGX:LGN=1:1 (Muraille et al. 2015) and the prediction of mixture rule.

Thus, equation (8-20), the sorption isotherms of M1, M2 and S2 are predicted by the isotherms of their components, as shown in Figure 8-15a, b and c. In general, M1 shows a stronger sorptive behavior than M2, due to the stronger sorption of AGX component. The S2 sorption isotherms is not too much different from M1 and M2. The variable  $\eta$  is defined as the fraction of the total moisture content of the mixture present in component 1, or  $\eta m$ , while the remaining part represented by  $(1-\eta)m$  is present in component 2 of the mixture, or

$$m = \eta m + (1 - \eta)m \quad (8-21)$$

Using equation (8-20), it is found that:

$$m = \eta m + (1 - \eta)m = w_1^0 m_1 + w_2^0 m_2 \quad (8-22)$$

where the subscript 1 stands for component 1, i.e. AGX in M1, GGM in M2, and M1 in S2, and subscript 2 stands for component 2, i.e. uLGN in M1, cLGN in M2, and M2 in S2. The equation (8-22) implies:

$$\eta = \frac{w_1^0 m_1}{m} \quad (8-23)$$

The parameter  $\eta$  as a function of RH is shown in Figure 8-15d, with the average values indicated by dashed lines. In this way, the relations between the moisture content of the component and compounds are established as:

$$m_1 = \eta \frac{m}{w_1^0} \text{ and } m_2 = (1 - \eta) \frac{m}{w_2^0} \quad (8-24)$$

These relations are used when given the moisture content of a compound to determine the moisture content of the components within that compound. This moisture content is needed to estimate the free swelling in the components of the mixture, which has to be known to determine the swelling of the compound, as will be seen below.

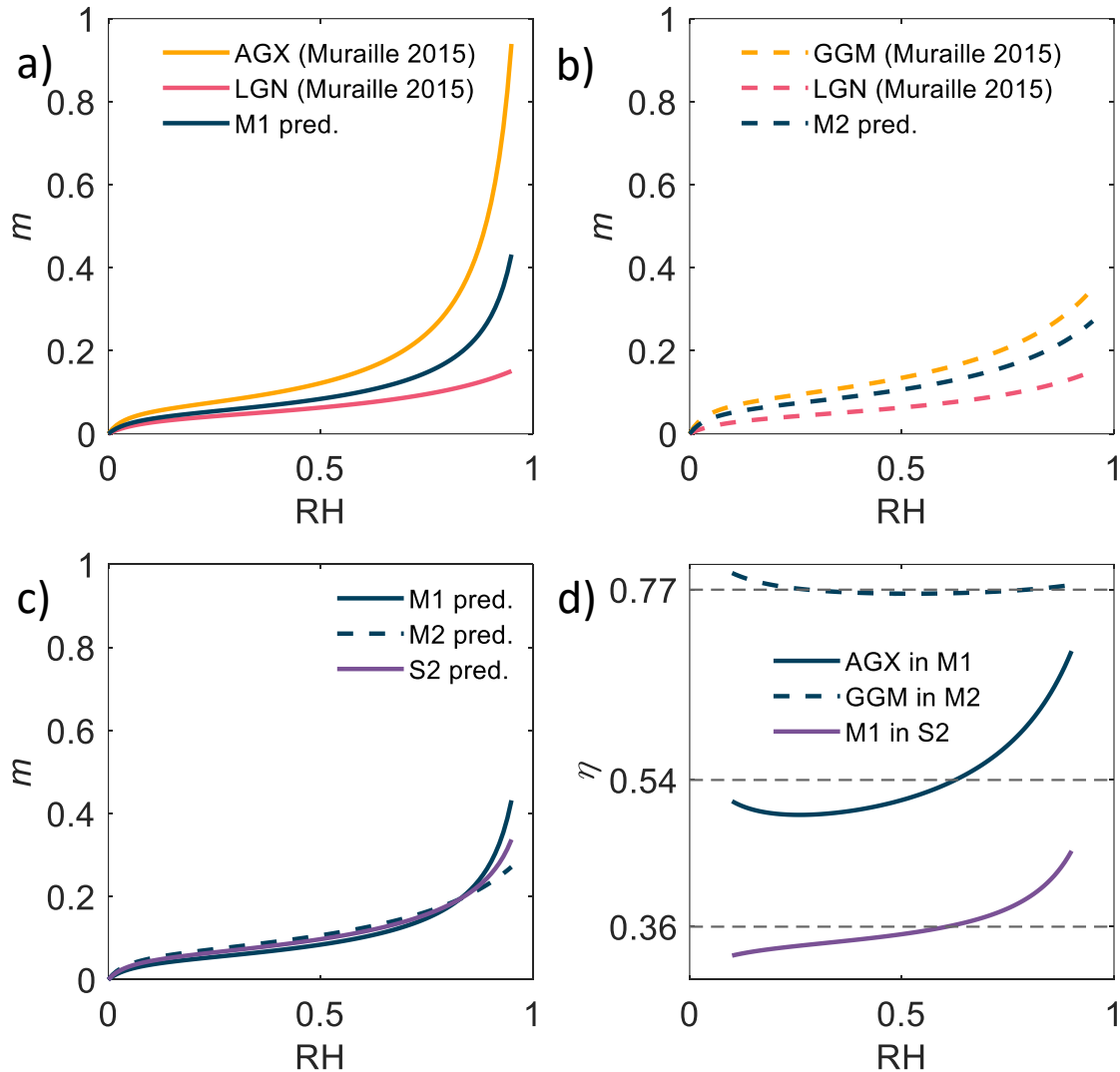


Figure 8-15 Sorption isotherms predicted by components based on mixture rule: a) M1 predicted by AGX:LGN=1:2. b) M2 predicted by GGM:LGN=7:4. c) S2 predicted by M1:M2=2:3. d) Parameter  $\eta$  as a function of RH.

### 8.3.2.3 Mixture rule analyses of matrices M1 and M2

The mixtures M1 and M2 are considered as homogeneous and isotropic materials. Their elastic moduli can be predicted by RoM with or without the presence of an interphase. Without an interphase, the RoMs read:

$$\begin{aligned}
K'_M &= f_{v1}^0 K_1 + f_{v2}^0 K_2 \\
E'_M &= f_{v1}^0 E_1 + f_{v2}^0 E_2 \\
G'_M &= f_{v1}^0 G_1 + f_{v2}^0 G_2 \\
f_{v1}^0 + f_{v2}^0 &= 1
\end{aligned}
\tag{8-25}$$

while when an interphase is present, the RoMs read:

$$\begin{aligned}
K'_M &= f_{v1} K_1 + f_{v2} K_2 + f_{vi} K_i \\
E'_M &= f_{v1} E_1 + f_{v2} E_2 + f_{vi} E_i \\
G'_M &= f_{v1} G_1 + f_{v2} G_2 + f_{vi} G_i \\
f_{v1} + f_{v2} + f_{vi} &= 1
\end{aligned}
\tag{8-26}$$

The subscripts  $M$ , 1, 2 and  $i$  denote compound, component 1 and 2, and interphase, respectively. As mentioned in the previous sections, the moisture dependence of elastic moduli is modeled as a function of porosity as shown in equation (8-13). It is noted that the elastic properties of the interphase are assumed to also depend on porosity similarly as the properties of the components do, thus equation (8-13) is also used for the interphase. The porosity is determined from the volumetric swelling strain of the compound using equation (8-10). The determination of the volumetric swelling strain of the compound is presented below (equations (8-27) and (8-28)), but since this swelling strain depends itself on the Young's moduli of the components, the elastic properties are discussed first. The volume fractions are determined based on equations (8-17) and (8-18).

The RoM predictions of the elastic properties of M1 are shown in Figure 8-16. Without the presence of an interphase, i.e. simple mixing without interaction, the RoM predictions are generally larger than the MD measurements. The interphase region due to the interaction of the two components is therefore assessed to be weaker than a simple mixture of the two components would be.

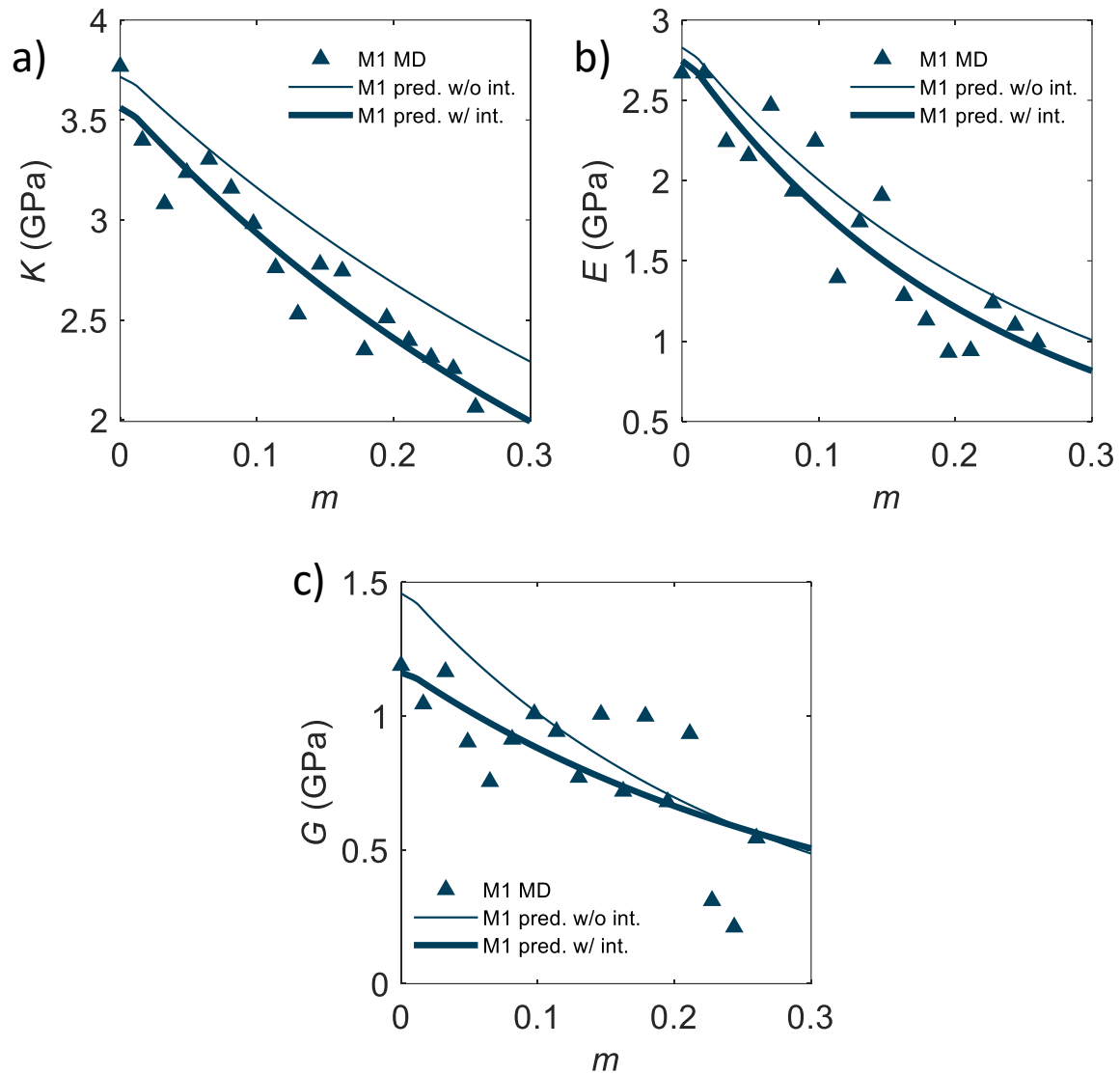


Figure 8-16 Elastic moduli of M1, comparison of MD measurements with RoM predictions without and with interphase: a) bulk moduli, b) Young's moduli and c) shear moduli.

The RoM predictions of M2 are shown in Figure 8-17. The bulk and Young's modulus predicted by RoM without interphase give higher values than the MD measurements. This means that the interphase is weaker than the simple mixture of the two components would be. The shear modulus predicted by RoM without interphase is almost the same as MD measurements.

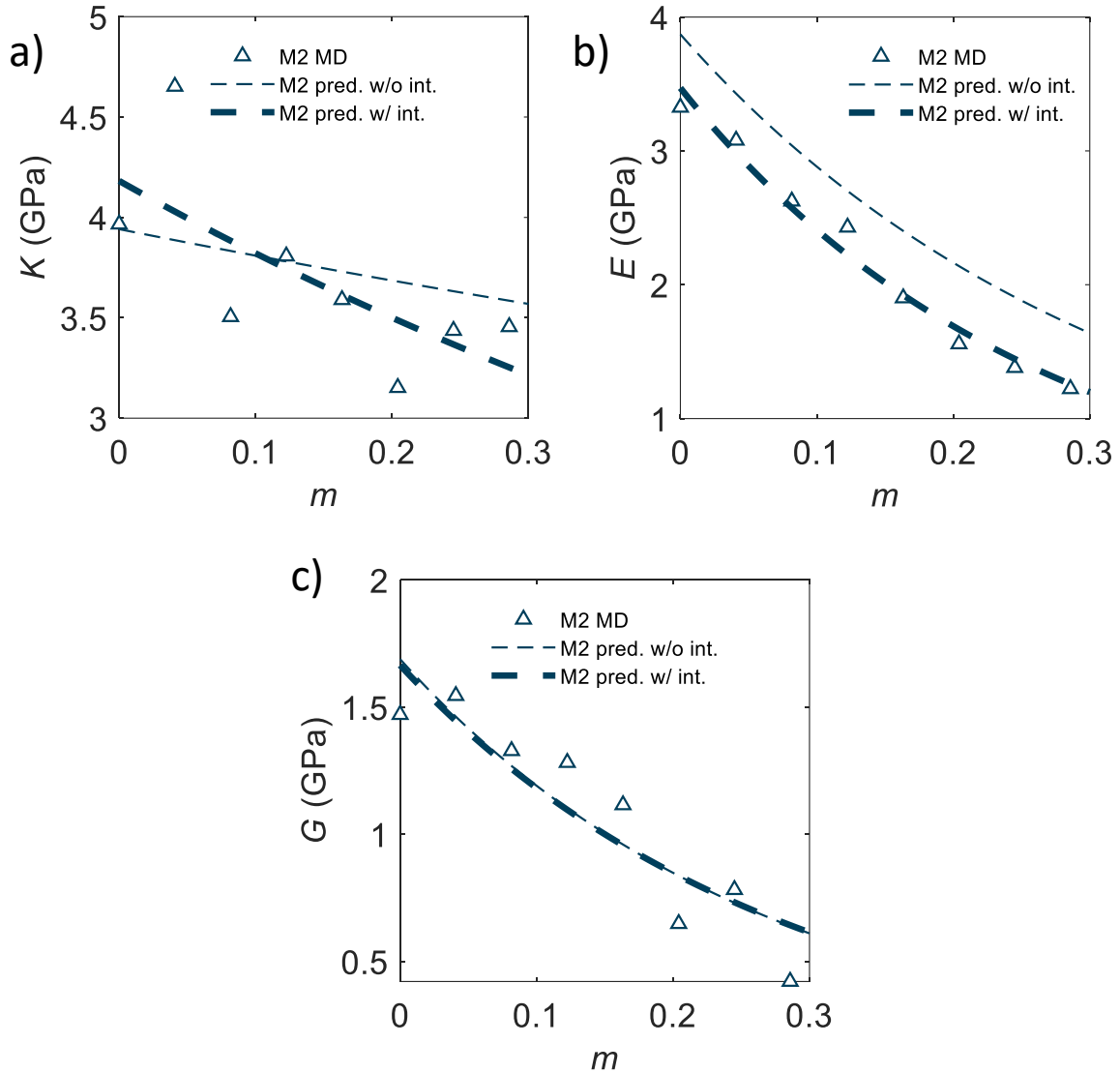


Figure 8-17 Elastic moduli of M2, comparison of MD measurements with RoM predictions without and with interphase: a) bulk moduli, b) Young's moduli and c) shear moduli.

The swelling strain of the matrices can be predicted by the mixture rule (Srisuk 2010), assuming the same swelling strain in mixture as in the components, and the internal stresses taken up by the components according to their volume fractions:

$$\Delta\varepsilon'_M = \frac{f_{v1}^0 E_1 \Delta\varepsilon_1 + f_{v2}^0 E_2 \Delta\varepsilon_2}{f_{v1}^0 E_1 + f_{v2}^0 E_2} \quad (8-27)$$

Note that the denominator equals the stiffness of the mixture predicted by RoM. Taking the interphase into account gives:

$$\Delta \varepsilon'_M = \frac{f_{v1} E_1 \Delta \varepsilon_1 + f_{v2} E_2 \Delta \varepsilon_2 + f_{vi} E_i \Delta \varepsilon_i}{f_{v1} E_1 + f_{v2} E_2 + f_{vi} E_i} \quad (8-28)$$

It is noted that, since the swelling strain depends on the stiffness and the stiffness depends on the porosity and thus swelling strain, equations (8-25) and (8-27), and equations (8-26) and (8-28) are solved iteratively, respectively.

The swelling strain RoM predictions with and without interphase are shown in Figure 8-18. It is observed that the prediction works very well even without consideration of an interphase.

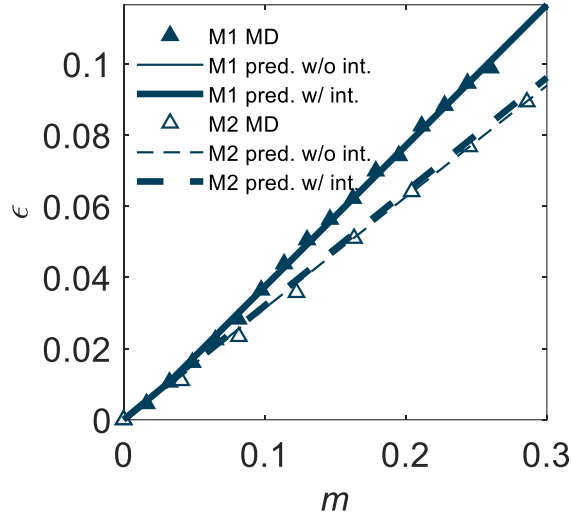


Figure 8-18 Swelling strains of M1 and M2, comparison of MD measurements with RoM predictions without and with interphase.

#### 8.3.2.4 Mixture rule analyses of S2 composite

The mixture rules for the S2 composite is different to the RoMs of the mixtures M1 and M2, as S2 is heterogeneous, consisting of a fibril CC and a matrix, and considered transversely isotropic. Due to the orthotropic behavior of the fibril, the fibril directions need to be taken into account. The CC fibril, denoted by subscript  $f$ , is moisture independent exhibiting neither swelling nor weakening. Assuming the fibril to be a transversely isotropic material, the CC phase follows the following elastic relations in the LT plane:

$$\begin{aligned} \sigma_{Lf} &= \frac{1}{1 - \nu_{LTf} \nu_{TLf}} (E_{Lf} \varepsilon_{Lf} + \nu_{TLf} E_{Lf} \varepsilon_{Tf}) \\ \sigma_{Tf} &= \frac{1}{1 - \nu_{LTf} \nu_{TLf}} (\nu_{LLf} E_{Tf} \varepsilon_{Lf} + E_{Tf} \varepsilon_{Tf}) \\ \tau_{LTf} &= G_{LTf} \gamma_{LTf} \end{aligned} \quad (8-29)$$

The properties of CC are given in Table 8-7, where  $E_L$  is estimated by this study as described in the method section and the other values are taken from literature (Mark 1967; Nakamura et al. 2004; Kulasinski et al. 2014b, 2015d; Chen et al. 2015):

Table 8-7 Elastic properties of CC (Mark 1967; Nakamura et al. 2004; Kulasinski et al. 2014b, 2015d; Chen et al. 2015).

| Young's modulus (GPa) |            | shear modulus (GPa) | Poisson's ratio   |                   |
|-----------------------|------------|---------------------|-------------------|-------------------|
| $E_L = 90$            | $E_T = 42$ | $G_{LT} = 4.4$      | $\nu_{LT} = 0.38$ | $\nu_{TT} = 0.48$ |

The elastic behavior of the composite is also assumed transversely isotropic, following the same equations (8-29). The elastic properties of the composite can be derived applying the following assumptions for the normal stress and strain in longitudinal and transverse directions, and for shear stress and strain:

$$\begin{aligned} \text{longitudinal} & & \sigma_L &= f_{vf}^0 \sigma_{Lf} + f_{vM1}^0 \sigma_{LM1} + f_{vM2}^0 \sigma_{LM2} \\ \text{direction} & & \varepsilon_L &= \varepsilon_{Lf} = \varepsilon_{LM1} = \varepsilon_{LM2} \end{aligned} \quad (8-30)$$

$$\begin{aligned} \text{transverse} & & \sigma_T &= \sigma_{Tf} = \sigma_{TM1} = \sigma_{TM2} \\ \text{direction} & & \varepsilon_L &= f_{vf}^0 \varepsilon_{Tf} + f_{vM1}^0 \varepsilon_{TM1} + f_{vM2}^0 \varepsilon_{TM2} \end{aligned} \quad (8-31)$$

$$\begin{aligned} \text{shear} & & \tau_{LT} &= \tau_{LTf} = \tau_{LTM1} = \tau_{LTM2} \\ & & \gamma_{LT} &= f_{vf}^0 \gamma_{LTf} + f_{vM1}^0 \gamma_{LTM1} + f_{vM2}^0 \gamma_{LTM2} \end{aligned} \quad (8-32)$$

Using these assumptions, the RoMs without interphase for S2 composite read:

$$\text{longitudinal modulus} \quad E'_L = f_{vf}^0 E_{Lf} + f_{vM1}^0 E_{M1} + f_{vM2}^0 E_{M2} \quad (8-33)$$

$$\text{transverse modulus} \quad E'_T = 1 / \left( \frac{f_{vf}^0}{E_{Tf}} + \frac{f_{vM1}^0}{E_{M1}} + \frac{f_{vM2}^0}{E_{M2}} \right) \quad (8-34)$$

$$\text{Poisson's ratio} \quad \nu'_{LT} = f_{vf}^0 \nu_{LTf} + f_{vM1}^0 \nu_{M1} + f_{vM2}^0 \nu_{M2} \quad (8-35)$$

$$\text{shear modulus} \quad G'_{LT} = 1 / \left( \frac{f_{vf}^0}{G_{LTf}} + \frac{f_{vM1}^0}{G_{M1}} + \frac{f_{vM2}^0}{G_{M2}} \right) \quad (8-36)$$

$$\text{longitudinal swelling} \quad \Delta \varepsilon'_L = \frac{f_{vM1}^0 E_{M1} \Delta \varepsilon_{M1} + f_{vM2}^0 E_{M2} \Delta \varepsilon_{M2}}{f_{vf}^0 E_{Lf} + f_{vM1}^0 E_{M1} + f_{vM2}^0 E_{M2}} \quad (8-37)$$

$$\text{transverse swelling} \quad \Delta \varepsilon'_T = f_{vM1}^0 (1 + \nu_{M1}) \Delta \varepsilon_{M1} + f_{vM2}^0 (1 + \nu_{M2}) \Delta \varepsilon_{M2} - \nu_{LT} \Delta \varepsilon_L \quad (8-38)$$

Note that, in the equation (8-38) for transverse swelling, the last term in the equation takes into account the Poisson's effect of the swelling of the composite in longitudinal direction. Due to the high stiffness of the fiber in longitudinal direction, the swelling of the composite in this direction is very small and the last term in equation (8-38) can be neglected.

Similarly, the RoMs with interphase for S2 composite read:

$$\text{longitudinal modulus} \quad E'_L = f_{vf}E_{Lf} + f_{vM1}E_{M1} + f_{vM2}E_{M2} + f_{vi}E_i \quad (8-39)$$

$$\text{transverse modulus} \quad E'_T = 1/\left(\frac{f_{vf}}{E_{Tf}} + \frac{f_{vM1}}{E_{M1}} + \frac{f_{vM2}}{E_{M2}} + \frac{f_{vi}}{E_i}\right) \quad (8-40)$$

$$\text{Poisson's ratio} \quad \nu'_{LT} = f_{vf}\nu_{LTf} + f_{vM1}\nu_{M1} + f_{vM2}\nu_{M2} + f_{vi}\nu_i \quad (8-41)$$

$$\text{shear modulus} \quad G'_{LT} = 1/\left(\frac{f_{vf}}{G_{LTf}} + \frac{f_{vM1}}{G_{M1}} + \frac{f_{vM2}}{G_{M2}} + \frac{f_{vi}}{G_i}\right) \quad (8-42)$$

$$\text{longitudinal swelling} \quad \Delta\varepsilon'_L = \frac{f_{vM1}E_{M1}\Delta\varepsilon_{M1} + f_{vM2}E_{M2}\Delta\varepsilon_{M2} + f_{vi}E_i\Delta\varepsilon_i}{f_{vf}E_{Lf} + f_{vM1}E_{M1} + f_{vM2}E_{M2} + f_{vi}E_i} \quad (8-43)$$

$$\text{transverse swelling} \quad \Delta\varepsilon'_T = f_{vM1}(1 + \nu_{M1})\Delta\varepsilon_{M1} + f_{vM2}(1 + \nu_{M2})\Delta\varepsilon_{M2} + f_{vi}(1 + \nu_i)\Delta\varepsilon_i \quad (8-44)$$

The prediction of Young's moduli is shown in Figure 8-19. The inclusion of an interphase improves the prediction. The role of interphase is opposite in the two directions. While stiffening the composite in longitudinal direction, it weakens the composite in transverse direction. The different behavior of the interphase region between CC and matrix in longitudinal and transverse directions shows that the interphase is no longer isotropic, but, due to the interaction between matrix and fiber, the interphase becomes transversely isotropic, more stiff in longitudinal direction and weaker in transverse direction. It is speculated that this anisotropy is due to the alignment of the GGM polymer along the fibril axis due to intensive interaction, which will be discussed in the next section in more detail. It is important to note that, while the elastic properties of CC are not moisture dependent, the elastic moisture properties of the S2 layer shows a moisture dependence, especially in transverse direction, which has a high influence on the structural behavior of wood in different moisture conditions.



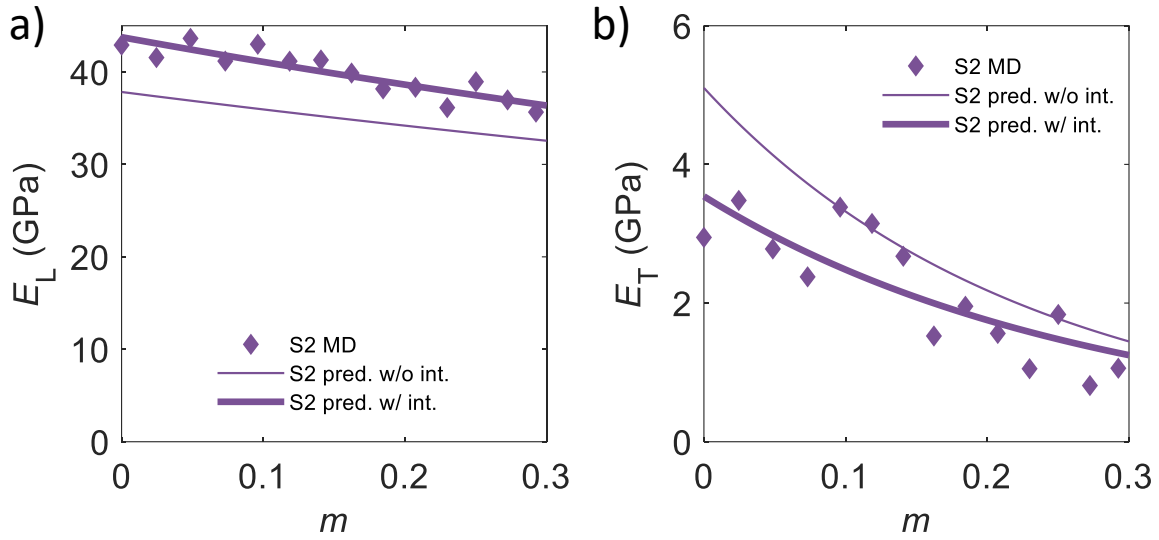


Figure 8-19 Young's moduli of S2, comparison of MD measurements with RoM predictions without and with interphase.

The prediction of shear modulus and Poisson's ratio are shown in Figure 8-20. While the RoM with interphase works better in predicting Poisson's ratio, the shear modulus is well predicted by both RoMs. The Poisson's ratio  $\nu_{LT}$  predicted by RoM without interphase is too low compared to the MD results, indicating a weaker interphase present between CC and matrix, which is in line with the transverse Young's modulus results.

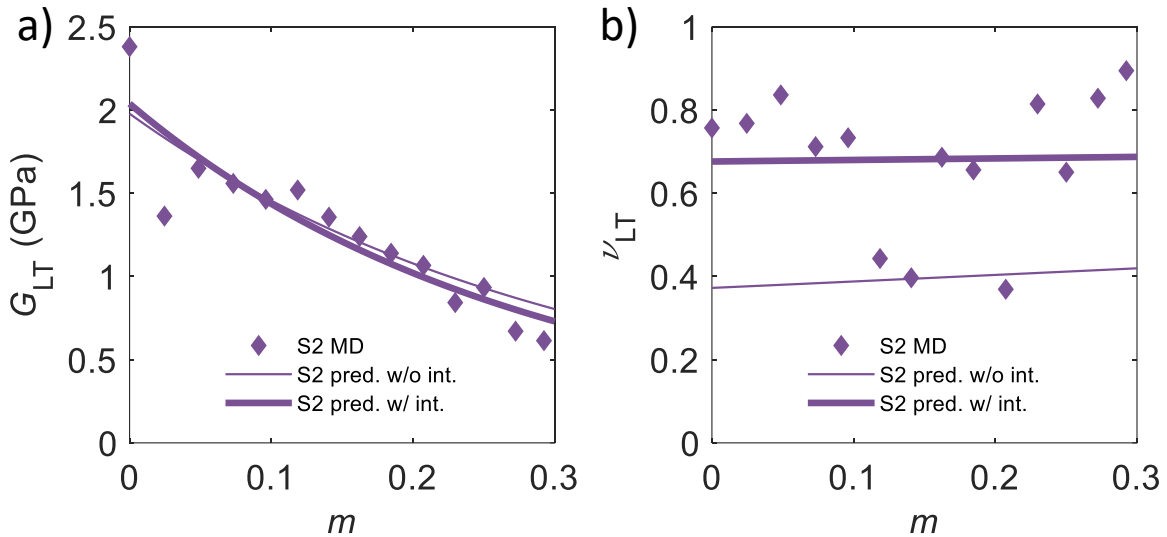


Figure 8-20 Shear modulus and Poisson's ratio of S2, comparison of MD measurements with RoM predictions without and with interphase.

### 8.3.3 Structure of S2 model and the mechanics of its fiber-matrix interface

Using the RoM, it is found that an interphase region is present around the fiber. In this section the structure of S2 is analyzed in more detail and the mechanics of its fiber-matrix interface is presented.

In Figure 8-21a, the S2 layer model is viewed from longitudinal direction in dry state. The dimensions of the S2 layer model is  $10.7 * 11.5 * 5.3 \text{ nm}^3$ , with a density of  $1.28 \text{ g cm}^{-3}$ , a value very close to the experimental ones (Kellogg and Wangaard 1969). The material distribution of the model is shown in Figure 8-21b. Visually inspection, aided by colors, yields that the location of mixture 2 (GGM+cLGN, red and blue) is next to CC forming an interphase region. Mixture 2 is then surrounded by the mixture 1 (AGX+uLGN, green and orange) forming the bulk matrix.

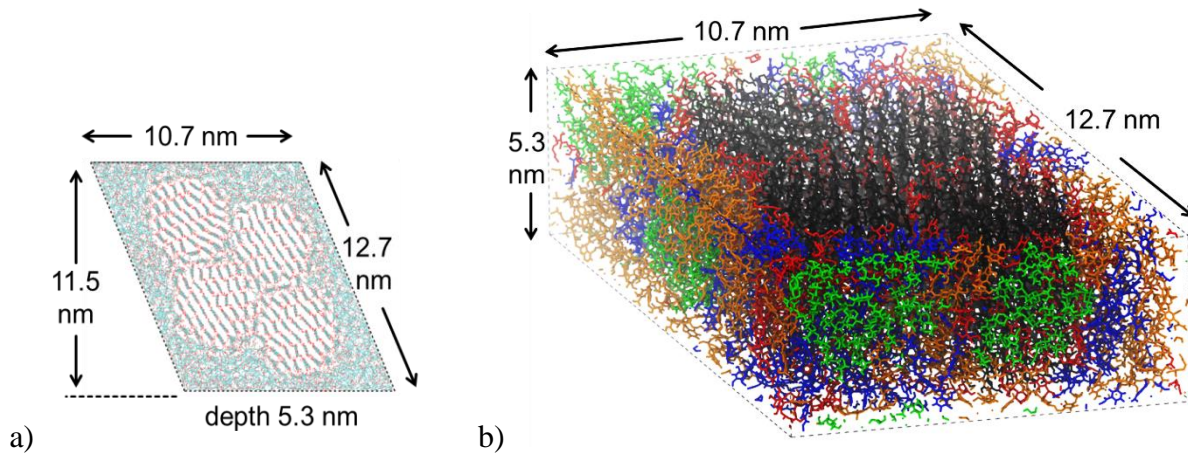


Figure 8-21 Final S2 layer model in dry state. a) View from longitudinal direction. Carbon, oxygen and hydrogen atoms are colored cyan, red and white, respectively. b) 3D view of dry S2 composite. Color denotes different components, namely CC in black, GGM in red, cLGN in blue, AGX in green and uLGN in orange.

### 8.3.4 Enrichment of matrix and water at interface

The spatial density distribution of the matrix and of water is calculated around the CC. The three-dimensional data is projected onto the transverse plane. The density distribution in the matrix under three different moisture contents, i.e. 0.02, 0.16 and 0.3, is shown in Figure 8-22a, b and c, respectively. With increasing moisture content, the dimensions of the system increase indicating the swelling of matrix material. Meanwhile, the density of matrix decreases with hydration (lighter color), meaning that new pore space is created, especially in the proximity of cellulose fiber surface. The dark spots at the CC interface indicate local density maxima of GGM aligning with the CC. As can be seen from Figure 8-22d, e and f, water density increases with moisture content and is evidently higher at the interface and in the interphase region around the fiber. It should be noted that the maximum value interfacial water density is around  $0.8 \text{ g cm}^{-3}$ , lower than that of bulk water ( $1 \text{ g cm}^{-3}$ ).

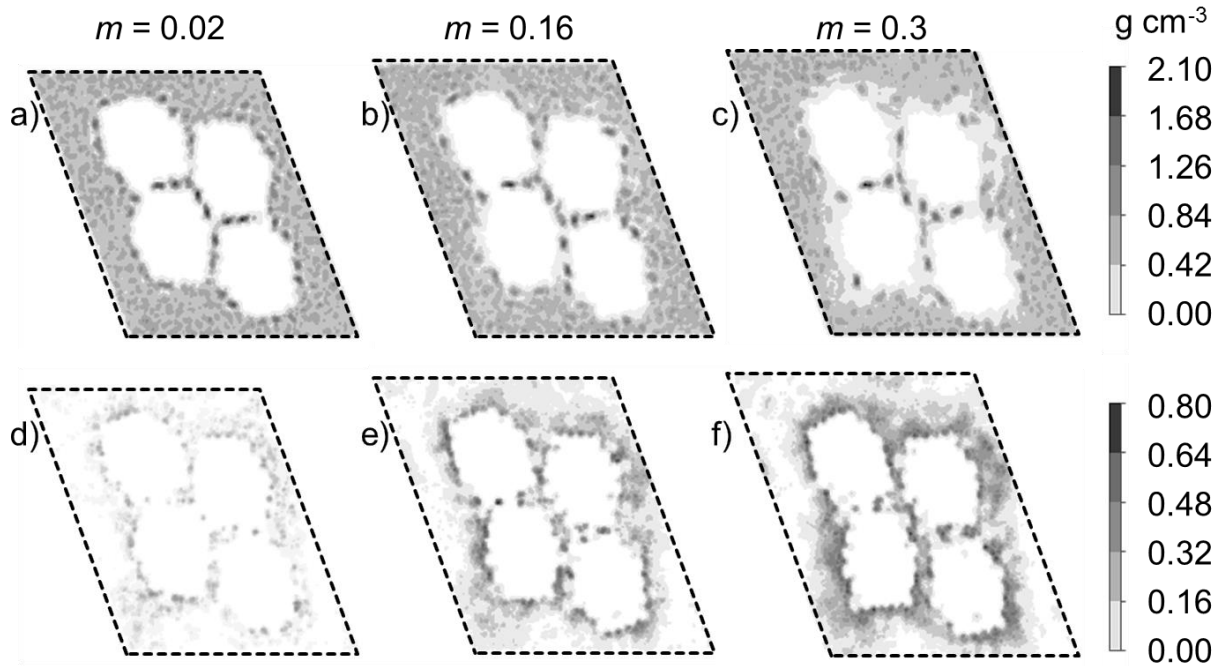


Figure 8-22 Spatial density distribution of a) b) c) matrix and d) e) f) water at three moisture contents. Note that the CC is left white for clarity, and is not representing its density.

The information can be further reduced into a one-dimensional plot, i.e. density as a function of distance to the CC surface  $d_{CC}$ , as shown in Figure 8-23. The density is zero within 0.2 nm of the CC surface, a result of prevailing repulsive forces in the immediate vicinity of the CC surface. This phenomenon is referred to as depletion. The depletion thickness reflects the interaction of the surface with the matrix or water (Huang et al. 2008). For both matrix and water, the density at the interface is higher than in the bulk, showing an enrichment. The difference is that while the matrix enrichment weakens with increment of moisture content, the water enrichment strengthens.

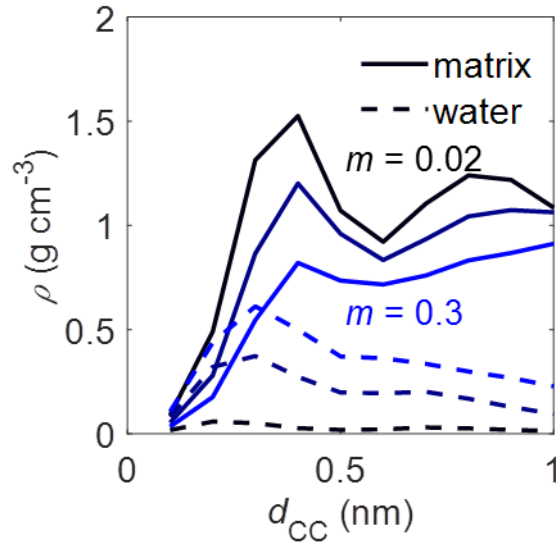


Figure 8-23 Density of matrix and water as a function of distance to the CC surface  $d_{CC}$ , for three moisture content, 0.02, 0.16 and 0.3.

The CC plays an important role in the sorption process of this composite system. While the core of the crystal fiber remains intact, the CC surface is heavily loaded with water molecules. The CC is the load bearing component of wood cell wall and the CC-matrix interface greatly defines the ability of load transfer, thus the overall mechanical performance of the composite. The interfacial enrichment may strongly affect the mechanics of wood cell wall which will be discussed further in the next section.

### 8.3.5 Interface weakening and hydrogen bonding

The interface shear strength is characterized via pulling test of the CC in presence of the S2 amorphous polymers, similarly to what was performed in Chapter 7. The shear stress - displacement of CC shows a stick-slip behavior. In the stick phase, shear stress increases while the displacement remains almost zero. Once the stress reaches a certain limit, called maximum shear stress  $\tau_{max}$ , the CC abruptly slides for some distance, called slip phase, and then sticks to a new location until the next slip event. The maximum shear stress  $\tau_{max}$  at different moisture contents is collected and shown in Figure 8-24. Moisture sorption reduces the shear stress by  $\sim 3$  times, indicating the weakening effect induced by moisture.

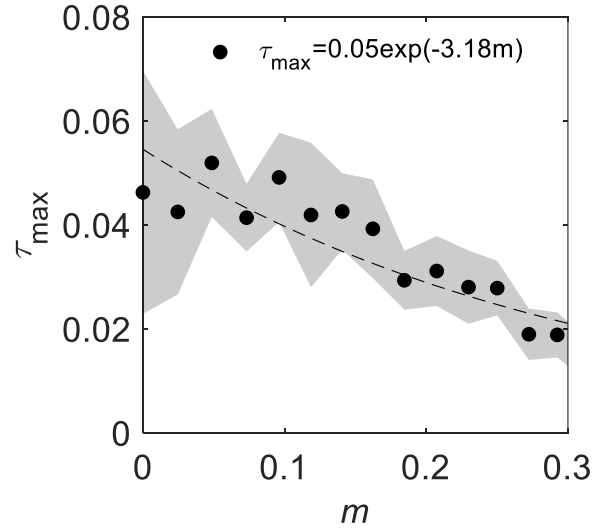


Figure 8-24 Maximum shear stress as a function of moisture content. Grey shade denote the standard deviation, and the dashed line is the dots fitted with a exponential function.

In S2 there are many kinds of hydrogen bonds formed between the different phases. One way of categorizing the hydrogen bonds is: within the matrix (M) and within the crystalline cellulose (CC), i.e. M-M, CC-CC, where the matrix is taken to be M1 and M2 together. The second group is HBs between matrix and fibril, i.e. M-CC, and the third group is between water (W) and matrix, i.e. W-M and between water and fibril, i.e. W-CC. Finally, the HBs between water molecules are considered, i.e. W-W. The number of hydrogen bond is normalized by the volume of S2 at dry state  $V_0$ . In addition to absolute number, the number of hydrogen bond can be rescaled using equation (8-45) and shown in Figure 8-25.

$$\widehat{\#HB} = \frac{\#HB(m) - \#HB(0.3)}{\#HB(0) - \#HB(0.3)} \quad (8-45)$$

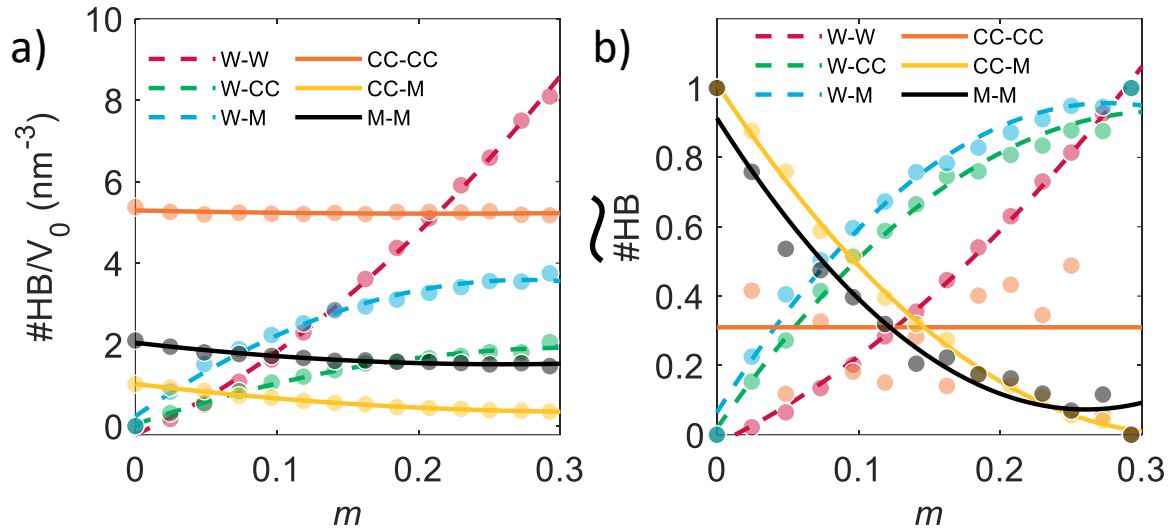


Figure 8-25 a) Absolute number of hydrogen bonds, b) rescaled number of hydrogen bonds within the S2 system in function of moisture content.

As can be seen in Figure 8-25a, at  $m \sim 0$ , the CC-CC HBs are the most abundant, accounting for  $\sim 65\%$  of the total number of HBs in S2, which agrees well with literature (O’Sullivan 1997). The CC-CC HBs stay almost unchanged as sorption goes on, supporting the assertion that CC is not affected by sorption. The adsorbed water stays at the surface instead of entering the crystal core and disrupting the HBs inside CC. It is noted that there is an important number of HBs within the matrix and at fibril-matrix interface.

With sorption, HBs within the matrix and at the fiber-matrix interface are broken, while the number of HBs affiliated with water rapidly grow. The previous section shows that water molecules tend to accumulate at the CC-matrix interface. The water replaces CC-matrix HBs with CC-water and matrix-water HBs, and thus weakening the interface, causing a reduction of maximum shear stress and its stiffness. The mechanical performance of fiber-reinforced composites depends on the stiffness and strength of the fiber-matrix interface. With the weakening of the interface induced by water, it can be expected that the ability of the interface to transfer load will diminish and irreversible deformation can happen.

The trend of HB changes can be seen more evidently after rescaling, shown in Figure 8-25b. It is noted that the rescaled number of CC-CC HBs seems to fluctuate a lot which is caused by amplification of the very small amount of total change, resulting in a rather small value for the denominator of equation (8-45). The number of matrix affiliated HBs diminishes and the number of water affiliated HBs increases. It is interesting to note that, after rescaling, the HBs of CC-M and M-M follow almost the same decreasing curve, while the HBs of W-M and W-CC follow the same increasing curve, showing similar behavior in HB breaking mechanism.

When the matrix material is categorized into finer subclasses, such as M1 and M2, or even the individual components, such as AGX, uLGN, GGM and cLGN, many more types of HBs emerge by combination of these categories. While some types remain largely unchanged with hydration and are thus omitted, the most affected types of HBs are shown in Figure 8-26. The  $x$ -axis is ordered in the ascending of  $\Delta\#HB/V_0$ . The CC-M HBs suffer the largest loss and the main reason is the significant loss of CC-GGM HBs. Within the matrix, the most loss is again bore by GGM-GGM. This leads to the conclusion that GGM acts as a sort of “glue” and its moisture dependence plays a fundamental role in the hygromechanical behavior of the composite, especially at the fiber-matrix interface and in the interphase region around the fiber, as will be discussed in detail in the next section.

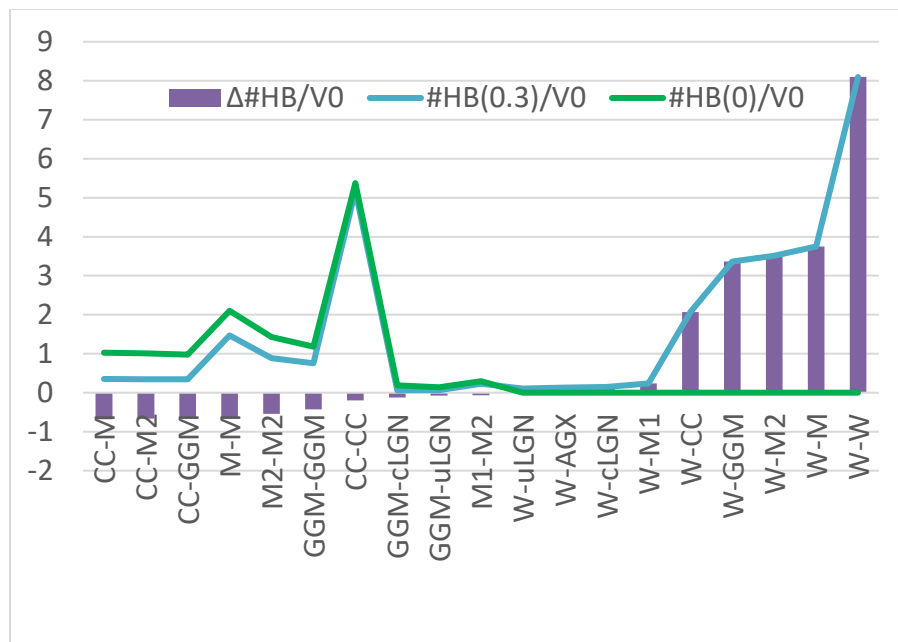


Figure 8-26 Rescaled number of different types of hydrogen bonds: dry condition in green line,  $m \sim 0.3$  in blue line and the difference in purple bars.

#### 8.4 Discussion and perspectives

Multiple evidences suggest the pivotal role of GGM in cell wall mechanics. For S2 in dry state, the GGM affiliated HBs are the second largest in number following the HBs formed within CC. The GGM HBs connect CC and the remaining part of the matrix and therefore is important for the overall mechanical performance of wood cell wall. Under hydrated condition, the GGM affiliated HBs suffer the most loss in number, especially the CC-GGM HBs. This loss is partly caused by the strong hydrophilicity of GGM as well as the large number of polar groups at the CC surface that are next to GGM. Moisture accumulates at the fiber-matrix interface. Such concentration of moisture leads to intensified disruption of interfacial hydrogen bonding, which consequently deteriorates the function of the interface of transferring shear stress. In many applications, wood is used as a load bearing component. It can be concluded that to achieve more stable wood material

with reduced tendency of swelling or weakening, the amount of GGM should be reduced, or the moisture sensitivity of GGM or of the CC surface should be modified. It is also possible that by introducing proper cross-linking between fiber and matrix the wood mechanical performance is improved (Stamm 1964).

Wood is known to be orthotropic. The swelling orthotropy is attributed to multiscale origins, including the alternation of late- and earlywood, the influence of rays, the arrangements of cells (Kollmann et al. 1968; Rafsanjani et al. 2014). In this study, the longitudinal swelling of S2 is almost negligible while the transverse swelling is comparable to the swelling of the matrix materials. The transverse mechanical performance of wood is strongly influenced by hydration. The sizable difference between longitudinal and transverse swelling and weakening of S2 supports that the swelling anisotropy is, at least partly, rooted at cell wall material scale. The mixture rule analyses reveal the mechanics of the interphase in S2 being orthotropic, i.e. stiffening and strengthening the composite in longitudinal direction, while weakening it in transverse directions. It can be concluded that the wood cell wall orthotropy stems not only from the oriented CC fiber but also the interphase formed by the interacting components that are mixed together.

It is noted that the modeling of S2 cell wall is a challenging task, for many critical aspects are still being revealed by ongoing experimental characterizations. The diameter of microfibrils varies from 3 to up to 60 nm according to various experimental reports (Salmén 2004; Fernandes et al. 2011; Terrett et al. 2019; Lyczakowski et al. 2019). This study models a microfibril consisting of four cellulose fibrils, which however should not be seen as the only possibility. Nonetheless, modeling of larger microfibrils can be achieved under the same protocol as shown in this study. It is noted that the hemicellulose GGM and lignin cLGN chains are chosen to be shorter than the experimental suggested lengths to facilitate the random insertion in the assembling procedure. This might pose an effect on S2 mechanics. In the future studies, larger systems can be built and thus allowing longer chains of GGM and cLGN.

## 8.5 Conclusion

A state-of-the-art atomistic model of softwood S2 layer is constructed using a bottom-up approach, taking great care to reflect the state of knowledge of the molecular structure of this cell layer. Individual components of S2 cell wall layer, including cellulose, glucomannan, xylan and two types of lignin, as well as two mixtures and different interfaces are built and mechanically characterized under the full hydration range via separate MD simulations. The work produces a complete set of micromechanical properties, including hydrogen bonding, swelling and weakening, over the full hydration range. Two configurations of 36-chain CC, with square and hexagonal cross-sections, are tested for layer adhesion energy and the hexagonal one is used for further modeling in S2 given its higher stability. Matrices of S2 are built and characterized using similar protocol. The ultimate S2 model has four cellulose crystals "glued" together by GGM. The CC and GGM bundle is wrapped by a mixture of cross-linked lignin and GGM, and then the matrix material made of AGX



and uLGN fills the remaining space. The resultant S2 system has a density of  $1.28 \text{ g cm}^{-3}$  and the mass ratio of each polymer is in accordance with the literature.

A complete compilation of hygromechanical data of S2-related polymers, their mixtures and composites, is presented, harvested from exercising hydration and mechanical tests. The swelling curves are fitted by a two-section piecewise linear function which is able to account for the initial nonlinear swelling region. Hemicelluloses are found to swell more than lignins. The interaction of AGX and uLGN is "repulsive", meaning that the mixture formed by the two swells more than its two individual constituents. The S2 shows strongly anisotropic swelling, with an almost negligible longitudinal swelling and a transverse swelling comparable to the swelling of the matrix materials. The weakening curves are fitted with power functions of porosity.

Comprehensive mixture rule analyses are carried out. The comparison between simple mixing and MD measurements reveal the effect of intermolecular interactions between different components and yield the properties of the interphase, i.e. the interacting region where properties differ from individual components. The interphases in M1, M2 and S2 feature densities lower than the bulk, indicating the structural mismatch. The interphase in M1 is found to be weaker than the bulk, supporting the previous claim that the interaction between AGX and uLGN is prone to "repulsion". The interphase in S2 is found to be anisotropic, probably due to an alignment of matrix molecules along the fibril axis, and thus to contribute to the overall anisotropy of S2 composite.

A detailed structural analysis of S2 composite reveals that the number of CC-CC HBs remains almost unchanged with hydration. Water mainly enters the fibril-matrix interface breaking mostly the GGM related HBs, the second most populous type of HBs after CC-CC HBs. According to Chapters 5 and 6, where HBs are found to strongly correlate with interfacial shear strength, this disruption of HB is highly likely to be the origin of moisture-induced shear stiffness/strength weakening of the S2 fibril-matrix interface.

To conclude, this chapter epitomizes the atomistic modeling methodology developed and utilized in the previous chapters, i.e. Chapter 3 and 4 which focus on the mechanics of bulk biopolymers and Chapter 5 and 6 on the mechanics of biopolymer interfaces. A compilation of hygromechanical data of S2 related systems is presented here. Through the mining of the dataset, insights about wood cell wall mechanics and the impact of hydration are gained at molecular level.

## Chapter 9 Conclusions and Perspectives

### 9.1 Summary

This thesis focuses on the moisture-related mechanical aspects of wood, one of the most important natural materials. Several unresolved mechanical issues regarding wood have their root deep in the molecular level interactions and nanoscopic hierarchical ultrastructure, the deciphering of which is hindered by the limited resolution of current experimental methods. In this thesis, molecular dynamics (MD) and, after upscaling, finite element modeling (FEM) are employed to interrogate the thickest layer of softwood cell wall, the second secondary layer S2, that is suspected to largely determine the mechanics of wood under full hydration range, elucidating the mechanisms at play on the atomistic scale and meanwhile reproducing ultrastructure and behavior of cell wall layer at polymeric composite scale.

Wood cell wall S2 layer consists of stiff crystalline cellulose fibrils, surrounded by soft matrix materials including hemicelluloses and lignins. The matrices are amorphous mixtures and are prone to sorption-induced isotropic swelling and weakening when subjected to environmental moisture, while the crystalline cellulose fibrils are rather anisotropic, with behavior almost independent of moisture conditions. Interfaces form where crystalline and amorphous phases come into contact. Recent experiments suggest that the fibrils may also come into contact forming interfacial connections referred to as "mechanical hotspot".

The plan of attack starts with the elaboration of the detailed microscopic picture of the moisture response of wood materials. One of the main hemicelluloses, arabinoglucuronoxylan (AGX), is chosen as the representative of wood hydrophilic biopolymers. The dry material possesses initial pores that are large enough to accommodate water molecules. The first adsorbed water fills the pores and the material shows a moderate swelling. With adsorption proceeding, polymer chains are pushed apart by water molecules causing breakage of polymer-polymer hydrogen bonds (HBs), increment of polymer-water contact area and creation of new porosity. Percolation appears at a moisture content  $m \sim 0.11$  and the breakage of HBs saturates at  $m \sim 0.18$ . Starting from  $m \sim 0.3$ , the newly adsorbed water molecules enlarge the existing water clusters instead of creating new ones. The impact of moisture adsorption manifests itself in a series of structural, physical and mechanical consequences. The heat of adsorption decreases, while the thermal expansion coefficient and heat capacity increase, all of which approach the respective values of bulk water. The mechanical moduli, specifically bulk, Young's and shear, decrease, referred to as weakening. It is found that all these thermodynamic and mechanical properties considered in a function of  $m$  collapse into one master curve after rescaling. Noteworthy is that this curve shows a crossover at  $m \sim 0.3$ , the mechanism of which is asserted to be the saturation of the first water adsorption layer and the growth of the second adsorption layer from this moisture content. Some sparse experimental reports observed similar saturations yet miss establishing the structure-property relationship.

Mechanics is the chief concern of this thesis. Moisture and heat have shown to induce at least two critical mechanical phenomena, namely non-linear swelling/expansion and weakening. The mechanistic interpretation of the influence of hydration and heating on a biopolymer is a topic of fundamental significance and broad implication. Uncondensed type of lignin is employed as the prototype polymer for this study. Hygric swelling and thermal expansion are shown to occur concomitantly with hydration and heating respectively, while mechanical weakening is also co-occurring with each phenomenon, in line with the frequently assumed phenomenological rule called the time-temperature-moisture superposition principle. A quantity called local stiffness is introduced to explain the weakening effect. Under the assumption of harmonic vibration and isotropy, the macroscopic elastic modulus is expressed as a function of the microscopic segmental motions of the polymer chains, a concise equation with strong predicting power. In effect, the predicted bulk moduli are in good agreement with the MD measurements, justifying the theoretical model. From an energetic point of view, the stiffness of the material stems from the strength of the primary and secondary bonds. While secondary bonds are influenced by both heat and moisture, the primary bonds are affected by heat alone. This indicates the fundamental difference between the action, long been assumed to be similar, of moisture and heat.

Complementary to the investigations of homogeneous amorphous systems, the thesis considers also heterogeneous structures. As cellulose nanocrystal (CC) reinforcements are the main component of wood cell wall material, two types of interfaces, CC-CC and CC-GGM, where GGM is referring to the hemicellulose galactoglucomannan, are studied in detail for their prevalence and importance. The mechanics of these interfaces is relevant not only for wood research but also for more general research on cellulose fiber-reinforced composites. The shear strength of the interfaces is measured using pulling tests. The interfaces, regardless of moisture level, show frictional stick-slip behavior with a periodicity corresponding to the length of the repeating unit of cellulose crystal, though the cases with dry interfaces have a more regular pattern than the wet cases. Such stick-slip behavior indicates the recovery of interface strength after irreversible deformation, the origin of which is ascribed to the re-formation of interfacial HBs. Systematic investigations of the influence of loading direction, misalignment and presence of moisture reveal direction-dependent behavior and weakening, all of which are explained by density, orientation or distribution of interfacial hydrogen bonds. Moreover, the density of HBs is found to correlate with interfacial measurements such as shear stress, sliding velocity and interface interaction energy, hence the force rendered by a single hydrogen bond is calculated to be  $\sim 1.3 \text{ E}^{-10} \text{ N}$ . The CC-GGM composite structure has an interphase, i.e. a region in the matrix next to the interface, that is influenced by CC and shows very different behavior from the bulk matrix. GGM polymer forms a rather ordered structure, seen as an alignment along the cellulose fiber axial direction, which is attributed to the strong interaction between CC and GGM. The interphase displays an enrichment in matrix and water atoms, which indicates the preferential adsorption happening near the interface. The stiffness of interphase is proportionate to the interface shear strength. For infinitely stiff interphase, a hypothetical case, the interfacial shear stress is solely controlled by HBs, whereas for the case of high compliance of the

interphase, the interface is considerably weakened. For both CC-CC and CC-GGM interfaces, moisture lowers the shear strength by about three times, implying that moisture may serve as an activator of interfacial sliding, a mechanism called the molecular switch.

Moisture-induced shape memory effect (SME) is one of the most intriguing hygromechanical manifestations of the behavior of wood. To decipher the mechanisms of SME, a finite element model of a prototype wood cell wall layer is built, with the hygromechanical properties of the components and the interfaces extracted from atomistic simulations. The swelling and weakening of the matrix and the weakening of the interface, as extracted by MD, are used as constitutive laws. Three representative systems of cell wall layer material are tested under a loading protocol that would resemble a practical treatment of wood to achieve SME. All systems show fixation of a deformed state while the model with undulating fiber pattern, mimicking the presence of so-called mechanical hotspots, exhibits a more prominent recovery and thus SME. The removal of interface moisture dependency eliminates the fixation thus the SME, demonstrating the critical role of interface mechanics in SME. In the view of energetics, for any material to show SME, there must be at least two meta-stable states, corresponding to two local minima in the hypersurface of potential energy. In dry conditions, the friction is high and therefore the system is trapped in one of the potential wells. The addition of moisture weakens the interface which lowers the energy barrier and therefore establishes a kinetically possible path allowing the system to a transformation between states with or without external mechanical loading. In short, it is speculated that the SME mechanism of wood cell wall material would consist of a fixation phase where deformation and potential energy are kinetically locked by the dry interface, and a recovery phase where the potential energy is released and the original shape recovered, as moisture activates the molecular switch which lowers the energy barrier between states.

With the understanding of the hygromechanics of wood polymers and interfaces achieved in the previous chapters, a natural and critical next step is to model an S2 layer composite in MD that offers, to the best efforts, a realistic representation of wood cell wall material. The bottom-up approach is used, where individual polymers, namely CC, GGM, AGX, condensed and uncondensed lignins (cLGN and uLGN), their mixtures, namely M1 and M2, are constructed and characterized in separate MD simulations harvesting the hygromechanical parameters of the systems. These components are then used as building blocks to build the atomistic model of S2 layer with the guidance of current experimental reports on the ultrastructure. The CC fibrils strongly restrain the swelling of the matrix along the fibril axial direction. Moisture is found to preferentially being adsorbed at the fibril-matrix interface, though no bulk water is formed as indicated by the adsorbed water density that stays below  $0.8 \text{ g cm}^{-3}$  for moisture content less than 0.3. Such moisture sorption weakens the shear strength of the interface by  $\sim 3$  times. Sorption, hydrogen bonding, swelling and weakening are all characterized for the composite following the same protocol as for the individual components and the two mixtures. The collected rich hygromechanical data permits a systematic analysis relying on the rule of mixture. The mismatch between the rule of mixture prediction and MD measurement calls for the consideration of the

interphase, a result of interaction between different components, with which the prediction greatly improves. GGM plays a pivotal role in associating the fiber and the matrix through hydrogen bonding.

## **9.2 Contribution to the research field**

In terms of scientific advances, the thesis has original contributions in the field of wood and polymer sciences, meta-stable systems, molecular dynamics methodology and multiscale modeling methodology.

This thesis contains systematic investigations of the single polymer systems, respecting the known molecular structures and studying in-depth their motions and interactions under full hydration range. The work provides new insights and explanations on mechanisms at play on the atomistic scale of several moisture-related phenomena. First, the work on xylan led to the identification of the role played by water configuration. Previous reports suggest the dominant role of hydrogen bond in mechanics of the wood polymers, and the adsorbed water would be casting its influence mainly through interruption of the hydrogen bonding network. This thesis shows as a new insight that the layering structure of adsorbed water may induce a profound transition, the crossover, observed in the master curve followed by a number of scaled thermodynamic and mechanical properties. Second, the origin of the mechanical weakening of biopolymer is demonstrated in both dynamical and energetical ways. The work on uncondensed lignin provides a route to disentangle the effects of moisture and heat. To do so, an indicator, the local stiffness, is proposed to theoretically relate the macroscopic modulus to molecular motions. Third, it is shown that, when mixing different polymers in a blend, interaction between the components in the compound can change the swelling and elastic properties of the mixture. For polymer mixtures in S2, this interaction mostly results in a decrease of density and a decrease in elastic properties. Fourth, the study of S2 with MD and rule of mixture identified that a transverse isotropic interphase region develops around the CC fibril, which displays a much higher stiffness in the axial direction of the fibril due to the alignment of GGM along with the CC phase. Finally, the interfaces behavior between CC and amorphous polymers as well as between CC-CC are shown to be characterized by a stick-slip behavior. Moisture at these interfaces may play the role of lubricant reducing the interfacial shear strength and mobilizing the sliding of the interfaces when loaded.

In terms of engineering and modeling advances, this research covers the identification of the materials and systems hygro-mechanical behavior in a comprehensive way. The studied polymers, their mixtures and interfaces comprising > 95% of the mass of softwood cell wall S2 layer are investigated with separate MD simulations under full hydration range. Critical information on swelling, elastic constants, hydrogen bonding, etc. is systematically presented. A state-of-the-art atomistic model of softwood S2 layer is constructed using a bottom-up approach. The harvested micromechanical properties of wood components and composites are validated with available

experimental reports, providing an unprecedented compilation of dataset which is critical, however, but was still missing for modeling of the moisture-related behavior of wood material.

Looking at a specific meta-stable mechanism in the intriguing moisture behavior of polymers such as S2, the mechanism of wood moisture-induced shape memory has yet to be completely understood. Experimental reports find that the phenomenon may originate from cell wall layer material. However, the in-depth understanding is hindered by the limited resolution of experiments and therefore modeling studies at lower scales are demanded. This thesis proposes a possible mechanism accentuating the key role of interface mechanics, a factor that has been much overlooked. This study combines computational methods by using finite element modeling of a prototype of wood cell wall layer based on the micromechanical parameters obtained from MD. Moisture-induced SME requires a molecular switch that is controlled by the breakage and reformation of hydrogen bonds upon moistening and drying, respectively, as revealed by the atomistic model of the interface behavior between CC-CC and CGM. With the interface law implemented, the SME is successfully reproduced for a system with undulating fiber mesh with hot-spots and the sub-mechanisms including fixation and recovery are elucidated. A conceptual picture of SME is presented where the deformed shape is kept kinetically by the high energy barrier and the elastic energy stored, energy to be released and the shape driven to recover once the energy barrier is lowered.

In terms of methodology, this thesis presents a computational framework that covers the full workflow of wood polymers hygromechanical modeling, i.e. the modeling of polymers, mixtures, interfaces and composites, hydration, thermodynamic and mechanical characterizations. Moreover, the atomistic insights are shown successfully to be upscaled to FE models which reproduce the shape memory effect of wood cell wall material. The multiscale modeling scheme can be applied to other wood behaviors and even other applications.

### **9.3 Outlook and future work**

The carried research converges to establish a state-of-the-art atomistic model of wood cell wall S2 layer while gathering a comprehensive micromechanical dataset. The developed model as well as methodology open to manifold possibilities in different scales of modeling, and several prospects are named here:

1. The configuration of S2 is diverse, and the four-cellulose crystals setup as used in this thesis is not the unique choice. Nanoconfined reinforcement shows significantly different mechanics to the larger-scale counterparts even when the mass ratio of fiber to the matrix is the same, namely size-dependency, making the characterization of different sizes of aggregates of cellulose fibers an interesting topic to explore.
2. The current study can be easily extended to include temperature effects which are an interesting topic for many reasons. Tweaking temperature grants access to many thermal

and thermodynamic insights, such as thermal expansion, the energy of hydrogen bonding and structural evolution.

3. An important characteristic of MD studies is the ability to output explicit trajectories of atoms. Statistics of the displacement provide rich information about the dynamics of the system such as molecular diffusion, permeability and heat conductivity, the study of which is desired for many fields. For example, many biopolymers, e.g. xylan, can potentially be used as packaging material where the permeability of oxygen is a critical index of performance.
4. In many conservation applications, additional chemicals are applied to wood. Famous examples are the Vasa and Mary Rose warships, precious wooden culture relics that were waterlogged over centuries and vulnerable to degradation. The current strategy of conservation is to impregnate archeological wood with polyethylene glycol. Fundamental research on molecular level interactions between wood polymers and polyethylene glycol should be warranted for better preservation.
5. Wood is often subject to harsh chemical treatment or environmental degradation, such as delignification or hemicellulose removal in industries like pulp and paper process and the UV light-induced aging. The cell wall material model in this thesis can serve as an excellent template or starting point for the research of such chemically treated wood. By partial removal of certain substances or reduction of the molecular weight of the polymers, wood samples of different compositions can be generated, and their mechanics studied.
6. Recently, the development of new wooden materials is of high interest in order to increase the use of wood as a sustainable material resource. New wooden materials are often based on the densification of wood and treatment of wood with other polymers or mineral materials. However, the possible spring-back of these materials to the original shape is a problem. Findings in this thesis could ameliorate the design of these new materials by better understanding the undesirable SME, by making the material interfaces at nanoscale less moisture sensitive, so that fixation is kept and no recovery occurs.
7. In plant biology, the atomistic models of wood cell wall can be used as a so-called "computational microscope" to capture the structural and dynamical aspects of plant growth and function, e.g. diffusion of nutrients.
8. The developed numerical framework can be applied to fibrous plants other than wood. One such promising source of natural fibers is flax which is gaining increasing popularity. While the cell wall structure of flax is very similar to that of wood, its chemical composition differs which, however, can be modeled using the same protocol developed here.

The current methodology could benefit from improvement as regards the following aspects:

1. Polymers are viscoelastic materials. The full characterization of such materials should involve dynamical mechanical analysis. This calls for the improvement of the sampling method because current simulations are limited to timespans of nano- to microseconds which are insufficient for modeling viscous behavior of wood polymers. The enhancement

of sampling will enable the modeling of time-dependent behavior such as relaxation and creep.

2. Wood is a strongly hygroscopic material and sorption is an important issue to deal with. While the current methodology introduces moisture through random insertion followed by relaxation, a more rigorous method could be to use Monte Carlo simulations in the grand canonical ensemble followed by relaxation in MD. Such improvement will allow the measurement of elastic constants in drained conditions and history-dependent behavior such as sorption hysteresis.
3. The multiscale approach combining MD and FE modeling can be greatly extended if poromechanical constitutive laws are implemented. Previously, using a poroelastic approach for sorption-induced deformation of biopolymer with adequate constitutive equations coupling mechanical and sorption behavior has been established valid for nanoporous media, where the state of the fluid is described by molar concentration and chemical potential of water, enabling the prediction of mechano-sorptive effect, etc. Also, along the line of poromechanical modeling which include coupling terms, MD studies could be used to investigate the molecular mechanisms that explains coupling, either of heat and moisture, as seen in lignin, or of moisture and mechanics.
4. Wood is a multiscale material and the upscaling over different scales, from molecular to cellular, growth ring and timber scale remains still a challenge. Adequate modeling at every scale and appropriate coupling of the different models at the different scales require, amongst other challenge development in upscaling and eventually downscaling, as phenomena modeled at higher scale might impact the phenomena at lower scales, such as cracking due to restrained shrinking when wood is dried.

The revealed shape-memory mechanism can be inspiring for innovative material design and fabrication:

1. The described mechanism for shape memory effect using moisture as the activator to break/restore hydrogen bonds as a molecular switch might lead to plentiful innovative ideas to fabricate new materials with well-designed functions, such as attenuators, valves triggered by moisture or other agents.
2. Materials with undulating fiber mesh with hotspots that can be activated or locked open a new horizon for composite materials that can change their stiffness when desired. Especially in the world of 3D woven composites, the behavior of the S2 layer could be a source of inspiration for developing new materials where 3D printing could be used as a manufacturing technique.

The molecular modeling of plant cell wall material has shown potential in elucidating the mechanisms of various physical processes and phenomena. There is a vast number of possibilities for future research. It can be expected that, with the upgrading of computational power, the development of enhanced sampling methods and the more solid and available structure information



of cell wall layer, the numerical modeling can achieve much more sophisticated material configuration and tackle even more complex behaviors.

## Bibliography

- Abraham MJ, Murtola T, Schulz R, et al (2015) Gromacs: High performance molecular simulations through multi-level parallelism from laptops to supercomputers. *SoftwareX* 1–2:19–25. doi: 10.1016/j.softx.2015.06.001
- Adler DC, Buehler MJ (2013) Mesoscale mechanics of wood cell walls under axial strain. *Soft Matter* 9:7138. doi: 10.1039/c3sm50183c
- Affdl JCH, Kardos JL (1976) The Halpin-Tsai equations: A review. *Polym Eng Sci* 16:344–352. doi: 10.1002/pen.760160512
- Agarwal UP (2006) Raman imaging to investigate ultrastructure and composition of plant cell walls: distribution of lignin and cellulose in black spruce wood (*Picea mariana*). *Planta* 224:1141–1153. doi: 10.1007/s00425-006-0295-z
- Agarwal UP, Ralph SA, Reiner RS, Baez C (2016) Probing crystallinity of never-dried wood cellulose with Raman spectroscopy. *Cellulose* 23:125–144. doi: 10.1007/s10570-015-0788-7
- Ahlgren PA, Goring DAI (1971) Removal of wood components during chlorite delignification of black spruce. *Can J Chem* 49:1272–1275
- Åkerholm M, Salmén L (2001) Interactions between wood polymers studied by dynamic FT-IR spectroscopy. *Polymer (Guildf)* 42:963–969. doi: 10.1016/S0032-3861(00)00434-1
- Åkerholm M, Salmén L (2003) The oriented structure of lignin and its viscoelastic properties studied by static and dynamic FT-IR spectroscopy. *Holzforschung* 57:459–465. doi: 10.1515/HF.2003.069
- Altaner CM, Jarvis MC (2008) Modelling polymer interactions of the ‘molecular Velcro’ type in wood under mechanical stress. *J Theor Biol* 253:434–445. doi: 10.1016/j.jtbi.2008.03.010
- Araki J, Wada M, Kuga S, Okano T (1999) Influence of surface charge on viscosity behavior of cellulose microcrystal suspension. *J Wood Sci* 45:258–261. doi: 10.1007/BF01177736
- Astley RJ, Harrington JJ, Stol K a. (1997) Mechanical modelling of wood microstructure, an engineering approach. 24:21–29
- Atalla RH (2009) Cellulose and the Hemicelluloses: Patterns for the Assembly of Lignin. 172–179. doi: 10.1021/bk-1998-0697.ch013
- Atalla RH, Agarwal UP (1985) Raman microprobe evidence for lignin orientation in the cell walls of native woody tissue. *Science (80- )* 227:636–638. doi: 10.1126/science.227.4687.636
- Barakat A, Winter H, Rondeau-Mouro C, et al (2007) Studies of xylan interactions and cross-linking to synthetic lignins formed by bulk and end-wise polymerization: a model study of lignin carbohydrate complex formation. *Planta* 226:267–281. doi: 10.1007/s00425-007-0479-1

- Barber NF (1968) A Theoretical Model of Shrinking Wood. *Holzforschung* 22:97–103. doi: 10.1515/hfsg.1968.22.4.97
- Bardage S, Donaldson L, Tokoh C, Daniel G (2007) Ultrastructure of the cell wall of unbeaten Norway spruce pulp fibre surfaces. *Nord Pulp Pap Res J* 19:448–452. doi: 10.3183/npprj-2004-19-04-p448-452
- Baumberger T, Heslot F, Perrin B (1994) Crossover from creep to inertial motion in friction dynamics. *Nature* 367:544–546. doi: 10.1038/367544a0
- Beever DK, Valentine L (2007) Studies on the sorption of moisture by polymers. II. The cellulose-cellulose acetate system. *J Appl Chem* 8:103–107. doi: 10.1002/jctb.5010080204
- Belbekhouche S, Bras J, Siqueira G, et al (2011) Water sorption behavior and gas barrier properties of cellulose whiskers and microfibrils films. *Carbohydr Polym* 83:1740–1748. doi: 10.1016/j.carbpol.2010.10.036
- Berendsen HJC, Grigera JR, Straatsma TP (1987) The missing term in effective pair potentials. *J Phys Chem* 91:6269–6271. doi: 10.1021/j100308a038
- Berendsen HJC, van der Spoel D, van Drunen R (1995) GROMACS: A message-passing parallel molecular dynamics implementation. *Comput Phys Commun* 91:43–56. doi: 10.1016/0010-4655(95)00042-E
- Bergander A, Salmén L (2002) Cell wall properties and their effects on the mechanical properties of fibers. *J Mater Sci* 37:151–156. doi: 10.1023/A:1013115925679
- Berglund J, Angles d’Ortoli T, Vilaplana F, et al (2016) A molecular dynamics study of the effect of glycosidic linkage type in the hemicellulose backbone on the molecular chain flexibility. *Plant J* 88:56–70. doi: 10.1111/tpj.13259
- Besombes S, Mazeau K (2005) The cellulose/lignin assembly assessed by molecular modeling. Part 1: adsorption of a threo guaiacyl  $\beta$ -O-4 dimer onto a I $\beta$  cellulose whisker. *Plant Physiol Biochem* 43:299–308. doi: 10.1016/j.plaphy.2005.02.005
- Beste A (2014) ReaxFF study of the oxidation of lignin model compounds for the most common linkages in softwood in view of carbon fiber production. *J Phys Chem A* 118:803–14. doi: 10.1021/jp410454q
- Biot MA (1941) General Theory of Three-Dimensional Consolidation. *J Appl Phys* 12:155–164. doi: 10.1063/1.1712886
- Bockris JO, Devanathan MA V., Müller K (1963) On the structure of charged interfaces. *Proc R Soc London Ser A Math Phys Sci* 274:55–79. doi: 10.1098/rspa.1963.0114
- Bonham VA, Barnett JR (2001) Fibre Length and Microfibril Angle in Silver Birch (*Betula pendula* Roth). *Holzforschung* 55:. doi: 10.1515/HF.2001.026
- Brinkmann A, Chen M, Couillard M, et al (2016) Correlating Cellulose Nanocrystal Particle Size and Surface Area. *Langmuir* 32:6105–6114. doi: 10.1021/acs.langmuir.6b01376

- Brouillet-Fourmann S, Carrot C, Lacabanne C, et al (2002) Evolution of interactions between water and native corn starch as a function of moisture content. *J Appl Polym Sci* 86:2860–2865. doi: 10.1002/app.11288
- Burgert I (2006) Exploring the micromechanical design of plant cell walls. *Am J Bot* 93:1391–1401. doi: 10.3732/ajb.93.10.1391
- Burgert I, Keplinger T (2013) Plant micro- and nanomechanics: experimental techniques for plant cell-wall analysis. *J Exp Bot* 64:4635–4649. doi: 10.1093/jxb/ert255
- Busse-Wicher M, Gomes TCF, Tryfona T, et al (2014) The pattern of xylan acetylation suggests xylan may interact with cellulose microfibrils as a twofold helical screw in the secondary plant cell wall of *Arabidopsis thaliana*. *Plant J* 79:492–506. doi: 10.1111/tpj.12575
- Busse-Wicher M, Grantham NJ, Lyczakowski JJ, et al (2016a) Xylan decoration patterns and the plant secondary cell wall molecular architecture. *Biochem Soc Trans* 44:74–78. doi: 10.1042/BST20150183
- Busse-Wicher M, Li A, Silveira RL, et al (2016b) Evolution of xylan substitution patterns in gymnosperms and angiosperms: implications for xylan interaction with cellulose. *Plant Physiol* 00539.2016. doi: 10.1104/pp.16.00539
- Büyükoztürk O, Buehler MJ, Lau D, Tuakta C (2011) Structural solution using molecular dynamics: Fundamentals and a case study of epoxy-silica interface. *Int J Solids Struct* 48:2131–2140. doi: 10.1016/j.ijsolstr.2011.03.018
- Callister Jr WD (2000) *Materials Science and Engineering - An Introduction* (5th ed.)
- Canzar S, El-Kebir M, Pool R, et al (2013) Charge Group Partitioning in Biomolecular Simulation. *J Comput Biol* 20:188–198. doi: 10.1089/cmb.2012.0239
- Carmeliet J, Derome D, Dressler M, Guyer RA (2013) Nonlinear Poro-Elastic Model for Unsaturated Porous Solids. *J Appl Mech* 80:020909. doi: 10.1115/1.4007921
- Casdorff K, Keplinger T, Burgert I (2017) Nano-mechanical characterization of the wood cell wall by AFM studies: comparison between AC- and QI<sup>TM</sup> mode. *Plant Methods* 13:60. doi: 10.1186/s13007-017-0211-5
- Casdorff K, Keplinger T, Rüggeberg M, Burgert I (2018) A close-up view of the wood cell wall ultrastructure and its mechanics at different cutting angles by atomic force microscopy. *Planta* 247:1123–1132. doi: 10.1007/s00425-018-2850-9
- Cave ID (1972) A theory of the shrinkage of wood. *Wood Sci Technol* 6:284–292. doi: 10.1007/BF00357050
- Chaléat CM, Michel-Amadry G, Halley PJ, Truss RW (2008) Properties of a plasticised starch blend – Part 2: Influence of strain rate, temperature and moisture on the tensile yield behaviour. *Carbohydr Polym* 74:366–371. doi: 10.1016/j.carbpol.2008.03.002
- Chang J, Toga KB, Paulsen JD, et al (2018) Thickness Dependence of the Young's Modulus of

- Polymer Thin Films. *Macromolecules* 51:6764–6770. doi: 10.1021/acs.macromol.8b00602
- Charlier L, Mazeau K (2012) Molecular Modeling of the Structural and Dynamical Properties of Secondary Plant Cell Walls: Influence of Lignin Chemistry. *J Phys Chem B* 116:4163–4174. doi: 10.1021/jp300395k
- Chase Jr. MW (1998) Nist-JANAF Thermochemical Tables, Fourth Edition
- Chen L, Li A, He X, Han L (2015) A multi-scale biomechanical model based on the physiological structure and lignocellulose components of wheat straw. *Carbohydr Polym* 133:135–143. doi: 10.1016/j.carbpol.2015.07.002
- Chen M (2019) Sorption-Induced Deformation of Nanoporous Materials
- Chen M, Coasne B, Derome D, Carmeliet J (2020) Role of cellulose nanocrystals on hysteretic sorption and deformation of nanocomposites. *Cellulose*. doi: 10.1007/s10570-020-03247-x
- Chen M, Coasne B, Derome D, Carmeliet J (2019) Coupling of Sorption and Deformation in Soft Nanoporous Polymers: Molecular Simulation and Poromechanics. *J Mech Phys Solids* 137:submitted. doi: 10.1016/j.jmps.2019.103830
- Chen M, Coasne B, Guyer R, et al (2018) Role of hydrogen bonding in hysteresis observed in sorption-induced swelling of soft nanoporous polymers. *Nat Commun* 9:3507. doi: 10.1038/s41467-018-05897-9
- Chen W, Lickfield GC, Yang CQ (2004) Molecular modeling of cellulose in amorphous state. Part I: model building and plastic deformation study. *Polymer (Guildf)* 45:1063–1071. doi: 10.1016/j.polymer.2003.11.020
- Choi YS, Singh R, Zhang J, et al (2016) Pyrolysis reaction networks for lignin model compounds: unraveling thermal deconstruction of  $\beta$ -O-4 and  $\alpha$ -O-4 compounds. *Green Chem* 18:1762–1773. doi: 10.1039/C5GC02268A
- Colmars J, Dubois F, Gril J (2014) One-dimensional discrete formulation of a hygrolock model for wood hygromechanics. *Mech Time-Dependent Mater* 18:309–328. doi: 10.1007/s11043-013-9229-x
- Cosgrove DJ (2005) Growth of the plant cell wall. *Nat Rev Mol Cell Biol* 6:850–861. doi: 10.1038/nrm1746
- Cosgrove DJ (2014) Re-constructing our models of cellulose and primary cell wall assembly. *Curr Opin Plant Biol* 22:122–131. doi: 10.1016/j.pbi.2014.11.001
- Cosgrove DJ, Jarvis MC (2012) Comparative structure and biomechanics of plant primary and secondary cell walls. *Front Plant Sci* 3:. doi: 10.3389/fpls.2012.00204
- Coste R, Pernes M, Tetard L, et al (2020) Effect of the Interplay of Composition and Environmental Humidity on the Nanomechanical Properties of Hemp Fibers. *ACS Sustain Chem Eng* 8:6381–6390. doi: 10.1021/acssuschemeng.0c00566

- Cousins WJ (1978) Young's modulus of hemicellulose as related to moisture content. *Wood Sci Technol* 12:161–167. doi: 10.1007/BF00372862
- Cousins WJ (1976) Elastic modulus of lignin as related to moisture content. *Wood Sci Technol* 10:9–17. doi: 10.1007/BF00376380
- Cousins WJ (1977) Elasticity of isolated lignin: Young's modulus by a continuous indentation method. *New Zeal J For Sci* 7:107–112
- Cousins WJ, Armstrong RW, Robinson WH (1975) Young's modulus of lignin from a continuous indentation test. *J Mater Sci* 10:1655–1658. doi: 10.1007/BF00554925
- Coussy O (2003) *Poromechanics*. John Wiley & Sons, Ltd, Chichester, UK
- Da Silva A, Kyriakides S (2007) Compressive response and failure of balsa wood. *Int J Solids Struct* 44:8685–8717. doi: 10.1016/j.ijsolstr.2007.07.003
- Dagnon KL, Shanmuganathan K, Weder C, Rowan SJ (2012) Water-triggered modulus changes of cellulose nanofiber nanocomposites with hydrophobic polymer matrices. *Macromolecules* 45:4707–4715. doi: 10.1021/ma300463y
- Dai Z, Wang G, Liu L, et al (2016) Mechanical behavior and properties of hydrogen bonded graphene/polymer nano-interfaces. *Compos Sci Technol* 136:1–9. doi: 10.1016/j.compscitech.2016.09.005
- Davies GC, Bruce DM (1997) A stress analysis model for composite coaxial cylinders. *J Mater Sci* 32:5425–5437. doi: 10.1023/A:1018691500653
- Dawson C, Vincent JF V., Rocca A-M (1997) How pine cones open. *Nature* 390:668–668. doi: 10.1038/37745
- Debye P (1913) Interferenz von Röntgenstrahlen und Wärmebewegung. *Ann Phys* 348:49–92. doi: 10.1002/andp.19133480105
- Dellon LD, Yanez AJ, Li W, et al (2017) Computational Generation of Lignin Libraries from Diverse Biomass Sources. *Energy & Fuels* 31:8263–8274. doi: 10.1021/acs.energyfuels.7b01150
- Delmer DP (1999) CELLULOSE BIOSYNTHESIS: Exciting Times for A Difficult Field of Study. *Annu Rev Plant Physiol Plant Mol Biol* 50:245–276. doi: 10.1146/annurev.arplant.50.1.245
- Den Haan R, Van Zyl WH (2003) Enhanced xylan degradation and utilisation by *Pichia stipitis* overproducing fungal xylanolytic enzymes. *Enzyme Microb Technol* 33:620–628. doi: 10.1016/S0141-0229(03)00183-2
- Deng Q, Li S, Chen Y (2012) Mechanical properties and failure mechanism of wood cell wall layers. *Comput Mater Sci* 62:221–226. doi: 10.1016/j.commatsci.2012.05.050
- Derome D, Griffa M, Koebel M, Carmeliet J (2011) Hysteretic swelling of wood at cellular scale probed by phase-contrast X-ray tomography. *J Struct Biol* 173:180–190. doi: 10.1016/j.jstructbiol.2011.05.005

10.1016/j.jsb.2010.08.011

- Derome D, Kulasinski K, Zhang C, et al (2018) Using Modeling to Understand the Hygromechanical and Hysteretic Behavior of the S2 Cell Wall Layer of Wood. In: *Plant Biomechanics*. Springer, pp 247–269
- Derome D, Rafsanjani A, Hering S, et al (2013) The role of water in the behavior of wood. *J Build Phys* 36:398–421. doi: 10.1177/1744259112473926
- Derome D, Rafsanjani A, Patera A, et al (2012) Hygromorphic behaviour of cellular material: hysteretic swelling and shrinkage of wood probed by phase contrast X-ray tomography. *Philos Mag* 92:3680–3698. doi: 10.1080/14786435.2012.715248
- Ding SY, Zhao S, Zeng Y (2014) Size, shape, and arrangement of native cellulose fibrils in maize cell walls. *Cellulose* 21:863–871. doi: 10.1007/s10570-013-0147-5
- Dinwoodie JM (2000) *Timber: Its Nature and Behaviour*. Routledge, London
- Doblin MS, Kurek I, Jacob-Wilk D, Delmer DP (2002) Cellulose Biosynthesis in Plants: from Genes to Rosettes. *Plant Cell Physiol* 43:1407–1420. doi: 10.1093/pcp/pcf164
- Donaldson L (2007) Cellulose microfibril aggregates and their size variation with cell wall type. *Wood Sci Technol* 41:443–460. doi: 10.1007/s00226-006-0121-6
- Donaldson L, Frankland A (2004) Ultrastructure of iodine treated wood. *Holzforschung* 58:. doi: 10.1515/HF.2004.034
- Donaldson L, Xu P (2005) Microfibril orientation across the secondary cell wall of Radiata pine tracheids. *Trees* 19:644–653. doi: 10.1007/s00468-005-0428-1
- Dorrestijn E, Laarhoven LJJ, Arends IWCE, Mulder P (2000) The occurrence and reactivity of phenoxyl linkages in lignin and low rank coal. *J Anal Appl Pyrolysis* 54:153–192. doi: 10.1016/S0165-2370(99)00082-0
- Eichhorn YRJ (2001) The young's modulus of a microcrystalline cellulose. *Cellulose* 8:197–207. doi: 10.1023/A:1013181804540
- Eiss NS, McCann BP (1993) Frictional instabilities in polymer-polymer sliding. *Tribol Trans* 36:686–692. doi: 10.1080/10402009308983211
- El-Sehily BM (2016) Fracture Mechanics in Ancient Egypt. *Procedia Struct Integr* 2:2921–2928. doi: 10.1016/j.prostr.2016.06.365
- Elbaum R, Gorb S, Fratzl P (2008) Structures in the cell wall that enable hygroscopic movement of wheat awns. *J Struct Biol* 164:101–107. doi: 10.1016/j.jsb.2008.06.008
- Emri I, Pavsek V (1992) On the influence of moisture on the mechanical properties of polymers. *Met forum* 16:
- Endler A, Persson S (2011) Cellulose Synthases and Synthesis in Arabidopsis. *Mol Plant* 4:199–

211. doi: 10.1093/mp/ssq079

Erbaş A, Horinek D, Netz RR (2012) Viscous Friction of Hydrogen-Bonded Matter. *J Am Chem Soc* 134:623–630. doi: 10.1021/ja209454a

Ergun R, Lietha R, Hartel RW (2010) Moisture and Shelf Life in Sugar Confections. *Crit Rev Food Sci Nutr* 50:162–192. doi: 10.1080/10408390802248833

Eriksson O, Goring DAI, Lindgren BO (1980) Structural studies on the chemical bonds between lignins and carbohydrates in spruce wood. *Wood Sci Technol* 14:267–279. doi: 10.1007/BF00383454

Errington JR, Panagiotopoulos AZ (1998) A Fixed Point Charge Model for Water Optimized to the Vapor–Liquid Coexistence Properties. *J Phys Chem B* 102:7470–7475. doi: 10.1021/jp982068v

Escalante A, Gonçalves A, Bodin A, et al (2012) Flexible oxygen barrier films from spruce xylan. *Carbohydr Polym* 87:2381–2387. doi: 10.1016/j.carbpol.2011.11.003

Esker A, Becker U, Jamin S, et al (2009) Self-Assembly Behavior of Some Co- and Heteropolysaccharides Related to Hemicelluloses. 198–219. doi: 10.1021/bk-2004-0864.ch014

Fabre V, Quandalle G, Billon N, Cantournet S (2018) Time-Temperature-Water content equivalence on dynamic mechanical response of polyamide 6,6. *Polymer (Guildf)* 137:22–29. doi: 10.1016/j.polymer.2017.10.067

Fahlén J, Salmén L (2002) On the lamellar structure of the tracheid cell wall. *Plant Biol* 4:339–345. doi: 10.1055/s-2002-32341

Faisal T, Rey A, Pasini D (2013) A Multiscale Mechanical Model for Plant Tissue Stiffness. *Polymers (Basel)* 5:730–750. doi: 10.3390/polym5020730

Falcoz-Vigne L, Ogawa Y, Molina-Boisseau S, et al (2017) Quantification of a tightly adsorbed monolayer of xylan on cellulose surface. *Cellulose* 24:3725–3739. doi: 10.1007/s10570-017-1401-z

Fengel D, Stoll M (1973) Über die Veränderungen des Zellquerschnitts, der Dicke der Zellwand und der Wandschichten von Fichtenholz-Tracheiden innerhalb eines Jahrringes. *Holzforschung* 27:1–7. doi: 10.1515/hfsg.1973.27.1.1

Fernandes AN, Thomas LH, Altaner CM, et al (2011) Nanostructure of cellulose microfibrils in spruce wood. *Proc Natl Acad Sci U S A* 108:1195–1203. doi: 10.1073/pnas.1108942108

Fessler G, Sadeghi A, Glatzel T, et al (2019) Atomic Friction: Anisotropy and Asymmetry Effects. *Tribol Lett* 67:59. doi: 10.1007/s11249-019-1172-9

Frey-Wyssling A (1954) The Fine Structure of Cellulose Microfibrils. *Science (80- )* 119:80–82. doi: 10.1126/science.119.3081.80



- Gardner KH, Blackwell J (1974) The hydrogen bonding in native cellulose. *BBA - Gen Subj* 343:232–237. doi: 10.1016/0304-4165(74)90256-6
- Gellerstedt G (2015) Softwood kraft lignin: Raw material for the future. *Ind Crops Prod* 77:845–854. doi: 10.1016/j.indcrop.2015.09.040
- Gezici-Koç Ö, Erich SJF, Huinink HP, et al (2017) Bound and free water distribution in wood during water uptake and drying as measured by 1D magnetic resonance imaging. *Cellulose* 24:535–553. doi: 10.1007/s10570-016-1173-x
- Gibson L (2012) The hierarchical structure and mechanics of plant materials. *J R Soc Interface* 9:2749–66. doi: 10.1098/rsif.2012.0341
- Giddings TH (1980) Visualization of particle complexes in the plasma membrane of *Micrasterias denticulata* associated with the formation of cellulose fibrils in primary and secondary cell walls. *J Cell Biol* 84:327–339. doi: 10.1083/jcb.84.2.327
- Gierlinger N, Schwanninger M, Reinecke A, Burgert I (2006) Molecular Changes during Tensile Deformation of Single Wood Fibers Followed by Raman Microscopy. *Biomacromolecules* 7:2077–2081. doi: 10.1021/bm060236g
- Giese M, Blusch LK, Khan MK, et al (2014) Responsive Mesoporous Photonic Cellulose Films by Supramolecular Cotemplating. *Angew Chemie Int Ed* 53:8880–8884. doi: 10.1002/anie.201402214
- Gomes TCF, Skaf MS (2012) Cellulose-Builder: A toolkit for building crystalline structures of cellulose. *J Comput Chem* 33:1338–1346. doi: 10.1002/jcc.22959
- Gorshkova T, Brutch N, Chabbert B, et al (2012) Plant Fiber Formation: State of the Art, Recent and Expected Progress, and Open Questions. *CRC Crit Rev Plant Sci* 31:201–228. doi: 10.1080/07352689.2011.616096
- Grimvall G (1999) *Thermophysical Properties of Materials*. Elsevier
- Gröndahl M, Eriksson L, Gatenholm P (2004) Material Properties of Plasticized Hardwood Xylans for Potential Application as Oxygen Barrier Films. *Biomacromolecules* 5:1528–1535. doi: 10.1021/bm049925n
- Gröndahl M, Teleman A, Gatenholm P (2003) Effect of acetylation on the material properties of glucuronoxylan from aspen wood. *Carbohydr Polym* 52:359–366. doi: 10.1016/S0144-8617(03)00014-6
- Grüneisen E (1912) Theorie des festen Zustandes einatomiger Elemente. *Ann Phys* 344:257–306. doi: 10.1002/andp.19123441202
- Guo J, Du W, Wang S, et al (2017) Cellulose nanocrystals: A layered host candidate for fabricating intercalated nanocomposites. *Carbohydr Polym* 157:79–85. doi: 10.1016/j.carbpol.2016.09.065
- Habibi Y, Lucia LA, Rojas OJ (2010) Cellulose nanocrystals: Chemistry, self-assembly, and

- applications. *Chem Rev* 110:3479–3500. doi: 10.1021/cr900339w
- Hajihassani R, Mohebbi B, Najafi SK, Navi P (2018) Influence of combined hygro-thermo-mechanical treatment on technical characteristics of poplar wood. *Maderas Cienc y Tecnol* 0–0. doi: 10.4067/S0718-221X2018005011001
- Hansen CM (2007) HANSEN SOLUBILITY PARAMETERS A User ' s Handbook Second Edition
- Hanus J, Mazeau K (2006) The xyloglucan–cellulose assembly at the atomic scale. *Biopolymers* 82:59–73. doi: 10.1002/bip.20460
- Hao H, Tam L, Lu Y, Lau D (2018) An atomistic study on the mechanical behavior of bamboo cell wall constituents. *Compos Part B Eng* 151:222–231. doi: 10.1016/j.compositesb.2018.05.046
- Härdelin L (2018) Isolation and chemical modification of arabinoxylan and galactoglucomannan. Chalmers University of Technology
- Harper BD, Rao JM (1994) Some Effects of Water Immersion on the Mechanical Behavior of a Polyimide Film. *J Electron Packag* 116:317. doi: 10.1115/1.2905704
- Harper BD, Rao JM, Kenner VH, Popelar CH (1997) Hygrothermal effects upon stress relaxation in a polyimide film. *J Electron Mater* 26:798–804. doi: 10.1007/s11664-997-0254-x
- Harrington JJ, Astley RJ, Booker R, et al (1998) Modelling the elastic properties of softwood. *Holz als Roh- und Werkst* 56:43–50. doi: 10.1007/s001070050262
- Haynes W. M. (2017) CRC Handbook of Chemistry and Physics, 97th Edition
- Hermans PH, Platzek P (1939) Beiträge zur Kenntnis des Deformationsmechanismus und der Feinstruktur der Hydratzellulose. *Kolloid-Zeitschrift* 88:68–72. doi: 10.1007/BF01518890
- Higuchi T (2014) Biosynthesis of Lignin. In: *Biosynthesis and Biodegradation of Wood Components*. Elsevier, pp 141–160
- Hod O, Meyer E, Zheng Q, Urbakh M (2018) Structural superlubricity and ultralow friction across the length scales. *Nature* 563:485–492. doi: 10.1038/s41586-018-0704-z
- Hodge RM, Bastow TJ, Edward GH, et al (1996a) Free Volume and the Mechanism of Plasticization in Water-Swollen Poly(vinyl alcohol). *Macromolecules* 29:8137–8143. doi: 10.1021/ma951073j
- Hodge RM, Edward GH, Simon GP (1996b) Water absorption and states of water in semicrystalline poly(vinyl alcohol) films. *Polymer (Guildf)* 37:1371–1376. doi: 10.1016/0032-3861(96)81134-7
- Hofstetter K, Hellmich C, Eberhardsteiner J (2005) Development and experimental validation of a continuum micromechanics model for the elasticity of wood. *Eur J Mech - A/Solids* 24:1030–1053. doi: 10.1016/j.euromechsol.2005.05.006

- Höjje A, Gröndahl M, Tømmeraas K, Gatenholm P (2005) Isolation and characterization of physicochemical and material properties of arabinoxylans from barley husks. *Carbohydr Polym* 61:266–275. doi: 10.1016/j.carbpol.2005.02.009
- Hon DN-S, Shiraishi N (2013) *Wood and cellulosic chemistry*. Second edition, revised and expanded
- Horikawa Y (2017) Assessment of cellulose structural variety from different origins using near infrared spectroscopy. *Cellulose* 24:5313–5325. doi: 10.1007/s10570-017-1518-0
- Huang DM, Sendner C, Horinek D, et al (2008) Water slippage versus contact angle: A quasiuniversal relationship. *Phys Rev Lett* 101:. doi: 10.1103/PhysRevLett.101.226101
- Huang R, Becker AA, Jones IA (2012) Modelling cell wall growth using a fibre-reinforced hyperelastic–viscoplastic constitutive law. *J Mech Phys Solids* 60:750–783. doi: 10.1016/j.jmps.2011.12.003
- Inoue M, Norimotoi M, Tanahashi M, Rowell R (1993) Steam or heat fixation of compressed wood. *Wood fiber Sci* 25:224–235
- Israel Urieli (2018) Chapter 2b: Pure Substances: Ideal Gas (updated 1/17/11). [https://www.ohio.edu/mechanical/thermo/Intro/Chapt.1\\_6/Chapter2b.html](https://www.ohio.edu/mechanical/thermo/Intro/Chapt.1_6/Chapter2b.html). Accessed 14 Dec 2018
- Jackson CL, McKenna GB (1990) The melting behavior of organic materials confined in porous solids. *J Chem Phys* 93:9002–9011. doi: 10.1063/1.459240
- Jacobs A, Larsson PT, Dahlman O (2001) Distribution of Uronic Acids in Xylans from Various Species of Soft- and Hardwood As Determined by MALDI Mass Spectrometry. *Biomacromolecules* 2:979–990. doi: 10.1021/bm010062x
- Jakes JE, Plaza N, Zelinka SL, et al (2014) Wood as inspiration for new stimuli-responsive structures and materials. *Proc SPIE - Int Soc Opt Eng* 9055:90550K (13 pp.). doi: 10.1117/12.2045163
- Jarvis MC (2013) Cellulose Biosynthesis: Counting the Chains. *Plant Physiol* 163:1485–1486. doi: 10.1104/pp.113.231092
- Ji B, Gao H (2004) Mechanical properties of nanostructure of biological materials. *J Mech Phys Solids* 52:1963–1990. doi: 10.1016/j.jmps.2004.03.006
- Jian W, Zeng Y, Xiong H, Pang J (2011) Molecular simulation of the complex of konjac glucomannan–borate in water. *Carbohydr Polym* 85:452–456. doi: 10.1016/j.carbpol.2011.03.013
- Jin K, Qin Z, Buehler MJ (2015) Molecular deformation mechanisms of the wood cell wall material. *J Mech Behav Biomed Mater* 42:198–206. doi: 10.1016/j.jmbbm.2014.11.010
- John MJ, Anandjiwala RD (2008) Recent developments in chemical modification and characterization of natural fiber-reinforced composites. *Polym Compos* 29:187–207. doi:

10.1002/pc.20461

- Jones RAL, Kramer EJ, Rafailovich MH, et al (1989) Surface enrichment in an isotopic polymer blend. *Phys Rev Lett* 62:280–283. doi: 10.1103/PhysRevLett.62.280
- Jorgensen WL, Jenson C (1998) Temperature dependence of TIP3P, SPC, and TIP4P water from NPT Monte Carlo simulations: Seeking temperatures of maximum density. *J Comput Chem* 19:1179–1186. doi: 10.1002/(SICI)1096-987X(19980730)19:10<1179::AID-JCC6>3.0.CO;2-J
- Kataoka Y, Kondo T (1999) Quantitative analysis for the cellulose I $\alpha$  crystalline phase in developing wood cell walls. *Int J Biol Macromol* 24:37–41. doi: 10.1016/S0141-8130(98)00065-8
- Kawai S, Benassi A, Gnecco E, et al (2016) Superlubricity of graphene nanoribbons on gold surfaces. *Science* (80-) 351:957–961. doi: 10.1126/science.aad3569
- Keckes J, Burgert I, Frühmann K, et al (2003) Cell-wall recovery after irreversible deformation of wood. *Nat Mater* 2:810–813. doi: 10.1038/nmat1019
- Kellogg RM, Wangaard FF (1969) Variation in the cell-wall density of wood. *Wood Fiber Sci*
- Keplinger T, Cabane E, Berg JK, et al (2016) Smart Hierarchical Bio-Based Materials by Formation of Stimuli-Responsive Hydrogels inside the Microporous Structure of Wood. *Adv Mater Interfaces* 3:1600233. doi: 10.1002/admi.201600233
- Keplinger T, Konnerth J, Aguié-Béghin V, et al (2014) A zoom into the nanoscale texture of secondary cell walls. *Plant Methods* 10:1. doi: 10.1186/1746-4811-10-1
- Kim J-H, Kim J-H, Choi E-S, et al (2013) Colloidal silica nanoparticle-assisted structural control of cellulose nanofiber paper separators for lithium-ion batteries. *J Power Sources* 242:533–540. doi: 10.1016/j.jpowsour.2013.05.142
- Kim JS, Daniel G (2016) Variations in Cell Wall Ultrastructure and Chemistry in Cell Types of Earlywood and Latewood in English Oak (*Quercus Robur*). *IAWA J* 37:383–401. doi: 10.1163/22941932-20160142
- Kollmann F, Krech H (1960) Dynamische Messung der elastischen Holzeigenschaften und der Dämpfung Ein Beitrag zur zerstörungsfreien Werkstoffprüfung. *Holz als Roh- und Werkst* 18:41–54. doi: 10.1007/BF02615616
- Kollmann FFP, Cote W a, Kuenzi EW, Stamm AJ (1968) Principles of Wood Science and Technology
- Koziara KB, Stroet M, Malde AK, Mark AE (2014) Testing and validation of the Automated Topology Builder (ATB) version 2.0: prediction of hydration free enthalpies. *J Comput Aided Mol Des* 28:221–233. doi: 10.1007/s10822-014-9713-7
- Kroon-Batenburg LMJ, Bouma B, Kroon J (1996) Stability of Cellulose Structures Studied by MD Simulations. Could Mercerized Cellulose II Be Parallel? *Macromolecules* 29:5695–5699. doi:

10.1021/ma9518058

Kubicki JD, Yang H, Sawada D, et al (2018) The Shape of Native Plant Cellulose Microfibrils. *Sci Rep* 8:13983. doi: 10.1038/s41598-018-32211-w

Kulasinski K (2015) Physical and Mechanical Aspects of Moisture Adsorption in Wood Biopolymers Investigated with Atomistic Simulations. doi: 10.3929/ethz-a-010564673

Kulasinski K, Derome D, Carmeliet J (2017) Impact of hydration on the micromechanical properties of the polymer composite structure of wood investigated with atomistic simulations. *J Mech Phys Solids* 103:221–235. doi: 10.1016/j.jmps.2017.03.016

Kulasinski K, Guyer R, Derome D, Carmeliet J (2015a) Poroelastic model for adsorption-induced deformation of biopolymers obtained from molecular simulations. *Phys Rev E* 92:022605. doi: 10.1103/PhysRevE.92.022605

Kulasinski K, Guyer R, Derome D, Carmeliet J (2015b) Water Diffusion in Amorphous Hydrophilic Systems: A Stop and Go Process. *Langmuir* 31:10843–10849. doi: 10.1021/acs.langmuir.5b03122

Kulasinski K, Guyer R, Derome D, Carmeliet J (2015c) Water Adsorption in Wood Microfibril-Hemicellulose System: Role of the Crystalline–Amorphous Interface. *Biomacromolecules* 16:2972–2978. doi: 10.1021/acs.biomac.5b00878

Kulasinski K, Guyer R, Keten S, et al (2015d) Impact of moisture adsorption on structure and physical properties of amorphous biopolymers. *Macromolecules* 48:2793–2800. doi: 10.1021/acs.macromol.5b00248

Kulasinski K, Keten S, Churakov S V., et al (2014a) Molecular Mechanism of Moisture-Induced Transition in Amorphous Cellulose. *ACS Macro Lett* 3:1037–1040. doi: 10.1021/mz500528m

Kulasinski K, Keten S, Churakov S V., et al (2014b) A comparative molecular dynamics study of crystalline, paracrystalline and amorphous states of cellulose. *Cellulose* 21:1103–1116. doi: 10.1007/s10570-014-0213-7

Kulasinski K, Salmén L, Derome D, Carmeliet J (2016) Moisture adsorption of glucomannan and xylan hemicelluloses. *Cellulose* 23:1629–1637. doi: 10.1007/s10570-016-0944-8

Kumagai A, Endo T (2018) Comparison of the surface constitutions of hemicelluloses on lignocellulosic nanofibers prepared from softwood and hardwood. *Cellulose* 25:3885–3897. doi: 10.1007/s10570-018-1861-9

Laine K, Segerholm K, Wålinder M, et al (2016) Wood densification and thermal modification: hardness, set-recovery and micromorphology. *Wood Sci Technol* 50:883–894. doi: 10.1007/s00226-016-0835-z

Lavielle L (1991) Polymer-polymer friction: Relation to adhesion. *Wear* 151:63–75. doi: 10.1016/0043-1648(91)90346-V

Lawoko M, Henriksson G, Gellerstedt G (2005) Structural Differences between the

- Lignin–Carbohydrate Complexes Present in Wood and in Chemical Pulps. *Biomacromolecules* 6:3467–3473. doi: 10.1021/bm058014q
- Lee CM, Kubicki JD, Fan B, et al (2015) Hydrogen-Bonding Network and OH Stretch Vibration of Cellulose: Comparison of Computational Modeling with Polarized IR and SFG Spectra. *J Phys Chem B* 119:15138–15149. doi: 10.1021/acs.jpcc.5b08015
- Lee S-H, Wang S, Pharr GM, Xu H (2007) Evaluation of interphase properties in a cellulose fiber-reinforced polypropylene composite by nanoindentation and finite element analysis. *Compos Part A Appl Sci Manuf* 38:1517–1524. doi: 10.1016/j.compositesa.2007.01.007
- Leeman JR, Saffer DM, Scuderi MM, Marone C (2016) Laboratory observations of slow earthquakes and the spectrum of tectonic fault slip modes. *Nat Commun* 7:11104. doi: 10.1038/ncomms11104
- Li S, Bashline L, Zheng Y, et al (2016a) Cellulose synthase complexes act in a concerted fashion to synthesize highly aggregated cellulose in secondary cell walls of plants. *Proc Natl Acad Sci* 113:11348–11353. doi: 10.1073/pnas.1613273113
- Li S, Dickinson LC, Chinachoti P (1998) Mobility of “Unfreezable” and “Freezable” Water in Waxy Corn Starch by  $^2\text{H}$  and  $^1\text{H}$  NMR. *J Agric Food Chem* 46:62–71. doi: 10.1021/jf9609441
- Li X, Shi X, Wang M, Du Y (2011) Xylan chitosan conjugate - A potential food preservative. *Food Chem* 126:520–525. doi: 10.1016/j.foodchem.2010.11.037
- Li Y, Fu Q, Yu S, et al (2016b) Optically Transparent Wood from a Nanoporous Cellulosic Template: Combining Functional and Structural Performance. *Biomacromolecules* 17:1358–1364. doi: 10.1021/acs.biomac.6b00145
- Li Y, Zhu H, Gu H, et al (2013) Strong transparent magnetic nanopaper prepared by immobilization of  $\text{Fe}_3\text{O}_4$  nanoparticles in a nanofibrillated cellulose network. *J Mater Chem A* 1:15278. doi: 10.1039/c3ta12591b
- Lindner B, Petridis L, Schulz R, Smith JC (2013) Solvent-Driven Preferential Association of Lignin with Regions of Crystalline Cellulose in Molecular Dynamics Simulation. *Biomacromolecules* 14:3390–3398. doi: 10.1021/bm400442n
- Lindström H, Evans JW, Verrill SP (1998) Influence of Cambial Age and Growth Conditions on Microfibril Angle in Young Norway Spruce (*Picea abies* [L.] Karst.). *Holzforschung* 52:573–581. doi: 10.1515/hfsg.1998.52.6.573
- Liu Z, Li X, Xie W, Deng H (2017) Extraction, isolation and characterization of nanocrystalline cellulose from industrial kelp (*Laminaria japonica*) waste. *Carbohydr Polym* 173:353–359. doi: 10.1016/j.carbpol.2017.05.079
- Lodge TP, McLeish TCB (2000) Self-Concentrations and Effective Glass Transition Temperatures in Polymer Blends. *Macromolecules* 33:5278–5284. doi: 10.1021/ma9921706

- López-Albarrán P, Pizzi A, Navarro-Santos P, et al (2017) Oligolignols within lignin-adhesive formulations drive their Young's modulus: A ReaxFF-MD study. *Int J Adhes Adhes* 78:227–233. doi: 10.1016/j.ijadhadh.2017.08.003
- Luonteri E, Siika-aho M, Tenkanen M, Viikari L (1995) Purification and characterization of three  $\alpha$ -arabinosidases from *Aspergillus terreus*. *J Biotechnol* 38:279–291. doi: 10.1016/0168-1656(94)00139-4
- Luzar A, Chandler D (1993) Structure and hydrogen bond dynamics of water–dimethyl sulfoxide mixtures by computer simulations. *J Chem Phys* 98:8160–8173. doi: 10.1063/1.464521
- Lyczakowski JJ, Bourdon M, Terrett OM, et al (2019) Structural Imaging of Native Cryo-Preserved Secondary Cell Walls Reveals the Presence of Macrofibrils and Their Formation Requires Normal Cellulose, Lignin and Xylan Biosynthesis. *Front Plant Sci* 10:. doi: 10.3389/fpls.2019.01398
- Ma J, Li X, Bao Y (2015a) Advances in cellulose-based superabsorbent hydrogels. *RSC Adv* 5:59745–59757. doi: 10.1039/C5RA08522E
- Ma L, Gaisinskaya-Kipnis A, Kampf N, Klein J (2015b) Origins of hydration lubrication. *Nat Commun* 6:6060. doi: 10.1038/ncomms7060
- Ma M, Benassi A, Vanossi A, Urbakh M (2015c) Critical Length Limiting Superlow Friction. *Phys Rev Lett* 114:055501. doi: 10.1103/PhysRevLett.114.055501
- Ma Q, Tran Q, Pan C, et al (1998) Polymer/metal Interfaces in Interconnect Structures: Moisture Diffusion and Stress Corrosion Effects. *MRS Proc* 511:329. doi: 10.1557/PROC-511-329
- Malde AK, Zuo L, Breeze M, et al (2011) An Automated Force Field Topology Builder (ATB) and Repository: Version 1.0. *J Chem Theory Comput* 7:4026–4037. doi: 10.1021/ct200196m
- Mar BD, Kulik HJ (2017) Depolymerization pathways for branching lignin spirodienone units revealed with ab initio steered molecular dynamics. *J Phys Chem A* 121:532–5430. doi: 10.1021/acs.jpca.6b11414
- Mark RE (1967) *Cell Wall Mechanics of Tracheids*. Yale University Press
- Mazeau K (2015) The hygroscopic power of amorphous cellulose: A modeling study. *Carbohydr Polym* 117:585–591. doi: 10.1016/j.carbpol.2014.09.095
- Mazeau K, Charlier L (2012) The molecular basis of the adsorption of xylans on cellulose surface. *Cellulose* 19:337–349. doi: 10.1007/s10570-011-9643-7
- Mazeau K, Heux L (2003) Molecular Dynamics Simulations of Bulk Native Crystalline and Amorphous Structures of Cellulose. *J Phys Chem B* 107:2394–2403. doi: 10.1021/jp0219395
- Mazeau K, Moine C, Krausz P, Gloaguen V (2005) Conformational analysis of xylan chains. *Carbohydr Res* 340:2752–2760. doi: 10.1016/j.carres.2005.09.023
- Meshitsuka G, Lee ZZ, Nakano J, Eda S (1982) Studies on the Nature of Lignin - Carbohydrate

- Bonding. *J Wood Chem Technol* 2:251–267. doi: 10.1080/02773818208085134
- Mikkonen KS, Stevanic JS, Pirkkalainen K, et al (2012) Microfibrillated cellulose reinforced galactoglucomannan and arabinoxylan films. In: *ECCM 2012 - Composites at Venice, Proceedings of the 15th European Conference on Composite Materials*
- Mishnaevsky L, Qing H (2008) Micromechanical modelling of mechanical behaviour and strength of wood: State-of-the-art review. *Comput Mater Sci* 44:363–370. doi: 10.1016/j.commatsci.2008.03.043
- Moon RJ, Martini A, Nairn J, et al (2011) Cellulose nanomaterials review: structure, properties and nanocomposites. *Chem Soc Rev* 40:3941. doi: 10.1039/c0cs00108b
- Moreau C, Villares A, Capron I, Cathala B (2015) Tuning supramolecular interactions of cellulose nanocrystals to design innovative functional materials. *Ind Crops Prod.* doi: 10.1016/j.indcrop.2016.02.028
- Mottiar Y, Vanholme R, Boerjan W, et al (2016) Designer lignins: harnessing the plasticity of lignification. *Curr Opin Biotechnol* 37:190–200. doi: 10.1016/j.copbio.2015.10.009
- Muraille L, Aguié-Beghin V, Chabbert B, et al (2017) Bioinspired lignocellulosic films to understand the mechanical properties of lignified plant cell walls at nanoscale. *Sci Rep* 7:44065. doi: 10.1038/srep44065
- Muraille L, Pernes M, Habrant A, et al (2015) Impact of lignin on water sorption properties of bioinspired self-assemblies of lignocellulosic polymers. *Eur Polym J* 64:21–35. doi: 10.1016/j.eurpolymj.2014.11.040
- Murata K, Masuda M (2006) Microscopic observation of transverse swelling of latewood tracheid: effect of macroscopic/mesoscopic structure. *J Wood Sci* 52:283–289. doi: 10.1007/s10086-005-0760-5
- Murphy DM, Koop T (2005) Review of the vapour pressures of ice and supercooled water for atmospheric applications. *Q J R Meteorol Soc* 131:1539–1565. doi: 10.1256/qj.04.94
- Mutwil M, Debolt S, Persson S (2008) Cellulose synthesis: a complex complex. *Curr Opin Plant Biol* 11:252–257. doi: 10.1016/j.pbi.2008.03.007
- Naik DL, Fronk TH (2013) Effective properties of cell wall layers in bast fiber. *Comput Mater Sci* 79:309–315. doi: 10.1016/j.commatsci.2013.06.040
- Nakamura K, Wada M, Kuga S, Okano T (2004) Poisson's Ratio of Cellulose Ia and cellulose II. *J Polym Sci Part B Polym Phys* 42:1206–1211. doi: 10.1002/polb.10771
- Navi P, Heger F (2004) Combined Densification and Thermo-Hydro-Mechanical Processing of Wood. *MRS Bull* 29:332–336. doi: 10.1557/mrs2004.100
- Navi P, Pizzi A (2015) Property changes in thermo-hydro-mechanical processing. *Holzforschung* 69:. doi: 10.1515/hf-2014-0198



- Neagu RC, Gamstedt EK (2007) Modelling of effects of ultrastructural morphology on the hydroelastic properties of wood fibres. *J Mater Sci* 42:10254–10274. doi: 10.1007/s10853-006-1199-9
- Newman RH (1999) Estimation of the Relative Proportions of Cellulose I alpha and I beta in Wood by Carbon-13 NMR Spectroscopy. *Holzforschung* 53:. doi: 10.1515/HF.1999.055
- Newman RH, Hill SJ, Harris PJ (2013) Wide-Angle X-Ray Scattering and Solid-State Nuclear Magnetic Resonance Data Combined to Test Models for Cellulose Microfibrils in Mung Bean Cell Walls. *Plant Physiol* 163:1558–1567. doi: 10.1104/pp.113.228262
- Nielsen LF (1984) Elasticity and Damping of Porous Materials and Impregnated Materials. *J Am Ceram Soc* 67:93–98. doi: 10.1111/j.1151-2916.1984.tb09622.x
- Nishino T, Takano K, Nakamae K (1995) Elastic modulus of the crystalline regions of cellulose polymorphs. *J Polym Sci Part B Polym Phys* 33:1647–1651. doi: 10.1002/polb.1995.090331110
- Nishiyama Y (2009) Structure and properties of the cellulose microfibril. *J Wood Sci* 55:241–249. doi: 10.1007/s10086-009-1029-1
- Nishiyama Y, Langan P, Chanzy H (2002) Crystal Structure and Hydrogen-Bonding System in Cellulose I $\beta$  from Synchrotron X-ray and Neutron Fiber Diffraction. *J Am Chem Soc* 124:9074–9082. doi: 10.1021/ja0257319
- Nixon BT, Mansouri K, Singh A, et al (2016) Comparative Structural and Computational Analysis Supports Eighteen Cellulose Synthases in the Plant Cellulose Synthesis Complex. *Sci Rep* 6:28696. doi: 10.1038/srep28696
- Nogi M, Yano H (2009) Optically transparent nanofiber sheets by deposition of transparent materials: A concept for a roll-to-roll processing. *Appl Phys Lett* 94:233117. doi: 10.1063/1.3154547
- O’Sullivan AC (1997) Cellulose: The structure slowly unravels. *Cellulose* 4:173–207. doi: 10.1023/A:1018431705579
- Oehme DP, Doblin MS, Wagner J, et al (2015) Gaining insight into cell wall cellulose microfibril organisation by simulating microfibril adsorption. *Cellulose* 22:3501–3520. doi: 10.1007/s10570-015-0778-9
- Olsson AM, Salmen L (2004) The softening behavior of hemicelluloses related to moisture. *ACS Symp Ser* 864:184–197. doi: 10.1021/bk-2004-0864.ch013
- Onogi S, Sasaguri K, Adachi T, Ogihara S (1962) Time–humidity superposition in some crystalline polymers. *J Polym Sci* 58:1–17. doi: 10.1002/pol.1962.1205816601
- Oostenbrink C, Villa A, Mark AE, Van Gunsteren WF (2004) A biomolecular force field based on the free enthalpy of hydration and solvation: The GROMOS force-field parameter sets 53A5 and 53A6. *J Comput Chem* 25:1656–1676. doi: 10.1002/jcc.20090

- Özparpucu M, Rüggeberg M, Gierlinger N, et al (2017) Unravelling the impact of lignin on cell wall mechanics: a comprehensive study on young poplar trees downregulated for CINNAMYL ALCOHOL DEHYDROGENASE (CAD). *Plant J* 91:480–490. doi: 10.1111/tpj.13584
- Pakzad A, Simonsen J, Yassar RS (2012) Gradient of nanomechanical properties in the interphase of cellulose nanocrystal composites. *Compos Sci Technol* 72:314–319. doi: 10.1016/j.compscitech.2011.11.020
- Park YB, Cosgrove DJ (2012a) A Revised Architecture of Primary Cell Walls Based on Biomechanical Changes Induced by Substrate-Specific Endoglucanases. *PLANT Physiol* 158:1933–1943. doi: 10.1104/pp.111.192880
- Park YB, Cosgrove DJ (2012b) Changes in Cell Wall Biomechanical Properties in the Xyloglucan-Deficient *xxt1/xxt2* Mutant of Arabidopsis. *Plant Physiol* 158:465–475. doi: 10.1104/pp.111.189779
- Park YB, Cosgrove DJ (2015) Xyloglucan and its interactions with other components of the growing cell wall. *Plant Cell Physiol* 56:180–194. doi: 10.1093/pcp/pcu204
- Parodi E, Peters GWM, Govaert LE (2018) Prediction of plasticity-controlled failure in polyamide 6: Influence of temperature and relative humidity. *J Appl Polym Sci* 135:45942. doi: 10.1002/app.45942
- Patankar KA, Dillard DA, Case SW, et al (2008) Hygrothermal characterization of the viscoelastic properties of Gore-Select® 57 proton exchange membrane. *Mech Time-Dependent Mater* 12:221–236. doi: 10.1007/s11043-008-9059-4
- Patera A, Derome D, Griffa M, Carmeliet J (2013) Hysteresis in swelling and in sorption of wood tissue. *J Struct Biol* 182:226–234. doi: 10.1016/j.jsb.2013.03.003
- Payne CM, Himmel ME, Crowley MF, Beckham GT (2011) Decrystallization of Oligosaccharides from the Cellulose I $\beta$  Surface with Molecular Simulation. *J Phys Chem Lett* 2:1546–1550. doi: 10.1021/jz2005122
- Pereira CS, Silveira RL, Dupree P, Skaf MS (2017) Effects of Xylan Side-Chain Substitutions on Xylan–Cellulose Interactions and Implications for Thermal Pretreatment of Cellulosic Biomass. *Biomacromolecules* 18:1311–1321. doi: 10.1021/acs.biomac.7b00067
- Petridis L, O'Neill HM, Johnsen M, et al (2014) Hydration Control of the Mechanical and Dynamical Properties of Cellulose. *Biomacromolecules* 15:4152–4159. doi: 10.1021/bm5011849
- Petridis L, Pingali SV, Urban V, et al (2011a) Self-similar multiscale structure of lignin revealed by neutron scattering and molecular dynamics simulation. *Phys Rev E* 83:061911. doi: 10.1103/PhysRevE.83.061911
- Petridis L, Schulz R, Smith JC (2011b) Simulation analysis of the temperature dependence of lignin structure and dynamics. *J Am Chem Soc* 133:20277–87. doi: 10.1021/ja206839u

- Petridis L, Smith JC (2009) A molecular mechanics force field for lignin. *J Comput Chem* 30:457–467. doi: 10.1002/jcc.21075
- Pettersen RC (1984) *The Chemical Composition of Wood*. pp 57–126
- Pienaar FRP, Eaton NJ, Pizzi A (1989) Elastic moduli of amorphous cellulose—a conformational analysis approach. *J Macromol Sci Part B* 28:115–129. doi: 10.1080/00222348908212330
- Piggott MR (1989) Tailored Interphases in Fibre Reinforced Polymers. *MRS Proc* 170:265. doi: 10.1557/PROC-170-265
- Pitera JW, van Gunsteren WF (2001) One-Step Perturbation Methods for Solvation Free Energies of Polar Solutes. *J Phys Chem B* 105:11264–11274. doi: 10.1021/jp012003j
- Pitkethly MJ, Doble JB (1990) Characterizing the fibre/matrix interface of carbon fibre-reinforced composites using a single fibre pull-out test. *Composites* 21:389–395. doi: 10.1016/0010-4361(90)90436-Z
- Plaza N, Zelinka SL, Stone DS, et al (2013) Plant-based torsional actuator with memory. *Smart Mater Struct* 22:072001. doi: 10.1088/0964-1726/22/7/072001
- Prakobna K, Galland S, Berglund LA (2015) High-Performance and Moisture-Stable Cellulose–Starch Nanocomposites Based on Bioinspired Core–Shell Nanofibers. *Biomacromolecules* 16:904–912. doi: 10.1021/bm5018194
- Price DL, Fernandez-Alonso F (2013) *An Introduction to Neutron Scattering*. pp 1–136
- Qing H, Mishnaevsky L (2010) 3D multiscale micromechanical model of wood: From annual rings to microfibrils. *Int J Solids Struct* 47:1253–1267. doi: 10.1016/j.ijsolstr.2010.01.014
- Qing H, Mishnaevsky L (2009) 3D hierarchical computational model of wood as a cellular material with fibril reinforced, heterogeneous multiple layers. *Mech Mater* 41:1034–1049. doi: 10.1016/j.mechmat.2009.04.011
- Rafsanjani A, Derome D, Carmeliet J (2015) Poromechanical modeling of moisture induced swelling anisotropy in cellular tissues of softwoods. *RSC Adv* 5:3560–3566. doi: 10.1039/C4RA14074E
- Rafsanjani A, Stiefel M, Jefimovs K, et al (2014) Hygroscopic swelling and shrinkage of latewood cell wall micropillars reveal ultrastructural anisotropy. *J R Soc Interface* 11:20140126–20140126. doi: 10.1098/rsif.2014.0126
- Reale Batista MD, Drzal LT (2018) Carbon fiber/epoxy matrix composite interphases modified with cellulose nanocrystals. *Compos Sci Technol* 164:274–281. doi: 10.1016/j.compscitech.2018.05.010
- Reid JSG (1997) *Carbohydrate Metabolism: Structural Carbohydrates*. In: *Plant Biochemistry*. Elsevier, pp 205–236
- Reising AB, Moon RJ, Youngblood JP (2012) Effect of particle alignment on mechanical

properties of neat cellulose nanocrystal films. *J-for* 2:32–41

- Rennel J, Dillén S (2001) Pulp and Paper: Wood Sources. In: *Encyclopedia of Materials: Science and Technology*. Elsevier, pp 7913–7917
- Riggleman RA, Douglas JF, de Pablo JJ (2010) Antiplasticization and the elastic properties of glass-forming polymer liquids. *Soft Matter* 6:292–304. doi: 10.1039/B915592A
- Rindler A, Vay O, Hansmann C, Müller U (2017) Dimensional stability of multi-layered wood-based panels: a review. *Wood Sci Technol* 51:969–996. doi: 10.1007/s00226-017-0940-7
- Roduner E Thermodynamics of Finite Size Systems. In: *Nanoscopic Materials*. Royal Society of Chemistry, Cambridge, pp 119–162
- Rowland SP, Roberts EJ (1972) The nature of accessible surfaces in the microstructure of cotton cellulose. *J Polym Sci Part A-1 Polym Chem* 10:2447–2461. doi: 10.1002/pol.1972.150100819
- Ruel K, Joseleau J. . (2005) Deposition of hemicelluloses and lignins during secondary wood cell wall assembly. *Hemicellul Work* 103–113
- Rusli R, Eichhorn SJ (2008) Determination of the stiffness of cellulose nanowhiskers and the fiber-matrix interface in a nanocomposite using Raman spectroscopy. *Appl Phys Lett* 93:033111. doi: 10.1063/1.2963491
- Saifouni O, Destrebecq J-F, Froidevaux J, Navi P (2016) Experimental study of the mechanosorptive behaviour of softwood in relaxation. *Wood Sci Technol* 50:789–805. doi: 10.1007/s00226-016-0816-2
- Sakurada I, Nukushina Y, Ito T (1962) Experimental determination of the elastic modulus of crystalline regions in oriented polymers. *J Polym Sci* 57:651–660. doi: 10.1002/pol.1962.1205716551
- Salmén L (2004) Micromechanical understanding of the cell-wall structure. *Comptes Rendus - Biol* 327:873–880. doi: 10.1016/j.crv.2004.03.010
- Salmén L, Bergström E (2009) Cellulose structural arrangement in relation to spectral changes in tensile loading FTIR. *Cellulose* 16:975–982. doi: 10.1007/s10570-009-9331-z
- Salmén L, Burgert I (2009) Cell wall features with regard to mechanical performance. A review COST Action E35 2004–2008: Wood machining – micromechanics and fracture. *Holzforschung* 63:121–129. doi: 10.1515/HF.2009.011
- Salmén L, Fahlén J (2006) Reflections on the ultrastructure of softwood fibers. *Cellul Chem Technol* 40:181–185
- Salmén L, Olsson AM, Stevanic JS, et al (2012) Structural organisation of the wood polymers in the wood fibre structure. *BioResources* 7:521–532
- Samuels AL, Kaneda M, Rensing KH (2006) The cell biology of wood formation: from cambial

divisions to mature secondary xylem This review is one of a selection of papers published in the Special Issue on Plant Cell Biology. *Can J Bot* 84:631–639. doi: 10.1139/b06-065

Scheller HV, Ulvskov P (2010) Hemicelluloses. *Annu Rev Plant Biol* 61:263–289. doi: 10.1146/annurev-arplant-042809-112315

Schlaich A, Knapp EW, Netz RR (2016) Water Dielectric Effects in Planar Confinement. *Phys Rev Lett* 117:048001. doi: 10.1103/PhysRevLett.117.048001

Seborg CO, Stamm AJ (1931) Sorption of Water Vapor by Paper-Marking Materials I—Effect of Beating 1. *Ind Eng Chem* 23:1271–1275. doi: 10.1021/ie50263a018

Sedlmeyer FB (2011) Xylan as by-product of biorefineries: Characteristics and potential use for food applications. *Food Hydrocoll* 25:1891–1898. doi: 10.1016/j.foodhyd.2011.04.005

Sell J, Zimmermann T (1993) Radial fibril agglomerations of the S2 on transverse-fracture surfaces of tracheids of tension-loaded spruce and white fir. *Holz als Roh- und Werkst* 51:384–384. doi: 10.1007/BF02628234

Sell J, Zimmermann T (1998) The fine structure of the cell wall of hardwoods on transverse-fracture surfaces. *Holz als Roh- und Werkst* 56:365–366. doi: 10.1007/s001070050334

Shanmuganathan K, Capadona JR, Rowan SJ, Weder C (2010) Bio-inspired mechanically-adaptive nanocomposites derived from cotton cellulose whiskers. *J Mater Chem* 20:180–186. doi: 10.1039/B916130A

Shinjo K, Hirano M (1993) Dynamics of friction: superlubric state. *Surf Sci* 283:473–478. doi: 10.1016/0039-6028(93)91022-H

Shrake A, Rupley JA (1973) Environment and exposure to solvent of protein atoms. Lysozyme and insulin. *J Mol Biol* 79:351–371. doi: 10.1016/0022-2836(73)90011-9

Silberstein MN, Pillai P V., Boyce MC (2011) Biaxial elastic–viscoplastic behavior of Nafion membranes. *Polymer (Guildf)* 52:529–539. doi: 10.1016/j.polymer.2010.11.032

Sing KSW (1985) Reporting physisorption data for gas/solid systems with special reference to the determination of surface area and porosity (Recommendations 1984). *Pure Appl Chem* 57:603–619. doi: 10.1351/pac198557040603

Sinko R, Keten S (2015) Traction-separation laws and stick-slip shear phenomenon of interfaces between cellulose nanocrystals. *J Mech Phys Solids* 78:526–539. doi: 10.1016/j.jmps.2015.02.012

Sinko R, Keten S (2014) Effect of moisture on the traction-separation behavior of cellulose nanocrystal interfaces. *Appl Phys Lett* 105:243702. doi: 10.1063/1.4904708

Sinko R, Mishra S, Ruiz L, et al (2014) Dimensions of Biological Cellulose Nanocrystals Maximize Fracture Strength. *ACS Macro Lett* 3:64–69. doi: 10.1021/mz400471y

Sinko R, Qin X, Keten S (2015) Interfacial mechanics of cellulose nanocrystals. *MRS Bull* 40:340–

348. doi: 10.1557/mrs.2015.67

Sinko R, Vandamme M, Bažant ZP, Keten S (2016) Transient effects of drying creep in nanoporous solids: understanding the effects of nanoscale energy barriers. *Proc R Soc A Math Phys Eng Sci* 472:20160490. doi: 10.1098/rspa.2016.0490

Skaar C (1988) *Wood-Water Relations*. Springer Berlin Heidelberg, Berlin, Heidelberg

Soboyejo W (2002) *Mechanical Properties of Engineered Materials*

Soper AK, Phillips MG (1986) A new determination of the structure of water at 25°C. *Chem Phys* 107:47–60. doi: 10.1016/0301-0104(86)85058-3

Sorieul M, Dickson A, Hill S, Pearson H (2016) Plant Fibre: Molecular Structure and Biomechanical Properties, of a Complex Living Material, Influencing Its Deconstruction towards a Biobased Composite. *Materials (Basel)* 9:618. doi: 10.3390/ma9080618

Speck T, Burgert I (2011) Plant Stems: Functional Design and Mechanics. *Annu Rev Mater Res* 41:169–193. doi: 10.1146/annurev-matsci-062910-100425

Srisuk N (2010) A Micromechanics Model of Thermal Expansion Coefficient In Fibre Reinforced Composites

Srndovic JS (2011) Interactions between Wood Polymers in Wood Cell Walls and Cellulose/Hemicellulose Biocomposites

St. Lawrence S, Willett JL, Carriere CJ (2001) Effect of moisture on the tensile properties of poly(hydroxy ester ether)

Stamm A, Woodruff S (1941) Convenient Six-Tube Vapor Sorption Apparatus. *Ind Eng Chem Anal Ed* 13:836–838. doi: 10.1021/i560099a034

Stamm AJ (1938) Calculations of the Void Volume in Wood. *Ind Eng Chem* 30:1280–1281. doi: 10.1021/ie50347a017

Stamm AJ (1964) *Wood and cellulose science*

Stevanic JS, Mikkonen KS, Xu C, et al (2014) Wood cell wall mimicking for composite films of spruce nanofibrillated cellulose with spruce galactoglucomannan and arabinoglucuronoxylan. *J Mater Sci* 49:5043–5055. doi: 10.1007/s10853-014-8210-7

Stevanic JS, Salmén L (2009) Orientation of the wood polymers in the cell wall of spruce wood fibres. *Holzforschung* 63:.. doi: 10.1515/HF.2009.094

Šturcová A, Davies GR, Eichhorn SJ (2005) Elastic Modulus and Stress-Transfer Properties of Tunicate Cellulose Whiskers. *Biomacromolecules* 6:1055–1061. doi: 10.1021/bm049291k

Suarez-Martinez PC, Batys P, Sammalkorpi M, Lutkenhaus JL (2019) Time–Temperature and Time–Water Superposition Principles Applied to Poly(allylamine)/Poly(acrylic acid) Complexes. *Macromolecules* 52:3066–3074. doi: 10.1021/acs.macromol.8b02512

- Sun Z, Zhao X, Wang X, Ma J (2014) Multiscale modeling of the elastic properties of natural fibers based on a generalized method of cells and laminate analogy approach. *Cellulose* 21:1135–1141. doi: 10.1007/s10570-014-0201-y
- Tabor D (2013) *Gases, liquids and solids: and other states of matter*. Cambridge University Press
- Takeichi Y, Yoshida M, Kitano K, et al (2013) In situ measurement of tensile elastic moduli of individual component polymers with a 3D assembly mode in wood cell walls. *J Wood Sci* 59:104–111. doi: 10.1007/s10086-012-1315-1
- Tam L, Lau D (2016) Micromechanics of Wood Cell Wall. *MRS Adv* 1:3837–3845. doi: 10.1557/adv.2016.50
- Tam L, Zhou A, Yu Z, et al (2017) Understanding the effect of temperature on the interfacial behavior of CFRP-wood composite via molecular dynamics simulations. *Compos Part B Eng* 109:227–237. doi: 10.1016/j.compositesb.2016.10.030
- Tanaka F, Iwata T (2006) Estimation of the Elastic Modulus of Cellulose Crystal by Molecular Mechanics Simulation. *Cellulose* 13:509–517. doi: 10.1007/s10570-006-9068-x
- Tanner SF, Hills BP, Parker R (1991) Interactions of sorbed water with starch studied using proton nuclear magnetic resonance spectroscopy. *J Chem Soc Faraday Trans* 87:2613. doi: 10.1039/ft9918702613
- Tashiro K, Kobayashi M (1991) Theoretical evaluation of three-dimensional elastic constants of native and regenerated celluloses: role of hydrogen bonds. *Polymer (Guildf)* 32:1516–1526. doi: 10.1016/0032-3861(91)90435-L
- Teixeira J, Bellissent-Funel MC (1990) Dynamics of water studied by neutron scattering. *J Phys Condens Matter* 2:. doi: 10.1088/0953-8984/2/S/011
- Tejado A, Alam MN, Antal M, et al (2012) Energy requirements for the disintegration of cellulose fibers into cellulose nanofibers. *Cellulose* 19:831–842. doi: 10.1007/s10570-012-9694-4
- Teklal F, Djebbar A, Allaoui S, et al (2018) A review of analytical models to describe pull-out behavior – Fiber/matrix adhesion. *Compos Struct* 201:791–815. doi: 10.1016/j.compstruct.2018.06.091
- Teleman A, Lundqvist J, Tjerneld F, et al (2000) Characterization of acetylated 4-O-methylglucuronoxylan isolated from aspen employing <sup>1</sup>H and <sup>13</sup>C NMR spectroscopy. *Carbohydr Res* 329:807–815. doi: 10.1016/S0008-6215(00)00249-4
- Terashima N (1990) A New Mechanism for Formation of a Structurally Ordered Protolignin Macromolecule in the Cell-Wall of Tree Xylem. *J Pulp Pap Sci* 16:J150–J155
- Terashima N, Kitano K, Kojima M, et al (2009) Nanostructural assembly of cellulose, hemicellulose, and lignin in the middle layer of secondary wall of ginkgo tracheid. *J Wood Sci* 55:409–416. doi: 10.1007/s10086-009-1049-x
- Terrett OM, Lyczakowski JJ, Yu L, et al (2019) Molecular architecture of softwood revealed by

- solid-state NMR. *Nat Commun* 10:. doi: 10.1038/s41467-019-12979-9
- Theodorou DN, Suter UW (1986) Atomistic Modeling of Mechanical Properties of Polymeric Glasses. *Macromolecules* 19:139–154. doi: 10.1021/ma00155a022
- Thomas LH, Forsyth VT, Sturcova A, et al (2013) Structure of Cellulose Microfibrils in Primary Cell Walls from Collenchyma. *PLANT Physiol* 161:465–476. doi: 10.1104/pp.112.206359
- Thuvander F, Kifetew G, Berglund LA (2002) Modeling of cell wall drying stresses in wood. *Wood Sci Technol* 36:241–254. doi: 10.1007/s00226-001-0134-0
- Trache D, Hussin MH, Haafiz MKM, Thakur VK (2017) Recent progress in cellulose nanocrystals: sources and production. *Nanoscale* 9:1763–1786. doi: 10.1039/C6NR09494E
- Ugolev BN (2014) Wood as a natural smart material. *Wood Sci Technol* 48:553–568. doi: 10.1007/s00226-013-0611-2
- Ünlü CH, Günister E, Atici O (2009) Synthesis and characterization of NaMt biocomposites with corn cob xylan in aqueous media. *Carbohydr Polym* 76:585–592. doi: 10.1016/j.carbpol.2008.11.029
- Usov I, Nyström G, Adamcik J, et al (2015) Understanding nanocellulose chirality and structure–properties relationship at the single fibril level. *Nat Commun* 6:7564. doi: 10.1038/ncomms8564
- Valentin D, Paray F, Guetta B (1987) The hygrothermal behaviour of glass fibre reinforced Pa66 composites: A study of the effect of water absorption on their mechanical properties. *J Mater Sci* 22:46–56. doi: 10.1007/BF01160550
- van Zanten JH, Rufener KP (2000) Brownian motion in a single relaxation time Maxwell fluid. *Phys Rev E* 62:5389–5396. doi: 10.1103/PhysRevE.62.5389
- Verbeek C (ed) (2012) *Products and Applications of Biopolymers*. InTech
- Vermaas J V., Dellon LD, Broadbelt LJ, et al (2019a) Automated Transformation of Lignin Topologies into Atomic Structures with LigninBuilder. *ACS Sustain Chem Eng* 7:3443–3453. doi: 10.1021/acssuschemeng.8b05665
- Vermaas J V., Petridis L, Qi X, et al (2015) Mechanism of lignin inhibition of enzymatic biomass deconstruction. *Biotechnol Biofuels* 8:217. doi: 10.1186/s13068-015-0379-8
- Vermaas J V., Petridis L, Ralph J, et al (2019b) Systematic parameterization of lignin for the CHARMM force field. *Green Chem* 21:109–122. doi: 10.1039/C8GC03209B
- Vural D, Gainaru C, O’Neill H, et al (2018a) Impact of hydration and temperature history on the structure and dynamics of lignin. *Green Chem* 20:1602–1611. doi: 10.1039/C7GC03796A
- Vural D, Smith JC, Petridis L (2018b) Dynamics of the lignin glass transition. *Phys Chem Chem Phys* 20:20504–20512. doi: 10.1039/C8CP03144D



- Waller I (1923) Zur Frage der Einwirkung der Wärmebewegung auf die Interferenz von Röntgenstrahlen. *Zeitschrift für Phys* 17:398–408. doi: 10.1007/BF01328696
- Wang H, Lin E, Xu G (2017) Molecular dynamics simulation of asphalt-aggregate interface adhesion strength with moisture effect. *Int J Pavement Eng* 18:414–423. doi: 10.1080/10298436.2015.1095297
- Wang M, Yao MN, Jian WJ, et al (2010) Molecular dynamics simulations of the interactions between konjac glucomannan and soy protein isolate. *Agric Sci China* 9:1538–1542. doi: 10.1016/S1671-2927(09)60248-0
- Wang Y, Chantreau M, Sibout R, Hawkins S (2013) Plant cell wall lignification and monolignol metabolism. *Front Plant Sci* 4:. doi: 10.3389/fpls.2013.00220
- Wei Z, Sinko R, Keten S, Luijten E (2018) Effect of Surface Modification on Water Adsorption and Interfacial Mechanics of Cellulose Nanocrystals. *ACS Appl Mater Interfaces* 10:8349–8358. doi: 10.1021/acsami.7b18803
- Weiss M, Elmer F-J (1996) Dry friction in the Frenkel-Kontorova-Tomlinson model: Static properties. *Phys Rev B* 53:7539–7549. doi: 10.1103/PhysRevB.53.7539
- Weng Z, Su Y, Wang D-W, et al (2011) Graphene-Cellulose Paper Flexible Supercapacitors. *Adv Energy Mater* 1:917–922. doi: 10.1002/aenm.201100312
- Wessling B (1991) Electrical conductivity in heterogeneous polymer systems. V (1): Further experimental evidence for a phase transition at the critical volume concentration. *Polym Eng Sci* 31:1200–1206. doi: 10.1002/pen.760311608
- Westbye P, Köhnke T, Gatenholm P (2008) Fractionation and characterization of xylan rich extracts from birch. *Holzforschung* 62:. doi: 10.1515/HF.2008.005
- Williams ML, Landel RF, Ferry JD (1955) The Temperature Dependence of Relaxation Mechanisms in Amorphous Polymers and Other Glass-forming Liquids. *J Am Chem Soc* 77:3701–3707. doi: 10.1021/ja01619a008
- Wohlert J, Berglund LA (2011) A Coarse-Grained Model for Molecular Dynamics Simulations of Native Cellulose. *J Chem Theory Comput* 7:753–760. doi: 10.1021/ct100489z
- Wu J, Yuan Q (2002) Gas permeability of a novel cellulose membrane. *J Memb Sci* 204:185–194. doi: 10.1016/S0376-7388(02)00037-6
- Wu X, Moon RJ, Martini A (2014) Tensile strength of I $\beta$  crystalline cellulose predicted by molecular dynamics simulation. *Cellulose* 21:2233–2245. doi: 10.1007/s10570-014-0325-0
- Wu X, Moon RJ, Martini A (2013a) Crystalline cellulose elastic modulus predicted by atomistic models of uniform deformation and nanoscale indentation. *Cellulose* 20:43–55. doi: 10.1007/s10570-012-9823-0
- Wu X, Moon RJ, Martini A (2013b) Atomistic Simulation of Frictional Sliding Between Cellulose I $\beta$  Nanocrystals. *Tribol Lett* 52:395–405. doi: 10.1007/s11249-013-0223-x

- Xia W, Qin X, Zhang Y, et al (2018) Achieving Enhanced Interfacial Adhesion and Dispersion in Cellulose Nanocomposites via Amorphous Interfaces. *Macromolecules* 51:10304–10311. doi: 10.1021/acs.macromol.8b02243
- Xia W, Song J, Jeong C, et al (2017) Energy-Renormalization for Achieving Temperature Transferable Coarse-Graining of Polymer Dynamics. *Macromolecules* 50:8787–8796. doi: 10.1021/acs.macromol.7b01717
- Xiao C, Zhang T, Zheng Y, et al (2016a) Xyloglucan Deficiency Disrupts Microtubule Stability and Cellulose Biosynthesis in Arabidopsis, Altering Cell Growth and Morphogenesis. *Plant Physiol* 170:234–249. doi: 10.1104/pp.15.01395
- Xiao S, He J, Zhang Z (2016b) Nanoscale deicing by molecular dynamics simulation. *Nanoscale* 8:14625–14632. doi: 10.1039/C6NR02398C
- Xiao X, Hu J (2016) Animal Hairs as Water-stimulated Shape Memory Materials: Mechanism and Structural Networks in Molecular Assemblies. *Sci Rep* 6:26393. doi: 10.1038/srep26393
- Xin D, Han Q (2013) Investigation of moisture diffusion in cross-linked epoxy moulding compound by molecular dynamics simulation. *Mol Simul* 39:322–329. doi: 10.1080/08927022.2012.725204
- Xu C, Leppänen A-S, Eklund P, et al (2010) Acetylation and characterization of spruce (*Picea abies*) galactoglucomannans. *Carbohydr Res* 345:810–816. doi: 10.1016/j.carres.2010.01.007
- Xu C, Pranovich A, Vähäsalo L, et al (2008) Kinetics of Acid Hydrolysis of Water-Soluble Spruce O-Acetyl Galactoglucomannans. *J Agric Food Chem* 56:2429–2435. doi: 10.1021/jf703702y
- Yamamoto H (2004) Role of the gelatinous layer on the origin of the physical properties of the tension wood. *J Wood Sci* 50:197–208. doi: 10.1007/s10086-003-0556-4
- Yamamoto H, Kojima Y (2002) Properties of cell wall constituents in relation to longitudinal elasticity of wood. *Wood Sci Technol* 36:55–74. doi: 10.1007/s00226-001-0128-y
- Yamasaki T, Enomoto A, Kato A, et al (2011) Structural unit of xylans from sugi (*Cryptomeria japonica*) and hinoki (*Chamaecyparis obtusa*). *J Wood Sci* 57:76–84. doi: 10.1007/s10086-010-1139-9
- Yanez AJ, Li W, Mabon R, Broadbelt LJ (2016) A Stochastic Method to Generate Libraries of Structural Representations of Lignin. *Energy & Fuels* 30:5835–5845. doi: 10.1021/acs.energyfuels.6b00966
- Yang H, Yan R, Chen H, et al (2006) In-Depth Investigation of Biomass Pyrolysis Based on Three Major Components: Hemicellulose, Cellulose and Lignin. *Energy & Fuels* 20:388–393. doi: 10.1021/ef0580117
- Yoshizawa H, Israelachvili J (1993) Fundamental mechanisms of interfacial friction. 2. Stick-slip friction of spherical and chain molecules. *J Phys Chem* 97:11300–11313. doi: 10.1021/j100145a031

- Youssefian S, Rahbar N (2015) Molecular Origin of Strength and Stiffness in Bamboo Fibrils. *Sci Rep* 5:11116. doi: 10.1038/srep11116
- Yu L, Lyczakowski JJ, Pereira CS, et al (2018) The Patterned Structure of Galactoglucomannan Suggests It May Bind to Cellulose in Seed Mucilage. *Plant Physiol* 178:1011–1026. doi: 10.1104/pp.18.00709
- Zaccai G (2000) How Soft Is a Protein? A Protein Dynamics Force Constant Measured by Neutron Scattering. *Science* (80- ) 288:1604–1607. doi: 10.1126/science.288.5471.1604
- Zarges J-C, Kaufhold C, Feldmann M, Heim H-P (2018) Single fiber pull-out test of regenerated cellulose fibers in polypropylene: An energetic evaluation. *Compos Part A Appl Sci Manuf* 105:19–27. doi: 10.1016/j.compositesa.2017.10.030
- Zhang C, Coasne B, Guyer R, et al (2020) Moisture-induced crossover in the thermodynamic and mechanical response of hydrophilic biopolymer. *Cellulose* 27:89–99. doi: 10.1007/s10570-019-02808-z
- Zhang N, Li S, Xiong L, et al (2015) Cellulose-hemicellulose interaction in wood secondary cell-wall. *Model Simul Mater Sci Eng* 23:085010. doi: 10.1088/0965-0393/23/8/085010
- Zhang T, Li X, Guo L (2017) Initial Reactivity of Linkages and Monomer Rings in Lignin Pyrolysis Revealed by ReaxFF Molecular Dynamics. *Langmuir* 33:11646–11657. doi: 10.1021/acs.langmuir.7b02053
- Zhang T, Mahgoudy-Louyeh S, Tittmann B, Cosgrove DJ (2014) Visualization of the nanoscale pattern of recently-deposited cellulose microfibrils and matrix materials in never-dried primary walls of the onion epidermis. *Cellulose* 21:853–862. doi: 10.1007/s10570-013-9996-1
- Zhang T, Zheng Y, Cosgrove DJ (2016) Spatial organization of cellulose microfibrils and matrix polysaccharides in primary plant cell walls as imaged by multichannel atomic force microscopy. *Plant J* 85:179–192. doi: 10.1111/tpj.13102
- Zhang Y, Batys P, O’Neal JT, et al (2018) Molecular Origin of the Glass Transition in Polyelectrolyte Assemblies. *ACS Cent Sci* 4:638–644. doi: 10.1021/acscentsci.8b00137
- Zhao C, Liu Q, Ren L, et al (2017) A 3D micromechanical study of hygroscopic coiling deformation in *Pelargonium* seed: from material and mechanics perspective. *J Mater Sci* 52:415–430. doi: 10.1007/s10853-016-0341-6
- Zhao H, Chen Z, Du X, Chen L (2019) Contribution of different state of adsorbed water to the sub-Tg dynamics of cellulose. *Carbohydr Polym* 210:322–331. doi: 10.1016/j.carbpol.2019.01.087
- Zhao S, Zhang Z, Sèbe G, et al (2015) Multiscale Assembly of Superinsulating Silica Aerogels Within Silylated Nanocellulosic Scaffolds: Improved Mechanical Properties Promoted by Nanoscale Chemical Compatibilization. *Adv Funct Mater* 25:2326–2334. doi: 10.1002/adfm.201404368

- Zhao Z, Crespi VH, Kubicki JD, et al (2014) Molecular dynamics simulation study of xyloglucan adsorption on cellulose surfaces: effects of surface hydrophobicity and side-chain variation. *Cellulose* 21:1025–1039. doi: 10.1007/s10570-013-0041-1
- Zhu H, Jia Z, Chen Y, et al (2013) Tin Anode for Sodium-Ion Batteries Using Natural Wood Fiber as a Mechanical Buffer and Electrolyte Reservoir. *Nano Lett* 13:3093–3100. doi: 10.1021/nl400998t
- Zhu H, Luo W, Ciesielski PN, et al (2016a) Wood-Derived Materials for Green Electronics, Biological Devices, and Energy Applications. *Chem Rev* 116:9305–9374. doi: 10.1021/acs.chemrev.6b00225
- Zhu M, Song J, Li T, et al (2016b) Highly Anisotropic, Highly Transparent Wood Composites. *Adv Mater* 28:5181–5187. doi: 10.1002/adma.201600427
- Zhu Y, Hu J, Luo H, et al (2012) Rapidly switchable water-sensitive shape-memory cellulose/elastomer nano-composites. *Soft Matter* 8:2509. doi: 10.1039/c2sm07035a
- Zillig W (2009) Moisture transport in wood using a multiscale approach. 202
- Zimmermann T, Thommen V, Reimann P, Hug HJ (2006) Ultrastructural appearance of embedded and polished wood cell walls as revealed by Atomic Force Microscopy. *J Struct Biol* 156:363–369. doi: 10.1016/j.jsb.2006.06.007